Applications of Single-Walled Carbon Nanotubes in Organic Electronics

Doctoral Thesis

Brendan Mirka, B. Eng.

Supervisor: Prof. Benoît H. Lessard

uOttawa

University of Ottawa

Department of Chemical and Biological Engineering

© Brendan Mirka, Ottawa, Canada, 2022

All Rights Reserved

Ph.D. in Chemical Engineering University of Ottawa

Department of Chemical and Biological Engineering Ottawa ON, Canada

TITLE: Applications of Single-Walled Carbon Nanotubes in Organic Electronics

AUTHOR: Brendan Mirka

B. Eng., Chemical Engineering

Laurentian University, Sudbury ON, Canada

SUPERVISOR: Professor Benoît H. Lessard

NUMBER OF PAGES: 207

Abstract

Electronic applications have expanded to encompass a variety of materials. In particular, allotropes of carbon interest researchers for their electronic applications. Knowledge of carbon allotropes and their applications has expanded significantly since the discovery of C_{60} Buckminsterfullerene in 1985, the discovery of multi- and single-walled carbon nanotubes in the early 1990s, and the isolation of graphene in 2004. Single-walled carbon nanotubes (SWNTs) have the potential to bring next-generation electronic devices to fruition. Such devices could be flexible, conformable, and inexpensive. SWNT-based electronics are promising for chemical and biological sensing applications, for example, where high carrier mobilities are unnecessary, and material conformity and inexpensive processing are significant advantages. Considerable progress has been made in separating semiconducting SWNTs from metallic SWNTs, enabling SWNT incorporation into semiconducting electronic technologies. Selective sorting of semiconducting SWNTs using π-conjugated polymers is an effective and efficient technique to enrich large quantities of ultra-pure semiconducting SWNTs. Following semiconducting enrichment, SWNTs can be incorporated into electronic devices.

This thesis focuses on the enrichment of semiconducting SWNTs via conjugated polymer extraction and incorporating the resulting polymer-SWNT dispersions into thin-film transistors (TFTs). Novel copolymers were investigated for their capacity to selectively sort and disperse large-diameter sc-SWNTs synthesized using the plasma torch technique. Absorption and Raman spectroscopy were employed to monitor the efficacy of the conjugated polymer extraction procedure. Following enrichment, the polymer-SWNT dispersions were incorporated into TFTs. The interaction between the conjugated polymer and the SWNT and the conjugated polymer and dielectric was an essential component of TFT optimization. Furthermore, the procedure of sorting and dispersing sc-SWNTs is investigated for its effect on TFT performance and was another component of TFT optimization. TFTs were electrically characterized in terms of carrier mobility, threshold voltage, hysteresis, and current on/off ratio. The film morphology of the SWNT TFTs was also investigated. Atomic force microscopy and Raman mapping were used to provide insight into the nanometre and micrometre scale film morphology, respectively.

Abstrait

Les applications électroniques se sont développées pour englober une variété de matériaux. En particulier, les allotropes du carbone intéressent les chercheurs pour leurs applications électroniques. La découverte des allotropes de carbone et de leurs applications s'est élargie considérablement depuis la découverte du Buckminsterfullerène C60 en 1985, la découverte de nanotubes de carbone à paroi unique et multiples des années 1990 et l'isolement du graphène en 2004. Les nanotubes de carbone à paroi unique (SWNT) ont le potentiel d'apporter les appareils électroniques de nouvelle génération. De tels dispositifs pourraient être flexibles, conformables et peu coûteux. L'électronique basée sur SWNT est prometteuse pour les applications de détection chimiques et biologiques, par exemple, où les mobilités élevées des porteurs ne sont pas nécessaires, et où la conformité des matériaux et le traitement peu coûteux sont des avantages significatifs. Des progrès considérables ont été réalisés dans la séparation des SWNT semi-conducteurs de mélanges de SWNT métalliques, permettant l'incorporation de SWNT dans les technologies électroniques semi-conductrices. L'isolement sélectif des SWNT semi-conducteurs à l'aide de polymères π-conjugués est une technique efficace pour enrichir de grandes quantités de SWNT semi-conducteurs qui sont ultrapurs. Après enrichissement semi-conducteur, les SWNT peuvent être incorporés dans des dispositifs électroniques.

Cette thèse porte sur l'enrichissement des SWNT semi-conducteurs via l'extraction de polymères conjugués et l'incorporation des dispersions polymère-SWNT donnant des transistors à couches minces (TFT). De nouveaux copolymères ont été étudiés pour leur capacité à isoler et disperser sélectivement des sc-SWNT à grand diamètre. L'absorption et la spectroscopie Raman ont été utilisées pour caractériser l'efficacité de la procédure d'extraction du polymère conjugué. Après enrichissement, les dispersions polymère-SWNT ont été incorporées dans des TFTs. L'interaction entre le polymère conjugué et le SWNT et le polymère conjugué et le diélectrique était un élément essentiel de l'optimisation TFT. En outre, la procédure de l'isolement et de dispersion des sc-SWNT est étudiée pour son effet sur les performances du TFT et était un autre composant de l'optimisation du TFT. Les TFT ont été caractérisés électriquement en termes de mobilité des porteuses, de tension de seuil, d'hystérésis et de rapport marche/arrêt du courant. La morphologie du film des TFT SWNT a également été étudiée. La microscopie à force atomique et

la cartographie Raman ont été utilisées pour donner un aperçu de la morphologie du film à l'échelle nanométrique et micrométrique, respectivement.

Acknowledgements

I want to begin my acknowledgements by expressing my deep and sincere gratitude for my supervisor, Prof. Benoît Lessard. Prof. Lessard allowed me to pursue graduate work with his research group and has continued to express his confidence in and enthusiasm for my research. Prof. Lessard allowed me to work autonomously and develop my skills as a researcher. He has helped tremendously in launching my career, and for that, I am deeply grateful. I would also like to acknowledge my colleague, Dr. Nicole Rice, to whom I owe tremendous gratitude. With her seemingly limitless depth of knowledge and her unwavering assistance to myself and others, Dr. Rice has been invaluable to my work as a colleague and a friend. Additionally, I want to thank all of the members of the Lessard Research Group for building such a positive and uplifting work environment, albeit at times to the detriment of others in the graduate students' office. For years to come, I will have fond memories of my time as a graduate student, and I owe that to the Lessard Research Group.

I thank my parents for nurturing my curiosity and encouraging my intellectual pursuits. Reading was omnipresent within my household from a young age, and the pursuit of knowledge was continuously reinforced within my family. For these same reasons, I want to extend my gratitude to the people in my family who have supported my aspirations at each step.

Most of all, I want to thank my partner, Kayla. Since I decided to pursue graduate studies, Kayla has been enthusiastic and supportive. In the time it has taken for me to complete my degree, she has been patient and supportive, and has made several sacrifices. For that, I am eternally grateful. Her support for my work has never wavered, and she will continue to be my greatest inspiration during my career as a researcher.

List of Peer-Reviewed Publications

1. **Mirka, B.**; Rice, N. A.; Williams, P.; Tousignant, M. N.; Boileau, N. T.; Bodnaryk, W. J.; Fong, D.; Adronov, A.; Lessard, B. H. Excess Polymer in Single-Walled Carbon Nanotube Thin-Film Transistors: Its Removal Prior to Fabrication Is Unnecessary. ***ACS Nano*** **2021**, *15*, 8252–8266.
2. **Mirka, B.**; Fong, D.; Rice, N. A.; Melville, O. A.; Adronov, A.; Lessard, B. H. Polyfluorene-Sorted Semiconducting Single-Walled Carbon Nanotubes for Applications in Thin-Film Transistors. ***Chem. Mater.*** **2019**, *31*, 2863–2872.
3. **Mirka, B.**; Rice, N. A.; Richard, C. M.; Lefebvre, D.; Bodnaryk, W. J.; Fong, D.; Adronov, A.; Lessard, B. H. Contact Engineering in Single-Walled Carbon Nanotube Thin-Film Transistors. ***ACS Appl. Nano Mater.*****, 2022**, Manuscript Accepted. ID: an-2022-02052f.
4. Birajdar, S. S.; **Mirka, B.**; Gawade, V. K.; Puyad, A. L.; Lessard, B. H.; Bhosale, Sidhanath V.; Bhosale, Sheshanath V. Furan Functionalized Naphthalenediimide Semiconductors with Different N-alkyl Chains for n-type Organic Thin-Film Transistor Applications. ***Dyes and Pigments***, **2022**, *206*, 110603.
5. Brixi, S.; Melville, O. A.; **Mirka, B.**; He, Y.; Hendsbee, A. D.; Meng, H.; Li, Y.; Lessard, B. H. Air and Temperature Sensitivity of n-type Polymer Materials to Meet and Exceed the Standard of N2200. ***Sci. Rep.*** **2020**, *10*, 4014.
6. Rice, N. A.; Bodnaryk, W. J.; **Mirka, B.**; Melville, O. A.; Adronov, A.; Lessard, B. H. Polycarbazole-Sorted Semiconducting Single-Walled Carbon Nanotubes for Incorporation into Organic Thin Film Transistors. ***Adv. Electron. Mater.*** **2019**, *5*, 1800539.
7. Melville, O. A.; Grant, T. M.; **Mirka, B.**; Boileau, N. T.; Park, J.; Lessard, B. H. Ambipolarity and Air Stability of Silicon Phthalocyanine Organic Thin-Film Transistors. ***Adv. Electron. Mater.*** **2019**, *5*, 1900087.
8. Boileau, N. T.; Cranston, R.; **Mirka, B.**; Melville, O. A.; Lessard, B. H. Metal Phthalocyanine Organic Thin-Film Transistors: Changes in Electrical Performance and Stability in Response to Temperature and Environment. ***RSC Adv.*** **2019**, *9*, 21478–21485.
9. Boileau, N. T.; Melville, O. A.; **Mirka, B.**; Cranston, R.; Lessard, B. H. P and N Type Copper Phthalocyanines as Effective Semiconductors in Organic Thin-Film Transistor Based DNA Biosensors at Elevated Temperatures. ***RSC Adv.*** **2019**, *9*, 2133–2142.

10. Tousignant, M. N.; Ourabi, M.; Niskanen, J.; **Mirka, B.**; Bodnaryk, W. J.; Adronov, A.; Lessard, B. H. Poly(ionic liquid) Dielectric for High performing P- and N-type Single Walled Carbon Nanotube Transistors. ***Flex. Print. Electron.*** **2022**, Manuscript Accepted. ID: FPE-100695.R1.

Table of Contents

List of Figures

**Figure captions have been shortened for brevity.*

List of Tables

**Table captions have been shortened for brevity.*

List of Abbreviations

(n, m)	SWNT Chiral Indices
A	Area
a_1, a_2	SWNT Unit Vectors
$a_{C\text{-}C}$	Carbon-Carbon Bond Length (1.44 Å)
AFM	Atomic Force Microscopy
ALD	Atomic Layer Deposition
b_1, b_2	SWNT Reciprocal Lattice Vectors
BGBC	Bottom-Gate Bottom-Contact
BGTC	Bottom-Gate Top-Contact
BWF	Breit-Wigner-Fano Lineshape
C	Capacitance
C_h	Chiral Vector
C_i	Capacitance Density
CoMoCAT	SWNT Synthetic Route, CO Disproportionation Over Cobalt-Molybdenum Catalyst
CPE	Conjugated Polymer Extraction
CVD	Chemical Vapour Deposition
DGU	Density Gradient Ultracentrifugation
DOS	Density of States
d_t	SWNT diameter
E_x	Electric Field (in the x-direction)
G-band	SWNT Tangential Phonon Mode
G^+	SWNT Axial Tangential Phonon Mode
G^-	SWNT Circumferential Tangential Phonon Mode
H	Hysteresis
HiPco	SWNT Synthetic Route, High-Pressure Disproportionation of Carbon Monoxide
HOMO	Highest-Occupied Molecular Orbital
I_{OFF}	Off Current
I_{ON}	On Current

$I_{ON/OFF}$	Current ON/OFF Ratio
I_{SD}	Source-Drain Current
K_1	Reciprocal Vector along SWNT Circumference
K_2	Reciprocal Vector Along SWNT Axis
L	Channel Length
LUMO	Lowest-Unoccupied Molecular Orbital
M_{11}	Metallic SWNT First van-Hove Singularity
M_n	Number-Average Molecular Weight
m-SWNT	Metallic Single-Walled Carbon Nanotube
M-TLM	Modified Transmission Line Method
M_w	Weight-Average Molecular Weight
MWNT	Multi-Walled Carbon Nanotube
OPV	Organic Photovoltaic
OSC	Organic Semiconductor
OTFT	Organic Thin-Film Transistor
OTS	Octyltrichlorosilane
PCF	Polymer, Poly(9,9'-didodecylfluorene-*co*-N-(2'-decyltetradecane)-carbazole)
PDDF	Polymer, Poly(9,9-di-*n*-dodecylfluorene)
pDTFF	Poly(dithiafulvalene-*co*-thiophene)
PEN	Polymer, Poly(Ethylene Naphthalate)
PFMB	Polymer, Poly[(2,7-(9,9-dihexade-cylfluorene)-*alt*-2,5-dimethoxybenzene]
PFO-BPy	Polymer, Poly(9,9-di-*n*-octylfluorene-*co*-bipyridine)
PVD	Physical Vapour Deposition
Q	Charge Density
RBM	Radial Breathing Mode
R_C	Contact Resistance
R_{Ch}	Channel Resistance
R_CW	Width-Normalized Contact Resistance
RFID	Radio Frequency Identification
R_{TOT}	Total Resistance

S_{11}	Semiconducting SWNT First van-Hove Singularity
S_{22}	Semiconducting SWNT Second van-Hove Singularity
S_{33}	Semiconducting SWNT Third van-Hove Singularity
sc-SWNT	Semiconducting Single-Walled Carbon Nanotube
SWNT	Single-Walled Carbon Nanotube
t	Dielectric Thickness
T	SWNT Translation Vector
TFT	Thin-Film Transistor
TLM	Transmission Line Method
v_d	Drift Velocity
V_D	Voltage at Drain Electrode
V_{GS}	Gate-Source Voltage
VRH	Variable Range Hopping Model for Charge Transport
V_S	Voltage at Source Electrode
V_{SD}	Source-Drain Voltage
V_T	Threshold Voltage
V_x	Voltage at Location "x" Within the Channel
W	Channel Width
Γ, K, and M	Points of High-Symmetry Within the SWNT Brillouin Zone
ε_0	Vacuum Permittivity (8.854×10^{-12} F/m)
θ	SWNT Chiral Angle
κ	Relative Permittivity (Dielectric Constant)
μ	Mobility
ϕ_i	Absorption Peak Ratio

Chapter 1: Introduction

1.1 Overview

1.1.1 Carbon-Based Electronics

Carbon-based semiconductors have attracted attention from scientists and engineers for their unique advantages compared to inorganic semiconductors.[1,2] Use of carbon-based semiconductors facilitates the development of flexible and inexpensive electronics,[3] which can be fabricated and operated at much lower temperatures than inorganic electronics.[4] Commercial applications have incorporated these materials into different applications, such as organic light-emitting diodes (OLEDs),[5,6] radio frequency identification (RFID) tags,[7] organic photovoltaics,[8,9] and biological and chemical sensors.[10-12] Allotropes of carbon represent a new and emerging class of carbon-based semiconductors.[13] Significant advancements in the era of carbon allotropes began with the discovery of C_{60} Buckminsterfullerene in 1985, which consists of a sphere of sp^2-hybridized carbon with π-electrons confined to zero-dimensions.[14] Following the discovery of Buckminsterfullerene, Ijima discovered multi-walled carbon nanotubes (MWNTs) in 1991, and single-walled carbon nanotubes (SWNTs) in 1993.[15,16] Advances in carbon nanomaterials continued with the isolation of graphene – a single-atom-thick, quasi-two-dimensional sheet of sp^2-hybridized carbon. Though theorized by P. R. Wallace in 1947, graphene was not isolated until 2004, which Novoselov and Geim accomplished.[13,17] Carbon-based semiconductors are poised to produce alternative forms of electronics.[18] SWNTs are ideal candidates for organic semiconductors integrated into carbon-based electronics.[19,20] SWNTs have been incorporated into integrated circuits,[21-25] further demonstrating their potential as next-generation electronic materials. However, all synthetic routes of SWNTs produce a mixture of SWNTs with varying helicity and diameter. Depending on the helicity, SWNTs can be either semiconducting (sc-SWNTs) or metallic (m-SWNTs) species, with about one-third metallic.[26] Interestingly, graphene and m-SWNTs are the first stable organic metals where no further doping or activation is required.[13] In semiconducting applications, such as thin-film transistors (TFTs) or organic photovoltaics (OPVs), the presence of m-SWNTs in the SWNT film is detrimental to device performance due to the formation of short-circuit pathways within the SWNT layer. For semiconducting applications to exploit SWNTs, the sc- and m-SWNTs must be separated. Additionally, SWNTs are highly insoluble, making solution-processing difficult. Certain conjugated polymers with aromatic

backbones can selectively exfoliate sc-SWNTs and disperse them in organic solvents.[27,28] Following conjugated polymer extraction, sc-SWNTs can be incorporated into thin-film transistors using solution-based techniques.[29-31]

1.1.2 Scope of Thesis

The work in this thesis focuses on conjugated polymer extraction of semiconducting single-walled carbon nanotubes and their incorporation into thin-film transistors. In particular, this thesis investigates conditions of sc-SWNT dispersion preparation, and how dispersion preparation affects transistor performance. **Chapter 1** provides the relevant background material for the work covered in **Chapters 2** to **Four**. **Chapter 1** begins with an introduction to carbon-based semiconductors and organic electronics, and then discusses single-walled carbon nanotubes. Concepts of single-walled carbon nanotubes are introduced, including descriptions of the geometry and electrical properties, and synthesis. Following is a review of selective sorting of semiconducting single-walled carbon nanotubes using conjugated polymer extraction. The effects on selectivity from the conjugated polymer backbone, side-chain length, molecular weight, and electronic structure are described. Next, single-walled carbon nanotube dispersion characterization using spectroscopic techniques is described. The discussion then focuses on SWNT thin-film transistors. Topics covered include fabrication of SWNT TFTs, charge transport, and applications.

Chapter 2 discusses work done sorting sc-SWNTs using a novel conjugated polymer and the resulting polymer: sc-SWNT dispersion incorporated into thin-film transistors. A novel co-polymer consisting of a fluorene and a carbazole moiety (PFMB) was used to sort and disperse sc-SWNTs. The sc-SWNT purity was analyzed using absorbance and Raman spectroscopy. Following successful sorting, the PFMB-SWNT dispersion was incorporated into thin-film transistors to demonstrate its capacity to be integrated into electronics.

Chapter 3 continues from the work done in **Chapter 2**. In **Chapter 3**, the central theme is the necessity of excess polymer in single-walled carbon nanotube dispersions and challenging the long-held belief that its removal is necessary. The work done in **Chapter 3** shows that replacing a time-consuming filtration step with a solvent-rinse step can effectively remove the excess polymer from the SWNT film, thereby making large-scale SWNT TFT fabrication more amenable. SWNT TFTs were fabricated with varying conditions of polymer presence, and the resulting TFTs

were electrically characterized. Atomic force microscopy and Raman spectroscopic mapping were used to investigate the SWNT film morphology within the TFT channel.

Chapter 4 focuses on contact engineering of SWNT TFTs. When studying SWNT TFTs using Au electrodes, poor adhesion of Au to the substrate is a concern. **Chapter 4** discusses work done at incorporating different contact interlayers into SWNT TFTs. SWNT TFTs were fabricated using Au electrodes with different contact interlayers, including molybdenum trioxide (MoO3), manganese (Mn), chromium (Cr), and 2,9-dimethyl-4,7-diphenyl-1,10-phenanthroline (BCP). Incorporation of a contact interlayer drastically improved device reproducibility. Furthermore, SWNT TFTs were characterized in air and nitrogen. Atmospheric effects on SWNT TFT performance with different contact interlayers are discussed.

Chapter 5 summarizes the work completed in this thesis and provides recommendations for future research on this subject. **Chapter 6** describes contributions towards co-authored peer-reviewed literature.

1.2 Organic Electronics

This section will provide the theoretical background on organic electronics, organic semiconductors, and organic thin-film transistors.

1.2.1 Carbon-Based Semiconductors and Organic Thin-Film Transistors

An increasing number of electronic applications rely on materials that are flexible, conformable, inexpensive, and amenable to solution-based fabrication. Unfortunately, traditional inorganic electronic materials are unable to meet these demands. Though inorganic electronic devices possess exceptional electrical conductivity, they are rigid, brittle, and inflexible. Inorganic materials cannot conform to curved surfaces, making them impractical for applications such as wearable electronics, which are designed to conform to the human body. Additionally, inorganic semiconductors are expensive and often require high-temperature fabrication. Large-scale, inexpensive fabrication techniques like solution-based printing are challenging to incorporate into inorganic electronic fabrication. Carbon-based semiconductors are semiconductors based on organic small molecules, polymers, or carbon allotropes, and are amenable to the subset of electronic applications that require flexibility and inexpensive processing.[32] Though the performance of carbon-based semiconductors is often considerably lower than the performance of inorganic semiconductors, carbon-based semiconductors possess advantages that make them ideal candidates for specific next-generation electronic devices. Carbon-based semiconductors can be flexible, facilitating their use in niche applications, where flexibility is a requirement.

Carbon-based semiconductors can be incorporated into electronics using inexpensive means, such as solution-based printing. Printing techniques enable fabrication on a large scale and at a low cost. Furthermore, carbon-based semiconductors have versatility; there are many to select based on the application. The expansive library of carbon-based semiconductors enables tuning the properties, and carbon-based semiconductors can be altered to adjust their properties towards a specific application. Organic materials were thought to be exclusively insulating materials until the seminal work done by Shirakawa *et al*. showed that poly(acetylene) films could conduct electricity.[33] Charge transport in carbon-based semiconductors occurs as a response of delocalized π-electrons. Carbon-based semiconductors consist of alternating single (σ) and double (π + σ) bonds and are referred to as sp^2-hybridized when double bonds are present. The π-electrons are located in the p_z orbitals, perpendicular to the molecular chain. There are two p_z orbitals. Therefore,

there are two states for π-electrons to be present: π (bonding) and π* (anti-bonding). The π* orbital is a higher energy orbital, and the excitement of electrons into the π* orbital results in the delocalization of the π-electrons. When the molecular (or polymeric) structure is arranged such that the π-electrons can be delocalized, the molecule (or polymer) is π-conjugated. The energy difference between the π and the π* orbitals, or the highest-occupied molecular orbital (HOMO) and the lowest-unoccupied molecular orbital (LUMO), is the energy gap of the material.[34] The requirement for π-conjugation is that the material is sp^2-hybridized.

Organic thin-film transistors (OTFTs) are prospective applications of organic semiconductors.[35] For many conceptions of flexible electronic devices, OTFTs are poised to be the building block that enables operation. OTFTs have attracted significant interest for applications in screen displays, particularly in OLEDs, due to their flexibility and low manufacturing cost.[36] Moreover, applications of OTFTs have expanded beyond OLEDs. Widespread attention is on OTFT applications in RFID detectors,[7] chemical and biological sensors,[37] wearable electronics, including biosensors and health monitors,[38,39] and complementary logic.[4,40] These applications reflect the versatility of OTFTs on several dimensions. OTFTs can be fabricated on several substrate types, including paper,[41] Kapton,[42] poly(ethylene naphthalate) (PEN),[43] and glass.[44] There is also a vast library of carbon-based semiconductors to choose from when fabricating OTFTs. Furthermore, different dielectric materials can be incorporated into OTFTs, including flexible polymer dielectrics.[40] OTFTs typically operate under p-type conditions, but n-type performance can be achieved under certain conditions and for certain materials.[45]

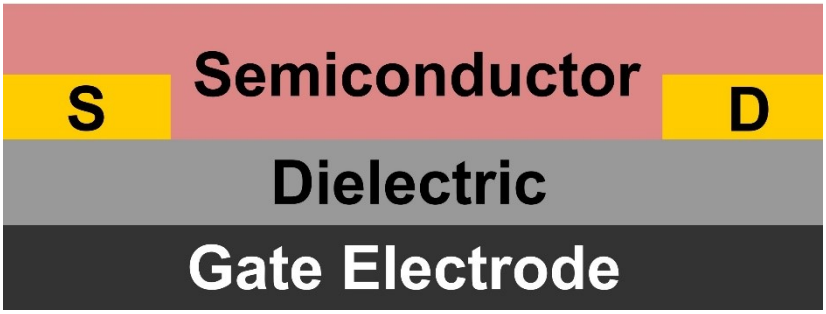

Figure 1.1: Cross-section of a thin-film transistor.

1.2.2 MOSFET Model for Thin-Film Transistors

A thin-film transistor (TFT) is an electronic switch modulated by a gate electrode. A TFT consists of a conductive gate electrode and a semiconductor material. An insulating dielectric separates the gate electrode and the semiconductor, and the semiconductor is connected to a source electrode and a drain electrode. The dielectric is polarized by applying a potential between the source and gate electrodes, inducing charges to accumulate at the semiconductor-dielectric interface. The density of charges accumulated at the interface, (Q, [C/m^2]), is proportional to the dielectric's capacitance density (C_i, [F/m^2]), which can be estimated using the parallel-plate model.

$$C_i = \frac{Q}{V} = \frac{\varepsilon_0 \kappa}{t} \tag{1}$$

Therefore, the charge density is $Q = C_i V$. In a TFT, the source electrode is grounded ($V_S = 0\ V$), therefore the potential difference between the gate and source electrodes is $V_{GS} = V_G - V_S = V_G$. The potential difference between the gate electrode and any point "x" within the channel is $V_{Gx} = V_G - V_x = V_{GS} - V_x$ (where $V_S \leq V_x \leq V_D$). A threshold voltage (V_T) exists such that an applied V_{GS} below V_T will not result in charge accumulation at the interface. For an applied V_{GS} above V_T, charges accumulate at the semiconductor-dielectric interface with a charge density $Q = C_i (V_{GS} - V_T - V_x)$. Since V_x changes within the channel, the charge density also changes within the channel. At the source electrode ($x = 0,\ V_x = V_S$), the charge density is $Q = C_i (V_{GS} - V_T)$. At the drain electrode ($x = L,\ V_x = V_D$), the charge density is $Q = C_i (V_{GS} - V_T - V_D)$, where V_D is the voltage at the drain electrode. **Figure 1.2** depicts the change in Q within the TFT channel.

$$|V_{GS}| < |V_T|,\ Q = 0 \tag{2}$$

$$|V_{GS}| \geq |V_T|,\ Q = C_i (V_{GS} - V_T - V_x) \tag{3}$$

At the Source Electrode: $x = 0$, $Q = C_i (V_{GS} - V_T)$ (4)

At the Drain Electrode: $x = L$, $Q = C_i (V_{GS} - V_T - V_D)$ (5)

$$V_S \leq V_x \leq V_D \tag{6}$$

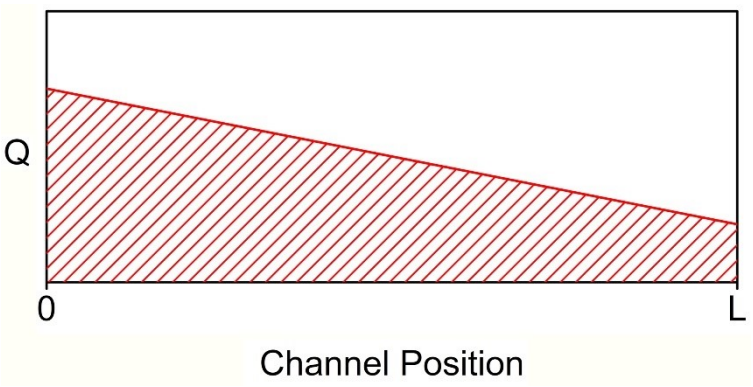

Figure 1.2: The charge density (Q) within the TFT channel, for a channel length of L. Within the channel, the source electrode is located at *0* and the drain electrode is located at L.

By applying a gate-source voltage, $|V_{GS}| \geq |V_T|$, a layer of charge accumulates at the semiconductor-dielectric interface. However, the charges remain static and are not moving between the source and drain electrodes. A potential is applied between the source and drain electrodes (V_{DS}) to move the charges from the source to the drain electrodes, $V_{DS} = V_D - V_S = V_D$ (since V_S is grounded). The drift velocity of the charges, v_d, is the product of the mobility (μ) and the electric field between the source and drain (E_x, defined as the x-direction). μ is the ratio of the v_d to E_x. For this model, v_d is assumed to be constant. The current between the source and drain electrodes is the source-drain current, I_{SD}. The channel width (W) is the electrode dimension perpendicular to the current flow (defined as the y-direction).

$$v_d = \mu E_x \tag{7}$$

$$I_{SD} = \int_0^W v_d Q dy = v_d Q W \tag{8}$$

$$v_d = \frac{I_{SD}}{QW} \tag{9}$$

$$E_x = \frac{dV_x}{dx} \tag{10}$$

$$\frac{I_{SD}}{QW} = \mu \frac{dV_x}{dx} \tag{11}$$

$$\text{For } V_{GS} \geq V_T,\ Q = C_i (V_{GS} - V_T - V_x) \tag{12}$$

$$I_{SD} = \mu W C_i (V_{GS} - V_T - V_x) \frac{dV_x}{dx} \quad (13)$$

Integrating the above equation over the channel length (L) and the source-drain voltage (V_{SD}) gives the source-drain current in the form below.

$$I_{SD} = \frac{\mu W C_i}{L} [(V_{GS} - V_T)V_{SD} - \frac{1}{2}V_{SD}^2] \quad (14)$$

The above equation is only valid for the case of $|V_{SD}| < |V_{GS} - V_T|$. For the case of $|V_{SD}| = |V_{GS} - V_T|$ the charge density at the drain electrode is $Q = C_i (V_{GS} - V_T - V_D) = 0$. Therefore, there is no charge accumulation at the drain electrode when $|V_{SD}| = |V_{GS} - V_T|$. When $|V_{SD}| > |V_{GS} - V_T|$, then at some point within the channel, the charge density becomes negative, i.e., the minority charge carrier is polarized. Often, this does not happen since most semiconductors are unipolar, i.e., they only conduct one charge carrier. The charge density becomes zero within the channel, causing the source-drain current to saturate. The location at which the charge density becomes zero is the pinch-off point.[34] When a TFT is operating under the condition of $|V_{SD}| > |V_{GS} - V_T|$, then it is said to be operating in the saturation regime, and the I_{SD} equation is updated by setting V_{DS} equal to $V_{GS} - V_T$. **Figure 1.3** depicts the charge density profiles for the linear regime, the transition from linear to saturation, and the saturation regime.

$$I_{DS} = \frac{\mu W C_i}{2L} (V_{GS} - V_T)^2 \quad (15)$$

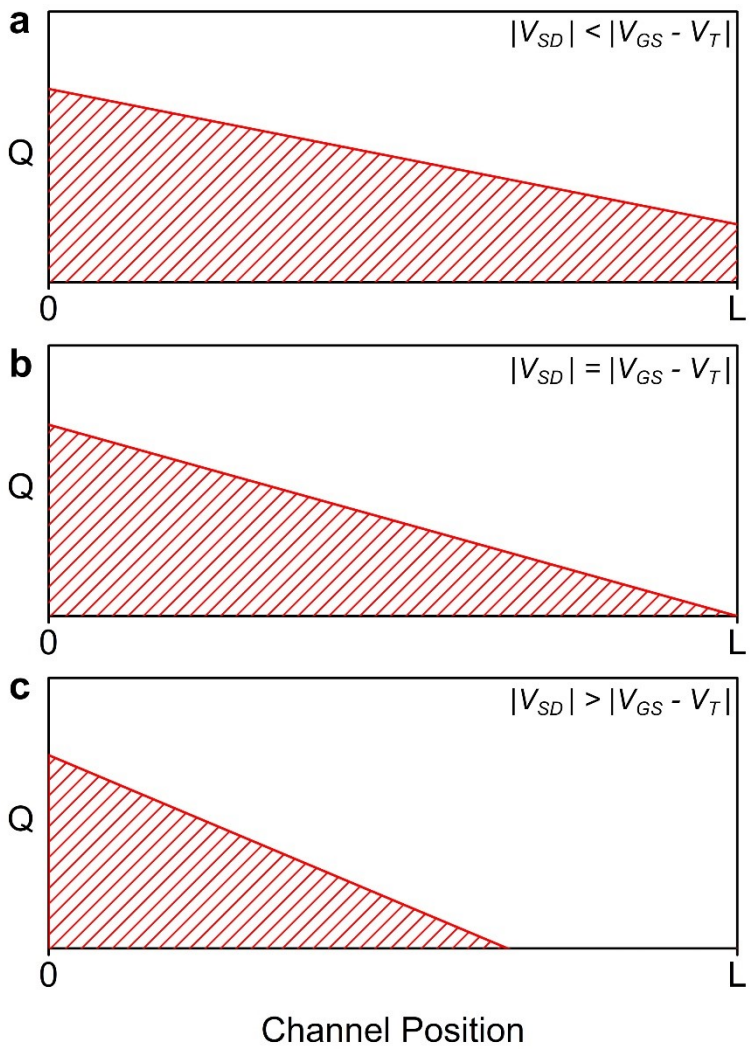

Figure 1.3: Charge density profile (Q) for the a) linear regime, b) transition from linear to saturation, and c) saturation regime.

1.2.3 Current-Voltage Characteristics

Current-voltage characteristics for TFTs can be plotted in two curves: output and transfer curves. **Figure 1.4a** shows an example of an output curve, and **Figure 1.4b** shows an example of a transfer curve. In an output curve, the gate-source voltage is held constant, and the source-drain current is measured as the source-drain voltage is swept. The gate-source voltage is increased incrementally, and multiple curves are generated. In a transfer curve, the source-drain voltage is kept constant, and the source-drain current is measured as the gate-source voltage is swept. Transfer curves are used to extract TFT metrics. The on/off current ratio ($I_{on/off}$) is measured as the

ratio of the on-current to the off-current, the mobility (μ) is extracted from the slope of the curve, and the threshold voltage (V_T) is extracted from the x-intercept.

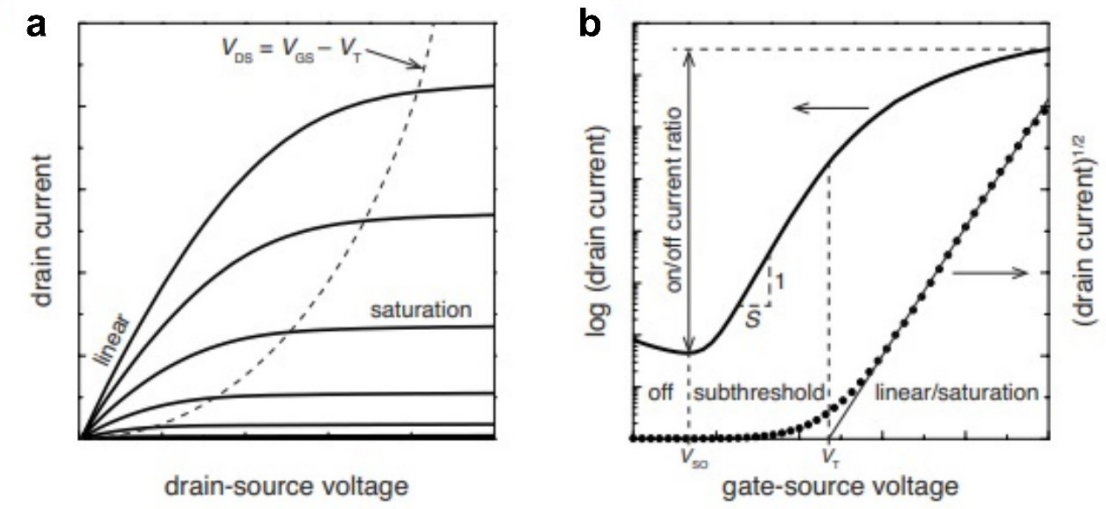

Figure 1.4: Examples of a) an output curve and b) a transfer curve. Figure reproduced from Herlogsson, L., ref. 46.

***Linear Regime,* $|V_{SD}| < |V_{GS} - V_T|$**

In the case of TFTs operating in the linear regime, the source-drain current is plotted against the gate-source voltage. The μ is extracted from the transconductance (g_m), which is the slope of the transfer curve (dI_{SD}/dV_{GS}). The V_T is estimated from the extrapolated x-intercept of the slope minus half of the source-drain voltage (V_{SD}). In the following equations, W is the channel width, and L is the channel length.

$$I_{SD} = \frac{W\mu C_i}{L}\left((V_{GS} - V_T)V_{SD} - \frac{V_{SD}^2}{2}\right) \tag{16}$$

$$\mu = \frac{L}{WC_iV_{SD}}\frac{\partial I_{SD}}{\partial V_{GS}} \tag{17}$$

$$V_T = V_{GS}(\text{x-intercept}) - \frac{V_{SD}}{2} \tag{18}$$

Saturation Regime, $|V_{SD}| > |V_{GS} - V_T|$

For TFTs operating in the saturation regime, the square root of the source-drain current ($\sqrt{I_{SD}}$) is plotted against the gate-source voltage (V_{GS}). The μ is extracted from the square of the slope, and the threshold voltage is the extrapolated x-intercept of the slope.

$$I_{SD} = \frac{W\mu C_i}{2L}(V_{GS} - V_T)^2 \tag{19}$$

$$\mu = \frac{2L}{WC_i}\left(\frac{\partial\sqrt{I_{SD}}}{\partial V_{GS}}\right)^2 \tag{20}$$

$$V_T = V_{GS}(x\text{-}intercept) \tag{21}$$

1.2.4 MOSFET Model Assumptions and Implications for the Measured Mobility

The MOSFET model discussed above assumes that the capacitance density (C_i) can be estimated using the parallel-plate capacitor model, in which case C_i is dependent only on the dielectric constant and layer thickness. For dense SWNT networks that resemble a continuous film, the parallel-plate model provides a good estimation of C_i. However, for sparse SWNT networks (< ~15 SWNTs/μm) the parallel-plate model overestimates C_i and thus underestimates mobility.[47] Cao and coworkers proposed a cylindrical capacitance model, which considers the electrostatic coupling between SWNTs within the film, including their intrinsic quantum capacitance.[48] The model requires the average SWNT diameter and the linear density of the SWNT network.

$$C_{eff} = \frac{\Lambda_0^{-1}}{\left\{C_Q^{-1} + \frac{1}{2\pi\kappa\varepsilon_0}\ln\left[\frac{\Lambda_0}{R\pi}\sinh\left(\frac{2\pi t}{\Lambda_0}\right)\right]\right\}} \tag{22}$$

C_{eff} is the effective capacitance density, Λ_0^{-1} is the SWNT linear density (SWNT/μm), C_Q is the SWNT quantum capacitance (4.0×10^{-10} F/m), κ is the dielectric constant of the insulator, ε_0 is the vacuum permittivity (8.854×10^{-12} F/m), R is the SWNT radius, and t is the insulator thickness.

The MOSFET model also assumes ohmic contacts, which further affects the mobility measurement. At low voltages below the threshold voltage, the current density is given by Ohm's law and is due to the motion of free electrons within the semiconductor. At higher voltages above the threshold voltage the current density transitions to the space-charge-limited regime and is given

by the Mott-Gurney law.[49] By assuming that the contacts exhibit ohmic behaviour, it is assumed that there is no barrier to charge injection from the contacts to the semiconductor, and that the current density is not limited by the contacts. There is contact resistance at the interface between the contact and semiconductor. Hence, the MOSFET model will underestimate the measured mobility. Details on correcting the mobility for contact resistance are provided in **Chapter 4**, section **4.5.3**.

1.3 Single-Walled Carbon Nanotubes

1.3.1 Introduction to Single-Walled Carbon Nanotubes

Single-walled carbon nanotubes (SWNTs) have been studied intensively due to their electronic, optical, and mechanical properties. The superlative properties exhibited by SWNTs include flexibility, high electrical conductivity,[20] and high tensile strength.[50] Due to these superlative properties, SWNTs have been incorporated into several forms of electronic devices, including organic photovoltaics,[51,52] thin-film transistors,[53,54] chemical sensors,[55] biological sensors,[56] and other nanoscale electronic devices.[57] This section will cover the synthesis of SWNTs, the properties and geometry of SWNTs, and techniques used to sort semiconducting SWNTs.

1.3.2 Synthesis of SWNTs

SWNTs can be synthesised using several methods. The oldest method of producing SWNTs is the arc discharge process. During the arc discharge process, a carbon anode is brought close to a carbon cathode in a Helium environment, and a large electric current is passed between the two electrodes. The current ignites the Helium into plasma, which evaporates the carbon atoms. The carbon atoms then condense into carbon nanotubes, usually as multi-walled carbon nanotubes (MWNTs). The generation of SWNTs requires a catalyst in the arc discharge process, such as a carbon anode containing a small amount of Cobalt catalyst.[58,59] Laser ablation can also be used to produce SWNTs. Smalley *et al*. produced SWNTs using laser pulses to ablate a carbon source containing 0.5 atomic % of cobalt and nickel catalyst. A stream of inert gas carried the SWNTs to a cold finger, where they were collected.[60] Kim *et al*. demonstrated the synthesis of SWNTs *via* evaporation of a carbon source with metallic catalyst using induction from a plasma torch.[61]

Alternatively, SWNTs can be synthesised using chemical vapour deposition (CVD) techniques. CVD techniques produce SWNTs by dissociating a hydrocarbon gas over a transition metal catalyst, followed by dissolution and saturation of carbon atoms in the metal nanoparticle. The carbon within the saturated metal catalyst precipitates into an sp^2-hybridized tubular form, ultimately forming SWNTs.[58] Common CVD methods of SWNT synthesis include high-pressure disproportionation of carbon monoxide (HiPco).[62] To produce HiPco SWNTs, CO mixed with iron catalyst is injected into a reactor. Solid carbon is formed *via* the Boudouard reaction, and the iron catalyst facilitates SWNT nucleation and growth.[62] Similarly, SWNTs can be produced *via* CO disproportionation at high temperatures over a cobalt-molybdenum catalyst (CoMoCAT).[63] Different SWNT synthetic routes will produce SWNTs with different diameter ranges. Arc discharge produces SWNTs in the range of 1.2 – 1.7 nm, laser ablation produces a diameter range of 1.0 – 1.4, HiPco produces a range of 0.8 – 1.1, and CoMoCAT produces a range of 0.7 – 0.9.[27]

1.3.3 Properties of Single-Walled Carbon Nanotubes

Single-walled carbon nanotubes consist of sp^2-hybridized carbon and are analogous to a sheet of graphene rolled into a seamless cylinder. SWNTs have a diameter of ~1 – 2 nm and a length of about 1 μm – 1 mm, making SWNTs quasi-one-dimensional. Each SWNT can is described by its chiral vector, $\boldsymbol{C_h}$, the magnitude of which is the SWNT's circumference. The chiral vector is defined by a set of indices (n, m) which denote the number of unit vectors $\boldsymbol{a_1}$ and $\boldsymbol{a_2}$ contained in the chiral vector.[64] Thus, a SWNT's geometry is entirely specified by the pair of integers (n, m). **Figure 1.5** depicts the geometry of an "unrolled" SWNT.

$$\boldsymbol{C_h} = n\boldsymbol{a_1} + m\boldsymbol{a_2} \tag{23}$$

$$\boldsymbol{a_1} = \left(\frac{\sqrt{3}}{2},\ \frac{1}{2}\right)a \tag{24}$$

$$\boldsymbol{a_2} = \left(\frac{\sqrt{3}}{2}, -\frac{1}{2}\right)a \tag{25}$$

$$a = \sqrt{3}\, a_{C\text{-}C} = 2.49 \text{ Å} \tag{26}$$

$$d_t = |\mathbf{C_h}|/\pi = \frac{a}{\pi}\sqrt{n^2 + m^2 + nm} \tag{27}$$

$$cos\theta = \frac{2n+m}{2\sqrt{n^2 + m^2 + nm}} \tag{28}$$

$0° \leq \theta \leq 30°$

In the equations above, $a_{C\text{-}C}$ is the carbon-carbon bond length (1.44 Å) within the honeycomb lattice.[58] The magnitude of the chiral vector defines the SWNT's diameter. The angle between the chiral vector and the zig-zag orientation is the chiral angle. SWNTs with $\theta = 0°$ are referred to as zig-zag SWNTs (n, 0), and SWNTs with $\theta = 30°$ are referred to as armchair SWNTs (n, n). SWNTs with $0° < \theta < 30°$ are chiral SWNTs and are defined by (n, m); an (n, m) SWNT is a mirror image of an (m, n) SWNT.

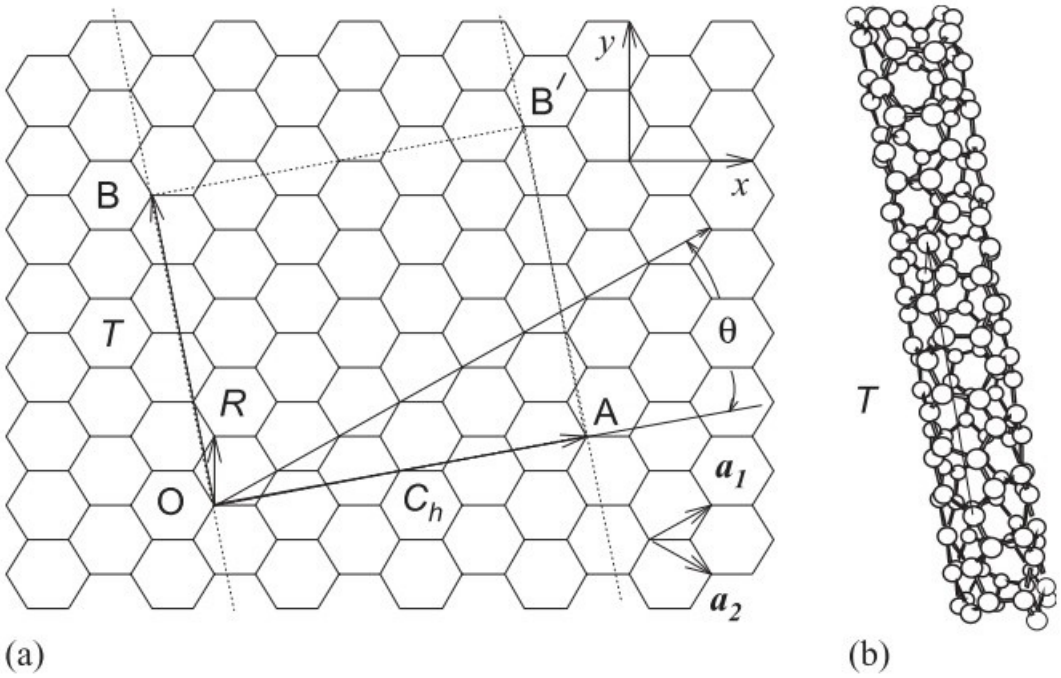

Figure 1.5: a) An unrolled SWNT, shown as a graphene honeycomb lattice. The chiral vector (**C**$_h$) connects the points OA, the translation vector (**T**) connects the points OB, and the rectangle defined by OABB' define the SWNT unit cell. The lattice structure displayed above is that of a (4, 2) SWNT, and the unit vectors a_1 and a_2 are displayed. Getting from point O to point A requires four units in the direction of $\boldsymbol{a_1}$ and two units in the direction of $\boldsymbol{a_2}$, which defines **C**$_h$. In b), a (4, 2) SWNT is shown, which is the lattice rolled up such that the points O and A are connected, and **C**$_h$ defines the circumference. Figure reproduced from Dresselhaus, M. S.; *et al*. ref. 64.

The two-dimensional lattice for graphene given in real space with unit vectors $\boldsymbol{a_1}$ and $\boldsymbol{a_2}$ can be converted to reciprocal space, or the Brillouin zone, with reciprocal lattice vectors $\boldsymbol{b_1}$ and $\boldsymbol{b_2}$.[61] **Figure 1.6** depicts the unit cell and Brillouin zone of a graphene sheet. Within the Brillouin

zone, three high-symmetry points, *Γ*, *K*, and *M*, exist at the centre, corner, and centre edge of the Brillouin zone, respectively. Along the SWNT axis, the translation vector, ***T***, defines the shortest repeat unit. Thus, in real space, the ***T*** and $\boldsymbol{C_h}$ describe the SWNT. The zone-folding approximation is used to describe the electronic properties of SWNTs.[65,66] In reciprocal space, the corresponding vectors are $\boldsymbol{K_1}$ along the SWNT circumference and $\boldsymbol{K_2}$ along the SWNT length axis. The reciprocal vector $\boldsymbol{K_1}$ gives discreet *k* vectors in the direction of $\boldsymbol{C_h}$, representing an electron's wavefront. These *k* vectors are referred to as cutting lines. Thus, an electron's wavevector is quantized in the circumferential direction. The conduction and valence bands overlap at the *K* point in the Brillouin zone. When the cutting lines of the circumferential wavevector intersect the *K* point, the SWNT has a non-zero density of states (DOS) at the Fermi level and thus has metallic properties and is referred to as a metallic (m-) SWNT. If the cutting lines do not intersect the *K* point, the SWNT behaves as a semiconductor. Thus, semiconducting and metallic properties depend on the SWNT's chirality and diameter.

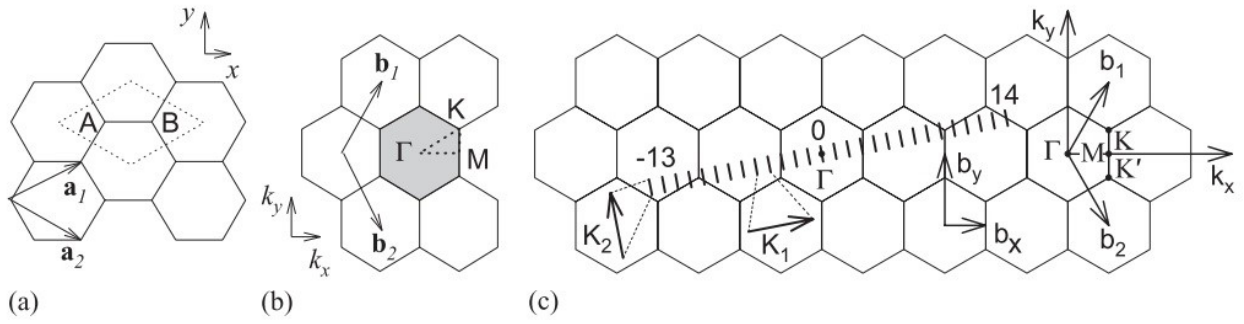

Figure 1.6: a) The carbon atoms at points A and B within the rhombus represent the unit cell of a SWNT, and $\boldsymbol{a_1}$ and $\boldsymbol{a_2}$ are the basis vectors. b) The shaded hexagonal region represents the Brillouin zone of a sheet or graphene, and $\boldsymbol{b_1}$ and $\boldsymbol{b_2}$ are the reciprocal lattice vectors. The high-symmetry points are displayed and are *Γ*, *K*, and *M* at the Brillouin zone's centre, edge, and centre edge, respectively. In c), the cutting lines are shown, which represent the wavefront of an electron travelling in the $\mathbf{K_1}$ direction (along the SWNT's circumference). Figure reproduced from Dresselhaus, M. S.; *et al*. ref. 64.

All armchair SWNTs (*n*, *n*) are metallic. As a general rule, for chiral SWNTs (*n*, *m*), if (*n*–*m*)mod(3)=0, then the SWNT is metallic, and if (*n*–*m*)mod(3)=1 or 2, then the SWNT is semiconducting.[58] SWNT synthesis produces a mixture of chiralities and diameters, producing a mixture of metallic and semiconducting SWNTs. About one-third of synthesised SWNTs are metallic.[26] In semiconducting applications, including thin-film transistors and photovoltaics, m-

SWNTs in the semiconducting layer are detrimental to device performance. Metallic SWNTs can short-circuit the channel, leading to low current on-off ratios. Before device fabrication, m-SWNTs need to be removed to maintain the semiconducting properties of a SWNT layer.

1.3.4 Sorting Single-Walled Carbon Nanotubes

Separation of sc-SWNTs is required prior to incorporation into semiconducting electronic devices. There are several methods of sorting sc-SWNTs that researchers have employed. Methods of sorting sc-SWNTs include electrophoresis,[67] agarose gel filtration,[68] aqueous two-phase extraction,[69] sorting using ssDNA with ion-exchange chromatography,[70] size exclusion chromatography,[71,72] density gradient ultracentrifugation,[73,74] and conjugated polymer extraction.[75] Density gradient ultracentrifugation (DGU) was a significant advancement towards obtaining electronically pure sc-SWNTs. In combination with surfactants, DGU can separate SWNTs based on chirality, facilitating studies of individual SWNT species.[76] Additionally, electronic devices could be fabricated using single-chirality SWNTs. Unfortunately, these methods produce a low yield of sc-SWNTs and are not ideal for increasing scale. These purification procedures are intensive and produce enriched sc-SWNTs on the microgram scale. DGU, for example, requires high centrifugation speeds up to, and even exceeding, 100 000 g. Specific conjugated polymers can be used to extract sc-SWNTs and prepare high-purity dispersions, some of which are commercially available. Conjugated polymer extraction is a simple and effective means of preparing high-purity dispersions of sc-SWNTs.

1.4 Conjugated Polymer Extraction

1.4.1 Overview of Conjugated Polymer Extraction

Conjugated polymer extraction (CPE) is the most effective and inexpensive method of sorting sc-SWNTs. Sc-SWNT purities above 99.99 % are achievable using commercial polymers.[21] The seminal work by Nicholas *et al*. demonstrated that specific aromatic polymers could selectively sort and disperse sc-SWNTs.[75] Polymers can be tuned to wrap around sc-SWNTs forming a non-covalent supramolecular complex, which leaves the SWNTs' electrical properties intact. Polymer solubility facilitates dispersion of individual, polymer-wrapped sc-SWNTs in organic solvents. The absence of m-SWNTs can be confirmed using absorbance and Raman spectroscopy.[77-79] Short-channel TFT measurements are required to determine more precise purities.[21] Conjugated polymer extraction is the most efficient method of sorting SWNTs for electronic applications.

The CPE procedure is simple and can be done in only a few hours. The procedure of CPE is depicted in **Figure 1.7**. First, polymer and pristine SWNTs are combined and mixed with a solvent. Next, the polymer: SWNT mixture is sonicated in order for the polymer to exfoliate the sc-SWNTs selectively. Selective exfoliation of sc-SWNTs during sonication may be due to differences in polarizability between sc-SWNTs and m-SWNTs. M-SWNTs are ~10^3 times more polarizable than sc-SWNTs.[80] During sonication, the m-SWNTs remain bundled in large aggregates. Next, the dispersed Polymer: sc-SWNTs are separated from the bundled m-SWNTs and other carbonaceous material using a mild centrifugation step. The supernatant from centrifugation consists of polymer-wrapped sc-SWNTs, alongside excess wrapping polymer that is not bound to sc-SWNTs. This excess polymer can be removed using a filtration step if desired.

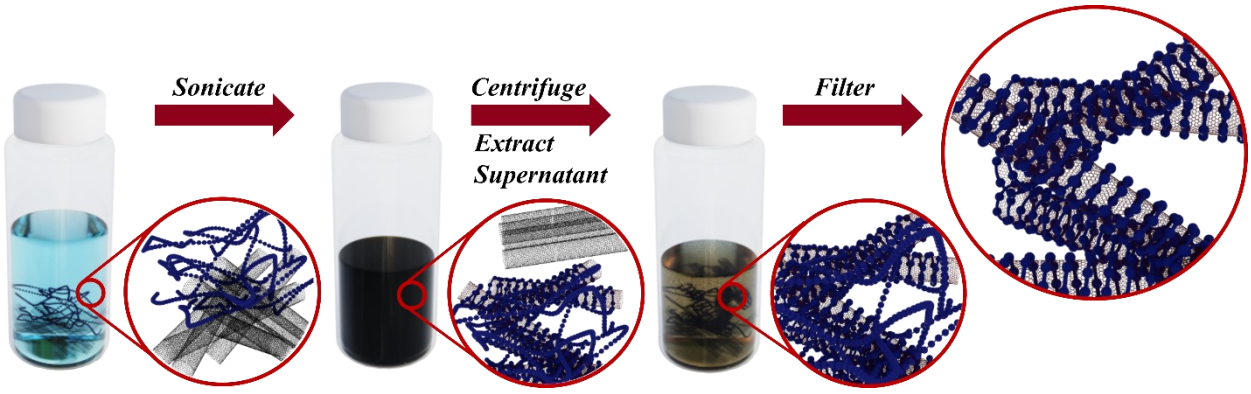

Figure 1.7: Schematic of the procedure for conjugated polymer extraction.

1.4.2 Polymer Backbones and Alkyl Side Chains

Conjugated polymers used to sort sc-SWNTs consist of an aromatic backbone. Most commonly, the polymer backbones are derivatives of fluorene,[81] carbazole,[82] or thiophene[83] moieties. Poly(fluorene)s and poly(fluorene) derivatives are the polymers most commonly used to enrich sc-SWNTs. There are several factors to consider when selecting a sorting polymer. For example, different polymer structures will select for different diameter ranges of sc-SWNTs. Different SWNT synthetic techniques produce SWNTs with different diameter ranges, so a given polymer might only be effective at selecting sc-SWNTs produced using a specific synthetic method. The electronic properties of the polymer must also be considered. For example, in photovoltaic applications, poly(thiophene)s are often used to sort sc-SWNTs, since poly(thiophene)s are also a common electron donor in a bulk heterojunction photovoltaic. Also, different applications will require different sc-SWNT diameters. Photovoltaics require small-diameter sc-SWNTs because the larger bandgap forms a favourable bulk heterojunction. Due to the small diameter requirement, poly(3-alkylthiophene)s are often used to sort sc-SWNTs for photovoltaics. Poly(3-alkylthiophene)s possess a less rigid polymer backbone and can therefore conform to the increased curvature of small diameter sc-SWNTs, and are used to sort the small diameter HiPco and CoMoCAT SWNTs.[83] To sort larger diameter SWNTs, polymers with a more rigid backbone can be used, such as a poly(fluorene-*co*-benzothiadiazole) copolymer.[84] The polymer backbone can be made more rigid by incorporating copolymers into the polymer backbone to select for large diameter SWNTs. Poly(2,7-carbazole)s select for smaller diameter

HiPco SWNTs.[82] However, copolymerization with a fluorene moiety, poly(carbazole-*co*-fluorene), shifts the selectivity towards large diameter SWNTs.[85]

Loi *et al*. studied the side chain length of homo poly(fluorene).[86] Side chains with six carbon atoms did not disperse SWNTs, eight carbons dispersed small-diameter sc-SWNTs, and ten carbons or more showed selectivity towards larger diameters. Malenfant *et al*. successfully enriched large-diameter sc-SWNTs using homo poly(fluorene)s with side chains containing up to 18 carbon atoms.[87] Optimal side chain length appears to be between 12 – 18 carbon atoms; side chains that are too long will reduce selectivity towards sc-SWNTs. Copolymers of poly(fluorene) are also used to sort large-diameter SWNTs. Poly(fluorene) copolymerized with a bipyridine moiety (PFO-BPy) is a commercially available polymer that can sort SWNTs of any diameter range.[81] Though PFO-BPy does not show diameter selectivity, the polymer can effectively sort large-diameter sc-SWNTs. Additionally, poly(fluorene)s can be copolymerized with electron-rich moieties to increase selectivity towards large-diameter sc-SWNTs.[88] Often overlooked compared to poly(fluorene)s, poly(carbazole)s also show selectivity towards sc-SWNTs, both small- and large-diameter.[85,89] Poly(thiophene)s also show selectivity towards sc-SWNTs, though usually small-diameter sc-SWNTs.[83] Poly(thiophene)s can be copolymerized to sort large-diameter sc-SWNTs, such as poly(dithiafulvalene-*co*-thiophene).[29] For TFT applications, large-diameter SWNTs are desired, dictating the choice of polymer.

Recently, there has been an effort to design polymers capable of sorting and dispersing sc-SWNTs in "green" solvents. Ritaine and Adronov reported that modifications to the polymer side-chains can facilitate dispersion in "greener" solvents.[90] The authors designed a poly(fluorene) with poly(ethylene glycol) side chains that could be cleaved at higher temperatures in order to increase the conductivity. The resulting polymer: sc-SWNT dispersion could be transferred from THF to triethylene glycol monomethyl ether and tetraethylene glycol dimethyl ether, which are considered "greener" solvents.[90]

1.4.3 Molecular Weight Effects

The molecular weight of the conjugated polymer must also be considered. For each conjugated polymer, there exists an ideal range of molecular weight. Polymer molecular weights that are too low or too high will result in dilute dispersions of sc-SWNTs, or reduced sc-SWNT selectivity. A molecular weight that is too low can cause incomplete exfoliation of the sc-SWNTs,

preventing individual sc-SWNTs from dispersing in the solvent. A molecular weight that is too high will increase the solution viscosity, which can reduce the reaggregation rates of polymer-wrapped SWNTs, causing m-SWNTs to be exfoliated and dispersed. Work done by Mayor investigated oligomers of poly(9,9-didodecylfluorene-2,7-diyl) (PDDF).[91] The resulting oligomer-SWNT complexes were unstable due to the oligomer's insufficient exfoliation of the SWNTs, causing SWNTs to reaggregate. Work done by Zaumseil *et al*. highlighted the importance of molecular weight in CPE.[92] Dispersions of sc-SWNTs were prepared in toluene and *o*-xylene using two different conjugated polymers, poly(9,9-dioctylfluorene) (PFO) and poly(9,9-dioctylfluorene-co-benzothiadiazole) (F8BT). For F8BT, weight-average molecular weights (M_w) of 27, 64.5, and 189 kDa were used, and for PFO, 15.4, 90.3, and 257 kDa was used. For the molecular weights used in the study, the authors concluded that the low to medium M_w provided the best results in terms of selectivity and yield. Increased M_w increases the solution viscosity, reducing the diffusion rate for polymer-wrapped SWNTs to aggregate. Reduction in diffusion stabilizes polymer-SWNT complexes that would otherwise be unstable, and therefore more m-SWNTs are dispersed. Thus, the results showed that a M_w range of 30 – 90 kDa was optimal in terms of yield and selectivity.[92]

Adronov *et al*. studied molecular weight effects on sc-SWNT sorting using poly[2,7-(9,9-dioctylfluorene)-alt-2,5- (3-dodecylthiophene)] (PFT).[93] The authors reported number-average molecular weights (M_n) of 5 – 85 kDa. Similar to the work done by Zaumseil *et al*., the ideal M_n range was found to be 10 – 35 kDa; too low M_n produced low-yield dispersions and too high M_n reduced sc-SWNT selectivity. Further work from the Adronov group investigated M_n using poly(2,7-*N*-alkylcarbazole)s with an M_n of 5 – 92 kDa.[89] Below a threshold M_n of ~27 kDa, the polymers did not show selectivity for sc-SWNTs. Above 27 kDa, the selectivity for sc-SWNTs was improved. The molecular weight of the polymer is an important parameter to consider when preparing dispersions of sc-SWNTs. Molecular weights that are too low or too high will produce sc-SWNT dispersions with poor yield or selectivity. Additionally, if the molecular weight is too high, the polymer may be insoluble, which will hinder sc-SWNT dispersion.

1.4.4 Solvent Effects

It is essential to consider the solvent when preparing sc-SWNT dispersions. Most importantly, the sorting polymer must be soluble, and the solvent must have a low SWNT solubility so that only polymer-SWNTs are dispersed. Additionally, the solvent density must be

lower than the SWNT density (~1.33 g/cm^3) so that the SWNT bundles can be removed using centrifugation.[27] Nicholas *et al*. found that dispersions prepared in chloroform contained a larger amount of m-SWNTs.[84] This was attributed to the density of chloroform, which is 1.5 g/cm^3. Due to the solvent density being greater than the SWNT density, SWNT bundles (SWNT aggregates not exfoliated by the polymer) were not removed entirely after centrifugation. The next consideration for a solvent is the solvent's polarity. The following section discusses the effects of solvent polarity. It is hypothesised that solvent polarity affects the mechanism of selectivity towards sc-SWNTs.

1.4.5 Electronic Considerations of sc-SWNT Selectivity and Possible Mechanism

There is no agreed-upon mechanism by which researchers can explain conjugated polymer extraction completely. However, there are some heuristics and hints at what the possible mechanism may involve. Experiments have shown that the mechanism of conjugated polymer sorting involves the polymer and SWNT electronics to a certain degree. Rice *et al*. were able to show that the electronic nature of the conjugated polymer backbone affects selectivity towards sc-SWNTs.[94] Two poly(fluorene-*co*-phenylene) copolymers were used, each with a different functional group on the phenylene unit: an electron-donating methoxy group was added to one copolymer, and an electron-withdrawing nitro group was added to the other copolymer. The electron-donating copolymer showed selectivity towards sc-SWNTs, while the electron-withdrawing copolymer showed selectivity towards m-SWNTs.[94] Adronov and coworkers have shown in other reports that the electronic nature of the polymer backbone affects the selectivity toward sc- and m-SWNTs.[95,96]

Bao and coworkers suggested that the sorting mechanism is related to differences in polarizability between sc- and m-SWNTs.[80] Metallic SWNTs are ~10^3 times more polarizable than sc-SWNTs. In non-polar solvents, dipole-dipole interactions can cause m-SWNTs to aggregate, thus facilitating their removal using centrifugation. Thus, the polarity of the solvent also plays a role, with non-polar solvents such as toluene, xylene, and decalin showing a capacity to prepare dispersions of sc-SWNTs.[27] However, there are reports of sc-SWNT dispersions being prepared in THF.[82] THF is a polar solvent; thus, its capacity to prepare dispersions of sc-SWNTs is inconsistent with the mechanism of SWNT polarizability. Similar to the hypothesis proposed by Bao, Malenfant and coworkers suggest that a possible sorting mechanism is due to the differences

in polarizability between sc- and m-SWNTs, but that pH is responsible.[97] At neutral to acidic pH levels, the O_2/H_2O redox potential is deeper than the sc-SWNT valence (1s) band, facilitating electron transfer from the sc-SWNT to the O_2/H_2O redox reaction and p-doping the sc-SWNT.[98] Thus, the presence of solvated oxygen and moisture on the surface p-dopes the sc-SWNTs. Charged sc-SWNTs induce dipoles in m-SWNTs, causing them to bundle. Upon titration with NaOH, the authors observed that the wrapping polymer was no longer selective towards sc-SWNTs, which was consistent with their proposed mechanism involving the pH at the sc-SWNT surface.[97] At basic pH levels, the O_2/H_2O redox potential is shifted above the sc-SWNT V(1s) level and p-doping of the sc-SWNTs does not occur.

1.4.6 Sorting Large-Diameter sc-SWNTs

In transistor applications, large-diameter SWNTs are desired. Larger diameter SWNTs (d_t > 1.2 nm) form an interface at the electrode with a reduced Schottky barrier for charge injection due to the inverse dependence of bandgap on diameter; the smaller bandgap is more energetically favourable for charge injection at the electrode interface.[19,99] Thus, increased diameters contribute to increased current on-off ratios.[81,100] Additionally, larger diameters lead to higher carrier mobility, as per the tight-binding model.[99] When sorting sc-SWNTs for TFT applications, it is desirable to sort larger diameter sc-SWNTs produced using the arc discharge,[27] laser ablation,[60] or plasma torch[61] techniques. Conjugated polymers that have been used to sort large-diameter sc-SWNTs include poly(dithiafulvalene-*co*-thiophene) (pDTFF) copolymers,[29] poly(fluorene-*co*-carbazole) (PCF) copolymers,[85] poly(fluorene-*co*-bipyridine) (PFO-BPy) copolymers,[54] homo poly(fluorene)s,[87] and poly(fluorene-*co*-pyridine) (P(FEt3M-Py-2,5).[101] Improved selectivity of large-diameter sc-SWNTs is related to the polymer backbone and the alkyl side chains. Increased rigidity in the polymer backbone reduces the capacity of the polymer to conform to the increased curvatures of the small-diameter sc-SWNTs; thus, the polymer backbone will conform to the surface of large-diameter sc-SWNTs, which possess reduced curvature. The length of the alkyl side chains also affects the diameter selectivity. For poly(fluorene) homopolymers, alkyl side chains lengths of eight or fewer carbon atoms can sort small-diameter sc-SWNTs but are incapable of dispersing sc-SWNTs in high yields with a diameter above ~1.1 nm.[81] Poly(fluorene) homopolymers with side chains containing 10 – 18 carbon atoms can selectivity disperse large-diameter sc-SWNTs.[87] Longer alkyl side chains provide greater surface coverage of large-diameter sc-SWNTs, thus improving the colloidal stability.

1.4.7 Optical Spectroscopy to Evaluate CPE Efficacy

Sc-SWNT purity is evaluated using optical spectroscopy and short-channel transistor measurements. Both techniques can confirm whether or not a sample is > 99 % pure in sc-SWNT species. Absorbance spectroscopy is a simple technique that is useful for obtaining a quick estimate of sc-SWNT purity. For larger diameter SWNTs, four peaks can be observed in the absorbance spectrum: three semiconducting peaks (S_{11}, S_{22}, and S_{33}) and one metallic peak (M_{11}). For larger diameter plasma synthesized SWNTs, the M_{11} peak is located in the range of 600 – 800 nm, and the S_{22} peak is located in the range of 800 – 1100 nm. As a quick estimate of purity, the ratio of the M_{11} to the S_{22} absorption envelopes can be used to estimate the sc-SWNT purity.[102] However, this method is ineffective for m-SWNT concentrations of 1 % or less due to errors in the baseline subtraction. The absorption peak ratio (ϕ_i) can be used to determine if a sample is >99 % pure in sc-SWNT species.[87] Calculation of ϕ_i involves taking the ratio of the S_{22} and M_{11} absorption envelope after baseline subtraction to the entire S_{22} and M_{11} absorption envelope. Values of $\phi_i >$ 0.40 indicate that the sample is >99 % in semiconducting species. **Figure 1.8** depicts the calculation of ϕ_i.

$$\phi_i = \frac{A_{SWNT}}{A_{SWNT} + A_{BASE}} \tag{29}$$

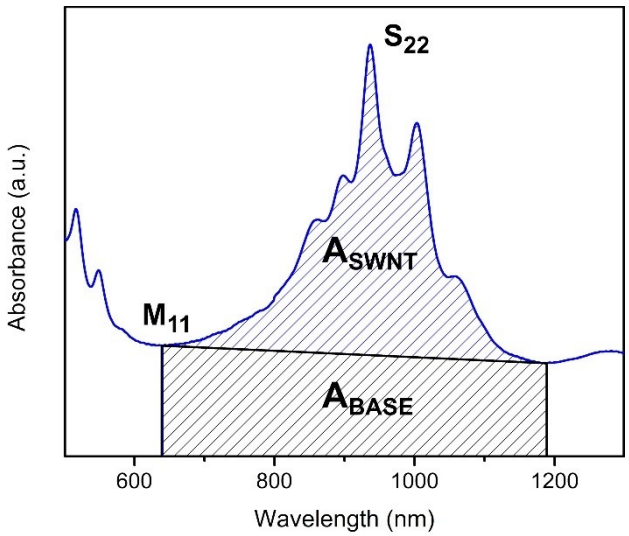

Figure 1.8: Absorption spectrum of SWNTs, focused on the second van Hove transition (S_{22}). The absorption peak ratio (ϕ_i) is the ratio of the S_{22} area after baseline subtraction to the entire absorption envelope.

Raman spectroscopy is a powerful technique for evaluating the purity of sc-SWNT dispersions. Both m- and sc-SWNTs resonate strongly at laser excitation wavelengths that overlap with the van Hove singularities and, therefore, can be detected in small quantities that would otherwise be undetectable using absorbance spectroscopy.[77,79] Literature reports have shown that three laser excitation wavelengths are sufficient to probe a sample for m-SWNTs: 514 nm, 633 nm, and 785 nm.[103] The radial breathing mode (RBM) is a phonon mode unique to SWNTs; its presence in the Raman spectrum (100 – 500 cm^{-1}) is direct evidence of the presence of sc- and m-SWNTs. The RBM mode represents an out-of-plane bond-stretching of the carbon atoms in the SWNT's radial direction. Thus, RBM frequency is inversely proportional to SWNT diameter.[64] The *G*-band is a phonon mode characteristic of sp^2-hybridized carbon and is observed in graphite and SWNTs. In SWNTs, the *G*-band mode can be divided into two features: the G^+ feature, which arises from carbon atom vibrations along the SWNT axis, and the G^- feature, which arises from vibrations along the circumferential direction. The *G*-band features for sc-SWNTs (G_{sc}^+ and G_{sc}^-) exhibit Lorentzian line shapes at ~1590 cm^{-1}. The line shape of the SWNT *G*-band feature can be used to distinguish m- and sc-SWNTs, and thus is an important mode of m-SWNT detection. The *G*-band feature of m-SWNTs (G_m^-) is asymmetric and can be fit using a Breit-Wigner-Fano (BWF) line shape.[64,104] Analysis of the RBM at a 785 nm excitation wavelength and the *G*-band region at a 633 nm excitation wavelength can be used to detect the presence of m-SWNTs. In the RBM region at 100 – 400 cm^{-1} peaks in the range of ~145 – 185 cm^{-1} (for large-diameter plasma-synthesized SWNTs) are attributable to m-SWNTs. In the *G*-band region, the presence of a BWF line shape at ~1590 cm^{-1} indicates the presence of m-SWNTs, as opposed to the Lorentzian line shape attributable to sc-SWNTs, which consists of two Lorentzian peaks: the G_{sc}^+ and G_{sc}^-.[104] An example of the RBM and *G*-band regions for sc-SWNTs sorted using a copolymer poly(fluorene-*co*-dimethoxybenzene) (PFMB) is displayed in **Figure 1.9a** and **b**, respectively.

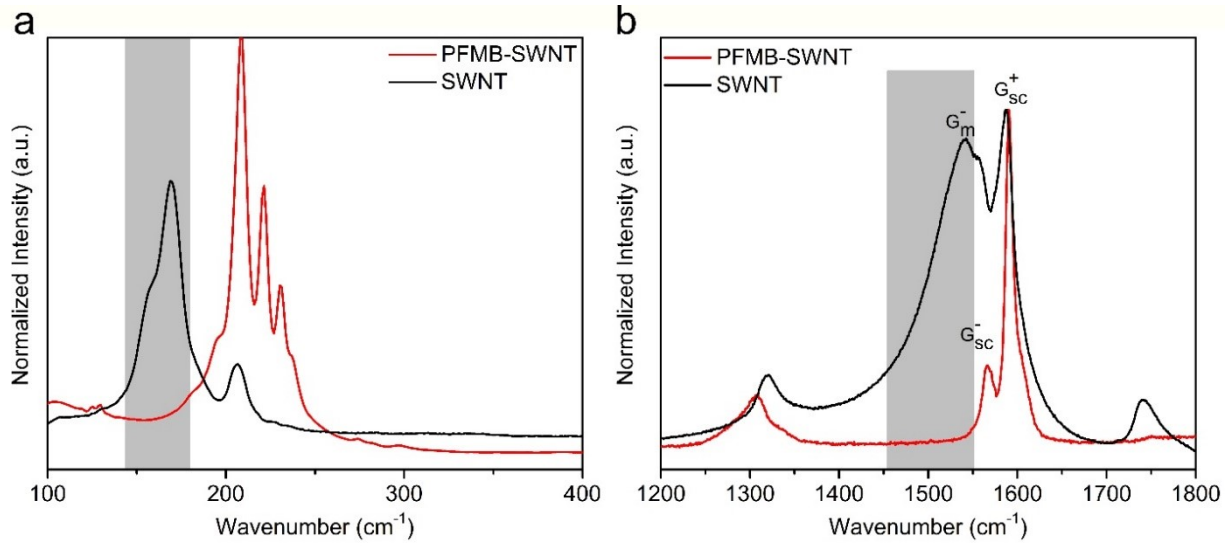

Figure 1.9: Raman spectra of PFMB-SWNT and pristine SWNTs at an excitation wavelength of (a) 785 nm (RBM region) and (b) 633 nm (*G*-band region). The grey boxes indicate the location of signals arising from metallic SWNTs. All spectra have been normalized to the G_{sc}^{+} peak, and for (a), the PFMB-SWNT spectrum has been multiplied by a factor of 5. Figure reproduced from Mirka, B.; *et al*. ref. 88.

1.5 SWNT Thin-Film Transistors

1.5.1 Overview

The market for electronic devices has expanded to include electronic devices that are flexible and inexpensive and possess the capacity for large-scale production. Such devices include organic light-emitting diodes (OLEDs), which have become ubiquitous in displays,[105] flexible sensors/monitors that are conformable to the human body or other curved surfaces,[106] flexible logic circuits to operate OLED displays and to enable flexible screens,[107] and conductive films operating as artificial human skin.[108] The applications mentioned above necessitate flexible and inexpensive semiconductor materials. SWNTs are prospective candidates for semiconductor materials in flexible TFTs due to their excellent electrical and mechanical properties.[50,109] Scalable techniques now exist to isolate sc-SWNTs from pristine SWNTs in stable dispersions, thus facilitating the incorporation of sc-SWNTs in TFTs using large-scale solution-based fabrication. Polymer-sorted sc-SWNTs can be incorporated into thin-film transistors (TFTs) as the semiconductor and deposited using solution processing techniques.[110] A TFT is an electronic switch modulated using a gate electrode. An applied voltage at the gate induces charge accumulation at the semiconductor-

dielectric interface, and an applied voltage between the source and drain electrodes forces the charges to flow across the channel.

Early adaptations of SWNT TFTs utilized chemical vapour deposition (CVD) techniques to grow SWNTs directly onto the substrate, followed by physical vapour deposition (PVD) of the source-drain electrodes onto the grown SWNT layer.[110] A single SWNT can be grown on a substrate to form a field-effect transistor (FET), which exhibits outstanding mobilities in the range of 10^3 - 10^5 $cm^2V^{-1}s^{-1}$.[111,112] SWNT thin-film transistors can be fabricated by growing SWNTs into a network. However, m-SWNTs are grown inevitably during CVD synthesis. A small number of m-SWNTs in the SWNT layer can eliminate the TFT's OFF-state if percolation pathways are formed within the TFT channel, short-circuiting the source-drain electrodes. It was necessary to fabricate TFTs with large channel lengths and low SWNT densities to reduce the probability of m-SWNTs forming percolation pathways between the source-drain electrodes, thus limiting the scale of SWNT TFTs. Concentrations of m-SWNTs as low as 1 % within the SWNT film can reduce the ON/OFF current ratio by three orders of magnitude.[113] Additionally, CVD-grown SWNTs are more expensive than SWNTs grown by arc discharge, laser ablation, or plasma torch techniques. The emergence of conjugated polymer extraction facilitated the preparation of ultra-pure dispersions of sc-SWNTs in organic solvents. Solution processing techniques are now commonly used to fabricate SWNT TFTs.

1.5.2 SWNT TFT Fabrication

An advantage of polymer-sorted sc-SWNTs is that they can be fabricated into TFTs using solution processing techniques. Solution processing techniques form thin-films of SWNTs directly from a SWNT dispersion. On a smaller scale, a standard solution processing technique is spin coating, where an aliquot of SWNT dispersion is dispensed onto a substrate and spun at high speeds until the solvent has evaporated, leaving behind a thin-film of SWNTs.[114] During solution processing, an adhesion promoter, such as poly-L-lysine, is often used to improve SWNT adhesion to the substrate surface and increase the SWNT density.[115] Solution-processed films of SWNTs can also be formed by immersing the substrate in a solution of SWNTs,[116] drop-casting,[117] dip-coating,[118] spray-coating,[119] or blade-coating.[120] SWNT TFTs fabricated using solution processing techniques have exhibited exceptional performance. However, CVD-grown SWNT TFTs' mobility gains are often lost in solution processing. Solution-processed SWNT TFTs often are less dense

compared to those grown by CVD, and a solution-cast SWNT film consists of a network of SWNTs oriented randomly. SWNT TFT fabrication techniques have been developed to improve the film morphology, such as SWNT alignment within the TFT channel using self-assembly[54,121] or solution shearing.[122] When SWNTs form a thin-film, SWNT junctions behave as resistors, and the random alignment of SWNTs within the film increases the path for charge transport. In addition, the wrapping polymer can be removed from the sc-SWNTs post-sorting using metal chelation agents[123] or cleavable polymers.[124] Enhanced fabrication techniques have demonstrated exceptional performance, and aligned SWNT TFTs have even exceeded the current density of inorganic semiconductors.[31] Other optimizations have focused on increasing the polarization at the SWNT-dielectric interface. A thin layer (< 100 nm) of high-κ dielectric material can be deposited on top of the SWNT layer, facilitating low-voltage operation.[114,125] Though the SWNT TFTs described above have demonstrated exceptional performance, their manufacture requires extensive fabrication, which can be laborious and time-consuming, and has been demonstrated only on a laboratory scale. The fruition of commercial-scale SWNT TFT applications necessitates compatibility with continuous, roll-to-roll printing techniques.

Printing technology offers the benefits of additive, inexpensive, and high-throughput manufacturing. Printing technology is the most efficient route towards producing commercial scale and inexpensive SWNT electronics. Inkjet,[126,127] aerosol jet,[128-130] and gravure[126] printing have been demonstrated to fabricate SWNT TFTs. Aerosol jet printing operates by atomizing the SWNT dispersion into an aerosol and depositing the aerosol in a high-pressure stream, a common printing technology in SWNT TFT manufacture.[128,131,132] Aerosol jet printing can also print the entire SWNT TFT (not just the SWNT layer), including the source-drain electrodes, gate electrode, and dielectric.[128,133] Inkjet printing deposits the SWNT ink in a drop-wise fashion without aerosolization, thereby reducing energy requirements.[80] However, the ink viscosity must be carefully controlled and optimized due to its effect on drop spacing, printing resolution, and machine clogging.[134] SWNT TFTs fabricated using a combination of gravure and inkjet printing have been demonstrated, where gravure printing deposited the gate and dielectric, and inkjet printing deposited the SWNTs and source-drain electrodes.[126]

1.5.3 Charge Transport in SWNT TFTs

Charge transport in SWNT films is difficult to model. Charge transport in SWNTs occurs as intra-tube transport (within a SWNT) and inter-tube transport (between SWNTs). For SWNTs longer than an electron's mean-free-path (>1 μm),[135] the intra-tube charge transport is governed by diffusive band transport limited by phonon and defect scattering. Hence, intra-tube carrier transport in individual SWNTs is inversely proportional to temperature due to increased phonon scattering rates at higher temperatures.[136] Perebeinos *et al*. developed an empirical model for the carrier mobility in a SWNT that is inversely proportional to temperature and directly proportional to the diameter.[136] However, the carrier mobility exhibited by a SWNT film is significantly lower than the intra-tube mobility of an individual SWNT. Inter-tube connections between SWNTs create a large channel resistance, which is exacerbated by variations in length and diameter. In particular, SWNT bundling can cause electric field screening, which causes incomplete gating of the bundled SWNTs. Solution-processed SWNT TFTs consist of networks of SWNTs randomly oriented, with many inter-connecting SWNTs. Percolation theory describes conduction in films of randomly oriented conducting wires, and percolation is dependent on the density and connectivity of these wires.[137] Below the percolation threshold density, there is negligible conduction, and above the percolation threshold conduction follows a power-law dependence on density. However, networks of SWNTs do not show the same dependence on SWNT density, and above network densities of ~10 SWNTs/μm, there does not seem to be a strong dependence of mobility on density.[47] However, carrier transport within a SWNT network involves effects due to SWNT junctions, charge trapping at the SWNT dielectric interface, limited gating caused by electric field screening, and variations in SWNT length and diameter. The variable range hopping (VRH) model describes the hopping of charges between localized states close to the Fermi level. The probability of a charge hopping from one localized state to another depends on the energetic difference between the states and the spatial difference.[138,139] VRH is often used to describe carrier transport in organic small molecules and conducting polymers. In the VRH model, charge hopping is thermally activated, and conductivity increases with temperature. For a more thorough review of charge transport in SWNT TFTs, the reader is referred to an excellent review by Zorn and Zaumseil.[140]

1.5.4 Applications of SWNT TFTs

Outstanding examples of SWNT TFT applications have been demonstrated in the literature. These examples demonstrate the role of SWNT TFTs in next-generation electronic devices. For example, SWNT TFTs are of interest in active-matrix backplanes. The flexibility and mechanical robustness of SWNTs attract interest for application into active-matrix backplanes for flexible OLED screens. Zhou *et al*. demonstrated CVD-grown SWNT TFTs in OLED backplanes.[107] However, incorporating SWNTs into active-matrix displays has been challenging due to the high mobility requirements, variability in performance, and shifts in threshold voltage.[30] Other applications exist for SWNT TFTs in active-matrix backplanes, such as sensing applications. Typically, the demands for SWNTs in active-matrix backplanes for sensing applications are less rigorous; the devices do not require higher mobilities, and the reduced bias stress does not exacerbate shifts in threshold voltage.[30] SWNTs are particularly well-suited for applications in pressure sensors due to their flexibility and ability to conform to curved surfaces. Takahashi *et al*. have investigated solution-processed SWNT TFTs in active-matrix backplanes for conformable pressure sensors.[115] By incorporating a pressure-sensitive rubber as the exposed layer, an active-matrix backplane composed of SWNT TFTs provides pressure mapping. Using a similar device setup, Yeom *et al*. fabricated flexible and stretchable pressure sensors using a doctor blade to print the source-drain electrodes and the dielectric.[141] Pressure detection is an advanced application of SWNT TFTs that can even have future applications in artificial skin.[106]

There is an interest in incorporating SWNT TFTs into complementary logic.[19,110,142] An application of particular interest for polymer-sorted sc-SWNTs has been the inverter. Furthermore, incorporation into inverters, especially complementary inverters, has been a challenge for SWNTs. Complementary logic requires p- and n-type TFTs in order to minimize power consumption and maximize voltage gain. Though intrinsically ambipolar, n-type conduction is often suppressed in SWNTs when exposed to ambient conditions. Under ambient conditions, adsorption of oxygen and moisture can shift the SWNT Fermi level into the valence band, and a redox reaction from the water traps electrons.[98] Therefore, attempts at integrating SWNTs into complementary inverters involved balancing the n- and p-type behaviour of the SWNTs. Javey *et al.* studied SWNT TFTs using thin layers (8 nm) of high-κ ZrO_2 dielectrics. Using thin layers of high-κ ZrO_2, the authors fabricated SWNT TFTs with very high p- and n-type mobilities and very low subthreshold slopes. Additionally, they were able to fabricate complementary inverters with voltage gains up to 60.[112]

Zhang *et al*. explored the use of atomic layer deposition (ALD) to deposit thin-films of high-κ dielectric, which also acts as a passivation layer. The authors studied two high-κ oxides: Al_2O_3 and HfO_3. The authors were able to achieve balanced p- and n-type charge transport and were able to fabricate complementary inverters.[143] Similar to the work done by Zhang *et al.*, Schießl *et al.* developed a novel PMMA-HfO_x hybrid dielectric to facilitate ambipolarity *via* a passivation layer. Fabrication of ambipolar SWNT TFTs facilitated the fabrication of complementary inverters.[114] An alternative to a passivation layer is to use n-type doping in order to achieve n-type behaviour. Schneider *et al.* utilized 1,2,4,5-Tetrakis(Tetramethylguanidino)Benzene to act simultaneously as an electron donor and a hole blocker. The authors were able to achieve unipolar n-type behaviour and were able to fabricate complementary inverters.[144] Following successful integration into complementary inverters, SWNT-based ring oscillators can be fabricated by connecting an odd number of ring oscillators.[21,22,145,146] Additionally, complementary logic applications of solution-processed SWNT TFTs include NAND gates,[147,148] NOR gates,[24,149] and radio frequency applications.[149]

1.6 References

(1) Gelinck, G.; Heremans, P.; Nomoto, K.; Anthopoulos, T. D. Organic Transistors in Optical Displays and Microelectronic Applications. *Adv. Mater.* **2010**, *22*, 3778–3798.

(2) Shirota, Y.; Kageyama, H. Charge Carrier Transporting Molecular Materials and Their Applications in Devices. *Chem. Rev.* **2007**, *107*, 953–1010.

(3) Takeda, Y.; Yoshimura, Y.; Shiwaku, R.; Hayasaka, K.; Sekine, T.; Okamoto, T.; Matsui, H.; Kumaki, D.; Katayama, Y.; Tokito, S. Organic Complementary Inverter Circuits Fabricated with Reverse Offset Printing. *Adv. Electron. Mater.* **2018**, *4*, 1700313.

(4) Klauk, H.; Zschieschang, U.; Pflaum, J.; Halik, M. Ultralow-Power Organic Complementary Circuits. *Nature* **2007**, *445*, 745–748.

(5) Forrest, S. R. The Path to Ubiquitous and Low-Cost Organic Electronic Appliances on Plastic. *Nature* **2004**, *428*, 911–918.

(6) Zou, S.-J.; Shen, Y.; Xie, F.-M.; Chen, J.-D.; Li, Y.; Tang, J.-X. Recent Advances in Organic Light-Emitting Diodes: Toward Smart Lighting and Displays. *Mater. Chem. Front.* **2020**, *4*, 788–820.

(7) Lai, S.; Casula, G.; Cosseddu, P.; Basiricò, L.; Ciavatti, A.; D'Annunzio, F.; Loussert, C.; Fischer, V.; Fraboni, B.; Barbaro, M.; Bonfiglio, A. A Plastic Electronic Circuit Based on Low Voltage, Organic Thin-Film Transistors for Monitoring the X-Ray Checking History of Luggage in Airports. *Org. Electron.* **2018**, *58*, 263–269.

(8) Inganäs, O. Organic Photovoltaics over Three Decades. *Adv. Mater.* **2018**, *30*, 1800388.

(9) Su, Y.-W.; Lan, S.-C.; Wei, K.-H. Organic Photovoltaics. *Mater. Today* **2012**, *15*, 554–562.

(10) Andre, R. S.; Ngo, Q. P.; Fugikawa-Santos, L.; Correa, D. S.; Swager, T. M. Wireless Tags with Hybrid Nanomaterials for Volatile Amine Detection. *ACS Sensors* **2021**, *6*, 2457–2464.

(11) Schroeder, V.; Savagatrup, S.; He, M.; Lin, S.; Swager, T. M. Carbon Nanotube Chemical Sensors. *Chem. Rev.* **2019**, *119*, 599–663.

(12) Lapointe, F.; Ding, J.; Lefebvre, J. Carbon Nanotube Transistors as Gas Sensors: Response Differentiation Using Polymer Gate Dielectrics. *ACS Appl. Polym. Mater.* **2019**, *1*, 3269–3278.

(13) Hirsch, A. The Era of Carbon Allotropes. *Nat. Mater.* **2010**, *9*, 868–871.

(14) Kroto, H. W.; Heath, J. R.; O'Brien, S. C.; Curl, R. F.; Smalley, R. E. C_{60}: Buckminsterfullerene. *Nature* **1985**, *318*, 162–163.

(15) Iijima, S. Helical Microtubules of Graphitic Carbon. *Nature* **1991**, *354*, 56–58.

(16) Iijima, S.; Ichihashi, T. Single-Shell Carbon Nanotubes of 1-nm Diameter. *Nature* **1993**, *363*, 603–605.

(17) Novoselov, K. S.; Geim, A. K.; Morozov, S. V.; Jiang, D.; Zhang, Y.; Dubonos, S. V.; Grigorieva, I. V.; Firsov, A. A. Electric Field Effect in Atomically Thin Carbon Films. *Science* **2004**, *306*, 666–669.

(18) Avouris, P.; Chen, Z.; Perebeinos, V. Carbon-Based Electronics. *Nat. Nanotechnol.* **2007**, *2*, 605–615.

(19) Tulevski, G. S.; Franklin, A. D.; Frank, D.; Lobez, J. M.; Cao, Q.; Park, H.; Afzali, A.; Han, S.; Hannon, J. B.; Haensch, W. Toward High-Performance Digital Logic Technology with Carbon Nanotubes. *ACS Nano* **2014**, *8*, 8730–8745.

(20) Schnorr, J. M.; Swager, T. M. Emerging Applications of Carbon Nanotubes. *Chem. Mater.* **2011**, *23*, 646–657.

(21) Lei, T.; Shao, L. L.; Zheng, Y. Q.; Pitner, G.; Fang, G.; Zhu, C.; Li, S.; Beausoleil, R.; Wong, H. S. P.; Huang, T. C.; Cheng, K. T.; Bao, Z. Low-Voltage High-Performance Flexible Digital and Analog Circuits Based on Ultrahigh-Purity Semiconducting Carbon Nanotubes. *Nat. Commun.* **2019**, *10*, 2161.

(22) Han, S. J.; Tang, J.; Kumar, B.; Falk, A.; Farmer, D.; Tulevski, G.; Jenkins, K.; Afzali, A.; Oida, S.; Ott, J.; Hannon, J.; Haensch, W. High-Speed Logic Integrated Circuits with Solution-Processed Self-Assembled Carbon Nanotubes. *Nat. Nanotechnol.* **2017**, *12*, 861–865.

(23) Zhu, C.; Chortos, A.; Wang, Y.; Pfattner, R.; Lei, T.; Hinckley, A. C.; Pochorovski, I.; Yan, X.; To, J. W.; Oh, J. Y.; Tok, J. B.-H.; Bao, Z.; Murmann, B. Stretchable Temperature-Sensing Circuits with Strain Suppression Based on Carbon Nanotube Transistors. *Nat. Electron.* **2018**, *1*, 183–190.

(24) Lee, D.; Yoon, J.; Lee, J.; Lee, B.-H.; Seol, M.-L.; Bae, H.; Jeon, S.-B.; Seong, H.; Im, S. G.; Choi, S.-J.; Choi, Y.-K. Logic Circuits Composed of Flexible Carbon Nanotube Thin-Film Transistor and Ultra-Thin Polymer Gate Dielectric. *Sci. Rep.* **2016**, *6*, 26121.

(25) Tang, J.; Cao, Q.; Tulevski, G.; Jenkins, K. A.; Nela, L.; Farmer, D. B.; Han, S.-J. Flexible CMOS Integrated Circuits Based on Carbon Nanotubes with Sub-10 ns Stage Delays. *Nat. Electron.* **2018**, *1*, 191–196.

(26) Saito, R.; Fujita, M.; Dresselhaus, G.; Dresselhaus, M. S. Electronic Structure of Chiral Graphene Tubules. *Appl. Phys. Lett.* **1992**, *60*, 2204–2206.

(27) Wang, H.; Bao, Z. Conjugated Polymer Sorting of Semiconducting Carbon Nanotubes and Their Electronic Applications. *Nano Today* **2015**, *10*, 737–758.

(28) Fong, D.; Adronov, A. Recent Developments in the Selective Dispersion of Single-Walled Carbon Nanotubes Using Conjugated Polymers. *Chem. Sci.* **2017**, *8*, 7292–7305.

(29) Wang, H.; Mei, J.; Liu, P.; Schmidt, K.; Jiménez-Osés, G.; Osuna, S.; Fang, L.; Tassone, C. J.; Zoombelt, A. P.; Sokolov, A. N.; Houk, K. N.; Toney, M. F.; Bao, Z. Scalable and Selective Dispersion of Semiconducting Arc-Discharged Carbon Nanotubes by Dithiafulvalene/Thiophene Copolymers for Thin Film Transistors. *ACS Nano* **2013**, *7*, 2659–2668.

(30) Zaumseil, J. Single-Walled Carbon Nanotube Networks for Flexible and Printed Electronics. *Semicond. Sci. Technol.* **2015**, *30*, 74001.

(31) Brady, G. J.; Way, A. J.; Safron, N. S.; Evensen, H. T.; Gopalan, P.; Arnold, M. S. Quasi-Ballistic Carbon Nanotube Array Transistors with Current Density Exceeding Si and GaAs. *Sci. Adv.* **2016**, *2*, e1601240.

(32) Klauk, H. *Organic Electronics: Materials, Manufacturing, and Applications*; Wiley-VCH: Weinheim, Germany, 2006.

(33) Shirakawa, H.; Louis, E. J.; MacDiarmid, A. G.; Chiang, C. K.; Heeger, A. J. Synthesis of Electrically Conducting Organic Polymers: Halogen Derivatives of Polyacetylene, $(CH)_x$. *J. Chem. Soc. Chem. Commun.* **1977**, No. 16, 578–580.

(34) Kumar, B.; Kaushik, B. K.; Negi, Y. S. Organic Thin Film Transistors: Structures, Models, Materials, Fabrication, and Applications: A Review. *Polym. Rev.* **2014**, *54*, 33–111.

(35) Bao, Z.; Locklin, J. *Organic Field-Effect Transistors*; CRC Press: Boca Raton, FL, USA, 2007.

(36) Zhu, H.; Shin, E.-S.; Liu, A.; Ji, D.; Xu, Y.; Noh, Y.-Y. Printable Semiconductors for Backplane TFTs of Flexible OLED Displays. *Adv. Funct. Mater.* **2020**, *30*, 1904588.

(37) Torsi, L.; Magliulo, M.; Manoli, K.; Palazzo, G. Organic Field-Effect Transistor Sensors: A Tutorial Review. *Chem. Soc. Rev.* **2013**, *42*, 8612–8628.

(38) Ling, Y.; An, T.; Yap, L. W.; Zhu, B.; Gong, S.; Cheng, W. Disruptive, Soft, Wearable Sensors. *Adv. Mater.* **2020**, *32*, 1904664.

(39) Kim, J.; Campbell, A. S.; de Ávila, B. E.-F.; Wang, J. Wearable Biosensors for Healthcare Monitoring. *Nat. Biotechnol.* **2019**, *37*, 389–406.

(40) Bilgaiyan, A.; Cho, S.-I.; Abiko, M.; Watanabe, K.; Mizukami, M. Flexible, High Mobility Short-Channel Organic Thin Film Transistors and Logic Circuits Based on 4H–21DNTT. *Sci. Rep.* **2021**, *11*, 11710.

(41) Kim, Y.-H.; Moon, D.-G.; Han, J.-I. Organic TFT Array on a Paper Substrate. *IEEE Electron Device Lett.* **2004**, *25*, 702–704.

(42) Lin, L.-K.; Tsai, J.-T.; Díaz-Amaya, S.; Oduncu, M. R.; Zhang, Y.; Huang, P.-Y.; Ostos, C.; Schmelzel, J. P.; Mohammadrahimi, R.; Xu, P.; Xu, P.; Gomez, A. M. U.; Shuvo, S. N.; Raghunathan, N.; Zhang, X.; Wei, A.; Bahr, D.; Peroulis, D.; Stanciu, L. A. Antidelaminating, Thermally Stable, and Cost-Effective Flexible Kapton Platforms for Nitrate Sensors, Mercury Aptasensors, Protein Sensors, and p-Type Organic Thin-Film Transistors. *ACS Appl. Mater. Interfaces* **2021**, *13*, 11369–11384.

(43) Gaucci, P.; Fruehauf, N.; Ilchmann, A.; Polzinger, B.; Eberhardt, W.; Kueck, H. Organic Thin Film Transistors on Back Molded Plastic Foil. *Flex. Print. Electron.* **2018**, *3*, 015008.

(44) Klauk, H.; Halik, M.; Zschieschang, U.; Eder, F.; Schmid, G.; Dehm, C. Pentacene Organic Transistors and Ring Oscillators on Glass and on Flexible Polymeric Substrates. *Appl. Phys. Lett.* **2003**, *82*, 4175–4177.

(45) Chua, L.-L.; Zaumseil, J.; Chang, J.-F.; Ou, E. C.-W.; Ho, P. K.-H.; Sirringhaus, H.; Friend, R. H. General Observation of n-Type Field-Effect Behavior in Organic Semiconductors. *Nature* **2005**, *434*, 194–199.

(46) Herlogsson, L. Electrolyte-Gated Organic Thin-Film Transistors, Linköping University, Linköping, Sweden, 2011.

(47) Schießl, S. P.; Rother, M.; Lüttgens, J.; Zaumseil, J. Extracting the Field-Effect Mobilities of Random Semiconducting Single-Walled Carbon Nanotube Networks: A Critical Comparison of Methods. *Appl. Phys. Lett.* **2017**, *111*, 193301.

(48) Cao, Q.; Xia, M.; Kocabas, C.; Shim, M.; Rogers, J. A.; Rotkin, S. V. Gate Capacitance Coupling of Singled-Walled Carbon Nanotube Thin-Film Transistors. *Appl. Phys. Lett.* **2007**, *90*, 2005–2008.

(49) Shen, Y.; Hosseini, A. R.; Wong, M. H.; Malliaras, G. G. How To Make Ohmic Contacts to Organic Semiconductors. *ChemPhysChem* **2004**, *5*, 16–25.

(50) Walters, D. A.; Ericson, L. M.; Casavant, M. J.; Liu, J.; Colbert, D. T.; Smith, K. A.; Smalley, R. E. Elastic Strain of Freely Suspended Single-Wall Carbon Nanotube Ropes. *Appl. Phys. Lett.* **1999**, *74*, 3803.

(51) Blackburn, J. L. Semiconducting Single-Walled Carbon Nanotubes in Solar Energy Harvesting. *ACS Energy Lett.* **2017**, *2*, 1598–1613.

(52) Salim, T.; Lee, H.-W.; Wong, L. H.; Oh, J. H.; Bao, Z.; Lam, Y. M. Semiconducting Carbon Nanotubes for Improved Efficiency and Thermal Stability of Polymer-Fullerene Solar Cells. *Adv. Funct. Mater.* **2016**, *26*, 51–65.

(53) Martel, R.; Schmidt, T.; Shea, H. R.; Hertel, T.; Avouris, P. Single- and Multi-Wall Carbon Nanotube Field-Effect Transistors. *Appl. Phys. Lett.* **1998**, *73*, 2447–2449.

(54) Brady, G. J.; Joo, Y.; Wu, M.-Y.; Shea, M. J.; Gopalan, P.; Arnold, M. S. Polyfluorene-Sorted, Carbon Nanotube Array Field-Effect Transistors with Increased Current Density and High On/Off Ratio. *ACS Nano* **2014**, *8*, 11614–11621.

(55) Yoon, B.; Liu, S. F.; Swager, T. M. Surface-Anchored Poly(4-Vinylpyridine)-Single-Walled Carbon Nanotube-Metal Composites for Gas Detection. *Chem. Mater.* **2016**, *28*, 5916–5924.

(56) Muguruma, H.; Hoshino, T.; Nowaki, K. Electronically Type-Sorted Carbon Nanotube-Based Electrochemical Biosensors with Glucose Oxidase and Dehydrogenase. *ACS Appl. Mater. Interfaces* **2015**, *7*, 584–592.

(57) Chico, L.; Crespi, V. H.; Benedict, L. X.; Louie, S. G.; Cohen, M. L. Pure Carbon Nanoscale Devices: Nanotube Heterojunctions. *Phys. Rev. Lett.* **1996**, *76*, 971–974.

(58) Dresselhaus, M. S.; Dresselhaus, G.; Avouris, P. *Carbon Nanotubes: Synthesis, Structure, Properties, and Applications*; Topics in Applied Physics Volume 80, Springer-Verlag: Berlin, Heidelberg, 2001.

(59) Bethune, D. S.; Kiang, C. H.; de Vries, M. S.; Gorman, G.; Savoy, R.; Vazquez, J.; Beyers, R. Cobalt-Catalysed Growth of Carbon Nanotubes with Single-Atomic-Layer Walls. *Nature* **1993**, *363*, 605–607.

(60) Thess, A.; Lee, R.; Nikolaev, P.; Dai, H.; Petit, P.; Robert, J.; Xu, C.; Lee, Y. H.; Kim, S. G.; Rinzler, A. G.; et al. Crystalline Ropes of Metallic Carbon Nanotubes. *Science.* **1996**, *273*, 483–487.

(61) Kim, K. S.; Cota-Sanchez, G.; Kingston, C. T.; Imris, M.; Simard, B.; Soucy, G. Large-Scale Production of Single-Walled Carbon Nanotubes by Induction Thermal Plasma. *J. Phys. D. Appl. Phys.* **2007**, *40*, 2375–2387.

(62) Nikolaev, P.; Bronikowski, M. J.; Bradley, R. K.; Rohmund, F.; Colbert, D. T.; Smith, K. A.; Smalley, R. E. Gas-Phase Catalytic Growth of Single-Walled Carbon Nanotubes from Carbon Monoxide. *Chem. Phys. Lett.* **1999**, *313*, 91–97.

(63) Kitiyanan, B.; Alvarez, W. E.; Harwell, J. H.; Resasco, D. E. Controlled Production of Single-Wall Carbon Nanotubes by Catalytic Decomposition of CO on Bimetallic Co–Mo Catalysts. *Chem. Phys. Lett.* **2000**, *317*, 497–503.

(64) Dresselhaus, M. S.; Dresselhaus, G.; Saito, R.; Jorio, A. Raman Spectroscopy of Carbon Nanotubes. *Phys. Rep.* **2005**, *409*, 47–99.

(65) Charlier, J.-C.; Blase, X.; Roche, S. Electronic and Transport Properties of Nanotubes. *Rev. Mod. Phys.* **2007**, *79*, 677–732.

(66) Ilani, S.; McEuen, P. L. Electron Transport in Carbon Nanotubes. *Annu. Rev. Condens. Matter Phys.* **2010**, *1*, 1–25.

(67) Tanaka, T.; Jin, H.; Miyata, Y.; Kataura, H. High-Yield Separation of Metallic and Semiconducting Single-Wall Carbon Nanotubes by Agarose Gel Electrophoresis. *Appl. Phys. Express* **2008**, *1*, 1140011–1140013.

(68) Liu, H.; Nishide, D.; Tanaka, T.; Kataura, H. Large-Scale Single-Chirality Separation of Single-Wall Carbon Nanotubes by Simple Gel Chromatography. *Nat. Commun.* **2011**, *2*, 309.

(69) Khripin, C. Y.; Fagan, J. A.; Zheng, M. Spontaneous Partition of Carbon Nanotubes in Polymer-Modified Aqueous Phases. *J. Am. Chem. Soc.* **2013**, *135*, 6822–6825.

(70) Zheng, M.; Jagota, A.; Semke, E. D.; Diner, B. A.; McLean, R. S.; Lustig, S. R.; Richardson, R. E.; Tassi, N. G. DNA-Assisted Dispersion and Separation of Carbon Nanotubes. *Nat. Mater.* **2003**, *2*, 338–342.

(71) Flavel, B. S.; Kappes, M. M.; Krupke, R.; Hennrich, F. Separation of Single-Walled Carbon Nanotubes by 1-Dodecanol-Mediated Size-Exclusion Chromatography. *ACS Nano* **2013**, *7*, 3557–3564.

(72) Flavel, B. S.; Moore, K. E.; Pfohl, M.; Kappes, M. M.; Hennrich, F. Separation of Single-Walled Carbon Nanotubes with a Gel Permeation Chromatography System. *ACS Nano* **2014**, *8*, 1817–1826.

(73) Arnold, M. S.; Green, A. A.; Hulvat, J. F.; Stupp, S. I.; Hersam, M. C. Sorting Carbon Nanotubes by Electronic Structure Using Density Differentiation. *Nat. Nanotechnol.* **2006**, *1*, 60–65.

(74) Arnold, M. S.; Stupp, S. I.; Hersam, M. C. Enrichment of Single-Walled Carbon Nanotubes by Diameter in Density Gradients. *Nano Lett.* **2005**, *5*, 713–718.

(75) Nish, A.; Hwang, J.-Y.; Doig, J.; Nicholas, R. J. Highly Selective Dispersion of Single-Walled Carbon Nanotubes Using Aromatic Polymers. *Nat. Nanotechnol.* **2007**, *2*, 640–646.

(76) Weisman, R. B.; Bachilo, S. M. Dependence of Optical Transition Energies on Structure for Single-Walled Carbon Nanotubes in Aqueous Suspension: An Empirical Kataura Plot. *Nano Lett.* **2003**, *3*, 1235–1238.

(77) Pimenta, M. A.; Marucci, A.; Empedocles, S. A.; Bawendi, M. G.; Hanlon, E. B.; Rao, A. M.; Eklund, P. C.; Smalley, R. E.; Dresselhaus, G.; Dresselhaus, M. S. Raman Modes of Metallic Carbon Nanotubes. *Phys. Rev. B* **1998**, *58*, 16016.

(78) Brown, S. D. M.; Jorio, A.; Corio, P.; Dresselhaus, M. S.; Dresselhaus, G.; Saito, R.; Kneipp, K. Origin of the Breit-Wigner-Fano Lineshape of the Tangential G-Band Feature of Metallic Carbon Nanotubes. *Phys. Rev. B* **2001**, *63*, 155414.

(79) Li, Z.; Ding, J.; Finnie, P.; Lefebvre, J.; Cheng, F.; Kingston, C. T.; Malenfant, P. R. L. Raman Microscopy Mapping for the Purity Assessment of Chirality Enriched Carbon Nanotube Networks in Thin-Film Transistors. *Nano Res.* **2015**, *8*, 2179–2187.

(80) Wang, H.; Hsieh, B.; Jiménez-Osés, G.; Liu, P.; Tassone, C. J.; Diao, Y.; Lei, T.; Houk, K. N.; Bao, Z. Solvent Effects on Polymer Sorting of Carbon Nanotubes with Applications in Printed Electronics. *Small* **2015**, *11*, 126–133.

(81) Mistry, K. S.; Larsen, B. A.; Blackburn, J. L. High-Yield Dispersions of Large-Diameter Semiconducting Single-Walled Carbon Nanotubes with Tunable Narrow Chirality Distributions. *ACS Nano* **2013**, *7*, 2231–2239.

(82) Rice, N. A.; Adronov, A. Selective Interactions of a High-Molecular-Weight Polycarbazole with Different Commercial Nanotube Samples. *J. Polym. Sci. Part A Polym. Chem.* **2014**, *52*, 2738–2747.

(83) Wang, H.; Koleilat, G. I.; Liu, P.; Jiménez-Osés, G.; Lai, Y.-C.; Vosgueritchian, M.; Fang, Y.; Park, S.; Houk, K. N.; Bao, Z. High-Yield Sorting of Small-Diameter Carbon Nanotubes for Solar Cells and Transistors. *ACS Nano* **2014**, *8*, 2609–2617.

(84) Hwang, J.-Y.; Nish, A.; Doig, J.; Douven, S.; Chen, C.-W.; Chen, L.-C.; Nicholas, R. J. Polymer Structure and Solvent Effects on the Selective Dispersion of Single-Walled Carbon Nanotubes. *J. Am. Chem. Soc.* **2008**, *130*, 3543–3553.

(85) Rice, N. A.; Bodnaryk, W. J.; Mirka, B.; Melville, O. A.; Adronov, A.; Lessard, B. H. Polycarbazole-Sorted Semiconducting Single-Walled Carbon Nanotubes for Incorporation into Organic Thin Film Transistors. *Adv. Electron. Mater.* **2019**, *5*, 1800539.

(86) Gomulya, W.; Costanzo, G. D.; de Carvalho, E. J. F.; Bisri, S. Z.; Derenskyi, V.; Fritsch, M.; Fröhlich, N.; Allard, S.; Gordiichuk, P.; Herrmann, A.; Marrink, S. J.; dos Santos, M. C.; Scherf, U.; Loi, M. A. Semiconducting Single-Walled Carbon Nanotubes on Demand by Polymer Wrapping. *Adv. Mater.* **2013**, *25*, 2948–2956.

(87) Ding, J.; Li, Z.; Lefebvre, J.; Cheng, F.; Dubey, G.; Zou, S.; Finnie, P.; Hrdina, A.; Scoles, L.; Lopinski, G. P.; Kingston, C. T.; Simard, B.; Malenfant, P. R. L. Enrichment of Large-Diameter Semiconducting SWCNTs by Polyfluorene Extraction for High Network Density Thin Film Transistors. *Nanoscale* **2014**, *6*, 2328–2339.

(88) Mirka, B.; Fong, D.; Rice, N. A.; Melville, O. A.; Adronov, A.; Lessard, B. H. Polyfluorene-Sorted Semiconducting Single-Walled Carbon Nanotubes for Applications in Thin-Film Transistors. *Chem. Mater.* **2019**, *31*, 2863–2872.

(89) Rice, N. A.; Subrahmanyam, A. V.; Laengert, S. E.; Adronov, A. The Effect of Molecular Weight on the Separation of Semiconducting Single-Walled Carbon Nanotubes Using Poly(2,7-Carbazole)S. *J. Polym. Sci. Part A Polym. Chem.* **2015**, *53*, 2510–2516.

(90) Ritaine, D.; Adronov, A. Functionalization of Polyfluorene-Wrapped Carbon Nanotubes Using Thermally Cleavable Side-Chains. *J. Polym. Sci.* **2022**, 1–13.

(91) Berton, N.; Lemasson, F.; Hennrich, F.; Kappes, M. M.; Mayor, M. Influence of Molecular Weight on Selective Oligomer-Assisted Dispersion of Single-Walled Carbon Nanotubes and Subsequent Polymer Exchange. *Chem. Commun.* **2012**, *48*, 2516–2518.

(92) Jakubka, F.; Schießl, S. P.; Martin, S.; Englert, J. M.; Hauke, F.; Hirsch, A.; Zaumseil, J. Effect of Polymer Molecular Weight and Solution Parameters on Selective Dispersion of Single-Walled Carbon Nanotubes. *ACS Macro Lett.* **2012**, *1*, 815–819.

(93) Imin, P.; Cheng, F.; Adronov, A. The Effect of Molecular Weight on the Supramolecular Interaction between a Conjugated Polymer and Single-Walled Carbon Nanotubes. *Polym. Chem.* **2011**, *2*, 1404–1408.

(94) Rice, N. A.; Subrahmanyam, A. V.; Coleman, B. R.; Adronov, A. Effect of Induction on the Dispersion of Semiconducting and Metallic Single-Walled Carbon Nanotubes Using Conjugated Polymers. *Macromolecules* **2015**, *48*, 5155–5161.

(95) Fong, D.; Bodnaryk, W. J.; Rice, N. A.; Saem, S.; Moran-Mirabal, J. M.; Adronov, A. Influence of Polymer Electronics on Selective Dispersion of Single-Walled Carbon Nanotubes. *Chem. - A Eur. J.* **2016**, *22*, 14560–14566.

(96) Bodnaryk, W. J.; Fong, D.; Adronov, A. Enrichment of Metallic Carbon Nanotubes Using a Two-Polymer Extraction Method. *ACS Omega* **2018**, *3*, 16238–16245.

(97) Ding, J.; Li, Z.; Lefebvre, J.; Du, X.; Malenfant, P. R. L. Mechanistic Consideration of pH Effect on the Enrichment of Semiconducting SWCNTs by Conjugated Polymer Extraction. *J. Phys. Chem. C* **2016**, *120*, 21946–21954.

(98) Aguirre, C. M.; Levesque, P. L.; Paillet, M.; Lapointe, F.; St-Antoine, B. C.; Desjardins, P.; Martel, R. The Role of the Oxygen/Water Redox Couple in Suppressing Electron Conduction in Field-Effect Transistors. *Adv. Mater.* **2009**, *21*, 3087–3091.

(99) Zhou, X.; Park, J.-Y.; Huang, S.; Liu, J.; McEuen, P. L. Band Structure, Phonon Scattering, and the Performance Limit of Single-Walled Carbon Nanotube Transistors. *Phys. Rev. Lett.* **2005**, *95*, 146805.

(100) Chen, Z.; Appenzeller, J.; Knoch, J.; Lin, Y.; Avouris, P. The Role of Metal−Nanotube Contact in the Performance of Carbon Nanotube Field-Effect Transistors. *Nano Lett.* **2005**, *5*, 1497–1502.

(101) Ouyang, J.; Ding, J.; Lefebvre, J.; Li, Z.; Guo, C.; Kell, A. J.; Malenfant, P. R. L. Sorting of Semiconducting Single-Walled Carbon Nanotubes in Polar Solvents with an Amphiphilic Conjugated Polymer Provides General Guidelines for Enrichment. *ACS Nano* **2018**, *12*, 1910–1919.

(102) Itkis, M. E.; Perea, D. E.; Jung, R.; Niyogi, S.; Haddon, R. C. Comparison of Analytical Techniques for Purity Evaluation of Single-Walled Carbon Nanotubes. *J. Am. Chem. Soc.* **2005**, *127*, 3439–3448.

(103) O'Connell, M. J.; Sivaram, S.; Doorn, S. K. Near-Infrared Resonance Raman Excitation Profile Studies of Single-Walled Carbon Nanotube Intertube Interactions: A Direct Comparison of Bundled and Individually Dispersed HiPco Nanotubes. *Phys. Rev. B* **2004**, *69*, 235415.

(104) Brown, S. D. M.; Jorio, A.; Corio, P.; Dresselhaus, M. S.; Dresselhaus, G.; Saito, R.; Kneipp, K. Origin of the Breit-Wigner-Fano Lineshape of the Tangential G-Band Feature of Metallic Carbon Nanotubes. *Phys. Rev. B* **2001**, *63*, 155414.

(105) Tsujimura, T. *OLED Display Fundamentals and Applications*; 2017.

(106) García Núñez, C.; Manjakkal, L.; Dahiya, R. Energy Autonomous Electronic Skin. *npj Flex. Electron.* **2019**, *3*, 1–24.

(107) Zou, J.; Zhang, K.; Li, J.; Zhao, Y.; Wang, Y.; Pillai, S. K. R.; Volkan Demir, H.; Sun, X.; Chan-Park, M. B.; Zhang, Q. Carbon Nanotube Driver Circuit for 6 × 6 Organic Light Emitting Diode Display. *Sci. Rep.* **2015**, *5* (11755), 1–9.

(108) Lipomi, D. J.; Vosgueritchian, M.; Tee, B. C. K.; Hellstrom, S. L.; Lee, J. A.; Fox, C. H.; Bao, Z. Skin-like Pressure and Strain Sensors Based on Transparent Elastic Films of Carbon Nanotubes. *Nat. Nanotechnol.* **2011**, *6*, 788–792.

(109) Schnorr, J. M.; Swager, T. M. Emerging Applications of Carbon Nanotubes. *Chem. Mater.* **2011**, *23*, 646–657.

(110) Park, S.; Vosguerichian, M.; Bao, Z. A Review of Fabrication and Applications of Carbon Nanotube Film-Based Flexible Electronics. *Nanoscale* **2013**, *5*, 1727–1752.

(111) Dürkop, T.; Getty, S. A.; Cobas, E.; Fuhrer, M. S. Extraordinary Mobility in Semiconducting Carbon Nanotubes. *Nano Lett.* **2004**, *4*, 35–39.

(112) Javey, A.; Kim, H.; Brink, M.; Wang, Q.; Ural, A.; Guo, J.; Mcintyre, P.; Mceuen, P.; Lundstrom, M.; Dai, H. High-κ Dielectrics for Advanced Carbon-Nanotube Transistors and Logic Gates. *Nat. Mater.* **2002**, *1*, 241–246.

(113) Sarker, B. K.; Shekhar, S.; Khondaker, S. I. Semiconducting Enriched Carbon Nanotube Aligned Arrays of Tunable Density and Their Electrical Transport Properties. *ACS Nano* **2011**, *5*, 6297–6305.

(114) Schießl, S. P.; Fröhlich, N.; Held, M.; Gannott, F.; Schweiger, M.; Forster, M.; Scherf, U.; Zaumseil, J. Polymer-Sorted Semiconducting Carbon Nanotube Networks for High-Performance Ambipolar Field-Effect Transistors. *ACS Appl. Mater. Interfaces* **2015**, *7*, 682–689.

(115) Takahashi, T.; Takei, K.; Gillies, A. G.; Fearing, R. S.; Javey, A. Carbon Nanotube Active-Matrix Backplanes for Conformal Electronics and Sensors. *Nano Lett.* **2011**, *11*, 5408–5413.

(116) Cao, X.; Chen, H.; Gu, X.; Liu, B.; Wang, W.; Cao, Y.; Wu, F.; Zhou, C. Screen Printing as a Scalable and Low-Cost Approach for Rigid and Flexible Thin-Film Transistors Using Separated Carbon Nanotubes. *ACS Nano* **2014**, *8*, 12769–12776.

(117) Mirka, B.; Rice, N. A.; Williams, P.; Tousignant, M. N.; Boileau, N. T.; Bodnaryk, W. J.; Fong, D.; Adronov, A.; Lessard, B. H. Excess Polymer in Single-Walled Carbon Nanotube Thin-Film Transistors: Its Removal Prior to Fabrication Is Unnecessary. *ACS Nano* **2021**, *15*, 8252–8266.

(118) Mirri, F.; Ma, A. W. K.; Hsu, T. T.; Behabtu, N.; Eichmann, S. L.; Young, C. C.; Tsentalovich, D. E.; Pasquali, M. High-Performance Carbon Nanotube Transparent Conductive Films by Scalable Dip Coating. *ACS Nano* **2012**, *6*, 9737–9744.

(119) Tenent, R. C.; Barnes, T. M.; Bergeson, J. D.; Ferguson, A. J.; To, B.; Gedvilas, L. M.; Heben, M. J.; Blackburn, J. L. Ultrasmooth, Large-Area, High-Uniformity, Conductive Transparent Single-Walled-Carbon-Nanotube Films for Photovoltaics Produced by Ultrasonic Spraying. *Adv. Mater.* **2009**, *21*, 3210–3216.

(120) Derenskyi, V.; Gomulya, W.; Rios, J. M. S.; Fritsch, M.; Fröhlich, N.; Jung, S.; Allard, S.; Bisri, S. Z.; Gordiichuk, P.; Herrmann, A.; et al. Carbon Nanotube Network Ambipolar Field-Effect Transistors with 10^8 On/Off Ratio. *Adv. Mater.* **2014**, *26*, 5969–5975.

(121) Joo, Y.; Brady, G. J.; Arnold, M. S.; Gopalan, P. Dose-Controlled, Floating Evaporative Self-Assembly and Alignment of Semiconducting Carbon Nanotubes from Organic Solvents. *Langmuir* **2014**, *30*, 3460–3466.

(122) Park, S.; Pitner, G.; Giri, G.; Koo, J. H.; Park, J.; Kim, K.; Wang, H.; Sinclair, R.; Wong, H. S. P.; Bao, Z. Large-Area Assembly of Densely Aligned Single-Walled Carbon Nanotubes Using Solution Shearing and Their Application to Field-Effect Transistors. *Adv. Mater.* **2015**, *27*, 2656–2662.

(123) Joo, Y.; Brady, G. J.; Kanimozhi, C.; Ko, J.; Shea, M. J.; Strand, M. T.; Arnold, M. S.; Gopalan, P. Polymer-Free Electronic-Grade Aligned Semiconducting Carbon Nanotube Array. *ACS Appl. Mater. Interfaces* **2017**, *9*, 28859–28867.

(124) Pochorovski, I.; Wang, H.; Feldblyum, J. I.; Zhang, X.; Antaris, A. L.; Bao, Z. H-Bonded Supramolecular Polymer for the Selective Dispersion and Subsequent Release of Large-Diameter Semiconducting Single-Walled Carbon Nanotubes. *J. Am. Chem. Soc.* **2015**, *137*, 4328–4331.

(125) Rother, M.; Schießl, S. P.; Zakharko, Y.; Gannott, F.; Zaumseil, J. Understanding Charge Transport in Mixed Networks of Semiconducting Carbon Nanotubes. *ACS Appl. Mater. Interfaces* **2016**, *8*, 5571–5579.

(126) Homenick, C. M.; James, R.; Lopinski, G. P.; Dunford, J.; Sun, J.; Park, H.; Jung, Y.; Cho, G.; Malenfant, P. R. L. Fully Printed and Encapsulated SWCNT-Based Thin Film Transistors via a Combination of R2R Gravure and Inkjet Printing. *ACS Appl. Mater. Interfaces* **2016**, *8*, 27900–27910.

(127) Bucella, S. G.; Salazar-Rios, J. M.; Derenskyi, V.; Fritsch, M.; Scherf, U.; Loi, M. A.; Caironi, M. Inkjet Printed Single-Walled Carbon Nanotube Based Ambipolar and Unipolar Transistors for High-Performance Complementary Logic Circuits. *Adv. Electron. Mater.* **2016**, *2*, 1600094.

(128) Cao, C.; Andrews, J. B.; Franklin, A. D. Completely Printed, Flexible, Stable, and Hysteresis-Free Carbon Nanotube Thin-Film Transistors via Aerosol Jet Printing. *Adv. Electron. Mater.* **2017**, *3*, 1700057.

(129) Liu, Z.; Zhao, J.; Xu, W.; Qian, L.; Nie, S.; Cui, Z. Effect of Surface Wettability Properties on the Electrical Properties of Printed Carbon Nanotube Thin-Film Transistors on SiO_2/Si Substrates. *ACS Appl. Mater. Interfaces* **2014**, *6*, 9997–10004.

(130) Xu, W.; Zhao, J.; Qian, L.; Han, X.; Wu, L.; Wu, W.; Song, M.; Zhou, L.; Su, W.; Wang, C.; Nie, S.; Cui, Z. Sorting of Large-Diameter Semiconducting Carbon Nanotube and Printed Flexible Driving Circuit for Organic Light Emitting Diode (OLED). *Nanoscale* **2014**, *6*, 1589–1595.

(131) Rother, M.; Brohmann, M.; Yang, S.; Grimm, S. B.; Schießl, S. P.; Graf, A.; Zaumseil, J. Aerosol-Jet Printing of Polymer-Sorted (6,5) Carbon Nanotubes for Field-Effect Transistors with High Reproducibility. *Adv. Electron. Mater.* **2017**, *3*, 1700080.

(132) Brohmann, M.; Rother, M.; Schießl, S. P.; Preis, E.; Allard, S.; Scherf, U.; Zaumseil, J. Temperature-Dependent Charge Transport in Polymer-Sorted Semiconducting Carbon Nanotube Networks with Different Diameter Distributions. *J. Phys. Chem. C* **2018**, *122*, 19886–19896.

(133) Andrews, J. B.; Mondal, K.; Neumann, T. V.; Cardenas, J. A.; Wang, J.; Parekh, D. P.; Lin, Y.; Ballentine, P.; Dickey, M. D.; Franklin, A. D. Patterned Liquid Metal Contacts for Printed Carbon Nanotube Transistors. *ACS Nano* **2018**, *12*, 5482–5488.

(134) Madec, M. B.; Smith, P. J.; Malandraki, A.; Wang, N.; Korvink, J. G.; Yeates, S. G. Enhanced Reproducibility of Inkjet Printed Organic Thin Film Transistors Based on Solution Processable Polymer-Small Molecule Blends. *J. Mater. Chem.* **2010**, *20*, 9155–9160.

(135) Wong, H.-S. P.; Akinwande, D. *Carbon Nanotube and Graphene Device Physics*; Cambridge University Press: Cambridge, United Kingdom, 2011.

(136) Perebeinos, V.; Tersoff, J.; Avouris, P. Electron-Phonon Interaction and Transport in Semiconducting Carbon Nanotubes. *Phys. Rev. Lett.* **2005**, *94*, 086802.

(137) Nan, C.-W.; Shen, Y.; Ma, J. Physical Properties of Composites Near Percolation. *Annu. Rev. Mater. Res.* **2010**, *40*, 131–151.

(138) Klauk, H. Organic Thin-Film Transistors. *Chem. Soc. Rev.* **2010**, *39*, 2643–2666.

(139) Tessler, N.; Preezant, Y.; Rappaport, N.; Roichman, Y. Charge Transport in Disordered Organic Materials and Its Relevance to Thin-Film Devices: A Tutorial Review. *Adv. Mater.* **2009**, *21*, 2741–2761.

(140) Zorn, N. F.; Zaumseil, J. Charge Transport in Semiconducting Carbon Nanotube Networks. *Appl. Phys. Rev.* **2021**, *8*, 041318.

(141) Yeom, C.; Chen, K.; Kiriya, D.; Yu, Z.; Cho, G.; Javey, A. Large-Area Compliant Tactile Sensors Using Printed Carbon Nanotube Active-Matrix Backplanes. *Adv. Mater.* **2015**, *27*, 1561–1566.

(142) Peng, L.; Zhang, Z.; Qiu, C. Carbon Nanotube Digital Electronics. *Nat. Electron.* **2019**, *2*, 499–505.

(143) Zhang, J.; Wang, C.; Fu, Y.; Che, Y.; Zhou, C. Air-Stable Conversion of Separated Carbon Nanotube Thin-Film Transistors from p-Type to n-Type Using Atomic Layer Deposition of High-κ Oxide and Its Application in CMOS Logic Circuits. *ACS Nano* **2011**, *5*, 3284–3292.

(144) Schneider, S.; Brohmann, M.; Lorenz, R.; Hofstetter, Y. J.; Rother, M.; Sauter, E.; Zharnikov, M.; Vaynzof, Y.; Himmel, H. J.; Zaumseil, J. Efficient n-Doping and Hole Blocking in Single-Walled Carbon Nanotube Transistors with 1,2,4,5-Tetrakis(tetramethylguanidino)benzene. *ACS Nano* **2018**, *12*, 5895–5902.

(145) Ha, M.; Xia, Y.; Green, A. A.; Zhang, W.; Renn, M. J.; Kim, C. H.; Hersam, M. C.; Frisbie, C. D. Printed, Sub-3V Digital Circuits on Plastic from Aqueous Carbon Nanotube Inks. *ACS Nano* **2010**, *4*, 4388–4395.

(146) Jang, S.; Kim, B.; Geier, M. L.; Prabhumirashi, P. L.; Hersam, M. C.; Dodabalapur, A. Fluoropolymer Coatings for Improved Carbon Nanotube Transistor Device and Circuit Performance and Circuit Performance. *Appl. Phys. Lett.* **2014**, *105*, 122107.

(147) Wang, H.; Wei, P.; Li, Y.; Han, J.; Lee, H. R.; Naab, B. D.; Liu, N.; Wang, C.; Adijanto, E.; Tee, B. C.-K.; Morishita, S.; Li, Q.; Gao, Y.; Cui, Y.; Bao, Z. Tuning the Threshold Voltage of Carbon Nanotube Transistors by n-type Molecular Doping for Robust and Flexible Complementary Circuits. *Proc. Natl. Acad. Sci. U. S. A.* **2014**, *111*, 4776–4781.

(148) Geier, M. L.; Prabhumirashi, P. L.; McMorrow, J. J.; Xu, W.; Seo, J.-W. T.; Everaerts, K.; Kim, C. H.; Marks, T. J.; Hersam, M. C. Subnanowatt Carbon Nanotube Complementary Logic Enabled by Threshold Voltage Control. *Nano Lett.* **2013**, *13*, 4810–4814.

(149) Wang, C.; Chien, J.-C.; Takei, K.; Takahashi, T.; Nah, J.; Niknejad, A. M.; Javey, A. Extremely Bendable, High-Performance Integrated Circuits Using Semiconducting Carbon Nanotube Networks for Digital, Analog, and Radio-Frequency Applications. *Nano Lett.* **2012**, *12*, 1527–1533.

\

Chapter 2: Polyfluorene-Sorted Semiconducting Single-Walled Carbon Nanotubes for Applications in Thin-Film Transistors

This chapter was published in the journal "Chemistry of Materials": Mirka, B.; Fong, D.; Rice, N. A.; Melville, O. A.; Adronov, A.; Lessard, B. H. Polyfluorene-Sorted Semiconducting Single-Walled Carbon Nanotubes for Applications in Thin Film Transistors. Chem. Mater. 2019, 31, 2863–2872.

Context

Our collaborators (Dr. Fong and Prof. Adronov) synthesized a novel copolymer poly(fluorene-*co*-dimethoxybenzene) to be used to sort and disperse semiconducting single-walled carbon nanotubes. I was interested in the efficacy of this polymer for sorting and dispersing large-diameter sc-SWNTs for incorporation into thin-film transistors. As outlined in **Chapter 1**, large-diameter sc-SWNTs are desired for applications in thin-film transistors. Additionally, I was interested in the procedure of conjugated polymer extraction and how it would relate to thin-film transistor performance. I wanted to investigate the necessity of the filtration step to remove the excess, unbound wrapping polymer from the sc-SWNT dispersion. Forgoing the filtration step would make the procedure less time-consuming and easier to implement on a large scale.

Contribution

I prepared the sc-SWNT dispersions *via* conjugated polymer extraction. I performed UV-vis-NIR spectroscopy, and Dr. Fong performed the Raman spectroscopy measurements to confirm purity. I processed the absorption and Raman spectroscopic data to confirm the efficacy of conjugated polymer sorting. I carried out all device fabrication, electrical characterization, and data analysis. I also performed the atomic force microscopy experiments. I wrote the manuscript with input from Prof. Lessard, Dr. Rice, Dr. Fong, Prof. Adronov, and Dr. Melville.

2.1 Abstract

Due to their superlative electrical and mechanical properties, single-walled carbon nanotubes (SWNTs) are capable of expanding the current scope of electronic device applications. Advancements in the selective isolation and purification of semiconducting SWNTs through the use of conjugated polymers have facilitated incorporation of high-quality SWNTs into solution-processed thin-film transistors (TFTs). In this study, we report an alternating copolymer based on fluorene and 2,5-dimethoxybenzene capable of selectively dispersing semiconducting SWNTs. The exceptional sc-SWNT purity (>99 %) of the dispersion was confirmed by UV-Vis and Raman spectroscopy, which exhibit negligible metallic SWNT features. TFTs fabricated with this polymer-SWNT complex exhibited maximum hole and electron mobilities of 19 cm^2/Vs and 7 cm^2/Vs, respectively, with on/off ratios as high as 10^7. Device fabrication parameters, including silane surface treatment, removal of excess polymer, and SWNT dispersion concentration, were investigated. Evaluation of hole and electron mobilities indicates that the presence of excess polymer in the polymer-SWNT dispersion did not adversely affect device performance. Atomic force microscopy measurements showed that our polymer-SWNT dispersions could form a complete percolation pathway between electrodes, with individual SWNTs exfoliated by the polymer.

2.2 Introduction

As the market for innovative electronic devices continues to grow and push beyond its current boundaries, the limits of traditional silicon-based electronics are becoming evident.[1] The demand for next-generation electronics that are flexible, lightweight, and inexpensive has necessitated research in the field of organic electronics. This area focuses on carbon-based electronic materials, including semiconductors,[2] dielectrics,[3] electrodes,[4,5] and substrates.[6] Of the numerous accessible organic semiconductors, single-walled carbon nanotubes (SWNTs) have emerged as one of the most promising materials, having received tremendous attention in the science and engineering communities since their discovery in the early 1990s.[7,8] SWNTs exhibit excellent electrical,[9] mechanical,[10] and optical properties,[11,12] making them suitable candidates for next-generation electronic materials. SWNT applications include photovoltaics,[13] chemical[14,15] and biological sensors,[16] and fluorescence-based biological imaging.[17] Their ability to form

flexible films, combined with their high tensile strength and electrical conductivity, make them particularly attractive for thin-film transistor (TFT) applications.[18,19]

SWNTs can be synthesized as discrete structures with a variety of possible chiralities, defined by a set of two integers referred to as chiral indices, (*n, m*).[20] Depending on the chiral indices, each SWNT can be classified as being metallic or semiconducting. As-produced SWNTs are a polydisperse mixture of chiralities, comprised of approximately one-third metallic (m-SWNT) and two-thirds semiconducting (sc-SWNT) chiralities.[20] This electrical inhomogeneity poses a significant problem for incorporating SWNTs into TFT semiconductor films, as m-SWNTs can form conduction pathways between the electrodes, effectively short-circuiting the transistor. Due to the presence of m-SWNTs, early examples of SWNT transistor devices were often plagued by low on/off current ratios as a result of high off-currents.[21,22]

Several methodologies have been used to selectively isolate sc-SWNTs from raw nanotube mixtures, including the use of surfactants with density gradient ultracentrifugation,[23,24] DNA dispersion,[25] gel chromatography,[26] and conjugated polymer extraction.[27,28] Among these different techniques, conjugated polymer extraction has been demonstrated to be one of the most simple and effective methods for obtaining highly-concentrated dispersions of sc-SWNTs, with possible purities in excess of 99 %.[28,29] The selectivity mechanism is not yet fully understood; however, several hypotheses have been proposed. Explanations all begin with the difference in the polarizability between m-SWNTs and sc-SWNTs.[30,31] Due to the fact that m-SWNTs are ~10^3 times more polarizable than sc-SWNTs, m-SWNTs can bundle together into large aggregates when non-polar solvents are used. Another theory proposes that the electronic nature of the conjugated polymer backbone influences the degree of selectivity; an electron-rich polymer backbone will favour dispersion of electron-poor sc-SWNTs, whereas more electron-poor conjugated polymer backbones will allow for dispersion of m-SWNTs.[30,32]

Despite the lack of a fully-explained mechanism, some basic design rules have emerged through the analysis of literature reports.[30] Factors that affect the selectivity and yield of a conjugated polymer extraction include choice of solvent,[33,34] sonication temperature,[35] polymer molecular weight,[36] polymer-SWNT mass ratio,[29] and alkyl side chain length.[37,38] In their study investigating the use of 9,9-dialkylfluorene homopolymers for dispersing large-diameter sc-SWNTs, Malenfant et al. found that alkyl side chain lengths of 10, 12, 14, and 18 carbons could

effectively produce high-quality sc-SWNT dispersions when the polymer number average molecular weight was greater than 10 kDa.[37] Smaller-diameter SWNTs, such as CoMoCAT or HiPco SWNTs, have been sorted successfully using regio-regular poly(3-dodecylthiophene),[39] polyfluorene derivatives such as poly(9,9-dioctylfluorene) (PFO),[40,41] and homopolymers or copolymers of poly(carbazole).[42,43] Successful sorting of large-diameter SWNTs for use in TFTs has been achieved with copolymers of dithiafulvalene/thiophene,[44] copolymers of fluorene/carbazole,[45] and homo and copolymers of poly(fluorene), including poly(9,9-bis(2-(2- (2-methoxyethoxy)ethoxy)ethyl)fluorene-*alt*-pyridine-2,5) [P- (FEt3M-Py-2,5)],[46] poly[(9,9-dioctylfluorenyl-2,7-diyl)-*alt-co*-(6,6'-[2,2'-bipyridine])] (PFO-BPy),[47] and poly(9,9-di-*n*-dodecylfluorene) (PDDF).[37]

Conjugated polymer extraction is a simple technique conducive to fabrication of sc-SWNT TFTs using solution-processing techniques. Solution-processing techniques, including solution shearing,[48] gravure printing,[49] aerosol jet printing,[18] and inkjet printing,[50] offer a low-cost route towards the production of flexible TFTs. For the preparation of high-performance TFT devices, incorporation of large-diameter sc-SWNTs produced by the arc discharge or plasma synthesis methods is desirable.[29] In accordance with the tight-binding model, the charge carrier mobilities of SWNTs are proportional to diameter.[51,52] Large diameter SWNTs exhibit a small Schottky barrier at the SWNT/electrode interface, reducing contact resistance to charge injection. For the realization of high-efficiency TFTs, multiple device parameters have been explored in the literature, including modification of device architecture,[53] complete removal of the polymer from sc-SWNTs post-fabrication,[54] alignment of sc-SWNTs within the transistor channel,[48,55] and doping of sc-SWNTs.[56] While many of these processes can yield transistors with exceptional results, most require additional fabrication steps that may reduce the feasibility of large-scale operations, especially if the procedure becomes too laborious for only marginal gains in performance. On an industrial scale, device performance will be a trade-off with operational cost insofar as device performance can meet specifications.

Herein we report the use of a fluorene alternating copolymer that contains 2,5-dimethoxybenzene, poly[(2,7-(9,9-dihexadecylfluorene)-*alt*-2,5-dimethoxybenzene)] (PFMB), which was used to prepare highly enriched (>99 %) sc-SWNT dispersions that were incorporated into TFTs. Transistors were prepared from polymer-SWNT dispersions of varying concentrations

before and after excess polymer removal and were characterized by charge mobility (μ), threshold voltage (V_T), hysteresis (H), on/off current ratio ($I_{on/off}$), and film morphology. The effect of dielectric surface modification with octyltrichlorosilane (OTS) on mobility and hysteresis was also explored.

2.3 Results and Discussion

2.3.1 Polymer Design and SWNT Dispersion

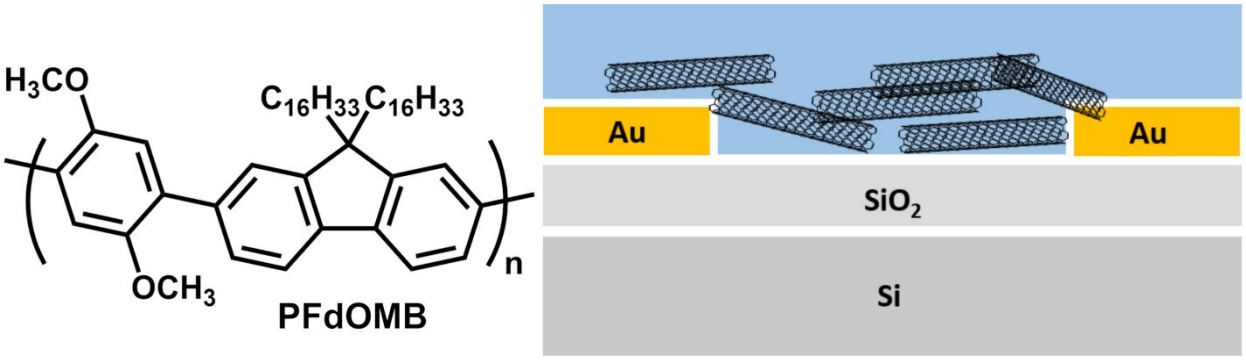

Figure 2.1: Structure of PFMB and schematic of the BGBC sc-SWNT TFT architecture used.

This work focused on utilizing a polyfluorene copolymer architecture that had previously demonstrated superior selectivity for small-diameter sc-SWNTs when mixed with HiPco SWNTs.[57] Modification of the polymer structure is required when replacing HiPco SWNTs with larger-diameter plasma tubes. In our study, the alkyl side chain length was increased from 12 to 16 carbon atoms. Furthermore, the 2,5-dimethoxybenzene group on the fluorene monomer alters the electronic character of the polymer backbone, making it more electron-rich, which could aid in selectively exfoliating electron-poor sc-SWNTs.[32] A polymer-SWNT mass ratio of 1.2:1 was found to be optimal at producing sc-SWNT dispersions while maintaining selectivity towards sc-SWNTs. Raw SWNT powder (> 1 nm in diameter) and PFMB were combined with a polymer-SWNT mass ratio of 1.2:1 and dispersed in toluene *via* batch sonication, centrifuged, and the resulting supernatant collected as our sc-SWNT enriched dispersion. This procedure was repeated multiple times to generate a stock dispersion, a portion of which was removed to be used as an excess polymer sample. The rest of the PFMB-SWNT dispersion was filtered through a 0.2 μm

membrane, rinsed with toluene in order to remove the excess polymer, and then re-suspended in toluene.

Absorption spectroscopy is a facile procedure for evaluating the quality of a sc-SWNT dispersion. For the diameter range of SWNTs potentially dispersed by our polymer, four groupings of optical transitions may be observed: three arise from semiconducting chiralities (S_{11}, S_{22}, and S_{33}), and one is from metallic (M_{11}) chiralities. For the SWNTs used in this study, the S_{22} absorption occurs in the range of 800 – 1100 nm, and the M_{11} absorption occurs in the range of 600 – 800 nm.[28] In an effort to account for SWNT concentration between the two sc-SWNT samples for incorporation into devices, the concentrations of the excess polymer and the excess polymer removed samples were adjusted until the S_{22} peaks were approximately equal, as shown in **Figure 2.2** (full absorption spectra can be found in **Figure 2.9** in the Supporting Information).

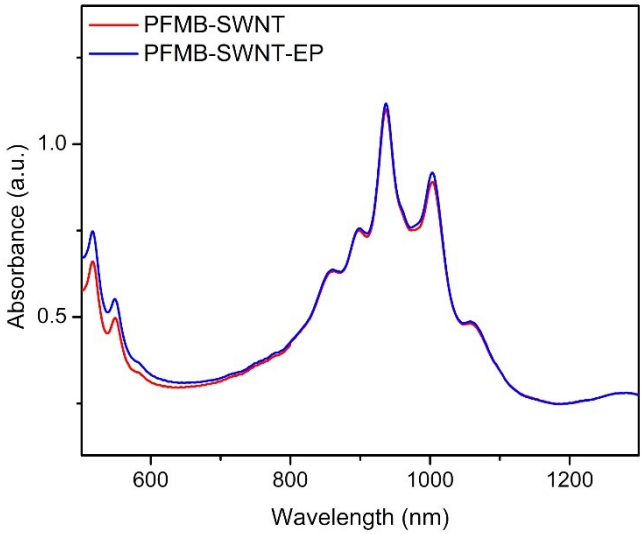

Figure 2.2: S_{22} absorption peaks of PFMB-SWNT, without and with (**EP**) excess polymer.

The presence of m-SWNTs in SWNT dispersions is deleterious to TFT device performance. An estimate of the relative amount of m-SWNTs present in our samples can be calculated from the intensity of the M_{11} absorption envelope compared to the intensity of the S_{22} absorption envelope.[58] However, this method is ineffective at low concentrations of m-SWNTs (below 1 %). Another method to qualitatively measure sc-SWNT purity is referred to as the

absorption peak ratio (ϕ_i).[37] While this method is unable to determine the quantitative concentration of semiconducting species, it is a useful tool for confirming that a sample is highly-enriched in sc-SWNTs. Determination of ϕ_i involves calculating the ratio of the S_{22} and M_{11} absorption areas after baseline subtraction to the entire S_{22} and M_{11} absorption area. $\phi_i \geq 0.40$ indicates that the dispersion is > 99 % enriched in sc-SWNTs.[37] For the dispersions used in this study, ϕ_i was calculated to be 0.447 and 0.439 for the PFMB-SWNT and the PFMB-SWNT-**EP**, respectively. Given that the PFMB-SWNT and PFMB-SWNT-**EP** were prepared from the same stock dispersion and that their S_{22} absorbance peaks are approximately equal, similar ϕ_i values for both samples are expected; the minor variation is most likely due to the presence of excess polymer in PFMB-SWNT-**EP** introducing error into the baseline absorbance. The calculated ϕ_i values confirm that the samples used in this study are greater than 99 % pure in sc-SWNTs. In their study investigating various 9,9-dialkylfluorene homopolymers for dispersion of large-diameter sc-SWNTs, Malenfant *et al*. reported ϕ_i values of 0.403 – 0.416 for various 9,9-dialkylfluorene homopolymers.[37] Our results indicate that our sc-SWNT dispersions are purer than other literature polyfluorene dispersions.

Raman spectroscopy is capable of detecting trace amounts of m-SWNT impurities that are below the detection limit of absorption spectroscopy.[59,60] Both sc-SWNTs and m-SWNTs can exhibit a strong resonance effect when the correct laser excitation wavelength is used. To fully characterize a polydisperse SWNT sample, a multitude of excitation wavelengths would be required. However, it has been demonstrated in the literature that using three laser excitation wavelengths (785, 633, and 514 nm) is sufficient for probing both the sc-SWNT and m-SWNT species that may be present in our sample.[61] **Figure 2.3a-b** show the *G*-band region at 633 nm excitation and the radial breathing mode (RBM) region at 785 nm, respectively; all spectra have been normalized to the *G*-band region at approximately 1590 cm^{-1}, and full spectra can be found in **Figure 2.10** in the Supporting Information. In **Figure 2.3a**, the *G*-band region for unsorted SWNTs at an excitation wavelength of 633 nm shows three distinct peaks: two Lorentzian line shapes (the G^+_{sc} and the G^-_{sc}) and a broad Breit-Wigner-Fano (BWF) line shape (G^-_m), indicating the presence of m-SWNTs.[62] The G^+_{sc} and G^-_{sc} Lorentzian peaks remain present in the PFMB-SWNT, however the BWF G^-_m is not present, indicating the removal of metallic nanotubes. Using an excitation wavelength of 785 nm, both m-SWNT and sc-SWNTs peaks can be observed in the RBM region from 100 – 400 cm^{-1}. **Figure 2.3b** shows the RBM spectra for both PFMB-SWNT

and unsorted SWNT dispersions at the 785 nm excitation wavelength, with the peaks in the range of 145 to 184 cm^{-1} corresponding to m-SWNTs.[60] The unsorted SWNT sample exhibits a strong peak centred around 168 cm^{-1}, indicating a significant amount of m-SWNTs present in the unsorted raw material. No such peak is present for the PFMB-SWNT sample in the RBM region at a laser excitation wavelength of 785 nm, confirming the high purity of our sc-SWNT dispersion.

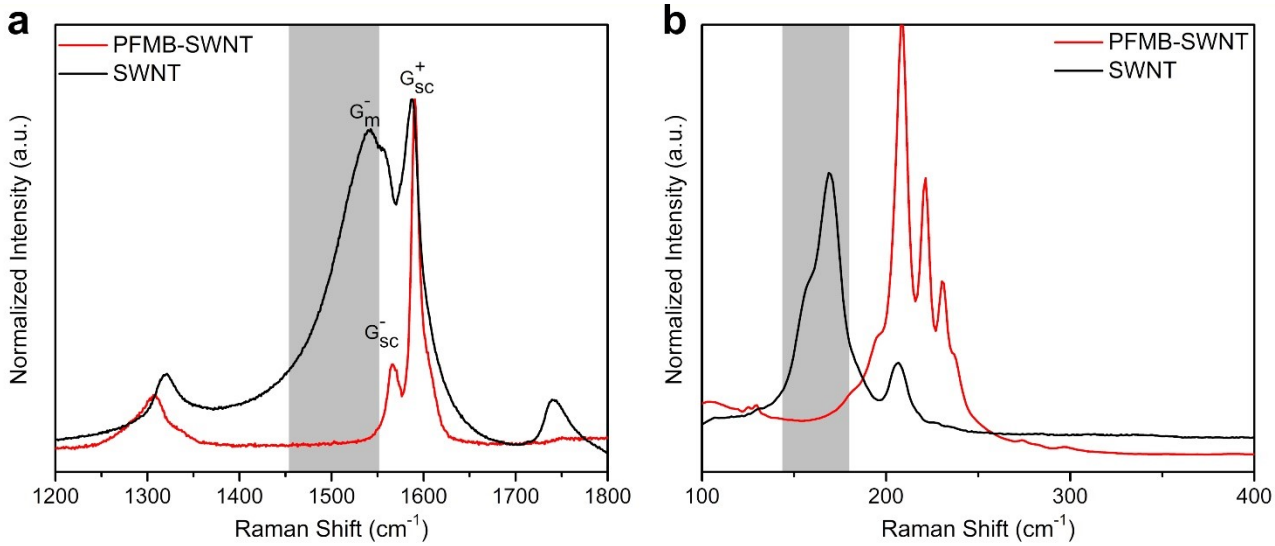

Figure 2.3: Raman spectra of PFMB-SWNT and pristine SWNTs at an excitation wavelength of (a) 633 nm (*G*-band region) and (b) 785 nm (RBM region). The grey boxes indicate the location of signals arising from metallic SWNTs. All spectra have been normalized to the G_{sc}^{+} peak, and for (b), the PFMB-SWNT spectrum has been multiplied by a factor of 5.

2.3.2 Thin-Film Transistor Results and Discussion

In this study, bottom-gate bottom-contact (BGBC) TFTs (**Figure 2.1**) were fabricated using sc-SWNT dispersions with excess polymer removed (PFMB-SWNT) and with excess polymer present (PFMB-SWNT-**EP**). Three chips (each containing 16 devices) were prepared from each sc-SWNT dispersion, and the values were averaged. All devices were characterized first in air before the atmosphere was removed from the chamber, and the same devices were characterized in vacuum ($P < 0.1$ Pa). Hole mobility was the dominant charge transport mechanism when the devices were characterized in air, while the same devices were predominately n-type when tested under vacuum. Averaged values for linear-region field-effect mobility (μ), threshold voltage (V_T), hysteresis (defined as the threshold voltage difference between the forward and reverse scans), and on/off current ratio ($I_{on/off}$) data for PFMB-SWNT and PFMB-SWNT-**EP** can

be found in **Table 2.1** for p-type devices (tested in air) and n-type conditions (tested under vacuum) for devices with a channel length (L) of 20 μm (data for other channel lengths can be found in **Table 2.2** in the Supporting Information).

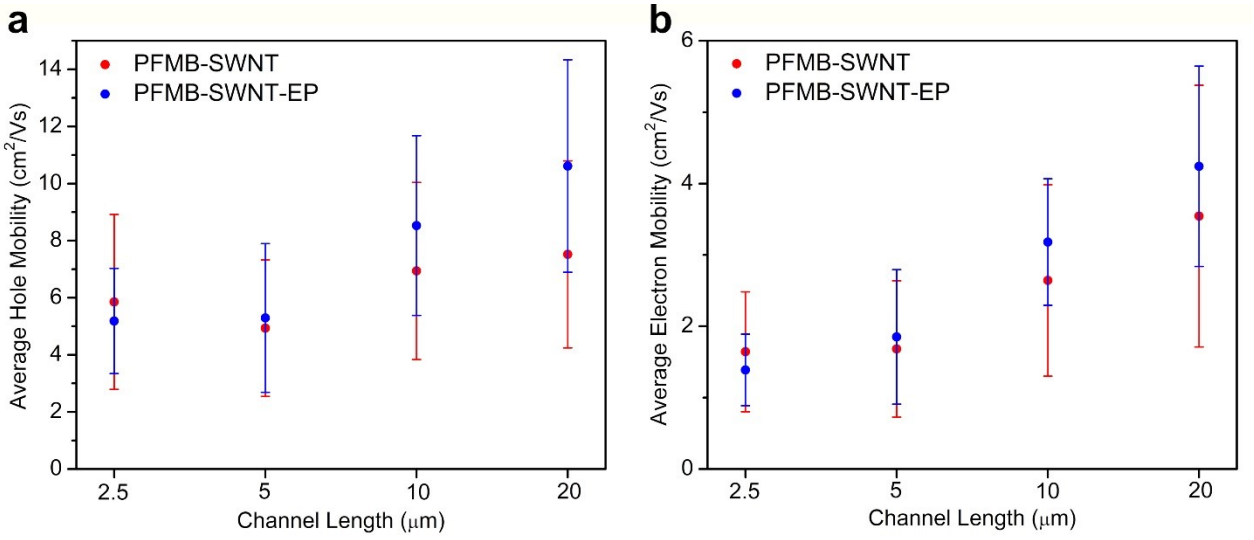

Figure 2.4: Comparison of average mobility vs. channel length for (a) p-type tested in air and (b) n-type tested under vacuum.

Figure 2.4 presents the average mobilities as a function of channel length for both PFMB-SWNT and PFMB-SWNT-**EP** devices, tested in p- and n-type conditions. For both samples and in both testing conditions, the mobility increases with increasing channel length. This effect is commonly observed for devices with a different W/L ratio as a result of contact resistance becoming more dominant at smaller channel lengths, thereby hindering charge injection.[63,64] Values for contact resistance can be found in the Supporting Information **Table 2.5**.

Table 2.1: Summary of average (μ_{av}) and maximum (μ_{max}) mobility, threshold voltage (V_T), hysteresis (H), and $I_{on/off}$ between PFMB-SWNT and PFMB-SWNT-**EP** for both p-type (tested in air) and n-type (tested under vacuum).

Channel Length = 20 µm, p-type, tested in Air (V_{SD} = -3 V)					
	$\mu_{h,av}$ (cm^2/Vs)	$\mu_{h,max}$ (cm^2/Vs)	$V_{T,av}$ (V)	$H_{,av}$ (V)	$I_{on/off}$
PFMB-SWNT	7.52 ± 3.27	14.72	1.51 ± 5.87	9.01 ± 4.45	$10^5 – 10^6$
PFMB-SWNT-**EP**	10.61 ± 3.72	19.06	-4.13 ± 3.40	6.03 ± 3.50	$10^5 – 10^7$
Channel Length = 20 µm, n-type, tested in Vacuum (V_{SD} = 3 V)					
	$\mu_{e,av}$ (cm^2/Vs)	$\mu_{e,max}$ (cm^2/Vs)	$V_{T,av}$ (V)	$H_{,av}$ (V)	$I_{on/off}$
PFMB-SWNT	3.54 ± 1.83	7.41	17.11 ± 7.69	7.99 ± 4.15	$10^3 – 10^4$
PFMB-SWNT-**EP**	4.24 ± 1.40	7.46	12.13 ± 1.41	2.36 ± 1.43	$10^5 – 10^6$

The results in **Table 2.1** show a slight contrast between PFMB-SWNT and PFMB-SWNT-**EP** samples tested in p- and n-type conditions in air and vacuum, respectively. Surprisingly, the devices containing excess polymer performed slightly better than those without by almost every metric. However, the differences are small and, in some cases, are not statistically significant. Nonetheless, the data suggest that the presence of excess polymer in the dispersion did not hinder device performance. These results could be an important consideration for future TFT applications; device fabrication using sc-SWNT dispersions with excess polymer will eliminate the filtration or high-speed centrifugation steps in the conjugated polymer extraction procedure, thereby improving the feasibility of commercial-scale operations.

We observed significant p-type characteristics with suppressed n-type behaviour (**Table 2.1**), which is typical for most literature examples of sc-SWNTs in TFTs. The dominance of p-type behaviour is manifested in the charge carrier mobilities; the $\mu_{h,av}$ for the PFMB-SWNT and PFMB-SWNT-**EP** samples are 112 % (7.52 cm^2/Vs) and 150 % (10.61 cm^2/Vs) higher than their corresponding $\mu_{e,av}$ (3.54 cm^2/Vs and 4.24 cm^2/Vs) respectively. The average threshold voltages ($V_{T,av}$) for both the PFMB-SWNT and PFMB-SWNT-**EP** samples under n-type conditions are also much larger than under p-type conditions (**Table 2.1**). Typically, n-type characteristics are suppressed in SWNT TFTs as a result of the large Schottky barriers present at the metal-SWNT interface.[65,66] In addition, hole conduction in SWNTs dominates in ambient conditions as a result of oxygen doping.[67,68] It should be noted that while our measured mobilities are not as high as the record-performing devices reported in the literature,[48,55] this can mostly be attributed to the fact

that we have a random network of sc-SWNTs in the transistor channels. The literature has repeatedly demonstrated that aligning the nanotubes can drastically enhance transistor mobility. However, these alignment techniques are often laborious and time-consuming, making them challenging to implement on a commercial scale. Furthermore, the mobilities that we obtained are on par or superior to other random-network SWNT TFTs in the literature.[60,69,70-72] An additional study was done to explore the effect of SWNT concentration on TFT performance, with the PFMB-SWNT and PFMB-SWNT-**EP** dispersions diluted to half of their initial concentration (described in detail in the Supporting Information). Unsurprisingly, a reduction in mobility was observed for TFTs fabricated utilizing dilute SWNT dispersions. The reduction in mobility was more drastic for TFTs utilizing dilute dispersions with excess polymer present, suggesting that a threshold concentration is required before device performance between dispersions with and without excess polymer present becomes comparable.

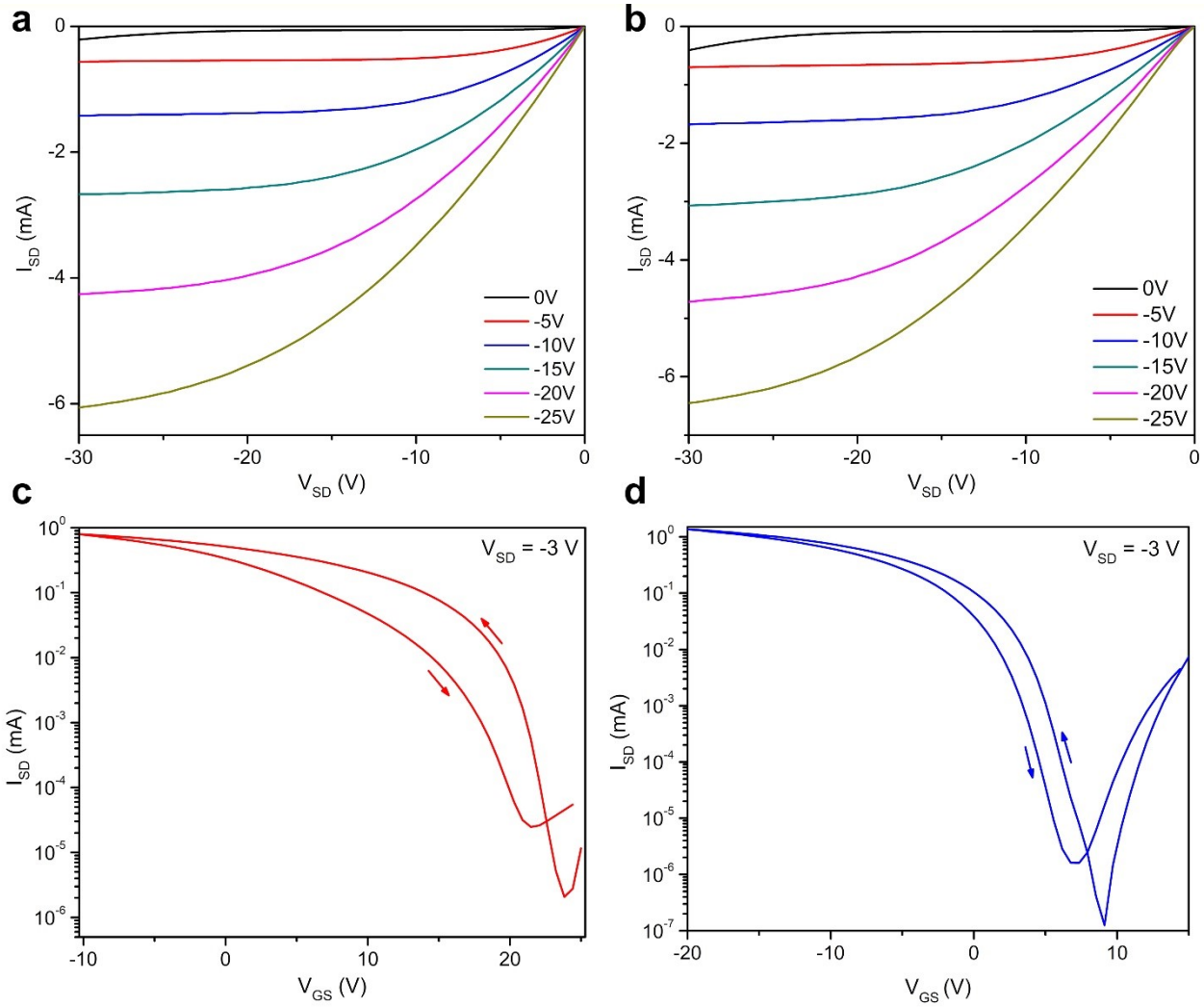

Figure 2.5: Example of output and transfer curves for (a) and (c) PFMB-SWNT, and (b) and (d) PFMB-SWNT-**EP**. All data for p-type devices, tested in air, for L = 20 µm.

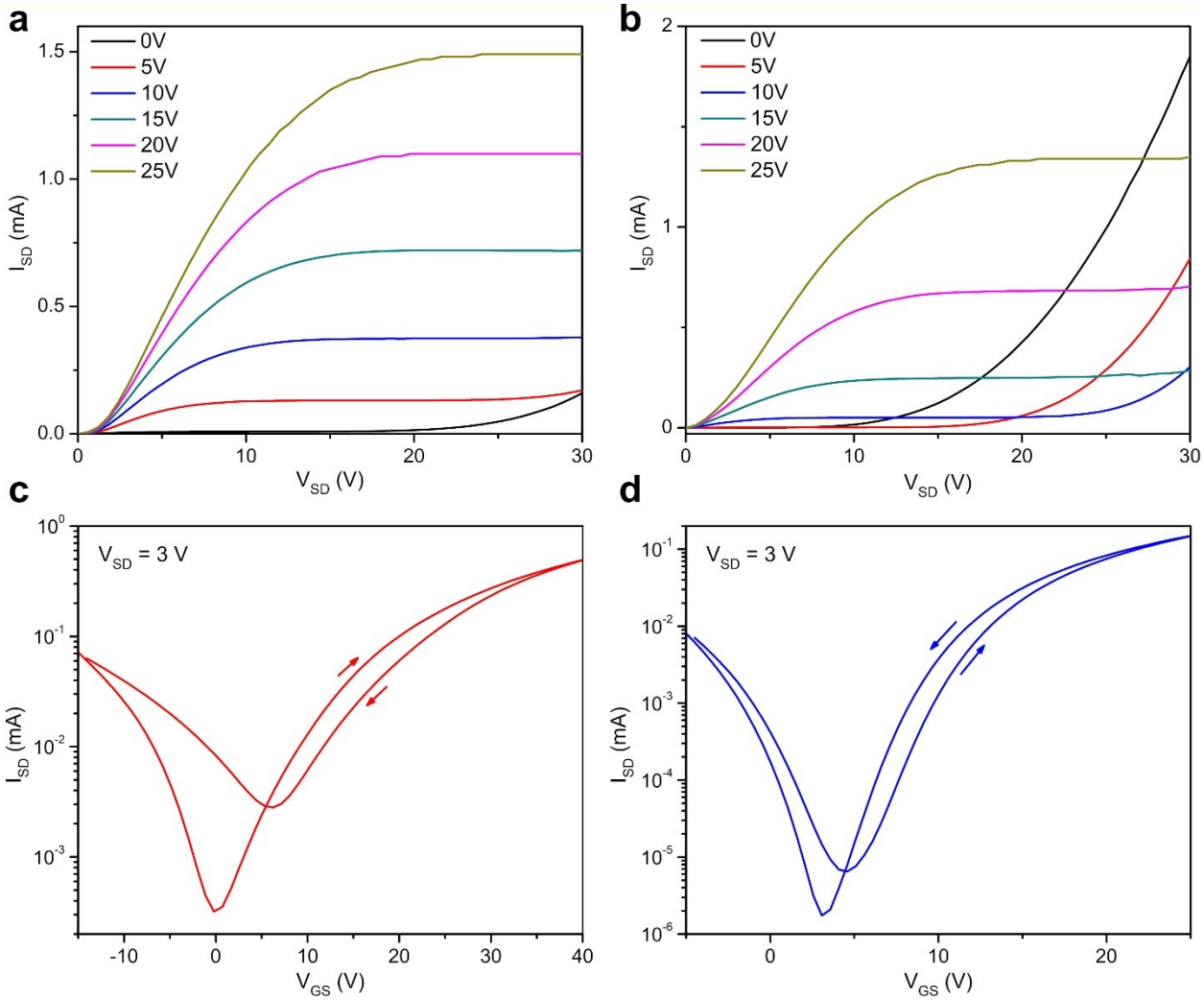

Figure 2.6: Example of output and transfer curves for (a) and (c) PFMB-SWNT, and (b) and (d) PFMB-SWNT-**EP**. All data was obtained for n-type devices, tested under vacuum, for *L*=20 µm.

A common problem plaguing SWNT TFTs is large operational hysteresis.[18] This large hysteresis is thought to be the combined result of adsorbed water and oxygen present at the interface between the sc-SWNT and dielectric surface.[73] Adsorbed water and oxygen can act as a charge trap, hindering mobility and increasing hysteresis between the forward and reverse sweeps. Self-assembled monolayers of octyltrichlorosilane (OTS) were investigated for their effect on hysteresis and charge carrier mobility. Studies exploring silane monolayers in TFTs prepared from small molecules[74] and SWNTs[75] have shown an increase in charge carrier mobility and a reduction in hysteresis, including octadecyltrichlorosilane,[74,75] and octadecyltrimethoxysialane.[74] Previous studies from our group have shown that self-assembled monolayers of OTS resulted in improved device performance.[45,76,77] The effect of surface treatment was characterized for both the drop-cast and the soak techniques and described in detail in the Supporting Information (see **Figure 2.12**, **Figure 2.13**, and **Figure 2.14** in the Supporting Information). After dielectric surface modification, higher mobilities were observed for almost all channel lengths for devices fabricated using the two different film formation techniques. With the exception of the 2.5 μm channel fabricated using the drop-cast technique, surface modification using OTS also resulted in a drastic reduction in the average hysteresis for all devices made with both the drop-cast and soak method. Interestingly, dielectric surface treatment with OTS also enhanced SWNT TFT ambipolarity. Under ambient conditions and in the absence of a passivation layer, SWNTs typically exhibit p-type characteristics with hole conduction as the dominant charge carrier. However, SWNTs are inherently ambipolar,[78] with the n-type behaviour significantly suppressed in air. In **Figure 2.5c** and **d**, a high I_{SD} is present at the beginning of the forward sweep in the positive V_{GS} range, indicating that electron transport is occurring in addition to the dominant hole transport. Without dielectric surface treatment **(Figure 2.14d)**, the transfer curve shows a much smaller I_{SD} at the beginning of the forward sweep with a reduced slope, indicating that n-type behaviour is suppressed to a greater degree when dielectric surface treatment is not used. Dielectric surface treatment replaces the silanol groups with a SAM of OTS, reducing the concentration of electron traps and facilitating electron transport (**Figure 2.6**).

Atomic force microscopy (AFM) measurements were performed within the transistor channels for PFMB-SWNT and PFMB-SWNT-**EP** devices. **Figure 2.7a-b** are representative AFM images for both PFMB-SWNT and PFMB-SWNT-**EP** devices, respectively, with a photo of the transistor shown below. The feature heights for PFMB-SWNT are in the range of 2 – 4 nm and

seldom exceed 4 nm, indicating excellent exfoliation of sc-SWNTs. Despite this, overall film formation for PFMB-SWNT was very inhomogeneous, with sc-SWNT density varying greatly throughout the channel. An alternating, inhomogeneous pattern of light and dense sc-SWNT coverage was observed. This could be discerned visually, with red spots in the transistor channel indicating areas of dense sc-SWNT film coverage. Compared to the film formation of PFMB-SWNT, AFM images of PFMB-SWNT**-EP** films in **Figure 2.7b** appear to be slightly more homogeneous, albeit less dense. However, the mobility error bars for PFMB-SWNT and PFMB-SWNT**-EP** devices shown in **Figure 2.4** are similar in magnitude. As with PFMB-SWNT, films prepared from PFMB-SWNT**-EP** have nanotube features in the range of 2 – 4 nm, confirming excellent bundle exfoliation. Unlike the PFMB-SWNT film, inhomogeneous light and dense coverage patterns are not observed visually within the transistor channel. Additionally, the AFM image for PFMB-SWNT**-EP** suggests that the excess polymer had been effectively removed after the rinsing step, leaving behind a film of sc-SWNTs in the channel. These AFM results suggest that the presence of excess polymer in the SWNT dispersion does not adversely affect the film formation compared to films formed from dispersions with excess polymer removed. Furthermore, using a SAM of OTS does not hinder the formation of the PFMB-SWNT percolation pathway.

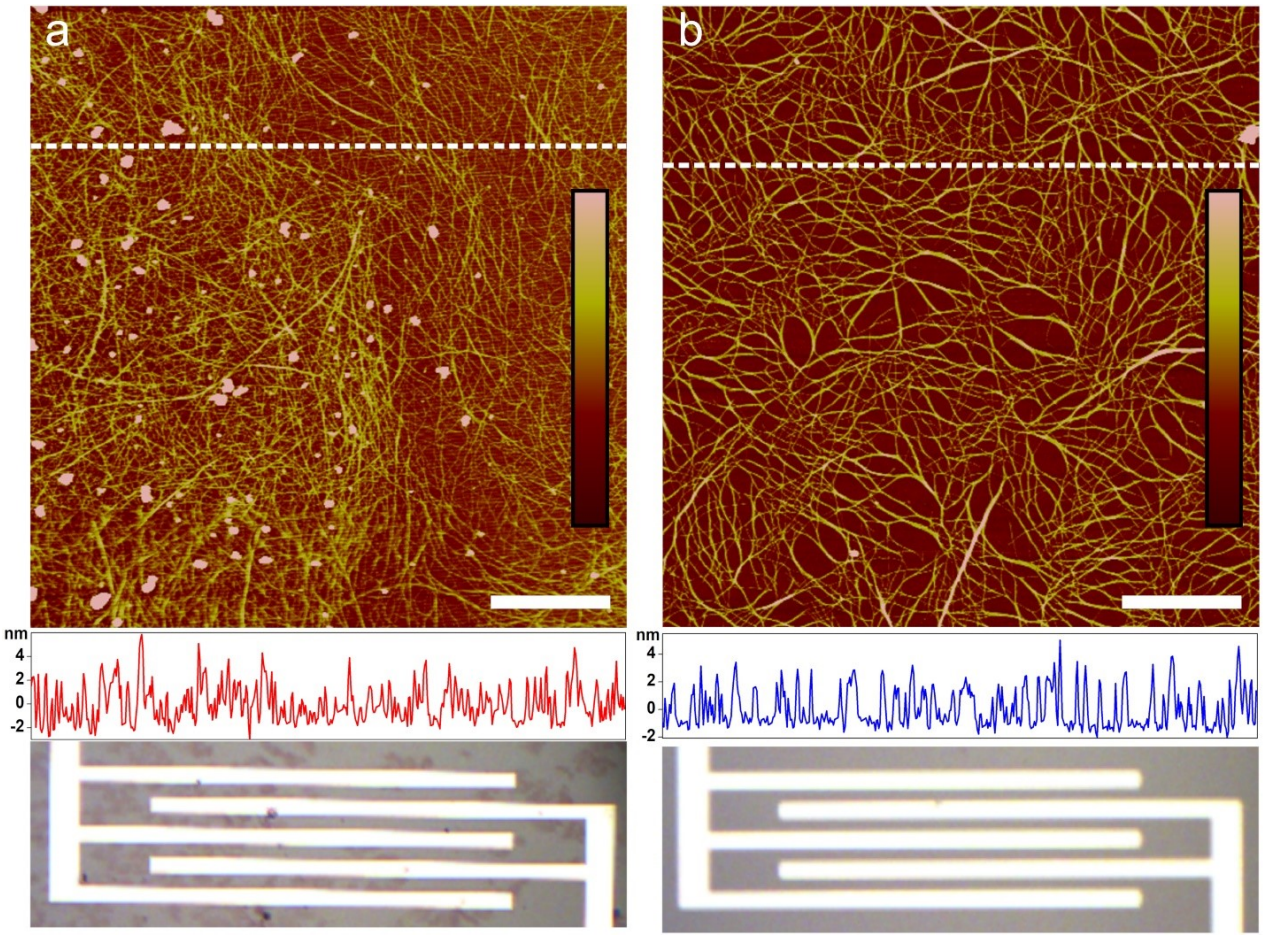

Figure 2.7: Representative AFM images of (a) PFMB-SWNT and (b) PFMB-SWNT-**EP**. Both images were taken on a 20 µm channel for substrates that were treated with OTS. The dashed lines indicate the location of the height profile displayed below each AFM image, and the white scale bars indicate 1 µm. A photograph of each film inside the channel is shown at the bottom.

2.4 Conclusion

In conclusion, we have successfully demonstrated the use of a novel polymer comprised of fluorene copolymerized with 2,5-dimethoxybenzene for selective discrimination of sc-SWNTs. Through the use of conjugated polymer extraction, we were able to consistently and reliably prepare dispersions of sc-SWNTs with semiconducting purities in excess of 99 %. Absorbance and Raman spectroscopies confirmed that the SWNT dispersions obtained were highly-pure in semiconducting species. We successfully incorporated the resulting polymer-SWNT complex into high performing ambipolar TFTs using a simple drop-cast technique. Dielectric modification with octyltrichlorosilane (OTS) is a simple and facile method for improving TFT performance, resulting in a reduction of operational hysteresis and an increase in both hole and electron mobility. Interestingly, we found that the presence of excess polymer did not hinder TFT performance compared to TFTs fabricated using dispersions with excess polymer removed. AFM measurements showed that both polymer-SWNT dispersions could form well-exfoliated SWNT films with complete percolation pathways between the electrodes and that a simple device rinsing step was sufficient to remove the majority of excess polymer from the device. The effect of the presence of excess polymer in the polymer-SWNT dispersion will be the focus of future studies, as the elimination of laborious filtration or centrifugation steps will help reduce fabrication time and the overall cost of devices.

2.5 Experimental Section

2.5.1 General

Reagents were purchased from commercial suppliers and used as received. NMR was performed on a Bruker Avance 600 MHz instrument and shift-referenced to the residual solvent resonance. Polymer molecular weights and dispersities were analyzed (relative to polystyrene standards) *via* GPC using a Waters 2695 Separations Module equipped with a Waters 2414 refractive index detector and a Jordi Fluorinated DVB mixed bed column in series with a Jordi Fluorinated DVB 10^5 Å pore size column. THF with 2% acetonitrile was used as the eluent at a flow rate of 2.0 $mL \cdot min^{-1}$.

2.5.2 Monomer Syntheses

The monomers 1,4-diiodo-2,5-dimethoxybenzene[79] **(1)** and 2,2'-(9,9-dihexadecylfluorene-2,7-diyl)bis(4,4,5,5-tetramethyl-1,3,2-dioxaborolane)[80] **(2)** were prepared according to literature procedures.

2.5.3 Polymer Synthesis

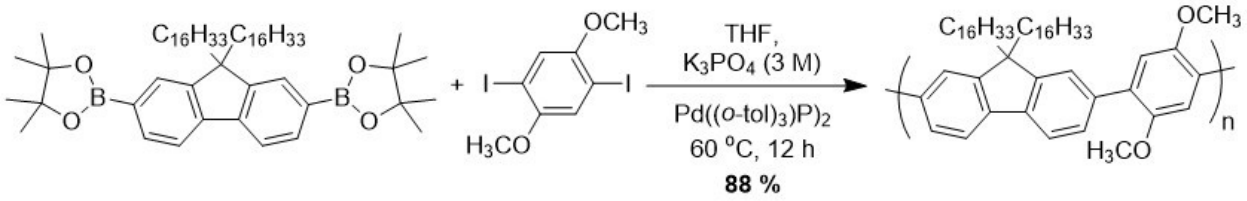

Figure 2.8: Synthetic route for PFMB.

A Schlenk tube equipped with a magnetic stir bar was charged with **1** (188.9 mg, 0.484 mmol), **2** (400.0 mg, 0.461 mmol), THF (1.9 mL), and 3M $K_3PO_{4(aq)}$ (1.9 mL). The biphasic mixture was degassed by three freeze-pump-thaw cycles, then, while frozen under liquid nitrogen, $[(o\text{-tol})_3P]_2Pd$ (17 mg, 23 μmol) was added under a positive pressure of nitrogen. The Schlenk tube was evacuated and backfilled with nitrogen four times, and the reaction mixture was heated to 60 °C and vigorously stirred for 12 h. The phases were allowed to separate, and the organic layer was isolated and filtered through a single plug of celite and neutral alumina. The plug was thoroughly washed with THF, and the filtrate was concentrated *in vacuo*. The crude polymer was precipitated into MeOH (~200 mL) and then filtered to afford PFMB as a yellow solid (281 mg, 81 %). ^{1}H-NMR (600 MHz; $CDCl_3$): δ 7.81 (m, 2H), 7.67 (m, 2H), 7.60 (m, 2H), 7.14 (s, 2H), 3.85 (s, 6H), 2.04 (m, 4H), 1.29-1.13 (m, 56H), 0.87 (t, 6H). GPC: M_n = 64.9 kDa, Đ = 2.45.

2.5.4 SWNT Dispersions

Plasma synthesized SWNTs were purchased from Raymor NanoIntegris (batch: RNB738-120, Semi-Pure SWNTs; diameter: 0.9 – 1.5 nm, length 0.3 – 4 μm). Raw SWNT powder and PFMB were weighed and combined into a vial at a polymer-SWNT mass ratio of 1.2:1 by weight with 20 mL of toluene. The mixture was sonicated for 1.5 h (chilled with ice) in a VWR Ultrasonic Cleaner bath sonicator. The polymer-SWNT dispersion was then centrifuged at 15,000 *g* for 20 min at 10 °C using a Thermo Scientific Sorvall ST 16R equipped with a Fiberlite F15 fixed angle rotor. After centrifugation, the supernatant was carefully removed. To ensure complete removal of

residual m-SWNTs, the supernatant was further purified using silica gel treatment developed by Malenfant and co-workers.[69] 20 – 25 mg of silica gel was added to the polymer-SWNT dispersion, and the mixture was sonicated (chilled with ice) for 45 min. After sonication, the dispersion was allowed to sit on the benchtop for 3 h under ambient conditions before centrifugation at 15,000 *g* for 20 min at 10 °C. Eight polymer-SWNT dispersions were created following the above procedure, and the supernatants were combined together to form a stock solution. A small portion of this stock solution was set aside for experiments involving excess polymer. The remainder of the dispersion was filtered through a Teflon membrane (0.2 μm pore diameter) and thoroughly rinsed with toluene to remove excess polymer (monitored using a UV lamp). The polymer/sc-SWNT material was scraped off the membrane and re-dispersed in toluene by 1 hour of sonication, and then a quick centrifugation was performed (10 min at 15,000 *g* and 10 °C) to confirm stability.

Absorption spectra were collected using a Cary 5000 spectrometer in dual beam mode, using 10 mm quartz cuvettes. Absorption spectra of all solutions were collected in toluene. The concentrations of the PFMB-SWNT and the PFMB-SWNT-**EP** dispersions were adjusted by adding additional toluene until the absorption intensity of S_{22} peaks at 937 nm were approximately equal (~1.1 a.u.).

Raman spectroscopy was performed using a Renishaw InVia Laser Raman spectrometer, using three different lasers: a 25 mW argon ion laser (514 nm, 1800 L/mm grating); a 500 mW HeNe Renishaw laser (633 nm, 1800 L/mm grating); and a 300 mW Renishaw laser (785 nm, 1200 L/mm grating). Extended scans (100 – 3200 cm^{-1}) and static scans (centred at 250 cm^{-1}, 10 accumulations averaged together) were collected for all three laser excitation wavelengths using the following laser powers: 1% for 514 and 785 nm (for all static scans and full SWNT spectrum), 0.1% for extended PFMB-SWNT scans at 785 nm; 5% for PFMB-SWNT extended scans, 10% for raw SWNT extended spectrum, and 50% for all static scans at 633 nm. To prepare samples for Raman, SiO_2 wafers were cleaned using deionized water and acetone. A pipette was used to drop the PFMB-SWNT dispersion onto a wafer, and the toluene was allowed to evaporate. A small amount of raw SWNT powder was suspended in chloroform using a bath sonicator and drop-casted onto a cleaned SiO_2 wafer. AFM measurements were collected using a Bruker Dimension Icon AFM with ScanAsyst-Air tips. All images were collected in tapping mode at a scan rate of 1 Hz,

an image size of 5 × 5 μm, and a resolution of 512 pixels. To process and edit the images, NanoScope Analysis v.1.8 was used.

2.5.5 TFT Device Fabrication

Pre-fabricated bottom-gate bottom-contact (BGBC) Generation 5 wafers purchased from Fraunhofer Institute for Photonic Microsystems (IPMS) were used as substrates for sc-SWNT TFTs. The architecture of the wafer consists of an n-doped silicon gate electrode, a 230 nm SiO_2 dielectric, and 30 nm gold source and drain electrodes with interdigitating channels deposited on top of a 10 nm ITO adhesion layer. Each wafer consists of 16 transistor channels with 4 different channel lengths: 2.5, 5, 10, and 20 μm, each with a width of 2000 μm. Preceding device fabrication, a dielectric modification step to treat the dielectric surface before depositing the sc-SWNT film was investigated. Silanol groups on the SiO_2 surface were allowed to react with octyltrichlorosilane (OTS) following a literature procedure to form a hydrophobic self-assembled monolayer (SAM).[76] Hysteresis and charge mobility were compared between devices with and without surface treatment to ascertain treatment efficacy (see Supporting Information for details). Two techniques were employed to fabricate sc-SWNT TFTs: the soak technique and the drop-cast technique. To fabricate a TFT using the soak technique, 200 μL of sc-SWNT dispersion was pipetted onto the wafer using a micropipette and allowed to sit for 15 minutes in a sealed vial. To fabricate a TFT using the drop-cast technique, a micropipette was used to deposit 0.5 μL of sc-SWNT dispersion into each transistor channel. The wafer would then sit until the toluene evaporated off. The subsequent rinsing and annealing steps were the same for both the soak and drop-cast techniques (see Supporting Information for details). Optimization studies showed that ideal device performance was obtained after four rinsing steps with toluene in 1 mL increments, followed by drying with a stream of N_2 for 3 – 5 s after each rinse in the same direction as rinsing. The wafer was then annealed in air at 200 °C for one hour.

2.6 Acknowledgements

The authors thank Raymor NanoIntegris for their kind contribution of plasma SWNTs used in this study, and J. Brusso for using her UV-Vis-NIR. The authors are very grateful for financial support from the Natural Sciences and Engineering Research Council of Canada (NSERC) through a Discovery Grant and Research Tools and Instruments grant for B. H. Lessard, an NSERC PGS-D for D. Fong, and an NSERC PDF for N. A. Rice. O. A. Melville thanks OGS for support.

2.7 Supporting Information

2.7.1 SWNT Optical Spectroscopy

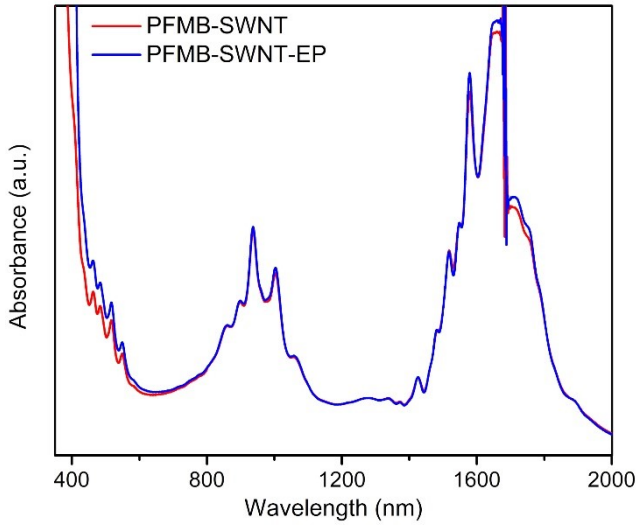

Figure 2.9: Full absorption spectra of PFMB-SWNT and PFMB-SWNT-**EP** dispersions.

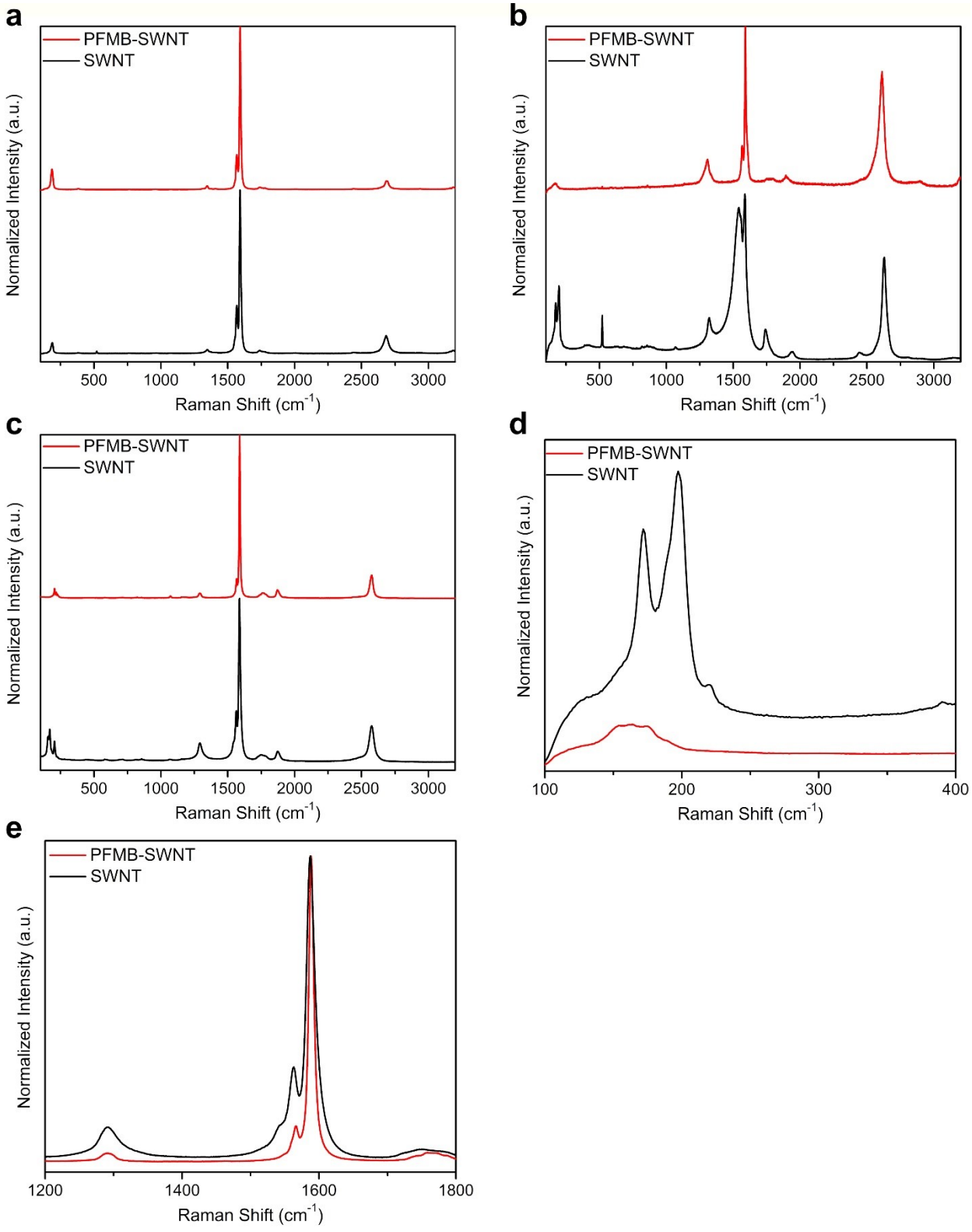

Figure 2.10: Full Raman spectra at (a) 514 nm, (b) 633 nm, (c) 785 nm for PFMB-SWNT and unsorted SWNT, (d) RBM region at 633 nm for PFMB-SWNT and unsorted SWNT, and (e) *G*-band region at 785 nm for PFMB-SWNT and unsorted SWNT.

2.7.2 Calculations

The transfer curves obtained in this study were measured in the linear regime. The measured drain current as a function of gate voltage is modelled using equation (1):

$$I_{SD} = \frac{W\mu C_i}{L}\left((V_{GS} - V_T)V_{SD} - \frac{V_{SD}^2}{2}\right) \quad (1)$$

where I_{SD} is the source-drain current, W is the channel width (2000 μm), μ is the charge carrier mobility (details given below), C_i is the dielectric capacitance, L is the channel length (2.5, 5, 10, or 20 μm), V_{GS} is the applied gate voltage, and V_T is the calculated threshold voltage (details given below).

The charge carrier mobility, μ, was extracted from the transfer curves in the linear regime using equation (2):

$$\mu = \frac{L}{WC_iV_{SD}}\frac{dI_{SD}}{dV_{GS}} \quad (2)$$

The threshold voltage was calculated from the x-intercept of the transfer curve using equation (3):

$$V_T = V_{GS}(\textit{x-intercept}) - \frac{V_{SD}}{2} \quad (3)$$

The hysteresis was calculated as the difference between the threshold voltages of the forward and reverse scans.

2.7.3 TFT Optimization

Two fabrication techniques were investigated for optimization: the drop-cast (DC) technique and the soak technique. To fabricate a TFT using the drop-cast technique, 0.5 μL of PFMB-SWNT dispersion was deposited into each transistor channel using a micropipette and allowed to sit until the toluene evaporated off. To fabricate a TFT using the soak technique, 200 μL of PFMB-SWNT dispersion was deposited onto the surface of a wafer and allowed to sit for 15 minutes inside of a sealed vial before the wafer was tilted and the excess solvent was allowed to run off. The subsequent steps involving the neat film, rinsing, and air annealing were the same for the drop-cast and soak techniques. After film deposition, the device was dried using a steady stream of N_2 for approximately 3 – 5 seconds, always in the same direction. The device was dried further in a vacuum oven at 50 °C for 30 minutes. At this stage, the device is referred to as “Neat

Film," indicating that no rinsing or annealing step was performed. After testing, the device was placed in an angled holder (45°) and rinsed with 1 mL of toluene. The device was then dried with a steady stream of N_2 in the same direction as rinsing and then further dried in a vacuum oven at 50 °C for 30 minutes before testing; this is referred to as Rinse 1. The rinsing-drying-testing steps were repeated until the device had been rinsed a total of 4 times. At this point, device performance had either plateaued or begun to degrade slightly. The final optimization stage was to investigate the effect of high-temperature annealing. The device was annealed in air at 200 °C for 1 hour and then tested. The annealed device is referred to as "Air Anneal." The average mobilities for each optimization step are presented in **Figure 2.11** for each channel length.

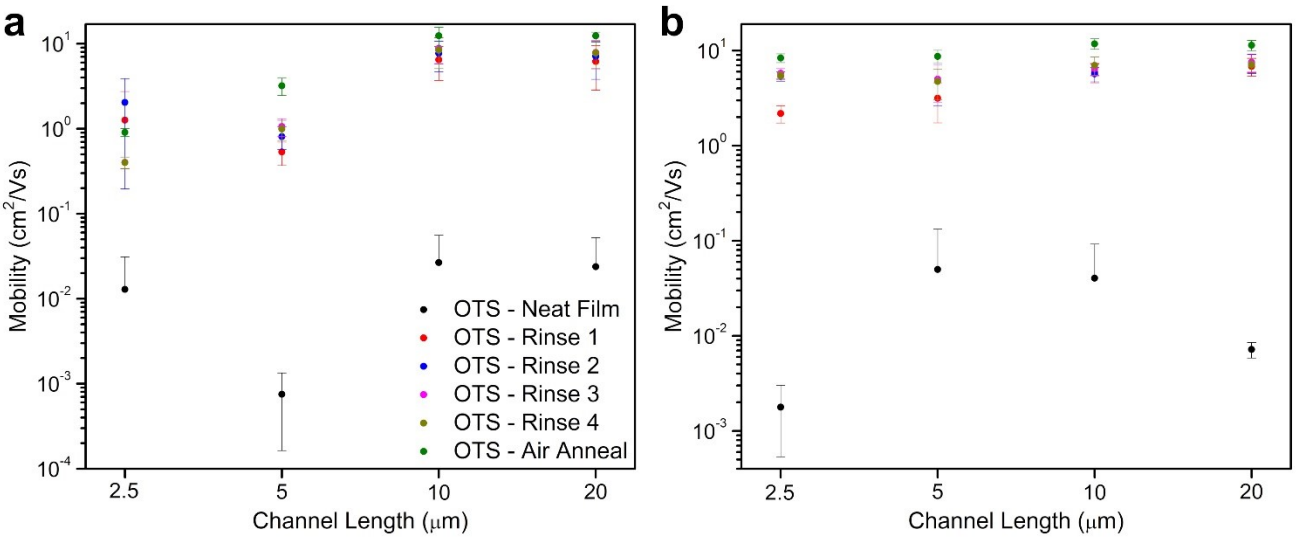

Figure 2.11: Optimization of rinsing steps (in terms of mobility) for PFMB-SWNT fabricated using (a) the drop-cast method and (b) the soak method. All data obtained in p-type conditions tested in air.

2.7.4 Dielectric Surface Treatment Study

To investigate the effect of dielectric surface treatment on device performance, devices were prepared with and without surface treatment using octyltrichlorosilane (OTS). Surface modification with OTS was performed following a literature procedure.[76] The wafers were thoroughly rinsed with acetone, followed by treatment with oxygen plasma for 15 minutes. The wafers were rinsed with deionized water and isopropanol and dried with a steady stream of N_2 before being placed in a solution of 1 % OTS in toluene and heated at 70 °C for 1 hour. The wafers were removed from the OTS solution, rinsed with toluene, and dried with a steady stream of N_2. Lastly, each wafer was dried in a vacuum oven at 70 °C for 1 hour. Wafers that were not surface treated were rinsed with acetone, treated with oxygen plasma in vacuum for 15 minutes, and rinsed with deionized water and isopropanol. Devices that received surface treatment are referred to as "OTS", whereas those not receiving surface treatment are referred to as "PT" (plasma-treated). Comparisons of average mobility and hysteresis are presented in **Figure 2.12** and **Figure 2.13**, respectively, for devices with and without surface treatment. Output and transfer curves with and without surface treatment are presented in **Figure 2.14**.

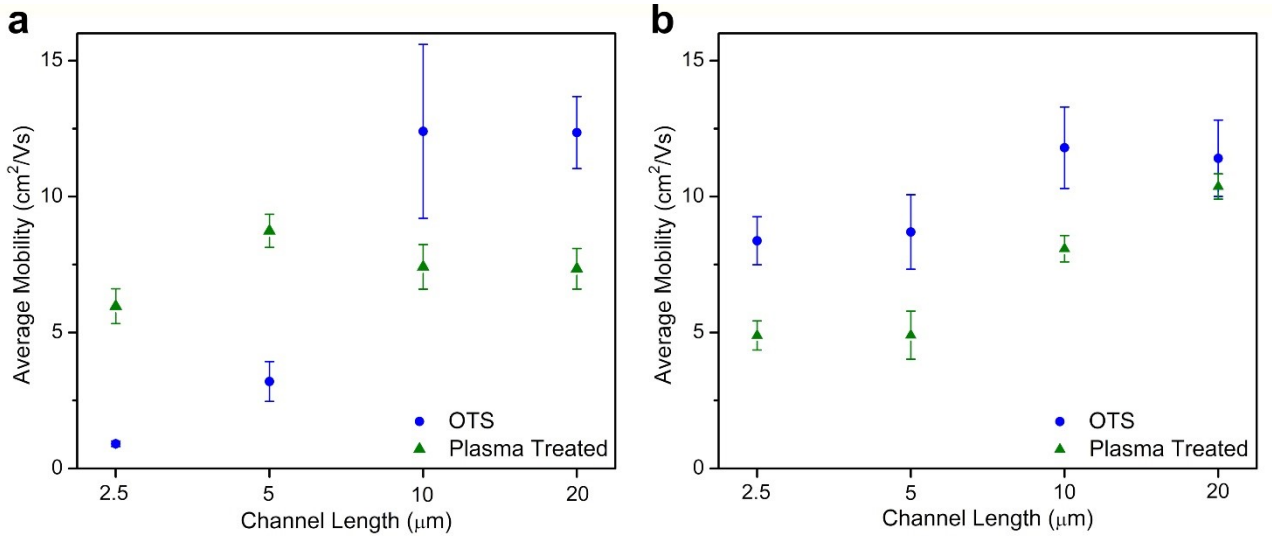

Figure 2.12: Comparison of average mobility between OTS and plasma treatment for PFMB-SWNT fabricated by (a) the drop-cast technique and (b) the soak technique. All data obtained in p-type conditions tested in air.

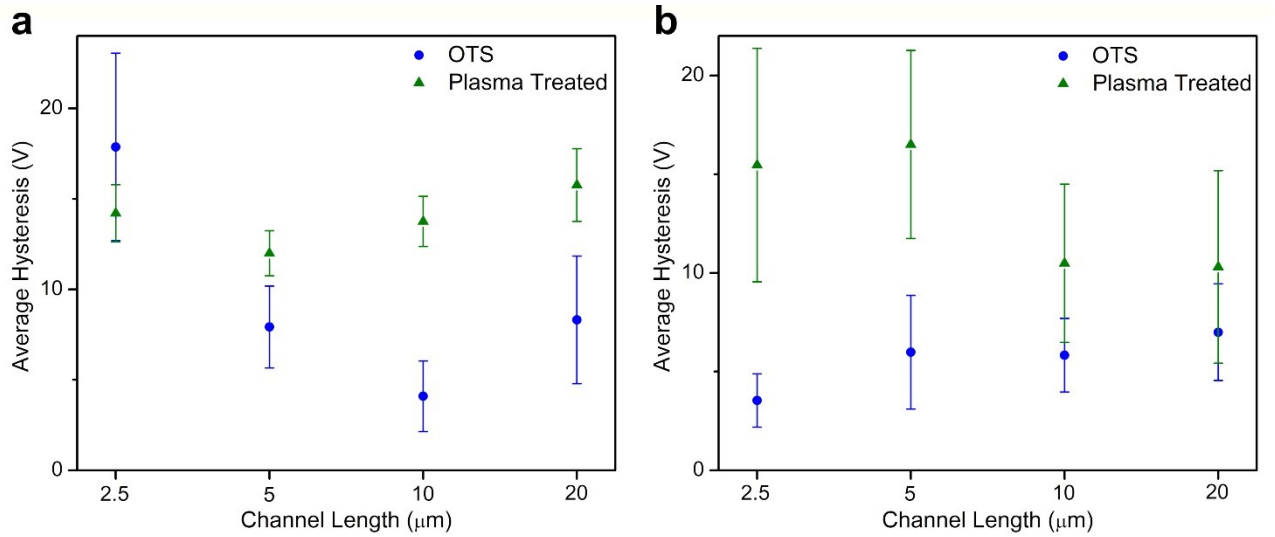

Figure 2.13: Comparison of hysteresis between OTS and plasma treatment for PFMB-SWNT fabricated by (a) the drop-cast technique and (b) the soak technique. All data obtained in p-type conditions tested in air.

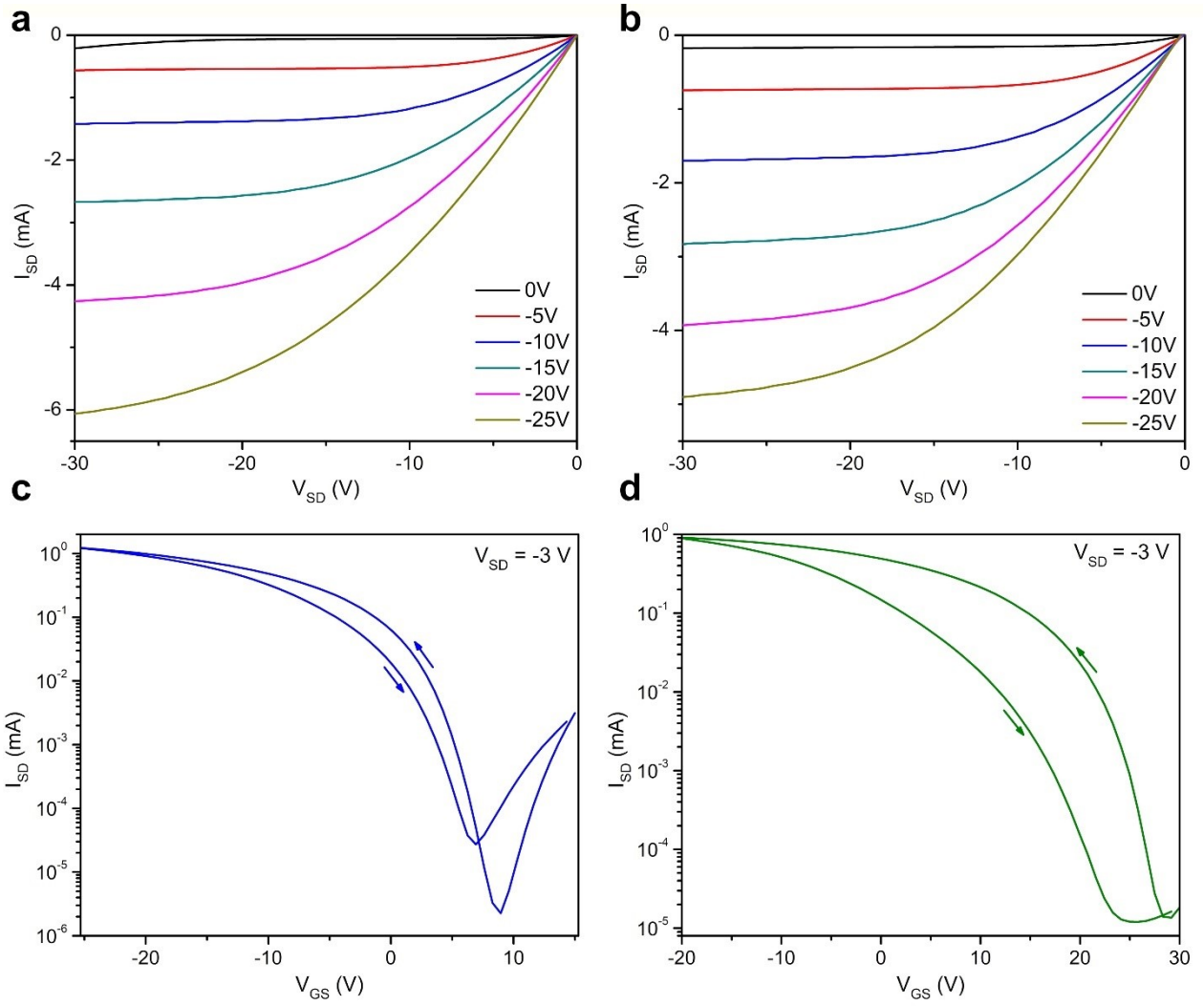

Figure 2.14: Example of Output and Transfer curves for PFMB-SWNT with (a) and (c) OTS dielectric treatment and (b) and (d) plasma treatment. All data obtained in p-type conditions tested in air for 20 µm channel lengths.

2.7.5 Concentration Study

To characterize the effect of sc-SWNT concentration on device performance, the concentrations of PFMB-SWNT and PFMB-SWNT-**EP** were each diluted to half of their original concentration. As is presented in **Table 2.2**, decreasing the concentration resulted in a 32% and a 70% drop in $\mu_{h,av}$ for the PFMB-SWNT and the PFMB-SWNT-**EP** devices, respectively. Under n-type conditions in vacuum a reduction in $\mu_{e,av}$ was also observed, with a 32% and a 55% reduction for the PFMB-SWNT and PFMB-SWNT-**EP** devices, respectively. The $\mu_{h,av}$ and $\mu_{e,av}$ data for each channel length is presented in **Figure 2.15** (data for other channel lengths can be found in **Table**

2.4). A reduction in concentration should result in a reduction in the number of sc-SWNTs per channel, hence the number of charge carriers per channel will be reduced, leading to an overall reduction in $\mu_{h,av}$ and $\mu_{e,av}$. As a comparison to the concentrated device performance metrics, the output curves and transfer curves can be found in **Figure 2.16** and **Figure 2.17**.

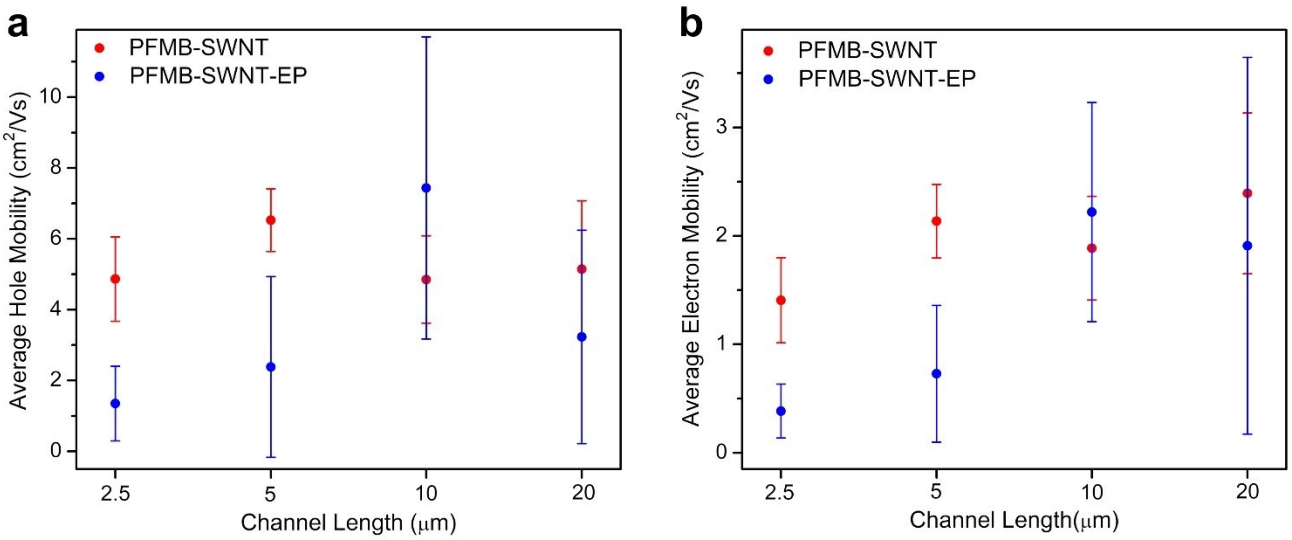

Figure 2.15: Comparison of average mobility vs. channel length for diluted samples tested in (a) p-type conditions (in air) and (b) n-type conditions (under vacuum).

Table 2.2: Summary of average (μ_{av}) and maximum (μ_{max}) mobility, threshold voltage (V_T), hysteresis (H), and $I_{on/off}$ between diluted PFMB-SWNT and PFMB-SWNT-**EP** for both p-type (tested in air) and n-type (tested under vacuum).

Channel Length = 20 µm, p-type, tested in Air (V_{SD} = -3 V)					
	$\mu_{h,av}$ (cm²/Vs)	$\mu_{h,max}$ (cm²/Vs)	$V_{T,av}$ (V)	H_{av} (V)	$I_{on/off}$
PFMB-SWNT	5.14 ± 1.92	10.23	5.31 ± 2.78	3.90 ± 0.99	10^5 - 10^6
PFMB-SWNT-**EP**	3.23 ± 3.01	10.96	2.26 ± 0.78	5.06 ± 2.19	10^6
Channel Length = 20 µm, n-type, tested in Vacuum (V_{SD} = 3 V)					
	$\mu_{e,av}$ (cm²/Vs)	$\mu_{e,max}$ (cm²/Vs)	$V_{T,av}$ (V)	H_{av} (V)	$I_{on/off}$
PFMB-SWNT	2.39 ± 0.74	4.34	11.17 ± 1.27	3.58 ± 1.89	10^3
PFMB -SWNT-**EP**	1.90 ± 1.73	6.52	6.50 ± 1.53	2.19 ± 1.42	10^5 - 10^6

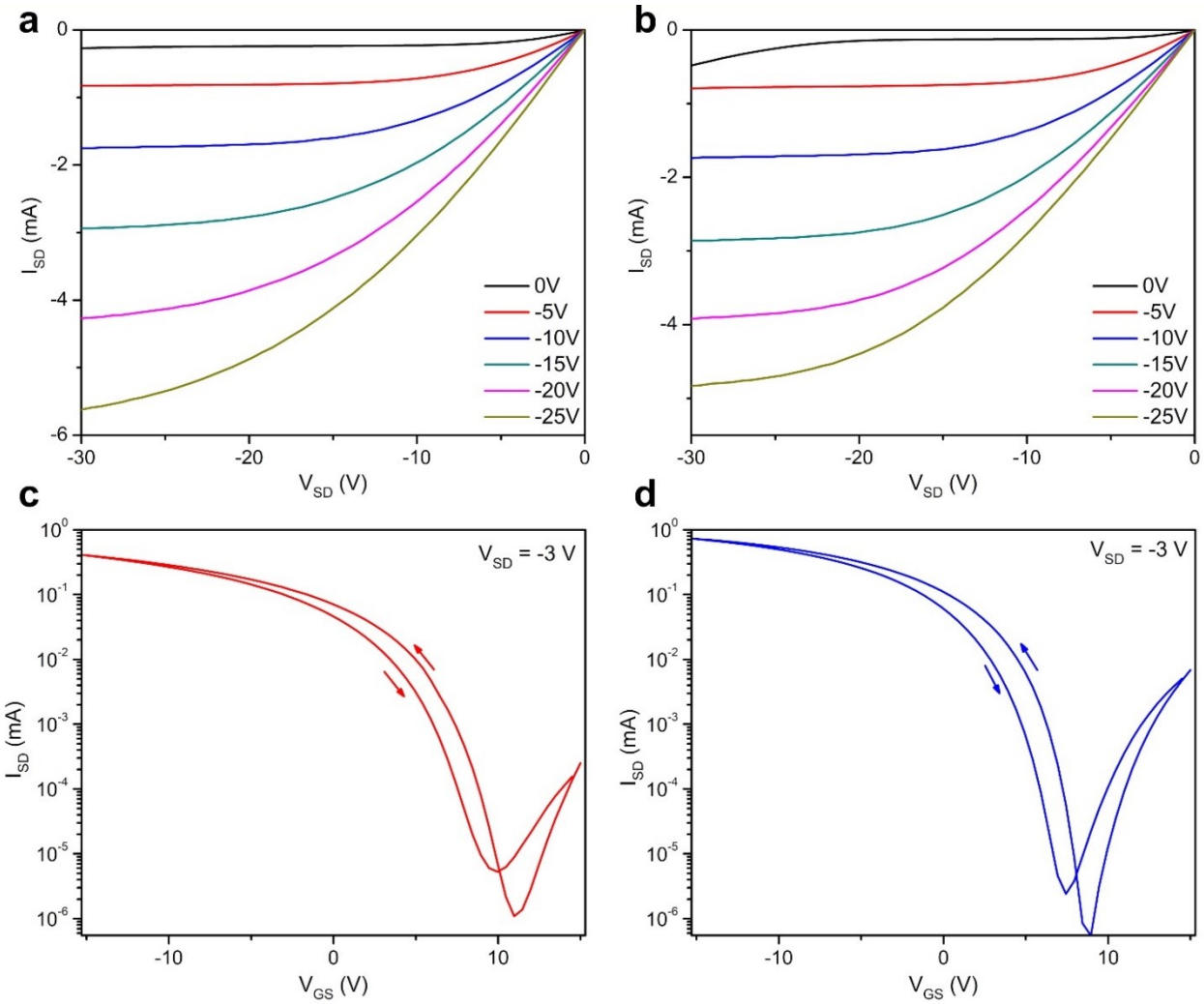

Figure 2.16: Example of output and transfer curves for diluted (a) and (c) PFMB-SWNT and (b) and (d) PFMB-SWNT-**EP**. All data obtained in p-type conditions tested in air for 20 µm channel lengths. Both samples were diluted by a factor of 2.

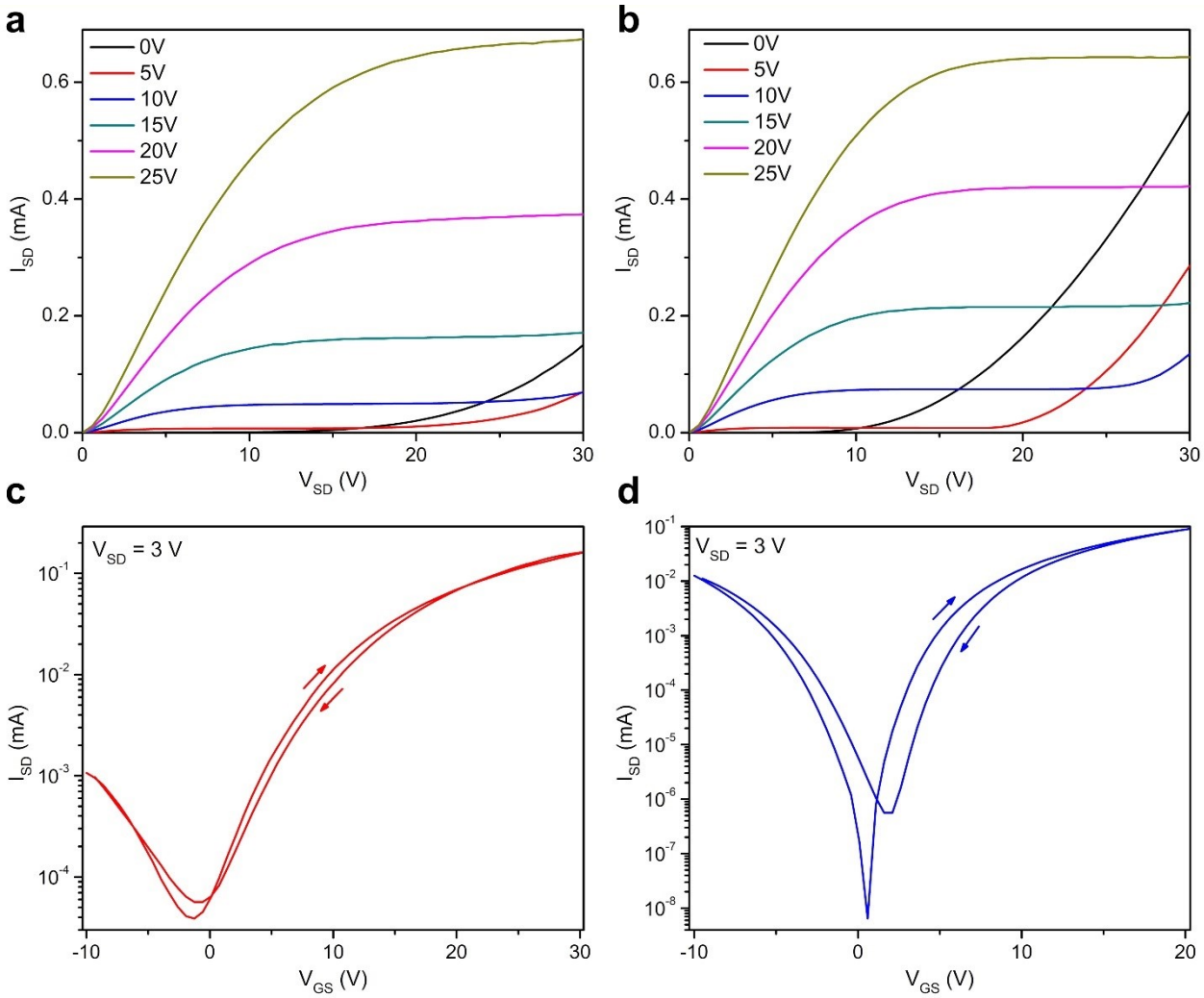

Figure 2.17: Example of output and transfer curves for diluted (a) and (c) PFMB-SWNT and (b) and (d) PFMB-SWNT-**EP**. All data obtained in n-type conditions were tested under vacuum for 20 µm channel lengths. Both samples were diluted by a factor of 2.

Differences in performance between the original and the dilute samples are likely the result of reduced sc-SWNT density within the transistor channels. In their study investigating the relationship between SWNT density, mobility, and on-current, Sangwan et al. found that mobility increased with an increasing SWNT density.[81] AFM measurements for both PFMB-SWNT and PFMB-SWNT-**EP** dilute samples, shown in **Figure 2.18**, confirm the reduction in SWNT coverage in the transistor channels for both samples. A comparison of the film formation between the original and diluted PFMB-SWNT and PFMB-SWNT-**EP** samples shows similar film formation characteristics. The line-height profiles for both PFMB-SWNT and PFMB-SWNT-**EP**

samples show that both again contain features that are between 2 – 4 nm in height. The film formed by diluted PFMB-SWNT is still relatively inhomogeneous, with alternating areas of light and dense coverage, whereas the film formation for the diluted PFMB-SWNT-**EP** sample is more uniform. Crucially, the film formed from diluted PFMB-SWNT-**EP** had fewer nanotube connections compared to **Figure 2.7b** in the manuscript, indicating a drastic loss of percolation pathways, and resulting in a significant drop in mobility for these devices. Overall, these results illustrate that solution concentration has a critical effect on the resulting density of SWNT in the device channels and, ultimately, the final device performance.

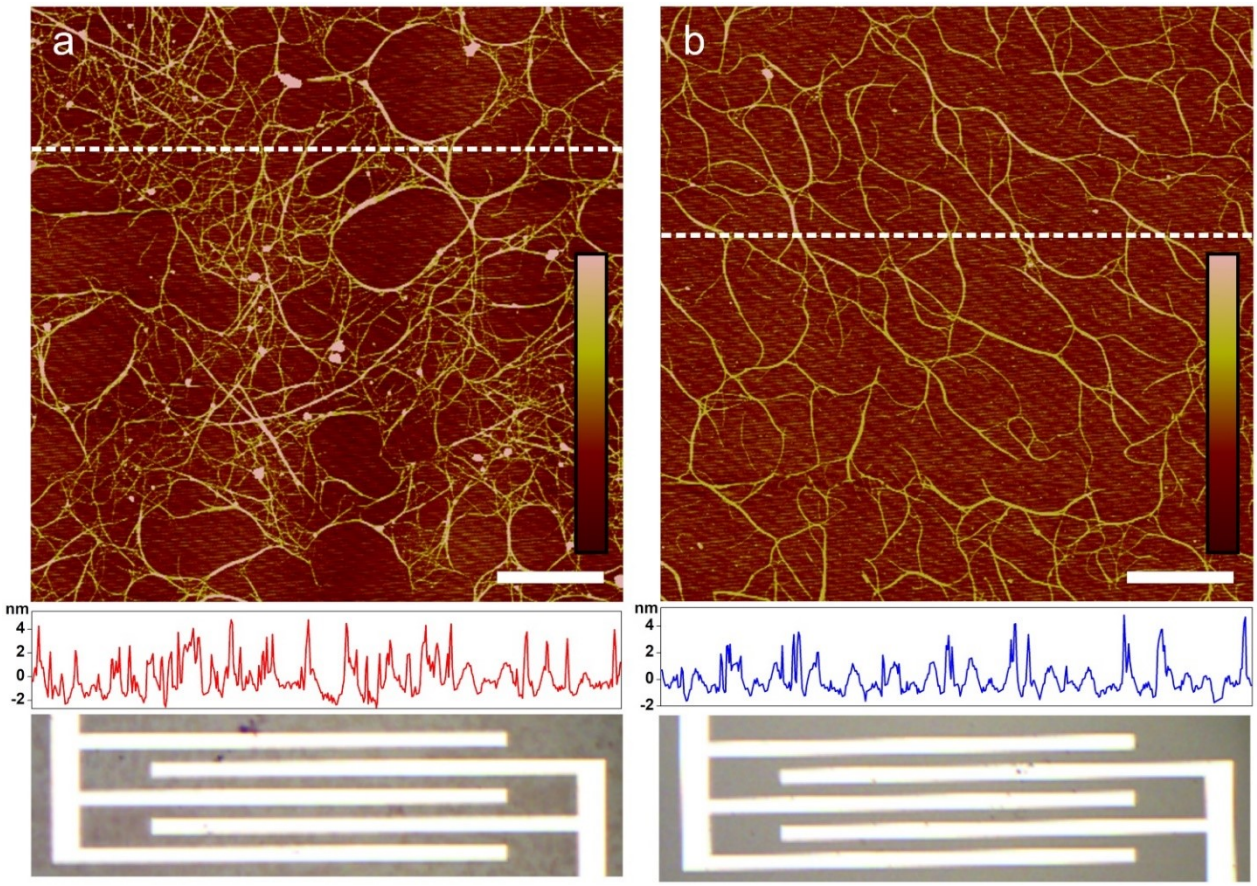

Figure 2.18: Representative AFM images of diluted (a) PFMB-SWNT and (b) PFMB-SWNT-**EP** samples. Both images were taken on a 20 µm channel for substrates that were treated with OTS. The dashed lines indicate the location of the height profile displayed below each AFM image, and the white scale bars indicate 1 µm. A photograph of each film inside the channel is shown at the bottom.

2.7.6 Additional TFT Data for 2.5, 5, and 10 µm Channel Lengths

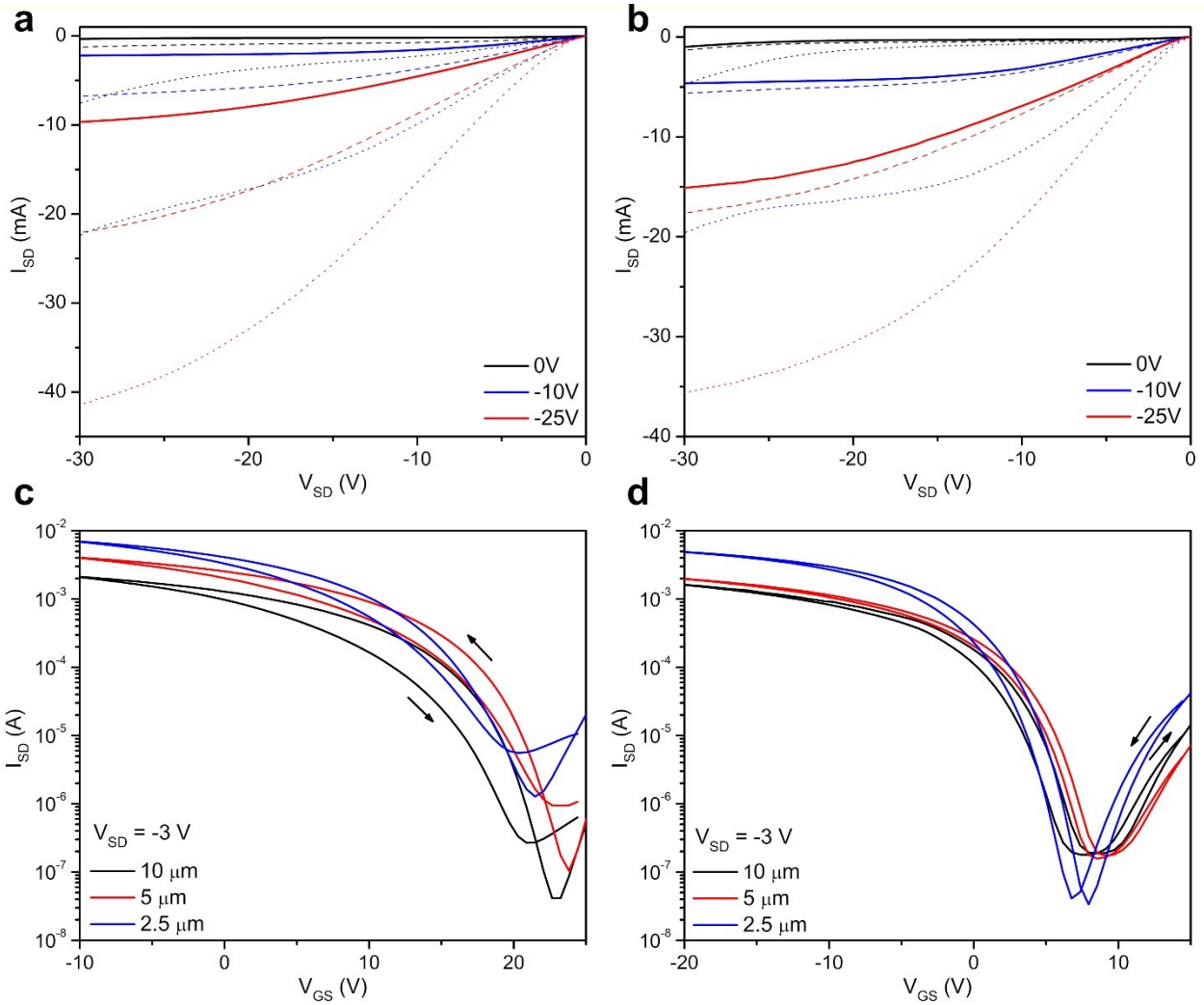

Figure 2.19: Example of output and transfer curves for (a) and (c) PFMB-SWNT, and (b) and (d) PFMB-SWNT-**EP**, p-type conditions (tested in air). The channel lengths included in the output curves are 10 µm (solid lines), 5 µm (dashed lines), and 2.5 µm channels (dotted lines).

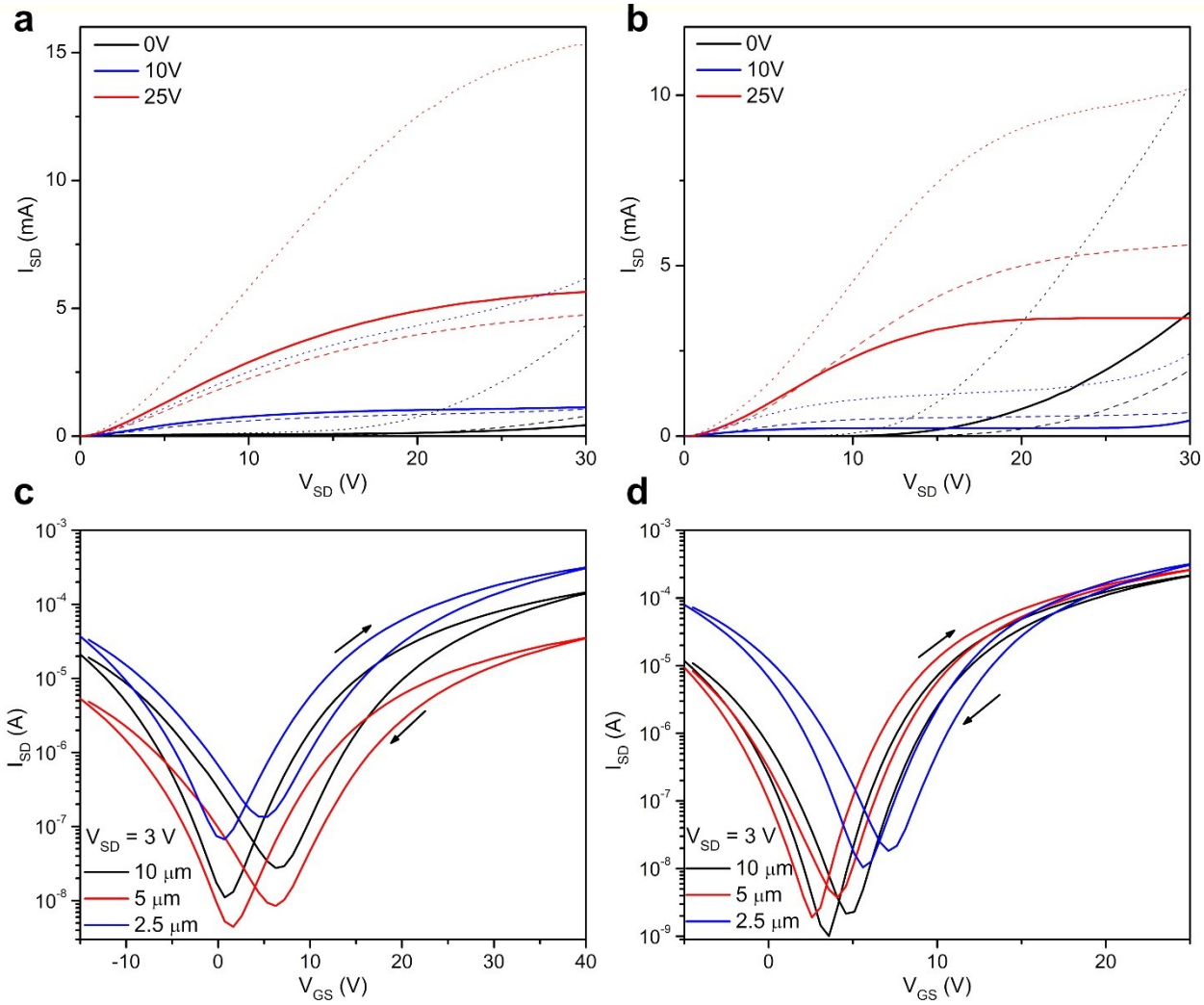

Figure 2.20: Example of output and transfer curves for (a) and (c) PFMB-SWNT, and (b) and (d) PFMB-SWNT-**EP**, n-type conditions (tested under vacuum). The channel lengths included in the output curves are 10 μm (solid lines), 5 μm (dashed lines), and 2.5 μm channels (dotted lines).

Table 2.3: Summary of average (μ_{av}) and maximum (μ_{max}) mobility, threshold voltage (V_T), hysteresis (H), and $I_{on/off}$ for 2.5, 5, and 10 µm channel lengths. Data presented for p-type devices (tested in air) and n-type devices (tested under vacuum).

Channel Length = 2.5 µm, p-type, tested in Air (V_{SD} = -3 V)					
	$\mu_{h,av}$ (cm^2/Vs)	$\mu_{h,max}$ (cm^2/Vs)	$V_{T,h,av}$ (V)	$H_{h,av}$ (V)	$I_{on/off,h}$
PFMB-SWNT	5.85 ± 3.06	11.50	7.22 ± 4.09	7.28 ± 3.59	10^3 - 10^4
PFMB-SWNT-**EP**	5.18 ± 1.84	8.97	-1.24 ± 4.48	4.70 ± 2.56	10^4 - 10^5
Channel Length = 2.5 µm, n-type, tested in Vacuum (V_{SD} = 3 V)					
	$\mu_{e,av}$ (cm^2/Vs)	$\mu_{e,max}$ (cm^2/Vs)	$V_{T,e,av}$ (V)	$H_{e,av}$ (V)	$I_{on/off,e}$
PFMB-SWNT	1.64 ± 0.83	3.49	13.57 ± 8.67	11.68 ± 4.12	10^3
PFMB-SWNT-**EP**	1.38 ± 0.50	2.78	12.09 ± 1.93	4.01 ± 2.87	10^4

Channel Length = 5 µm, p-type, tested in Air (V_{SD} = -3 V)					
	$\mu_{h,av}$ (cm^2/Vs)	$\mu_{h,max}$ (cm^2/Vs)	$V_{T,h,av}$ (V)	$H_{h,av}$ (V)	$I_{on/off,h}$
PFMB-SWNT	4.93 ± 2.39	11.22	5.41 ± 5.21	8.06 ± 3.68	10^4 - 10^5
PFMB-SWNT-**EP**	5.29 ± 2.60	11.61	-0.72 ± 5.07	6.26 ± 6.10	10^4 - 10^5
Channel Length = 5 µm, n-type, tested in Vacuum (V_{SD} = 3 V)					
	$\mu_{e,av}$ (cm^2/Vs)	$\mu_{e,max}$ (cm^2/Vs)	$V_{T,e,av}$ (V)	$H_{e,av}$ (V)	$I_{on/off,e}$
PFMB-SWNT	1.68 ± 0.95	4.13	15.70 ± 6.35	9.57 ± 3.99	10^3
PFMB-SWNT-**EP**	1.85 ± 0.94	5.09	11.72 ± 2.08	2.85 ± 2.73	10^4 - 10^5

Channel Length = 10 µm, p-type, tested in Air (V_{SD} = -3 V)					
	$\mu_{h,av}$ (cm^2/Vs)	$\mu_{h,max}$ (cm^2/Vs)	$V_{T,h,av}$ (V)	$H_{h,av}$ (V)	$I_{on/off,h}$
PFMB-SWNT	6.93 ± 3.10	12.82	4.59 ± 5.63	6.33 ± 2.80	10^4 - 10^5
PFMB-SWNT-**EP**	8.53 ± 3.14	13.90	-0.50 ± 4.38	5.01 ± 4.76	10^4 - 10^5
Channel Length = 10 µm, n-type, tested in Vacuum (V_{SD} = 3 V)					
	$\mu_{e,av}$ (cm^2/Vs)	$\mu_{e,max}$ (cm^2/Vs)	$V_{T,e,av}$ (V)	$H_{e,av}$ (V)	$I_{on/off,e}$
PFMB-SWNT	2.64 ± 1.34	5.88	14.87 ± 7.45	8.64 ± 3.64	10^3
PFMB-SWNT-**EP**	3.18 ± 0.88	5.12	11.50 ± 1.68	3.48 ± 2.08	10^5 - 10^6

Table 2.4: Summary of average (μ_{av}) and maximum (μ_{max}) mobility, threshold voltage (V_T), hysteresis (H), and $I_{on/off}$ for 2.5, 5, and 10 µm channel lengths for dilute devices. Data presented for p-type devices (tested in air) and n-type devices (tested under vacuum).

Channel Length = 2.5 µm, p-type, tested in Air - Dilute (V_{SD} = -3 V)					
	$\mu_{h,av}$ (cm^2/Vs)	$\mu_{h,max}$ (cm^2/Vs)	$V_{T,h,av}$ (V)	$H_{h,av}$ (V)	$I_{on/off,h}$
PFMB-SWNT	4.86 ± 1.19	6.66	6.75 ± 1.83	1.29 ± 2.34	10^2 – 10^3
PFMB-SWNT-**EP**	1.34 ± 1.05	4.35	1.27 ± 0.76	4.39 ± 1.63	10^4 - 10^5
Channel Length = 2.5 µm, n-type, tested in Vacuum – Dilute (V_{SD} = 3 V)					
	$\mu_{e,av}$ (cm^2/Vs)	$\mu_{e,max}$ (cm^2/Vs)	$V_{T,e,av}$ (V)	$H_{e,av}$ (V)	$I_{on/off,e}$
PFMB-SWNT	1.40 ± 0.39	2.20	13.21 ± 3.11	5.46 ± 2.32	10^3 – 10^4
PFMB-SWNT-**EP**	0.38 ± 0.24	0.99	8.39 ± 1.55	2.66 ± 2.79	10^4 - 10^5

Channel Length = 5 µm, p-type, tested in Air - Dilute (V_{SD} = -3 V)					
	$\mu_{h,av}$ (cm^2/Vs)	$\mu_{h,max}$ (cm^2/Vs)	$V_{T,h,av}$ (V)	$H_{h,av}$ (V)	$I_{on/off,h}$
PFMB-SWNT	6.52 ± 0.88	8.25	5.84 ± 1.25	1.90 ± 0.79	10^3 – 10^4
PFMB-SWNT-**EP**	2.38 ± 2.55	7.25	2.29 ± 0.47	4.10 ±1.75	10^5 – 10^6
Channel Length = 5 µm, n-type, tested in Vacuum – Dilute (V_{SD} = 3 V)					
	$\mu_{e,av}$ (cm^2/Vs)	$\mu_{e,max}$ (cm^2/Vs)	$V_{T,e,av}$ (V)	$H_{e,av}$ (V)	$I_{on/off,e}$
PFMB-SWNT	2.13 ± 0.33	3.06	12.74 ± 3.02	4.79 ±3.50	10^3
PFMB-SWNT-**EP**	0.72 ± 0.62	2.00	7.48 ± 1.21	3.05 ± 1.79	10^4 - 10^5

Channel Length = 10 µm, p-type, tested in Air – Dilute (V_{SD} = -3 V)					
	$\mu_{h,av}$ (cm^2/Vs)	$\mu_{h,max}$ (cm^2/Vs)	$V_{T,h,av}$ (V)	$H_{h,av}$ (V)	$I_{on/off,h}$
PFMB-SWNT	4.85 ± 1.23	6.79	5.60 ± 1.53	2.93 ± 0.74	10^4 - 10^5
PFMB-SWNT-**EP**	7.43 ± 4.26	13.57	2.97 ± 1.18	2.28 ± 1.08	10^4 - 10^5
Channel Length = 10 µm, n-type, tested in Vacuum – Dilute (V_{SD} = 3 V)					
	$\mu_{e,av}$ (cm^2/Vs)	$\mu_{e,max}$ (cm^2/Vs)	$V_{T,e,av}$ (V)	$H_{e,av}$ (V)	$I_{on/off,e}$
PFMB-SWNT	1.88 ± 0.47	2.96	13.65 ± 2.67	4.65 ± 2.37	10^3 – 10^4
PFMB-SWNT-**EP**	2.21 ± 1.01	4.00	8.28 ± 1.22	1.68 ± 0.98	10^5 – 10^6

2.7.7 Contact Resistance

Contact resistance was calculated using the modified transmission line method (M-TLM) method (Equation 4).[64] Total resistance (R_{Tot}) was calculated from the output curve as the inverse slope at a low source-drain voltage (V_{SD} < 600 mV) for each V_{GS}. $R_{Tot}W/L$ was plotted against $1/L$ for all channel lengths (2.5, 5, 10, and 20 μm). The resulting slope is R_CW, the width-normalized contact resistance. Values for contact resistance are shown in **Table 2.5**.

$$\frac{R_{Tot}W}{L} = \frac{1}{\mu C_i(V_{GS}-V_T)} + R_C W \frac{1}{L} \; where \; R_{Tot} = \left.\frac{dV_{DS}}{dI_{DS}}\right|_{V_{DS}\to 0V} \quad (4)$$

Table 2.5: Contact resistance (R_C) and width-normalized contact resistance (R_CW) for PFMB-SWNT and PFMB-SWNT-**EP** tested in p-type conditions in air and n-type conditions in vacuum.

	PFMB-SWNT		PFMB-SWNT-**EP**	
	P-type (Air)	N-type (Vac)	P-type (Air)	N-type (Vac)
R_C (Ω)	7382	156807	5975	88010
R_CW (Ω cm)	1476	31361	1195	17602

2.8 References

(1) Avouris, P.; Chen, Z.; Perebeinos, V. Carbon-Based Electronics. *Nat. Nanotechnol.* **2007**, *2*, 605–615.

(2) Torsi, L.; Magliulo, M.; Manoli, K.; Palazzo, G. Organic Field-Effect Transistor Sensors: A Tutorial Review. *Chem. Soc. Rev.* **2013**, *42*, 8612–8628.

(3) Heitzer, H. M.; Marks, T. J.; Ratner, M. A. Molecular Donor−Bridge−Acceptor Strategies for High-Capacitance Organic Dielectric Materials. *J. Am. Chem. Soc.* **2015**, *137*, 7189–7196.

(4) Cicoira, F.; Coppedé, N.; Iannotta, S.; Martel, R. Ambipolar Copper Phthalocyanine Transistors with Carbon Nanotube Array Electrodes. *Appl. Phys. Lett.* **2011**, *98*, 183303.

(5) Schnorr, J. M.; Swager, T. M. Emerging Applications of Carbon Nanotubes. *Chem. Mater.* **2011**, *23*, 646–657.

(6) Yamazaki, S.; Hamada, T.; Tomatsu, K.; Ueda, Y.; Nagase, T.; Kobayashi, T.; Murakami, S.; Matsukawa, K.; Naito, H. Electrical Characteristics of Polymer Field-Effect Transistors with Poly(Methylsilsesquioxane) Gate Dielectrics on Plastic Substrates. *Thin Solid Films* **2008**, *517*, 1343–1345.

(7) Iijima, S. Helical Microtubules of Graphitic Carbon. *Nature* **1991**, *354*, 56–58.

(8) Iijima, S.; Ichihashi, T. Single-Shell Carbon Nanotubes of 1-nm Diameter. *Nature* **1993**, *363*, 603–605.

(9) Brady, G. J.; Way, A. J.; Safron, N. S.; Evensen, H. T.; Gopalan, P.; Arnold, M. S. Quasi-Ballistic Carbon Nanotube Array Transistors with Current Density Exceeding Si and GaAs. *Sci. Adv.* **2016**, *2*, e1601240.

(10) Yu, M.-F.; Files, B. S.; Arepalli, S.; Ruoff, R. S. Tensile Loading of Ropes of Single Wall Carbon Nanotubes and Their Mechanical Properties. *Phys. Rev. Lett.* **2000**, *84*, 5552–5555.

(11) Terrones, M. Science and Technology of the Twenty-First Century: Synthesis, Properties, and Applications of Carbon Nanotubes. *Annu. Rev. Mater. Res.* **2003**, *33*, 419–501.

(12) Kataura, H.; Kumazawa, Y.; Maniwa, Y.; Umezu, I.; Suzuki, S.; Ohtsuka, Y.; Achiba, Y. Optical Properties of Single-Wall Carbon Nanotubes. *Synth. Met.* **1999**, *103*, 2555–2558.

(13) Salim, T.; Lee, H.-W.; Wong, L. H.; Oh, J. H.; Bao, Z.; Lam, Y. M. Semiconducting Carbon Nanotubes for Improved Efficiency and Thermal Stability of Polymer-Fullerene Solar Cells. *Adv. Funct. Mater.* **2016**, *26*, 51–65.

(14) Li, Z.; Ding, J.; Guo, C.; Lefebvre, J.; Malenfant, P. R. L. Decomposable S-Tetrazine Copolymer Enables Single-Walled Carbon Nanotube Thin Film Transistors and Sensors with Improved Sensitivity. *Adv. Funct. Mater.* **2018**, *28*, 1705568.

(15) Yoon, B.; Liu, S. F.; Swager, T. M. Surface-Anchored Poly(4-Vinylpyridine)-Single-Walled Carbon Nanotube-Metal Composites for Gas Detection. *Chem. Mater.* **2016**, *28*, 5916–5924.

(16) Muguruma, H.; Hoshino, T.; Nowaki, K. Electronically Type-Sorted Carbon Nanotube-Based Electrochemical Biosensors with Glucose Oxidase and Dehydrogenase. *ACS Appl. Mater. Interfaces* **2015**, *7*, 584–592.

(17) Diao, S.; Hong, G.; Antaris, A. L.; Blackburn, J. L.; Cheng, K.; Cheng, Z.; Dai, H. Biological Imaging without Autofluorescence in the Second Near-Infrared Region. *Nano Res.* **2015**, *8*, 3027–3034.

(18) Cao, C.; Andrews, J. B.; Franklin, A. D. Completely Printed, Flexible, Stable, and Hysteresis-Free Carbon Nanotube Thin-Film Transistors via Aerosol Jet Printing. *Adv. Electron. Mater.* **2017**, *3*, 1700057.

(19) Chortos, A.; Zhu, C.; Oh, J. Y.; Yan, X.; Pochorovski, I.; To, J. W. F.; Liu, N.; Kraft, U.; Murmann, B.; Bao, Z. Investigating Limiting Factors in Stretchable All-Carbon Transistors for Reliable Stretchable Electronics. *ACS Nano* **2017**, *11*, 7925–7937.

(20) Saito, R.; Fujita, M.; Dresselhaus, G.; Dresselhaus, M. S. Electronic Structure of Chiral Graphene Tubules. *Appl. Phys. Lett.* **1992**, *60*, 2204–2206.

(21) Kang, S. J.; Kocabas, C.; Ozel, T.; Shim, M.; Pimparkar, N.; Alam, M. A.; Rotkin, S. V.; Rogers, J. A. High-Performance Electronics Using Dense, Perfectly Aligned Arrays of Single-Walled Carbon Nanotubes. *Nat. Nanotechnol.* **2007**, *2*, 230–236.

(22) Kocabas, C.; Pimparkar, N.; Yesilyurt, O.; Kang, S. J.; Alam, M. A.; Rogers, J. A. Experimental and Theoretical Studies of Transport Through Large Scale, Partially Aligned Arrays of Single-Walled Carbon Nanotubes in Thin Film Type Transistors. *Nano Lett.* **2007**, *7*, 1195–1202.

(23) Green, A. A.; Hersam, M. C. Nearly Single-Chirality Single-Walled Carbon Nanotubes Produced via Orthogonal Iterative Density Gradient Ultracentrifugation. *Adv. Mater.* **2011**, *23*, 2185–2190.

(24) Seo, J.-W. T.; Yoder, N. L.; Shastry, T. A.; Humes, J. J.; Johns, J. E.; Green, A. A.; Hersam, M. C. Diameter Refinement of Semiconducting Arc Discharge Single-Walled Carbon Nanotubes via Density Gradient Ultracentrifugation. *J. Phys. Chem. Lett.* **2013**, *4*, 2805–2810.

(25) Zheng, M.; Jagota, A.; Semke, E. D.; Diner, B. A.; McLean, R. S.; Lustig, S. R.; Richardson, R. E.; Tassi, N. G. DNA-Assisted Dispersion and Separation of Carbon Nanotubes. *Nat. Mater.* **2003**, *2*, 338–342.

(26) Tanaka, T.; Jin, H.; Miyata, Y.; Fujii, S.; Suga, H.; Naitoh, Y.; Minari, T.; Miyadera, T.; Tsukagoshi, K.; Kataura, H. Simple and Scalable Gel-Based Separation of Metallic and Semiconducting Carbon Nanotubes. *Nano Lett.* **2009**, *9*, 1497–1500.

(27) Nish, A.; Hwang, J.-Y.; Doig, J.; Nicholas, R. J. Highly Selective Dispersion of Single-Walled Carbon Nanotubes Using Aromatic Polymers. *Nat. Nanotechnol.* **2007**, *2*, 640–646.

(28) Li, Z.; Ding, J.; Lefebvre, J.; Malenfant, P. R. L. Dopant-Modulated Conjugated Polymer Enrichment of Semiconducting SWCNTs. *ACS Omega* **2018**, *3*, 3413–3419.

(29) Mistry, K. S.; Larsen, B. A.; Blackburn, J. L. High-Yield Dispersions of Large-Diameter Semiconducting Single-Walled Carbon Nanotubes with Tunable Narrow Chirality Distributions. *ACS Nano* **2013**, *7*, 2231–2239.

(30) Fong, D.; Adronov, A. Recent Developments in the Selective Dispersion of Single-Walled Carbon Nanotubes Using Conjugated Polymers. *Chem. Sci.* **2017**, *8*, 7292–7305.

(31) Wang, H.; Hsieh, B.; Jiménez-Osés, G.; Liu, P.; Tassone, C. J.; Diao, Y.; Lei, T.; Houk, K. N.; Bao, Z. Solvent Effects on Polymer Sorting of Carbon Nanotubes with Applications in Printed Electronics. *Small* **2015**, *11*, 126–133.

(32) Fong, D.; Bodnaryk, W. J.; Rice, N. A.; Saem, S.; Moran-Mirabal, J. M.; Adronov, A. Influence of Polymer Electronics on Selective Dispersion of Single-Walled Carbon Nanotubes. *Chem. Eur. J.* **2016**, *22*, 14560–14566.

(33) Hwang, J.-Y.; Nish, A.; Doig, J.; Douven, S.; Chen, C.-W.; Chen, L.-C.; Nicholas, R. J. Polymer Structure and Solvent Effects on the Selective Dispersion of Single-Walled Carbon Nanotubes. *J. Am. Chem. Soc.* **2008**, *130*, 3543–3553.

(34) Jakubka, F.; Schießl, S. P.; Martin, S.; Englert, J. M.; Hauke, F.; Hirsch, A.; Zaumseil, J. Effect of Polymer Molecular Weight and Solution Parameters on Selective Dispersion of Single-Walled Carbon Nanotubes. *ACS Macro Lett.* **2012**, *1*, 815–819.

(35) Gomulya, W.; Rios, J. M. S.; Derenskyi, V.; Bisri, S. Z.; Jung, S.; Fritsch, M.; Allard, S.; Scherf, U.; dos Santos, M. C.; Loi, M. A. Effect of Temperature on the Selection of Semiconducting Single Walled Carbon Nanotubes Using Poly(3-Dodecylthiophene-2,5-Diyl). *Carbon* **2015**, *84*, 66–73.

(36) Imin, P.; Cheng, F.; Adronov, A. Supramolecular Complexes of Single Walled Carbon Nanotubes with Conjugated Polymers. *Polym. Chem.* **2011**, *2*, 411–416.

(37) Ding, J.; Li, Z.; Lefebvre, J.; Cheng, F.; Dubey, G.; Zou, S.; Finnie, P.; Hrdina, A.; Scoles, L.; Lopinski, G. P.; Kingston, C. T.; Simard, B.; Malenfant, P. R. L. Enrichment of Large-Diameter Semiconducting SWCNTs by Polyfluorene Extraction for High Network Density Thin Film Transistors. *Nanoscale* **2014**, *6*, 2328–2339.

(38) Gomulya, W.; Costanzo, G. D.; de Carvalho, E. J. F.; Bisri, S. Z.; Derenskyi, V.; Fritsch, M.; Fröhlich, N.; Allard, S.; Gordiichuk, P.; Herrmann, A.; Marrink, S. J.; dos Santos, M. C.; Scherf, U.; Loi, M. A. Semiconducting Single-Walled Carbon Nanotubes on Demand by Polymer Wrapping. *Adv. Mater.* **2013**, *25*, 2948–2956.

(39) Wang, H.; Koleilat, G. I.; Liu, P.; Jiménez-Osés, G.; Lai, Y.-C.; Vosgueritchian, M.; Fang, Y.; Park, S.; Houk, K. N.; Bao, Z. High-Yield Sorting of Small-Diameter Carbon Nanotubes for Solar Cells and Transistors. *ACS Nano* **2014**, *8*, 2609–2617.

(40) Berton, N.; Lemasson, F.; Tittmann, J.; Stürzl, N.; Hennrich, F.; Kappes, M. M.; Mayor, M. Copolymer-Controlled Diameter-Selective Dispersion of Semiconducting Single-Walled Carbon Nanotubes. *Chem. Mater.* **2011**, *23*, 2237–2249.

(41) Lemasson, F. A.; Strunk, T.; Gerstel, P.; Hennrich, F.; Lebedkin, S.; Barner-Kowollik, C.; Wenzel, W.; Kappes, M. M.; Mayor, M. Selective Dispersion of Single-Walled Carbon Nanotubes with Specific Chiral Indices by Poly(N-Decyl-2,7-Carbazole). *J. Am. Chem. Soc.* **2011**, *133*, 652–655.

(42) Rice, N. A.; Subrahmanyam, A. V.; Laengert, S. E.; Adronov, A. The Effect of Molecular Weight on the Separation of Semiconducting Single-Walled Carbon Nanotubes Using Poly(2,7-Carbazole)s. *J. Polym. Sci. Part A Polym. Chem.* **2015**, *53*, 2510–2516.

(43) Rice, N. A.; Adronov, A. Selective Interactions of a High-Molecular-Weight Polycarbazole with Different Commercial Nanotube Samples. *J. Polym. Sci. Part A Polym. Chem.* **2014**, *52*, 2738–2747.

(44) Wang, H.; Mei, J.; Liu, P.; Schmidt, K.; Jiménez-Osés, G.; Osuna, S.; Fang, L.; Tassone, C. J.; Zoombelt, A. P.; Sokolov, A. N.; Houk, K. N.; Toney, M. F.; Bao, Z. Scalable and Selective Dispersion of Semiconducting Arc-Discharged Carbon Nanotubes by Dithiafulvalene/Thiophene Copolymers for Thin Film Transistors. *ACS Nano* **2013**, *7*, 2659–2668.

(45) Rice, N. A.; Bodnaryk, W. J.; Mirka, B.; Melville, O. A.; Adronov, A.; Lessard, B. H. Polycarbazole-Sorted Semiconducting Single-Walled Carbon Nanotubes for Incorporation into Organic Thin Film Transistors. *Adv. Electron. Mater.* **2019**, *5*, 1800539.

(46) Ouyang, J.; Ding, J.; Lefebvre, J.; Li, Z.; Guo, C.; Kell, A. J.; Malenfant, P. R. L. Sorting of Semiconducting Single-Walled Carbon Nanotubes in Polar Solvents with an Amphiphilic Conjugated Polymer Provides General Guidelines for Enrichment. *ACS Nano* **2018**, *12*, 1910–1919.

(47) Brady, G. J.; Joo, Y.; Wu, M.-Y.; Shea, M. J.; Gopalan, P.; Arnold, M. S. Polyfluorene-Sorted, Carbon Nanotube Array Field-Effect Transistors with Increased Current Density and High On/Off Ratio. *ACS Nano* **2014**, *8*, 11614–11621.

(48) Park, S.; Pitner, G.; Giri, G.; Koo, J. H.; Park, J.; Kim, K.; Wang, H.; Sinclair, R.; Wong, H. S. P.; Bao, Z. Large-Area Assembly of Densely Aligned Single-Walled Carbon Nanotubes Using Solution Shearing and Their Application to Field-Effect Transistors. *Adv. Mater.* **2015**, *27*, 2656–2662.

(49) Noh, J.; Jung, M.; Jung, K.; Lee, G.; Lim, S.; Kim, D.; Kim, S.; Tour, J. M.; Cho, G. Integrable Single Walled Carbon Nanotube (SWNT) Network Based Thin Film Transistors Using Roll-to-Roll Gravure and Inkjet. *Org. Electron.* **2011**, *12*, 2185–2191.

(50) Homenick, C. M.; James, R.; Lopinski, G. P.; Dunford, J.; Sun, J.; Park, H.; Jung, Y.; Cho, G.; Malenfant, P. R. L. Fully Printed and Encapsulated SWCNT-Based Thin Film Transistors via a Combination of R2R Gravure and Inkjet Printing. *ACS Appl. Mater. Interfaces* **2016**, *8*, 27900–27910.

(51) Tulevski, G. S.; Franklin, A. D.; Frank, D.; Lobez, J. M.; Cao, Q.; Park, H.; Afzali, A.; Han, S.; Hannon, J. B.; Haensch, W. Toward High-Performance Digital Logic Technology with Carbon Nanotubes. *ACS Nano* **2014**, *8*, 8730–8745.

(52) Zhou, X.; Park, J.-Y.; Huang, S.; Liu, J.; McEuen, P. L. Band Structure, Phonon Scattering, and the Performance Limit of Single-Walled Carbon Nanotube Transistors. *Phys. Rev. Lett.* **2005**, *95*, 146805.

(53) Wang, H.; Cobb, B.; Van Breemen, A.; Gelinck, G.; Bao, Z. Highly Stable Carbon Nanotube Top-Gate Transistors with Tunable Threshold Voltage. *Adv. Mater.* **2014**, *26*, 4588–4593.

(54) Joo, Y.; Brady, G. J.; Kanimozhi, C.; Ko, J.; Shea, M. J.; Strand, M. T.; Arnold, M. S.; Gopalan, P. Polymer-Free Electronic-Grade Aligned Semiconducting Carbon Nanotube Array. *ACS Appl. Mater. Interfaces* **2017**, *9*, 28859–28867.

(55) Joo, Y.; Brady, G. J.; Arnold, M. S.; Gopalan, P. Dose-Controlled, Floating Evaporative Self-Assembly and Alignment of Semiconducting Carbon Nanotubes from Organic Solvents. *Langmuir* **2014**, *30*, 3460–3466.

(56) Schneider, S.; Brohmann, M.; Lorenz, R.; Hofstetter, Y. J.; Rother, M.; Sauter, E.; Zharnikov, M.; Vaynzof, Y.; Himmel, H. J.; Zaumseil, J. Efficient n-Doping and Hole Blocking in Single-Walled Carbon Nanotube Transistors with 1,2,4,5-Tetrakis(tetramethylguanidino)benzene. *ACS Nano* **2018**, *12*, 5895–5902.

(57) Rice, N. A.; Subrahmanyam, A. V.; Coleman, B. R.; Adronov, A. Effect of Induction on the Dispersion of Semiconducting and Metallic Single-Walled Carbon Nanotubes Using Conjugated Polymers. *Macromolecules* **2015**, *48*, 5155–5161.

(58) Itkis, M. E.; Perea, D. E.; Jung, R.; Niyogi, S.; Haddon, R. C. Comparison of Analytical Techniques for Purity Evaluation of Single-Walled Carbon Nanotubes. *J. Am. Chem. Soc.* **2005**, *127*, 3439–3448.

(59) Pimenta, M. A.; Marucci, A.; Empedocles, S. A.; Bawendi, M. G.; Hanlon, E. B.; Rao, A. M.; Eklund, P. C.; Smalley, R. E.; Dresselhaus, G.; Dresselhaus, M. S. Raman Modes of Metallic Carbon Nanotubes. *Phys. Rev. B* **1998**, *58*, 16016.

(60) Li, Z.; Ding, J.; Finnie, P.; Lefebvre, J.; Cheng, F.; Kingston, C. T.; Malenfant, P. R. L. Raman Microscopy Mapping for the Purity Assessment of Chirality Enriched Carbon Nanotube Networks in Thin-Film Transistors. *Nano Res.* **2015**, *8*, 2179–2187.

(61) O'Connell, M. J.; Sivaram, S.; Doorn, S. K. Near-Infrared Resonance Raman Excitation Profile Studies of Single-Walled Carbon Nanotube Intertube Interactions: A Direct Comparison of Bundled and Individually Dispersed HiPco Nanotubes. *Phys. Rev. B* **2004**, *69*, 235415.

(62) Brown, S. D. M.; Jorio, A.; Corio, P.; Dresselhaus, M. S.; Dresselhaus, G.; Saito, R.; Kneipp, K. Origin of the Breit-Wigner-Fano Lineshape of the Tangential G-Band Feature of Metallic Carbon Nanotubes. *Phys. Rev. B* **2001**, *63*, 155414.

(63) Jo, G.; Maeng, J.; Kim, T.-W.; Hong, W.-K.; Choi, B.-S.; Lee, T. Channel-Length and Gate-Bias Dependence of Contact Resistance and Mobility for In_2O_3 Nanowire Field Effect Transistors. *J. Appl. Phys.* **2007**, *102*, 084508.

(64) Schießl, S. P.; Fröhlich, N.; Held, M.; Gannott, F.; Schweiger, M.; Forster, M.; Scherf, U.; Zaumseil, J. Polymer-Sorted Semiconducting Carbon Nanotube Networks for High-Performance Ambipolar Field-Effect Transistors. *ACS Appl. Mater. Interfaces* **2015**, *7*, 682–689.

(65) Heinze, S.; Tersoff, J.; Martel, R.; Derycke, V.; Appenzeller, J.; Avouris, P. Carbon Nanotubes as Schottky Barrier Transistors. *Phys. Rev. Lett.* **2002**, *89*, 106801.

(66) Aguirre, C. M.; Levesque, P. L.; Paillet, M.; Lapointe, F.; St-Antoine, B. C.; Desjardins, P.; Martel, R. The Role of the Oxygen/Water Redox Couple in Suppressing Electron Conduction in Field-Effect Transistors. *Adv. Mater.* **2009**, *21*, 3087–3091.

(67) Geier, M. L.; Moudgil, K.; Barlow, S.; Marder, S. R.; Hersam, M. C. Controlled n-Type Doping of Carbon Nanotube Transistors by an Organorhodium Dimer. *Nano Lett.* **2016**, *16*, 4329–4334.

(68) Hur, S.-H.; Yoon, M.-H.; Gaur, A.; Shim, M.; Facchetti, A.; Marks, T. J.; Rogers, J. A. Organic Nanodielectrics for Low Voltage Carbon Nanotube Thin Film Transistors and Complementary Logic Gates. *J. Am. Chem. Soc.* **2005**, *127*, 13808–13809.

(69) Ding, J.; Li, Z.; Lefebvre, J.; Cheng, F.; Dunford, J. L.; Malenfant, P. R. L.; Humes, J.; Kroeger, J. A Hybrid Enrichment Process Combining Conjugated Polymer Extraction and Silica Gel Adsorption for High Purity Semiconducting Single-Walled Carbon Nanotubes (SWCNT). *Nanoscale* **2015**, *7*, 15741–15747.

(70) Rother, M.; Brohmann, M.; Yang, S.; Grimm, S. B.; Schießl, S. P.; Graf, A.; Zaumseil, J. Aerosol-Jet Printing of Polymer-Sorted (6,5) Carbon Nanotubes for Field-Effect Transistors with High Reproducibility. *Adv. Electron. Mater.* **2017**, *3*, 1700080.

(71) Derenskyi, V.; Gomulya, W.; Talsma, W.; Salazar-Rios, J. M.; Fritsch, M.; Nirmalraj, P.; Riel, H.; Allard, S.; Scherf, U.; Loi, M. A. On-Chip Chemical Self-Assembly of Semiconducting Single-Walled Carbon Nanotubes (SWNTs): Toward Robust and Scale Invariant SWNTs Transistors. *Adv. Mater.* **2017**, *29*, 1606757.

(72) Lee, M.-H.; Lee, S.-H.; Kim, J.; Lee, S. Y.; Lim, D.-H.; Hwang, K.; Hwang, H.; Jung, Y. C.; Noh, Y.-Y.; Kim, D.-Y. Selective Sorting of Semiconducting Single-Walled Carbon Nanotubes Using Thienylenevinylene-Based Conjugated Polymers with High Alkyl Side-Chain Density. *Carbon* **2017**, *125*, 571–581.

(73) Kim, W.; Javey, A.; Vermesh, O.; Wang, Q.; Li, Y.; Dai, H. Hysteresis Caused by Water Molecules in Carbon Nanotube Field-Effect Transistors. *Nano Lett.* **2003**, *3*, 193–198.

(74) Ito, Y.; Virkar, A. A.; Mannsfeld, S.; Oh, J. H.; Toney, M.; Locklin, J.; Bao, Z. Crystalline Ultrasmooth Self-Assembled Monolayers of Alkylsilanes for Organic Field-Effect Transistors. *J. Am. Chem. Soc.* **2009**, *131*, 9396–9404.

(75) Mcgill, S. A.; Rao, S. G.; Manandhar, P.; Xiong, P.; Hong, S. High-Performance, Hysteresis-Free Carbon Nanotube Field-Effect Transistors via Directed Assembly. *Appl. Phys. Lett.* **2006**, *89*, 163123.

(76) Melville, O. A.; Rice, N. A.; Therrien, I.; Lessard, B. H. Organic Thin-Film Transistors Incorporating a Commercial Pigment (Hostasol Red GG) as a Low-Cost Semiconductor. *Dye. Pigment.* **2018**, *149*, 449–455.

(77) Brixi, S.; Melville, O. A.; Boileau, N. T.; Lessard, B. H. The Influence of Air and Temperature on the Performance of PBDB-T and P3HT in Organic Thin Film Transistors. *J. Mater. Chem. C* **2018**, *6*, 11972-11979.

(78) Martel, R.; Derycke, V.; Lavoie, C.; Appenzeller, J.; Chan, K. K.; Tersoff, J.; Avouris, P. Ambipolar Electrical Transport in Semiconducting Single-Wall Carbon Nanotubes. *Phys. Rev. Lett.* **2001**, *87*, 256805.

(79) Fong, D.; Adronov, A. Investigation of Hybrid Conjugated/Nonconjugated Polymers for Sorting of Single-Walled Carbon Nanotubes. *Macromolecules* **2017**, *50*, 8002–8009.

(80) Fong, D.; Andrews, G. M.; McNelles, S. A.; Adronov, A. Decoration of Polyfluorene-Wrapped Carbon Nanotube Thin Films *via* Strain-Promoted Azide-Alkyne Cycloaddition. *Polym. Chem.* **2018**, *9*, 4460–4467.

(81) Sangwan, V. K.; Behnam, A.; Ballarotto, V. W.; Fuhrer, M. S.; Ural, A.; Williams, E. D. Optimizing Transistor Performance of Percolating Carbon Nanotube Networks. *Appl. Phys. Lett.* **2010**, *97*, 043111.

Chapter 3: Excess Polymer in Single-Walled Carbon Nanotube Thin-Film Transistors: Its Removal Prior to Fabrication Is Unnecessary

This study was published in the journal "ACS Nano": Mirka, B.; Rice, N. A.; Williams, P.; Tousignant, M. N.; Boileau, N. T.; Bodnaryk, W. J.; Fong, D.; Adronov, A.; Lessard, B. H. Excess Polymer in Single-Walled Carbon Nanotube Thin-Film Transistors: Its Removal Prior to Fabrication Is Unnecessary. ACS Nano 2021, 15, 8252–8266.

Context

Our previous study (**Chapter 2**) showed interesting results regarding the necessity of a filtration step in the conjugated polymer extraction procedure. However, we could not make firm conclusions from **Chapter 2** about the necessity of a filtration step in conjugated polymer extraction, and more research was required. We believed that investigating the necessity of a filtration step was important to the field because eliminating the step could remove a bottleneck. This study utilized two copolymers that we had demonstrated previously to sort and disperse semiconducting single-walled carbon nanotubes. We fabricated thin-film transistors using dispersions with different degrees of excess polymer. Furthermore, we utilized Raman spectroscopy and atomic force microscopy to characterize the film morphology of the polymer-SWNT films.

Contributions

Dr. Rice and I contributed to this work equally. Prof. Lessard, Dr. Rice, and I planned the research required for this study. The copolymers PCF and PFMB were synthesized by Dr. Bodnaryk and Dr. Fong, respectively. I prepared the polymer-SWNT dispersions, and Dr. Rice and I prepared dispersions with different polymer conditions. Dr. Rice and I contributed equally to thin-film transistor fabrication and characterization, Raman spectroscopy, Raman mapping, atomic force microscopy, and data analysis. Our colleague, Mr. Williams, designed the program used to analyze our atomic force microscopy images. Dr. Rice and I assisted Mr. Williams in the necessary program adjustments. Dr. Rice and I prepared the manuscript with input from Dr. Bodnaryk, Dr. Fong, Prof. Lessard, and Prof. Adronov. Mr. Boileau helped assemble the auto

tester set up, and Mr. Tousignant fabricated metal-insulator-metal capacitors to determine SiO_2 thickness.

3.1 Abstract

Ultrapure semiconducting single-walled carbon nanotube (sc-SWNT) dispersions produced through conjugated polymer sorting are ideal candidates for the fabrication of solution-processed organic electronic devices on a commercial scale. Protocols for sorting and dispersing ultrapure sc-SWNTs with conjugated polymers for thin-film transistor (TFT) applications have been well refined. Conventional wisdom dictates that the removal of excess unbound polymer through filtration or centrifugation is necessary to produce high-performance TFTs. However, this is time-consuming, wasteful, and resource-intensive. This report challenges this paradigm and demonstrates that excess unbound polymer during semiconductor film fabrication is not necessarily detrimental to device performance. Over 1200 TFT devices were fabricated from 30 unique polymer-sorted SWNT dispersions, prepared using two different alternating co-polymers. Detailed Raman spectroscopy, X-ray photoelectron spectroscopy (XPS) and atomic force microscopy (AFM) studies of the random-network semiconductor films demonstrate that a simple solvent rinse during TFT fabrication was sufficient to remove unbound polymer from the sc-SWNT films, thus eliminating laborious polymer removal before TFT fabrication. Furthermore, below a threshold polymer concentration, the presence of excess polymer during fabrication did not significantly impede TFT performance. Preeminent performance was achieved for devices prepared from native polymer-sorted SWNT dispersions containing the “original” amount of excess unbound polymer (immediately following enrichment). Lastly, we developed an open-source Machine Learning algorithm to quantitatively analyze AFM images of SWNT films for surface coverage, number of tubes, and tube alignment.

3.2 Introduction

Semiconducting single-walled carbon nanotubes (sc-SWNTs) are prospective nanomaterials for flexible, inexpensive, and solution-processable electronics. Within the past two decades, several techniques for sorting sc-SWNTs from raw heterogeneous materials have been developed. Conjugated polymer extraction has emerged as one of the most promising methodologies for facilitating both selective discrimination and dispersion of sc-SWNTs into organic solvents.[1-5] Protocols to prepare conjugated polymer-sorted SWNT dispersions are relatively quick and inexpensive in comparison to other sorting methodologies, utilizing techniques that can be easily translated from the benchtop to commercial scale. Polymer structure is crucial and, if chosen properly, can consistently yield sc-SWNT dispersions with purities in excess of 99.9 %.[6] These supramolecular polymer-SWNT complexes have been successfully incorporated into thin-film transistors (TFTs),[7-9] organic photovoltaic devices (OPVs),[10,11] and integrated circuits.[6,12-15] Throughout the past decade, researchers have made impressive gains in TFTs with semiconducting layers comprised of polymer-sorted sc-SWNTs, with devices consistently outperforming organic small-molecule and polymer semiconductors; polymer-sorted SWNT TFTs with performances that rival inorganic semiconductors have also been reported.[16] Many reports focus on improving TFT fabrication processes, with high field-effect mobilities (μ) achieved for both random[17] and aligned[16,18-20] SWNT networks, as well as devices with low operating voltages[6,12,21] and negligible hysteresis.[22,23] Furthermore, solution-processable polymer-sorted SWNT composites are ideal materials for flexible and printed electronics, with the potential for integration into commercial printing processes, including aerosol jet printing,[22,24,25] gravure printing,[26] or inkjet printing.[26,27] However, the realization of solution-based, inexpensive SWNT TFTs in commercial applications will require a trade-off between printing compatibility and performance. Each step from SWNT sorting and dispersion to TFT fabrication requires optimization for both device performance and commercial scalability.

Dispersing sc-SWNTs with conjugated polymers involves three general steps: (1) dispersion and sorting of the bulk SWNT material, (2) removal of impurities, and (3) removal of unbound excess polymer through filtration or centrifugation. The term "excess unbound polymer" refers to polymer that is not adsorbed to the SWNT and remains dissolved in solution. If the correct polymeric structure is chosen, the first two steps are relatively facile, generating high-quality sc-SWNT-enriched dispersions after several hours. The final step, however, is prohibitively time-

consuming and wasteful, potentially requiring a few weeks and consuming several litres of solvents on a laboratory scale. However, this step is assumed to be essential for preparing high-performance TFTs. It is widely accepted that excess wrapping polymer impedes device performance due to a Schottky barrier at the polymer-electrode interface and the poor electrical conductivity of the polymer. Consequently, several recent reports have examined complete removal of conjugated polymer post semiconductor film formation to yield bare sc-SWNTs, through the incorporation of degradable or reversible polymer linkages such as hydrogen bonding or acid-cleavable imines, or functionalities susceptible to metal chelation.[28-30]

While removal of excess wrapping polymer prior to device fabrication can theoretically improve device performance, it is detrimental to producing dispersions amenable to commercial printing processes. A recent report by Malenfant and co-workers exploring fully-printed TFTs prepared from a commercially available SWNT ink found that addition of excess wrapping polymer to the ink prior to deposition did not result in statistically significant differences in μ or $I_{ON/OFF}$ ratios.[26] Arias *et al.* compared spray-coated SWNT thin-films in OPVs with and without excess wrapping polymer and found that removal of unbound polymer prior to film deposition increased exciton trapping and limited long-range exciton transport due to increased SWNT bundling.[31] Neither of these reports included a comprehensive investigation into removal of unbound excess polymer following deposition of the semiconductor film or a thorough analysis of the impact on other important TFT parameters, including threshold voltage (V_T) and hysteresis (H).

The necessity of excess unbound polymer removal before SWNT TFT fabrication remains a strongly-held but under-challenged belief. In fact, incorporation of a carrier polymer in small molecule solution-processed organic electronic devices is a common technique for enhancing performance through improved semiconductor film morphology.[32-35] An insulating carrier polymer such as polystyrene is blended with an organic semiconductor (OSC) to promote phase separation during film fabrication. The phase separation can encourage the OSC to arrange into a highly uniform crystalline film at either the dielectric-semiconductor or the semiconductor-air interface, which results in improved μ and $I_{ON/OFF}$ ratios compared to pristine OSC films. This protocol is amenable to commercial-scale solution printing or blade coating techniques.

Herein, we report a systematic investigation into the influence of unbound excess polymer in sc-SWNT dispersions incorporated into random-network bottom-gate top-contact (BGTC) TFTs. We examine TFT performance from dispersions of as-produced polymer-sorted SWNTs (before filtration), after dispersion filtration, as well as after intentional addition of excess wrapping polymer. To confirm the generality of this phenomenon, two different alternating co-polymers were used to prepare ultrapure sc-SWNT dispersions at three different SWNT concentrations. For each SWNT concentration, five different ratios of excess polymer were investigated. The resulting 30 polymer-sorted SWNT dispersions were incorporated into TFTs and analyzed using Raman spectroscopy and atomic force microscopy (AFM) to confirm that below a threshold amount of excess polymer, a simple solvent rinse step during TFT fabrication is sufficient to completely remove excess unbound polymer from the SWNT film. At least 25 replicate TFTs were fabricated and characterized in terms of μ, V_T, $I_{ON/OFF}$ ratios, and H. Our results show that devices prepared from as-produced polymer-sorted SWNT dispersions (with excess unbound polymer present) perform no worse than TFTs prepared after removal of unbound polymer, challenging the notion that excess polymer removal is necessary for fabricating high-performing SWNT TFTs.

3.3 Results and Discussion

Two conjugated polymer scaffolds (**Figure 3.1a**), both previously demonstrated to be highly effective at dispersing sc-SWNTs,[36,37] were utilized in this study. The alternating co-polymers both contain fluorene, which is one of the most common polymer motifs used to disperse sc-SWNTs, particularly for TFT fabrication.[7,9,15,17-19,38] The incorporated co-monomers of carbazole for PCF and 1,4-dimethoxybenzene in PFMB possess different electronic and steric properties, enabling us to ascertain the generality of our findings. Plasma-grown SWNTs were dispersed following previously reported literature protocols[36,37] to prepare PCF-NT and PFMB-NT dispersions, as outlined in **Figure 3.1b** (details provided in the Methods section). A portion of the original as-produced dispersion (**EP**), which contains both polymer-wrapped sc-SWNTs and excess unbound polymer, was isolated before the remainder was filtered to remove all unbound polymer by rinsing with toluene until fluorescence was no longer observed in the filtrate. This rinsing step is not sufficient to displace conjugated polymer that is already bound to the surface of sc-SWNTs. The resultant polymer-sorted SWNT mat was re-suspended in toluene *via* a short

sonication and then centrifuged to remove any un-dispersed aggregates, yielding a dispersion with no excess polymer (**NP**).

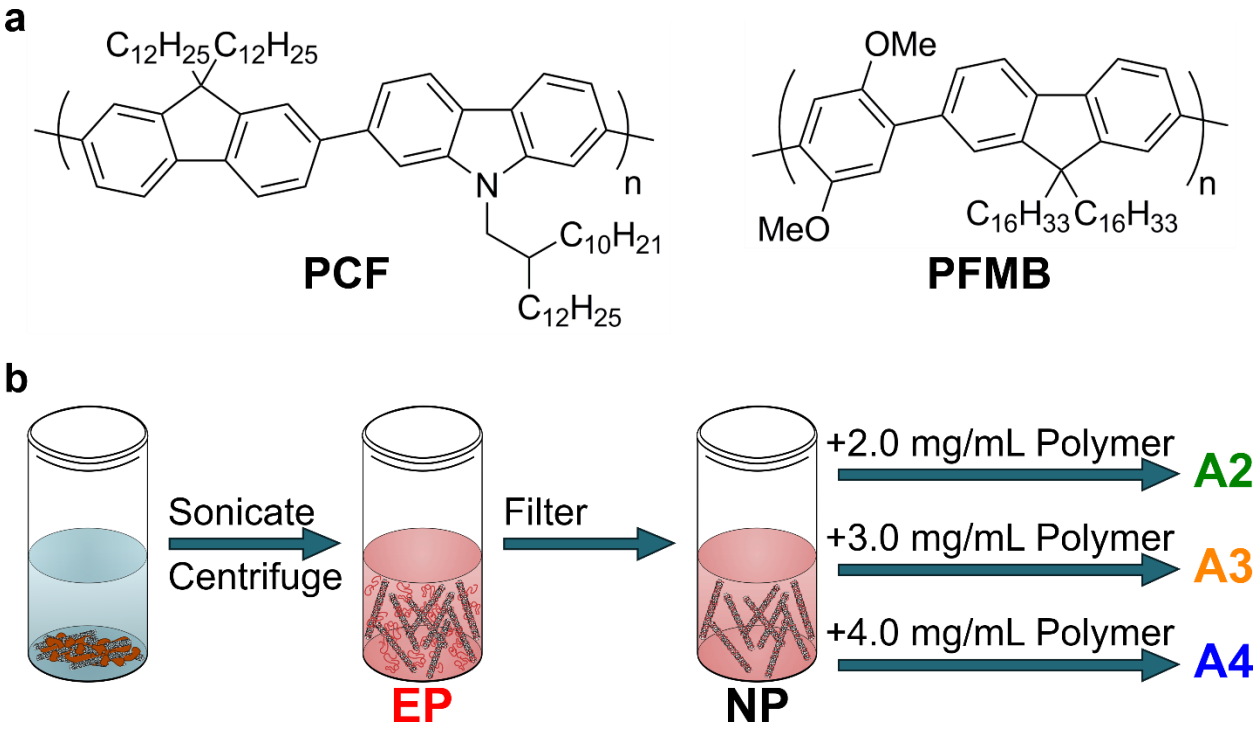

Figure 3.1: (a) Polymer structures for PCF and PFMB and (b) manufacturing process to prepare the polymer-sorted SWNT dispersions evaluated in TFTs. A portion of the original excess polymer (EP) dispersion was filtered to produce the no excess polymer (NP) sample. Controlled amounts of polymer were then re-added to aliquots of the NP dispersion.

For a more comprehensive investigation of the effect of excess polymer on TFT performance, controlled amounts of excess polymer were re-introduced to the **NP** dispersion at three different SWNT concentrations (**Table 3.1**). As SWNT network density in TFTs can drastically alter device performance,[39] it is essential that similar amounts of SWNTs are deposited to determine how excess polymer affects device performance. UV-Vis-NIR absorbance spectroscopy offers the simplest route to control SWNT concentration through indirect quantification of the relative amount of sc-SWNTs present in our samples.[17] The heterogeneous nature of polymer-sorted SWNT dispersions precludes the usage of molar extinction coefficients for direct quantification. **Figure 3.2a** depicts the S_{22} peak heights for PCF-NT-**NP** and PFMB-NT-**NP** samples (full absorbance spectra and ϕ_i calculations are in the Supporting Information, **Figure**

3.8). The peak locations and intensities at ~ 937 nm are closely matched, with a slight bathochromic shift for PCF-NT relative to PFMB-NT. This S_{22} peak was chosen as our concentration control since it does not overlap with the excess polymer absorbance and is thus unaffected by the concentration of excess polymer. **EP** and **NP** dispersion concentrations were adjusted with toluene to match three different values at ~ 937 nm (**Table 3.1** and **Figure 3.2b**), which will be referred to as: Concentrated (c, 2.7 a.u.), Dilution 1 (d1, 1.7 a.u.) and Dilution 2 (d2, 1.2 a.u.). After concentration matching the SWNTs, excess polymer was intentionally reintroduced into aliquots of the **NP** dispersions to yield dispersions with final excess polymer concentrations of 2, 3, and 4 mg/mL, referred to as **A2**, **A3**, and **A4**, respectively (**Figure 3.1b** and **Table 3.1**). This procedure yielded 15 unique SWNT dispersions for each polymer-sorted SWNT system: five different amounts of excess polymer, each at three different SWNT concentrations.

Table 3.1: Summary of sample codes. SWNT and polymer concentrations were adjusted independently for the 15 different dispersions.

		Amount of Excess Polymer				
SWNT Concentration	**Peak at ~ 937 nm**	**Original Dispersion***	**No Polymer†**	**Added 2 mg/mL§**	**Added 3 mg/mL§**	**Added 4 mg/mL§**
Concentrated	2.7	**EP**-c	**NP**-c	**A2**-c	**A3**-c	**A4**-c
Dilution 1	1.7	**EP**-d1	**NP**-d1	**A2**-d1	**A3**-d1	**A4**-d1
Dilution 2	1.2	**EP**-d2	**NP**-d2	**A2**-d2	**A3**-d2	**A4**-d2

**Dispersion was not filtered; contains excess unbound polymer from suspension of sc-SWNTs.*
†Dispersion was filtered to remove excess unbound polymer.
*§Amount of polymer added to an aliquot of the filtered (**NP**) polymer-sorted SWNT dispersion.*

We evaluated and optimized a simple rinsing step to remove unbound polymer from our thin-films using Raman spectroscopy. A significant amount of polymer is present in the **EP** and polymer-added samples, which could be observed visually with strong blue fluorescence from the dispersions when irradiated at 365 nm. Although conjugated polyfluorenes are candidate semiconductors for TFTs, their reported μ are several orders of magnitude lower than polymer-sorted SWNT TFTs.[40-43] Polymer-sorted SWNT thin-films were prepared on Si/SiO_2 wafers following previously reported procedures.[36,37] The SiO_2 dielectric was treated with

octyltrichlorosilane (OTS) to create a hydrophobic surface to facilitate better control during the drop-cast step and to help reduce operational hysteresis in the polymer-sorted SWNT transistors.[36,44] Polymer-sorted SWNT **EP**-c dispersions were drop-casted (0.5 µL) onto the OTS-treated SiO_2 wafers, with the solvent evaporated under ambient conditions to yield a random polymer-wrapped sc-SWNT network. Multiple wafers were prepared and subjected to different rinsing protocols (0 – 4 washes with 1 mL of toluene at a 45º angle). Control samples were prepared from polymer solutions (3 mg/mL in toluene) and rinsed in an identical manner, and all samples were annealed in air at 200 ºC for 1 h.

Raman spectra were collected using an excitation wavelength of 514 nm, as this wavelength is in resonance with sc-SWNTs in our samples and overlaps with the absorbance tail of the conjugated polymers. **Figure 3.2c** shows Raman spectra for PCF and PCF-NT-**EP**-c, while **Figure 3.2d** depicts the same data for PFMB and PFMB-NT-**EP**-c, with full Raman spectra provided in **Figure 3.9a-b**. The black spectra represent pristine polymer films prior to rinsing. PCF exhibits peaks at 1607 and 1627 cm^{-1}, while PFMB has a single peak at 1607 cm^{-1}. These peaks are distinct from the SWNT G_{sc}^{+} and G_{sc}^{-} (below 1600 cm^{-1}), enabling us to probe the polymer and SWNTs simultaneously. Polymer peaks are clearly visible in the as-produced polymer-sorted SWNT **EP**-c (no rinse) Raman spectra but decrease in intensity relative to the SWNT *G*-band with each additional rinsing step. Simultaneously, the strong polymer background fluorescence resulting in the non-zero baseline also decreases dramatically with each successive rinse. After 4 × 1 mL toluene rinses, peaks corresponding to PCF are no longer visible in the PCF-NT-**EP**-c spectra, and the broad fluorescence background is absent. This is corroborated by the absence of peaks and background fluorescence in the neat PCF film after four rinses, indicating complete removal of the polymer from the wafer surface (grey traces). Removal of excess unbound polymer was also confirmed through XPS analysis of the N 1s peak in PCF thin-films (**Figure 3.10**).

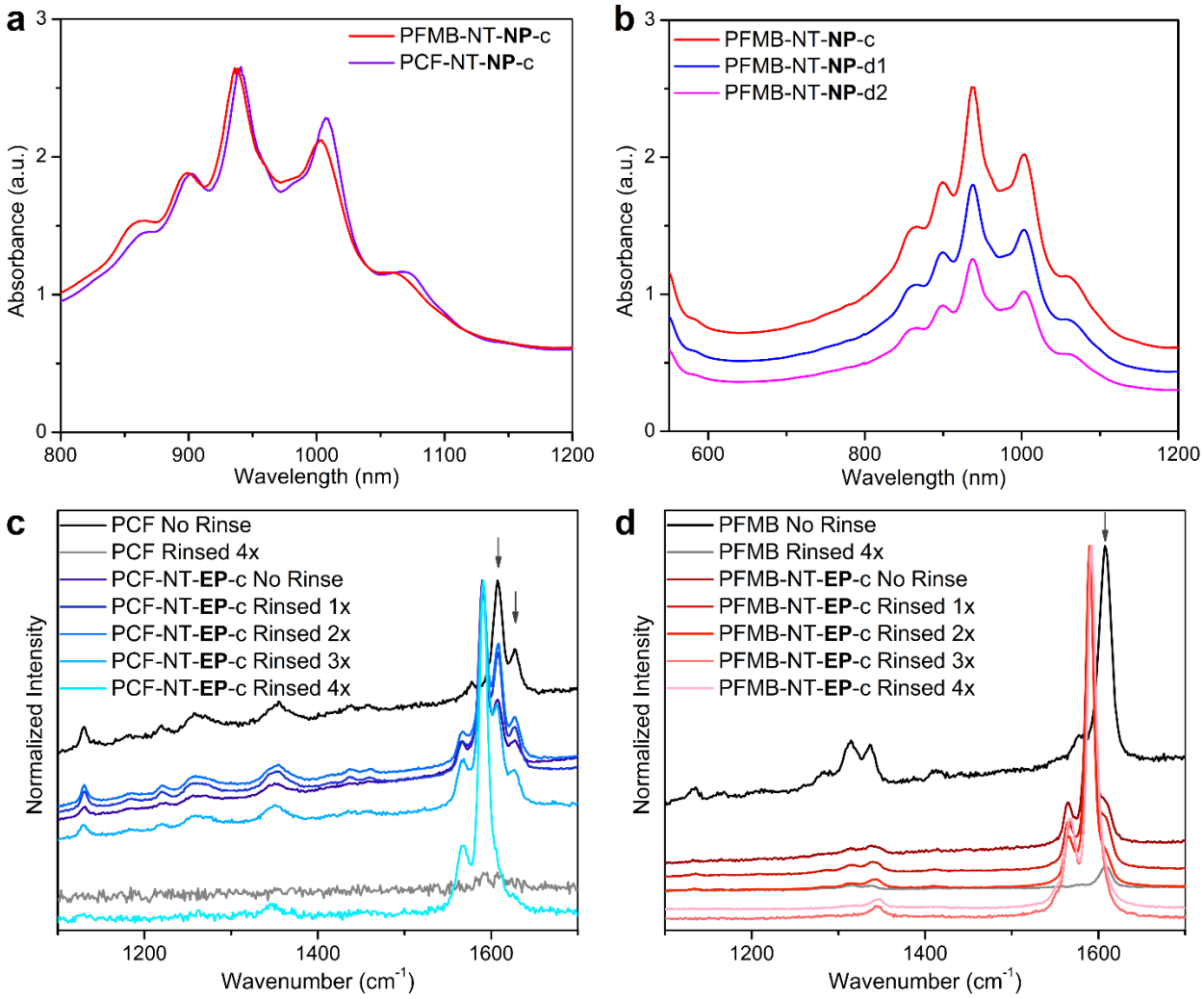

Figure 3.2: Absorption spectra of (a) concentration matching of the S_{22} peaks for PCF-NT-**NP**-c and PFMB-NT-**NP**-c to the peak at ~ 937 nm and (b) PFMB-NT-**NP** at the three different SWNT concentrations. Raman *G*-band spectra (excitation wavelength = 514 nm) of thin-films of (c) PCF-NT-**EP**-c and (d) PFMB-NT-**EP**-c after various toluene rinses. All polymer-sorted SWNT spectra have been normalized to the G_{sc}^{+} SWNT peak. Spectra from neat polymer films of PCF and PFMB are also shown; arrows indicate the location of polymer peaks.

The trend appears identical for PFMB-NT-**EP**-c, with 4 × 1 mL toluene sufficient to remove both the characteristic polymer peaks and fluorescence. However, it should be noted that a small polymer peak was still observed in the PFMB film that had been rinsed 4 × 1 mL with toluene, so it is possible that trace amounts of unbound polymer could still be present in the SWNT film, obscured by the strong *G*-band peak. Most importantly, the SWNT *G*-band is still present in both polymer-sorted SWNT **EP**-c thin-films after rinsing, indicating that SWNTs remain on the

OTS surface while the unbound polymer is washed off. These experiments demonstrate that a simple rinsing step removes nearly all the excess polymer from the drop-casted SWNT films, significantly improving upon the polymer removal step used to produce the filtered **NP**-c materials and obviating the need for time-consuming and resource-intensive filtration or centrifugation (**Figure 3.9c-d**). Our procedure is amenable to established fabrication techniques in the literature, as many SWNT TFT protocols already incorporate a solvent rinse step,[45-48] partly due to an anecdotal belief that residual unbound polymer could be removed. However, our investigation is the first systematic proof that this rinsing step can potentially remove all unbound excess polymer, even from dispersions that have not been filtered or centrifuged. Furthermore, the rinsing protocol outlined may be compatible with large-scale, low-cost roll-to-roll printing systems.

Bottom-gate top-contact (BGTC) TFTs (**Figure 3.3a-b**) were fabricated by drop-casting polymer-sorted SWNT dispersions (0.5 µL per TFT) onto OTS-treated Si/SiO_2 wafers. The solvent was dried under ambient conditions before the surface was rinsed (4 × 1 mL of toluene at a 45º angle), followed by annealing in air at 200 ºC for 1 hr. Gold source-drain electrodes (50 nm) were deposited using physical vapour deposition (PVD) through a shadow mask to yield 20 individual transistors per wafer. Duplicate wafers were prepared for each condition, with at least 25 unique TFTs per condition characterized (**Table 3.3**); all devices were characterized under ambient conditions. Representative output curves for PCF-NT-**NP**-d1 and PCF-NT-**EP**-d1 are shown in **Figure 3.3c-d**, respectively, with a comprehensive compilation of output curves for all other samples in **Figure 3.11** and **Figure 3.12**. All dispersions resulted in field-effect behaviour, with clearly defined linear and saturation regions and linear behaviour at the origin, indicating ohmic contacts.[49] Further discussion of the relationship between the presence of residual unbound polymer and contact resistance is not possible, as the long channel lengths (30 µm) of the TFTs means that channel resistance is dominant. **Figure 3.3e-f** show the transfer curves for all the devices fabricated for **EP**-d1, with 31 unique TFTs for PCF-NT and 29 TFTs for PFMB-NT; all transistors for both conditions have both on- and off-currents that are consistently within one order of magnitude. Representative transfer curves for all other conditions are shown in **Figure 3.13** and **Figure 3.14**.

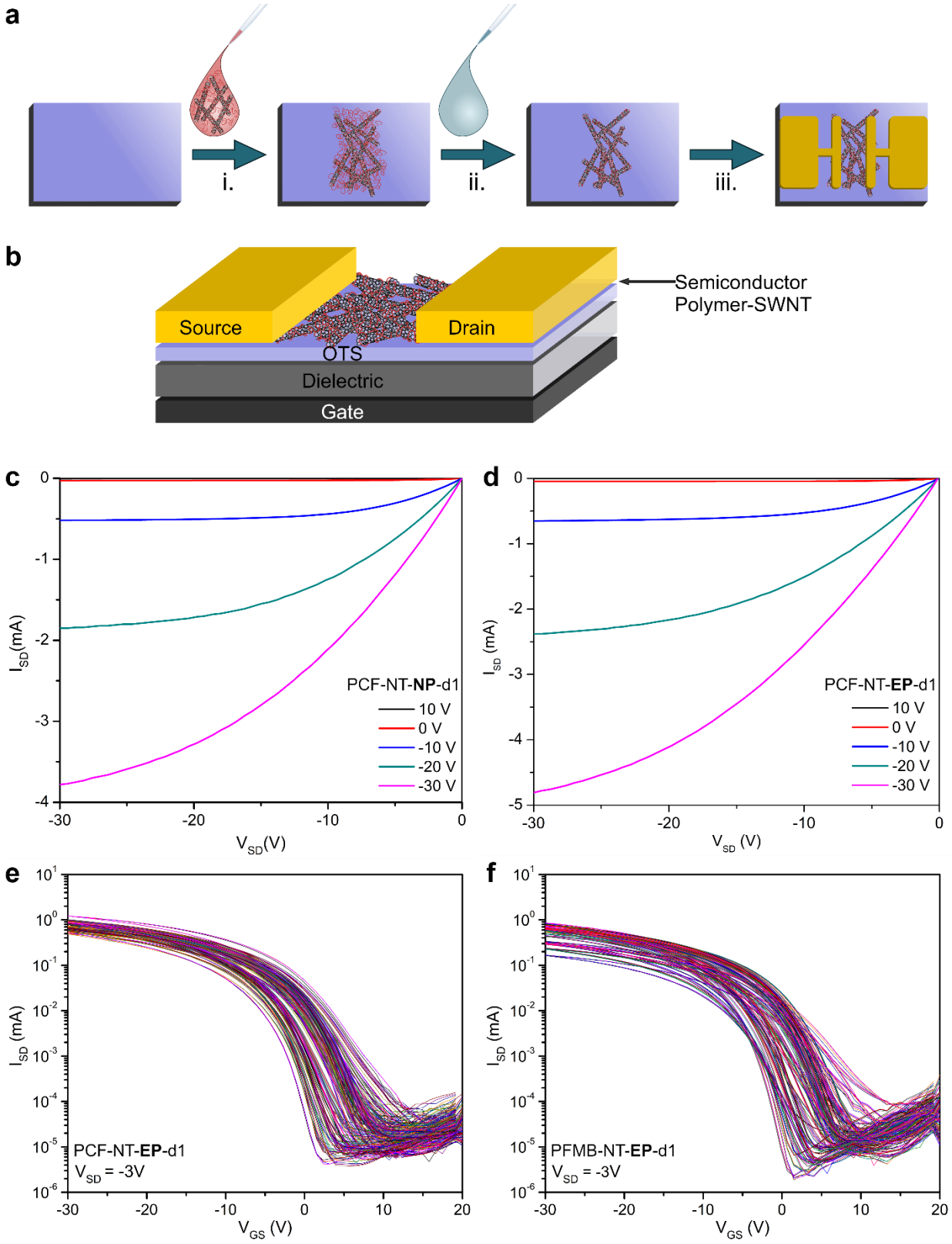

Figure 3.3: (a) Fabrication process for preparing polymer-sorted SWNT TFTs: (i.) 0.5 µL of polymer-sorted SWNT dispersion was drop-cast onto OTS-functionalized Si/SiO_2 wafers. The

solvent was allowed to dry before (ii.) rinsing with 4 × 1 mL of toluene and annealing at 200 ºC in air, and (iii.) deposition of gold electrodes using PVD. (b) Cross-section of BGTC TFT devices. Representative output curves for (c) PCF-NT-**NP**-d1 and (d) PCF-NT-**EP**-d1. Transfer curves for (e) all PCF-NT-**EP**-d1 and (f) all PFMB-NT-**EP**-d1 transistors that were characterized.

TFT characteristics for all polymer-sorted SWNT dispersions, including hole mobility (μ_h), threshold voltage (V_T), and the on/off ratio ($I_{ON/OFF}$), are summarized in **Figure 3.4**. Significant variability can be observed in solution-deposited random-network SWNT TFTs that are fabricated with identical procedures, and this variability can be obscured when only reporting average or highest values. To more accurately describe the full range of performance observed for our TFTs, the data is depicted within box plots, where: the box boundaries indicate the interquartile range, the horizontal line and the star within the box designate the median and the mean, respectively, the vertical lines represent the difference between the 5th and 95th percentiles, and the two solid dots identify the minimum and maximum data values.

Figure 3.4a-b show μ_h values for all PCF-NT and PFMB-NT TFTs, respectively. Unlike other organic semiconductors, polymer-sorted SWNTs form porous networks in TFTs, wherein higher SWNT concentrations increase tube interconnects and thus increase charge carriers present in the film.[50] For both polymer-sorted SWNT samples, TFTs prepared from **EP**, **A2**, **A3**, and **A4** all show an increase in mean μ_h as SWNT concentration is increased. Interestingly, **NP** samples for both polymer-sorted SWNT systems maintain relatively consistent μ_h at all three SWNT concentrations. However, we note that the data variance in μ_h for **NP** devices is often higher compared to **EP** and polymer-added devices, particularly for d2 and d1 dispersions, with smaller fluctuations between the maximum and minimum data values. This indicates the presence of excess unbound polymer could help to reduce device-to-device variability. Furthermore, measured $I_{ON/OFF}$ ratios for the **NP**-c samples had a propensity to be lower (**Figure 3.4e-f**) compared to the polymer-added and **EP** dispersions, indicating that the higher μ_h values may arise from SWNT bundling.[26] For TFTs prepared from dispersions at the same SWNT concentration, generally, μ_h decreased as more excess polymer was added. This decline was most dramatic at the lowest SWNT concentration (d2), where the ratio of added polymer to SWNTs was the largest. The reduction in μ_h upon increased polymer addition can be attributed to sparser SWNT networks and is elaborated upon in the AFM discussion. However, at the highest SWNT concentration investigated, **A2**-c and

A3-c samples had μ_h values that were very close to the **NP**-c samples. For both polymer systems, superlative μ_h were obtained for the **EP** dispersions. With the exception of PFMB-NT-**EP**-d2, all the **EP** dispersions displayed identical or superior μ_h compared to the **NP** dispersions at the same SWNT concentrations. This correlated with $I_{ON/OFF}$ values that were marginally higher compared to **NP** dispersions at the same concentrations.

For PCF-NT, the presence of excess polymer during device fabrication did not result in significant changes to V_T, with an average value of ~ -5 V for all SWNT concentrations and polymer loadings (**Figure 3.4c**). The range of measured V_T values was also consistent for all conditions, confirming that the majority of the excess unbound polymer is rinsed off the sc-SWNTs, as suggested by the previously discussed Raman data. Any residual polymer has little, if any, effect on V_T. There was minimal impact on H values (**Figure 3.15a**), with a minor increase observed for the polymer addition samples at d2. Interestingly, a slight decrease in the mean H and variance was observed for **EP**-c, and most of the polymer-added samples relative to PCF-NT-**NP**-c at the highest SWNT concentration, corroborating that TFTs prepared from excess-polymer samples were more consistent. Additional experiments of smaller polymer additions (0.4 and 0.8 mg/mL of polymer, **Figure 3.16**) were made to the PCF-NT-**NP** dispersion, with only minor variations in μ_h, V_T, $I_{ON/OFF}$ and H relative to **NP** and **EP** observed at all SWNT concentrations. No significant differences in data variance were observed for devices tested in vacuum (**Figure 3.17**), indicating that testing in air is not introducing significant variance to device performance. For PCF-NT, the combined results for μ_h, V_T, $I_{ON/OFF}$ and H indicate that there is no benefit associated with removing excess polymer before device fabrication, challenging the presumption that the polymer-removal step is essential for transistors where the conjugated polymer will remain bound to the SWNT surface during operation.

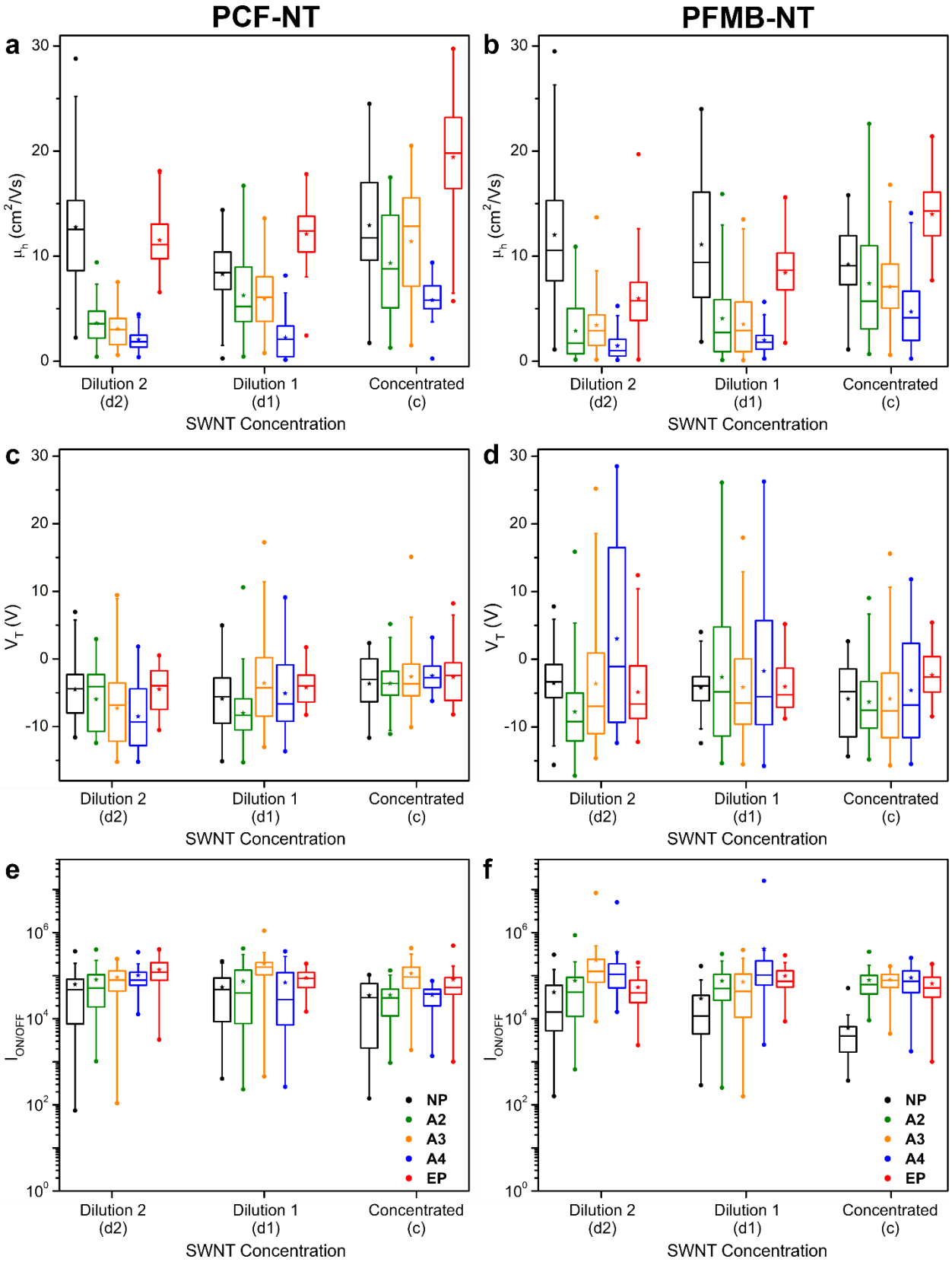
PCF-NT
PFMB-NT
a
b
c
d
e
f
μ_h (cm^2/Vs)
V_T (V)
$I_{ON/OFF}$
Dilution 2 (d2)
Dilution 1 (d1)
Concentrated (c)
SWNT Concentration
NP
A2
A3
A4
EP

Figure 3.4: Summary of average hole mobility (μ_h), threshold voltage (V_T), and on/off ratio ($I_{ON/OFF}$) for (a), (c), and (e) PCF-NT TFTs, and (b), (d), and (f) PFMB-NT TFTs, respectively. Data is shown in box plots, where: the box indicates the interquartile range, the horizontal line (within the box) is the median, and the star is the mean. Vertical lines indicate the difference between the 5th and 95th percentile, with the maximum and minimum values denoted by circles.

Analysis of V_T and H for PFMB-NT TFTs is more complicated as more significant variations are apparent for the different polymer additions, particularly for d2 samples. Analogous to PCF-NT results, TFTs prepared from PFMB-NT-**EP** and **NP** dispersions had mean V_T values around -5 V, with comparable maximum and minimum values (**Figure 3.4d**) and similar H values (**Figure 3.15b**) at all SWNT concentrations. Mean V_T for all polymer-added devices are also around -5 V. However, there was a significant increase in variance compared to **EP** and **NP** devices and a corresponding increase in H as the ratio of unbound polymer to SWNT in the dispersion increased. The largest divergence of TFT device performance was observed at d2, with a clear trend in increasing mean (and range) of V_T and H values with an increasing amount of polymer added. Interestingly, μ_h values for polymer-added PFMB-SWNT samples do not follow the same trends observed for V_T and H at d1 and d2, underscoring the importance of analyzing multiple device parameters.

The differences in performance between TFTs prepared from PCF-NT and PFMB-NT are most likely attributable to the polymer structure. The presence of 2,5-dimethoxybenzene in the PFMB backbone, some of which remain bound to the SWNT surface even after rinsing, may contribute to charge trapping and charging/discharging during the forward and reverse sweep, resulting in the more significant variations in H and V_T.[51] It is also possible that the extreme differences in V_T and H between PFMB and PCF, particularly at the higher polymer additions, could be further exacerbated by the potentially incomplete rinsing of PFMB, which is elaborated upon below. Despite this, PFMB-NT-**EP** displayed identical or superior TFT performance compared to PFMB-NT-**NP** when considering all device parameters combined, again demonstrating that the removal of excess polymer prior to device fabrication is unnecessary.

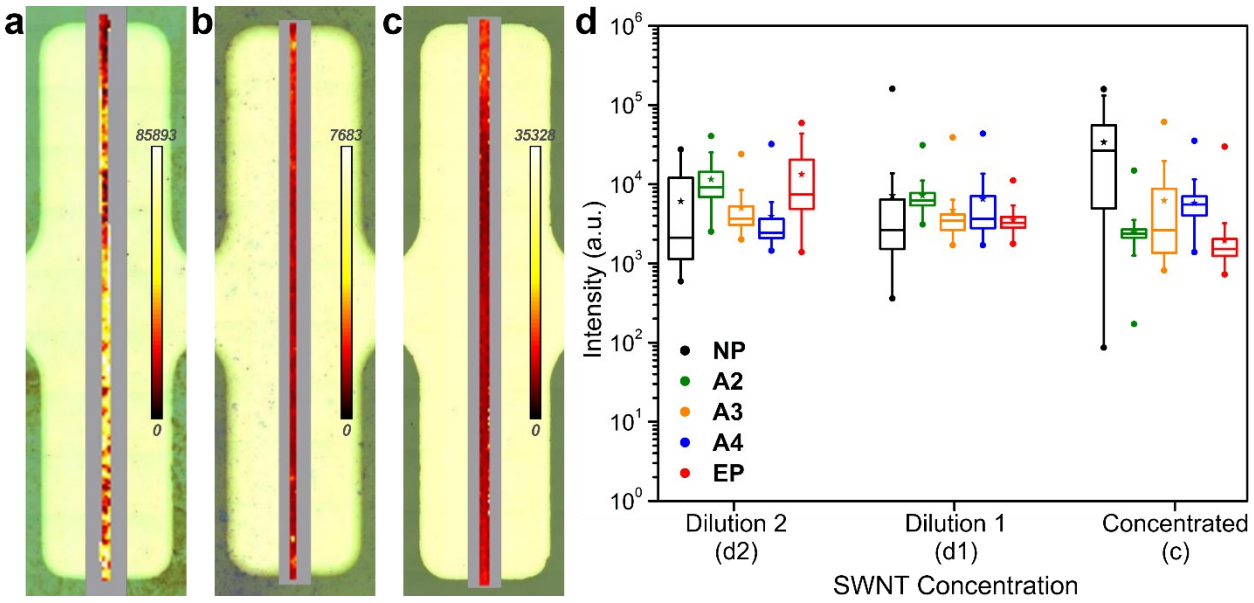

Figure 3.5: Raman map data (showing *G*-band intensity) overlaid on photos of TFT channels for (a) PCF-NT-**NP**-c, (b) PCF-NT-**EP**-c and (c) PCF-NT-**A4**-c. (d) Summary of *G*-band intensity data within the TFT channels for all PCF-NT samples. Data points that overlapped with the gold electrodes in (a), (b) and (c) (grey boxes) were not included in intensity measurements.

With the bulk of the excess polymer rinsed off before deposition of electrodes, changes in TFT performance for the polymer-added and **EP** dispersions compared to **NP** dispersions arise from the excess polymer chains influencing the sc-SWNT network during film formation. The device channels have widths of 1000 µm, while polymer-sorted SWNT networks have dimensions on the order of nanometers, so it is essential to describe film morphology on both the microscale and nanoscale. For the former, we utilized Raman mapping to characterize SWNT distribution throughout the entire channel for all PCF-SWNT dispersion conditions. Raman scans were performed using an excitation wavelength of 785 nm, with data analyzed by generating intensity at a point (centred on the SWNT *G*-band) maps; at least two different transistors (possessing μ_h close to the calculated mean) were imaged for each PCF-NT condition. Example maps for PCF-NT-**NP**-c, **EP**-c and **A4**-c are shown in **Figure 3.5a-c**, respectively, overlaid onto photos of the transistors (example maps for all other PCF-NT polymer additions and dilutions can be found in **Figure 3.18**). Data points that overlapped with the gold electrodes (grey areas) were masked out and not included in the analysis as the gold caused an enhancement in Raman intensity. Visually, the **NP**-c film is more heterogeneous than the **EP**-c and **A4**-c samples. In an effort to quantify these differences, *G*-band intensity data from each condition were combined to generate a box plot,

shown in **Figure 3.5d**. It is immediately apparent that the PCF-NT-**NP** thin-films have a larger variance in intensities at all SWNT concentrations, particularly **NP**-c. This corroborates our findings from the analysis of the TFT data and confirms that larger deviations in TFT performance from the **NP** dispersions are a result of inhomogeneous thin-film formation. Furthermore, the shift in the interquartile range for PCF-NT-**NP**-c to higher *G*-band intensity values compared to all the other polymer-sorted SWNT thin-films indicates the possible presence of significant SWNT bundling, which would explain the lower $I_{ON/OFF}$ values observed for some of these transistors.

Raman map values from the polymer-added and **EP** thin-films consistently have smaller interquartile ranges compared to the corresponding **NP** thin-films. Although drop-casting results in random networks of SWNTs, the presence of excess polymer appears to aid in the formation of superior SWNT networks by dispersing the sc-SWNTs more evenly throughout the transistor channels. This phenomenon is similar to the practice of using an insulating carrier polymer to aid in the formation of crystalline thin-films for small-molecule organic semiconductors.[32-35] This excess polymer can easily be removed through a simple rinsing step after the SWNTs have been deposited, indicating that forgoing the laborious polymer removal step not only saves time and materials but also facilitates the fabrication of higher-quality organic electronic devices.

We used AFM to investigate how excess polymer affects film quality and density on the nanoscale during sc-SWNT film formation. At least four unique images (5×5 μm^2) were obtained for each polymer-sorted SWNT variant for TFTs with μ_h values close to the mean. **Figure 3.6** shows representative AFM images for all PCF-NT TFTs (corresponding PFMB-NT images are in **Figure 3.19**). Random SWNT networks can be observed in all the AFM images, with the density of tube coverage varying with both SWNT concentration and the amount of excess polymer present. Although the images only depict a sixth of the channel width, the presence of a continuous network of SWNTs in all images, and the ability to achieve working transistors for all conditions, indicates that complete percolating networks are formed for all 30 unique dispersions.

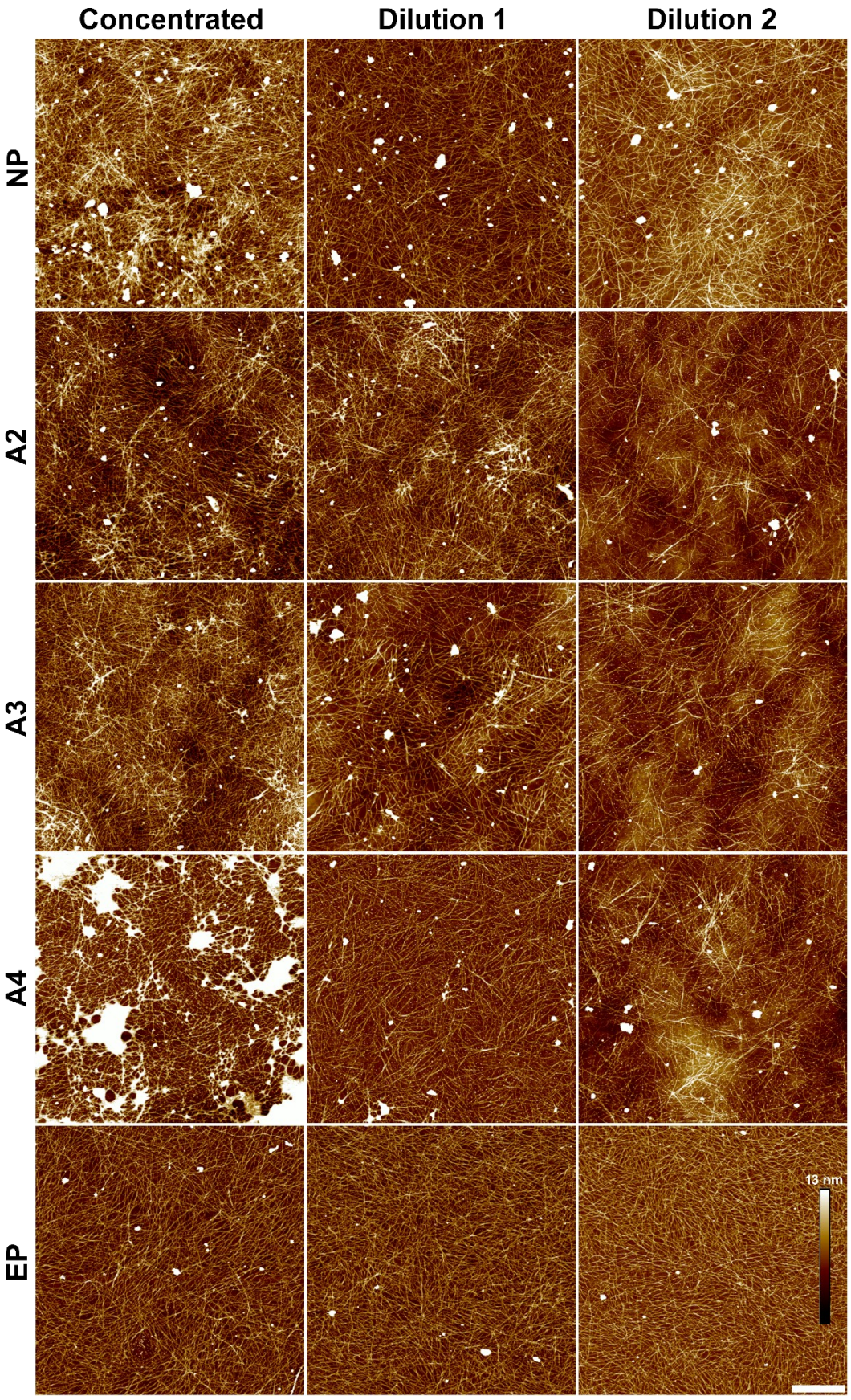
Concentrated
Dilution 1
Dilution 2
NP
A2
A3
A4
EP
13 nm

Figure 3.6: Representative AFM images for all PCF-NT TFTs, for all SWNT concentrations and polymer additions. All images have been plotted on a height scale of 13 nm, with the white scale bar representing 1 μm.

Superficial analysis of the images and line-height profiles (**Figure 3.20** and **Figure 3.21**) indicates that films prepared from **NP** dispersions have regions of both exfoliated monolayers and dense mats comprised of several layers of SWNTs that bundled together as solvent evaporated off. In contrast, the **EP** and polymer-addition dispersions typically resulted in well-exfoliated networks of SWNTs, with height profiles indicating most SWNT intersections are 2 – 3 tubes high. A lack of large amorphous features or broadening in the SWNT widths substantiates that excess polymer has been removed from PCF-NT-**EP** and polymer-added films at all SWNT concentrations, with the exception of PCF-NT-**A4**-c. In contrast, AFM images for PFMB-NT-**A3** and PFMB-NT-**A4** clearly show significant amounts of residual polymer coating the SWNTs, confirming our hypothesis that some residual PFMB polymer remains after four rinses at high polymer concentrations. Although the rinsing protocol is sufficient to remove unbound free polymer, above a threshold amount, additional polymer chains can aggregate on the tube surface. This residual excess polymer accumulates randomly on SWNTs, forming both thin and thick layers, resulting in higher average SWNT heights (**Figure 3.20**). The erratic nature of this additional polymer coating is a possible explanation for the increase in variance observed for V_T and H values in TFTs prepared from polymer-added PFMB-NT dispersions. However, as this coverage is not consistent, we cannot comment on exactly what effect it has on device performance in this study.

To fully elucidate how the presence of excess polymer affects the semiconductor films, it is essential to determine SWNT network density. Raman mapping can be utilized to estimate tube density; however, it requires generating a calibration curve with corresponding SEM images, which can be challenging at greater tube surface coverage.[52] Nanotube density is commonly estimated by manually counting individual tubes and/or SWNT intersections in a single AFM or SEM image;[18,47,50] such processes are time-consuming and subject to human error, especially for random networks at high SWNT surface coverage. A recent technique developed by Lopinski and coworkers utilizes volumetric analysis of AFM images to estimate the number of SWNTs in an AFM image and the degree of bundling.[53] An alternative to these techniques is to utilize Artificial Intelligence and Computer Vision to analyze the films in an automated fashion. There are multiple

advantages to automating the detection of nanotubes in AFM images. Firstly, errors associated with manually counting SWNTs can be eliminated, as algorithms can generate reproducible results. Secondly, the algorithm can scrutinize more images and a much larger surface area than could be feasibly done manually. Finally, the algorithm can not only determine the number of tubes but also facilitate quantitative analysis of the films on multiple levels, including determining length distributions and alignment angles of the SWNTs, which is valuable for analysis of aligned networks.[18,20,54,55]

Quantitative analysis of aligned SWNT networks requires that the characteristics of each nanotube (length, position, and orientation) be known throughout the film; these are collectively referred to as the "parameters" of the nanotube. Extracting these parameters from AFM images presents several technical challenges. First, traditional techniques such as Hough Transforms[56] failed to detect most SWNTs, necessitating a novel approach to decipher the dense visual medium. Second, segmentation of the image into SWNT and non-SWNT pixels requires sophisticated analysis as excess polymer, visual artefacts, and the inherent complexity of SWNT films prevent setting a fixed threshold to distinguish between a nanotube and the substrate.

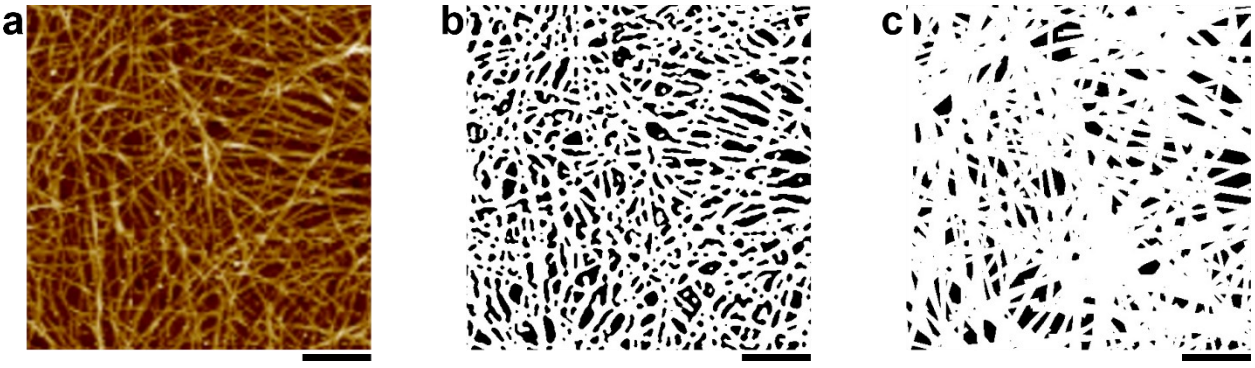

Figure 3.7: Summary of select algorithm steps used to analyze AFM images (detailed description in the Supporting Information): (a) original AFM image, (b) processed image after removal of non-SWNT artefacts and substrate surface, and (c) after genetic algorithm to iteratively solve for SWNTs. For clarity, the original AFM image has been cropped (black scale bar under each image represents 0.25 μm).

The proposed solution has two main stages: segmentation of the AFM data into nanotube and non-nanotube pixels, followed by extraction of SWNT parameters from the segmented AFM

data using a genetic algorithm (**Figure 3.7**, full details in Supporting Information). The first stage is comprised of several image processing steps using algorithms such as Otsu and Yen thresholding[57,58] and median blurs,[59] while in the second stage, the genetic algorithm iteratively solves for the film's nanotube parameters. Once a sufficiently high-quality solution is obtained, the set of SWNTs can then be analyzed quantitatively to generate descriptions of tube lengths and angles, as well as more complex metrics, including intersections or surface coverage.

Table 3.2: Summary of SWNT surface coverage in AFM images for PCF-NT TFTs.

	Surface Coverage (%)		
Sample	**c**	**d1**	**d2**
PCF-NT-NP	60* ± 6	56* ± 4	50* ± 10
PCF-NT-A0.4	53 ± 10	51 ± 10	53 ± 20
PCF-NT-A0.8	55 ± 14	57 ± 10	63 ± 3
PCF-NT-A2	61 ± 5	48 ± 10	17 ± 3
PCF-NT-A3	60 ± 4	26 ± 5	18 ± 3
PCF-NT-A4	50† ± 5	18 ± 6	17 ± 8
PCF-NT-EP	57 ± 2	54 ± 9	57 ± 3

* *Significant bundling in films.*
† *Value overestimated due to presence of excess polymer.*

Average values of surface coverage from PCF-NT dispersions, as determined by our novel algorithm, are outlined in **Table 3.2** (data for PFMB-NT dispersions can be found in **Table 3.4**). It should be noted that our algorithm is currently unable to distinguish between layer thicknesses, so films with a significant degree of bundling (like the **NP** samples) could potentially have values similar to those of dense monolayers. This will also result in underestimating the number of SWNTs calculated in the dense image. SWNT surface coverage was relatively consistent for the most concentrated SWNT dispersions (c) at all polymer loadings. Correspondingly, all TFTs at this SWNT concentration (with the exception of PCF-NT-**A4**-c) had μ_h values within the same order of magnitude as PCF-NT-**NP**-c. The discrepancy with PCF-NT-**A4**-c arises from the presence of excess polymer resulting in an overestimation by the algorithm of surface coverage. At lower SWNT concentrations, as the amount of polymer is increased, there is a corresponding

decrease in SWNT surface coverage, resulting in a dramatic drop in SWNT network density for PCF-NT-**A2**-d2, **A3**-d2 and **A4**-d2. This corresponds to the significant decrease in μ_h for these dispersions discussed previously. Reduction in SWNT surface coverage could be attributed to excess unbound polymer hindering interactions between the SWNTs and the dielectric surface, or from accumulation of additional wrapping polymer on the nanotube surface increasing the solubility of the supramolecular complexes, both of which would make the SWNTs more susceptible to being washed off the substrate during the rinsing step.

There is little change in values for the **NP** and **EP** films when comparing surface coverage between SWNT concentrations, which correlates with only minor decreases in μ_h for both as SWNT concentration decreased. Furthermore, surface coverage values between **NP** and **EP** films are identical within error, indicating that despite the presence of excess polymer during fabrication, **EP** dispersions resulted in identical surface coverage compared to **NP** dispersions. When combined with line-height profile analysis, it is apparent that more SWNT material is present in **NP** films, but only as deleterious bundles that negatively affect performance and reproducibility. The superior performance of **EP** TFTs can be attributed to the higher-quality, more uniform networks that are formed by the SWNTs due to the presence of the excess carrier polymer.

3.4 Conclusion

In conclusion, we demonstrate that TFTs fabricated from polymer-sorted SWNT dispersions containing residual excess polymer perform identically or even better than dispersions where the excess polymer is removed prior to device formation. This effect was especially pronounced at higher SWNT concentrations, which often yield premier TFT performance. The original as-produced polymer dispersions (**EP**) resulted in TFTs possessing superior μ_h and $I_{ON/OFF}$, with little change in V_T and H compared to devices prepared from dispersions with excess polymer removed. We hypothesize that the additional polymer chains hinder SWNT bundling during solvent evaporation and result in improved thin-film morphology. Raman spectroscopy confirmed that a facile solvent rinse after thin-film deposition removes all excess polymer from **EP** films. A novel open-source algorithm that we developed to facilitate rapid analysis of large numbers of AFM images confirms that SWNT surface coverage is consistent between **NP** and **EP** films.

The rinsing protocol described in this report was sufficient for semiconductor thin-films prepared from dispersions with large amounts of excess polymer. However, beyond a certain threshold amount of excess polymer (~ 3 mg/mL for PCF and ~ 2 mg/mL PFMB), some residual polymer remained after four rinses, with this phenomenon predominant in thin-films prepared from high SWNT concentrations. Modification of the rinsing step, combined with quick confirmation through a combination of Raman spectroscopy and AFM, should facilitate the development of rinsing protocols capable of completely removing excess polymer from any unique SWNT thin-film network.

Our findings have important implications for large-scale solution-processed SWNT TFTs. Removal of excess polymer from SWNT dispersions is an expensive and time-consuming bottleneck for industrial operations attempting to sort and disperse sc-SWNTs using conjugated polymers. Retention of excess polymer in SWNT dispersions can help stabilize the dispersion, prolonging the shelf life of the inks while also resulting in inks with viscosities that are more amendable to various printing technologies. Furthermore, the wafer rinse procedure disclosed here consumes about three orders of magnitude less solvent and eliminates material losses that occur with membrane filtration. The TFTs characterized in this study had relatively large channel lengths (30 μm), typical of devices that can be fabricated from high-throughput roll-to-roll printing techniques like gravure printing. Additional studies are underway to determine if the protocols outlined here can be translated to shorter channel TFTs fabricated through traditional lithographic processes for integrated circuit applications.

3.5 Experimental

3.5.1 General

All chemicals and solvents were purchased from commercial suppliers and used without further purification. Pre-diced prime grade silicon wafers (~ 300 nm thermal SiO_2 layer) were purchased from either University Wafer or Ossila. The dielectric capacitance density of the SiO_2 films was confirmed by fabrication of metal-insulator-metal capacitors prepared by depositing gold electrodes onto the wafers. PCF and PFMB polymers were synthesized following previously reported procedures[36,37] with, PCF: M_n = 46.3; Đ = 1.99; and PFMB: M_n = 75.8 kDa; Đ = 3.15.

3.5.2 Polymer-sorted SWNT Dispersions

3.5.2.1 Preparation of Original Excess Polymer (EP) and No Excess Polymer (NP) Dispersions

Semi-pure plasma torch SWNTs were purchased from Raymor NanoIntegris (Batch: RNB738-120, diameter: 0.9 – 1.5 nm, length: 0.3 – 4 μm, G/D Ratio 63.4). PCF-SWNT and PFMB-SWNT dispersions were prepared following the same procedure reported previously in the literature.[36,37] Dry polymer and pristine SWNT powder were combined in a vial at a ratio of 0.8:1 (8 mg PCF, 10 mg SWNT) for PCF-SWNT, and 1.2:1 (12 mg PFMB, 10 mg SWNT) for PFMB-SWNT. 20 mL of toluene was added, and the mixtures were sonicated in a bath sonicator (2.8 L VWR Ultrasonic bath cleaner) for 90 min, chilled with ice. Following sonication, the polymer-sorted SWNT dispersions were centrifuged at 15,000 *g* for 20 min at 10 °C (Thermo Scientific Sorvall ST 16R, equipped with a Fiberlite F15 fixed angle rotor). The supernatant, comprised of polymer-wrapped sc-SWNTs and dissolved excess polymer (not bound to SWNTs), was removed. The polymer dispersal procedure was repeated numerous times, with several (3 – 5) supernatants combined into a single vial. A treatment step using silica gel, developed by Malenfant *et al.*,[60] was performed to remove any potential trace m-SWNTs. Approximately 20 – 25 mg of silica gel was added to the polymer-sorted SWNT dispersions and sonicated for 45 min (bath sonicator, chilled with ice). After sonication, the dispersion was allowed to sit undisturbed on the benchtop for 3 hours before centrifugation at 15,000 *g* (20 min, 10 °C). The resulting ultrapure sc-SWNT dispersions were combined to prepare large stock polymer-sorted SWNT samples. A portion of both stock dispersions was set aside to be used as-is (original excess polymer, **EP**); the remainder was filtered under vacuum through a Teflon membrane (pore diameter: 0.2 μm). The polymer-sorted SWNT filter cakes were washed with toluene until the filtrate no longer fluoresced upon

irradiation with a UV lamp. The polymer-sorted SWNT mat was removed from the membrane and re-dispersed in 20 mL of toluene by bath sonication for 1 h (chilled with ice). The dispersion was centrifuged at 15,000 *g* for 10 min (10 °C) to ensure stability. These filtered dispersions are referred to as the no excess polymer (**NP**) sample.

Both the **EP** and **NP** dispersions were divided and diluted to three unique SWNT concentrations, controlled using absorption spectroscopy (Cary 5000 spectrometer in dual-beam mode, 1 cm quartz cuvette) through the height of the S_{22} absorption peak at ~ 937 nm: 1.2 a.u. (Dilution 2, d2), 1.7 a.u. (Dilution 1, d1), and 2.7 a.u. (Concentrated, c).

3.5.2.2 Preparation of Polymer-Added Dispersions

Polymer-added dispersions were prepared through the addition of controlled amounts of excess polymer into the **NP** dispersion described in the previous section. Neat polymer was weighed and dissolved in exact volumes of toluene to prepare stock polymer solutions of known concentration, such that a 500 µL aliquot would yield either 2.0, 3.0 or 4.0 mg/mL solutions of polymer. Both polymers are readily soluble in toluene at these concentrations at room temperature. A 500 µL aliquot of polymer solution was then pipetted into an empty vial and evaporated to dryness before 500 µL of the concentration-matched **NP** polymer-sorted SWNT dispersion was added. The polymer-added samples were sonicated for 20 min in a bath sonicator to re-dissolve the excess polymer residue. This yielded polymer-added polymer-sorted SWNT dispersions with excess polymer concentrations of 2.0 mg/mL (**A2**), 3.0 mg/mL (**A3**) or 4.0 mg/mL (**A4**), at the three different SWNT concentrations listed in the previous section. These samples were incorporated into TFTs within 24 h of preparation to avoid concentration changes arising from solvent evaporation.

3.5.3 Thin-film Characterization

3.5.3.1 Raman Spectroscopy

Confirmation of removal of metallic SWNTs (from PCF-NT and PFMB-NT **NP** dispersions) and characterization of excess polymer in drop-cast thin-films were performed through Raman spectroscopy (Renishaw inVia Raman microscope). Raman spectra were collected using three different laser excitation wavelengths: 514 nm (25 mW Argon ion laser, 1800 L/mm grating); 633 nm (500 mW HeNe Renishaw laser, 1800 L/mm grating); and 785 nm (300 mW Renishaw laser, 1200 L/mm grating). To evaluate sc-SWNT purity, excitation wavelengths of 633

and 785 nm were primarily used. Multiple extended scans (100 – 3200 cm^{-1}) were collected at each wavelength (5 % laser power for 633 nm, 0.1 % power for 785 nm); several static scans (centred at 250 cm^{-1}, 10 s integration time, 10 accumulations) were also collected (5 % laser power for 633 nm, 1 % power for 785 nm), with replicate scans from both experiments averaged together. Raman spectra for unpurified SWNTs (before polymer dispersal) were achieved by wetting a small amount of the raw powder with $CHCl_3$ and drop-casting this mixture onto a clean silicon wafer.

An excitation wavelength of 514 nm was used to investigate the removal of excess polymer from thin-films. The polymer and polymer-sorted SWNT thin-films were prepared *via* drop-cast (discussed in detail in the SWNT-TFT Fabrication section) and subjected to either no-rinse, 1, 2, 3 or 4 rinses with 1 mL of toluene. The substrate was dried for 30 s with N_2 between each rinse. Multiple extended scans (100 – 3200 cm^{-1}, 10 % laser power) were collected for each sample and averaged together to evaluate the loss of polymer peaks and the reduction in background fluorescence from the conjugated polymers.

Raman maps of TFT channels were collected using a Renishaw inVia Qontor confocal Raman microscope, equipped with a 785 nm laser (300 mW Renishaw laser, 1200 L/mm grating, 50 % power). The map area was defined by a rectangle drawn on a montage snapshot of the transistor channel. 4300 Raman scans (pinhole in, 1 accumulation for 4 s, centred at 1600 cm^{-1}) were obtained for each TFT, with step sizes of 3 and 5 μm in the x- and y-directions, respectively. Intensity at a point (1593 cm^{-1}) maps were generated using the WiRE 5.2 software. Data points that overlapped with the gold electrodes were excluded through the use of the mask feature.

3.5.3.2 Photoelectron Spectroscopy

X-ray photoelectron spectroscopy (XPS) was performed using a Kratos AXIS Supra X-ray photoelectron spectrometer using an Al K(alpha) monochromatic X-ray source (25mA, 15kV). Analyses were performed on an area with a diameter of 110 μm, with a pass energy of 160 eV or 40 eV for survey scans and high-resolution scans, respectively.

3.5.3.3 Atomic Force Microscopy

Atomic force microscopy (AFM) images were obtained using a Bruker Dimension Icon AFM, with ScanAsyst-Air tips in tapping mode using a scan rate of 1 Hz. At least two transistors were chosen, with μ_h values close to the mean for that condition, with at least two images taken for each transistor, resulting in a minimum of four AFM images per condition. All images were 5

μm × 5 μm, with a resolution of 2006 × 2006 pixels; basic image processing (flattening, removal of errant scan lines) was performed using NanoScope Analysis v.2.0.

3.5.3.4 Algorithmic Analysis

AFM images were analyzed using a novel computer vision approach implemented in python 3.7. The images were loaded, cropped and converted to grayscale using the OpenCV python module, resulting in a 512 × 512-pixel grayscale square. Visual artefacts were removed, and the image was segmented using a local Otsu approach implemented using the Scikit Image python package. Finally, the segmented image was solved for the nanotube parameters using the PyEasyGa python package. The Supporting Information provides detailed descriptions of the full algorithm process.

3.5.4 SWNT-TFT Fabrication

The Si/SiO_2 (oxide thickness of 300 nm) wafers (2 cm × 1.5 cm) were cleaned through sequential bath sonication (5 min, room temperature) washes with: soapy water, distilled water, acetone, and methanol. Wafers were dried with N_2 and treated in oxygen plasma for 15 minutes. Immediately after plasma treatment, the wafers were rinsed with distilled water and isopropanol, dried with N_2, and then treated for ca. 24 h in a 1 % (v/v) solution of octyltrichlorosilane (OTS, Sigma Aldrich) in toluene at 70 °C; this formed a self-assembled monolayer (SAM) of OTS on the SiO_2 surface. After removal from the OTS solutions, the wafers were rinsed with toluene, dried with N_2, and further dried in a vacuum oven at 70 °C to remove any residual solvent.

Polymer-sorted SWNT semiconductor thin-films were deposited onto the OTS-treated wafers using a solution-based drop-cast technique. The polymer-sorted SWNT composites were sonicated for 10 min immediately preceding SWNT deposition. For each TFT, 0.5 μL of SWNT dispersion was drop-cast onto the wafer surface, with the solvent allowed to evaporate under ambient conditions; a custom-built 3D printed holder was used to facilitate placement of the drops in the vicinity of the electrodes. The wafers were then rinsed four times with 1 mL of toluene at a 45° angle (using a Teflon holder), with the film dried with a steady stream of N_2 for ~ 30 s after each rinse, before being annealed in air for 1 h at 200 °C. Top-contact source-drain electrodes were deposited on the polymer-sorted SWNT thin-films through physical vapour deposition (Angstrom Engineering EvoVac thermal evaporator). Gold (99.99 %, Angstrom Engineering Inc.) electrodes with a channel length of 30 μm (width of 1000 μm) were deposited through shadow masks (Ossila),

with a target thickness of 50 nm at a rate of 1 Å/s. This resulted in 20 unique bottom-gate top-contact (BGTC) TFTs per wafer. At least two wafers were prepared for each of the 30 unique polymer-sorted SWNT dispersions.

3.5.5 SWNT-TFT Characterization

The p-type characteristics of all TFTs were measured under ambient conditions (in air, room temperature) using a Keithley 2614B SourceMeter, with LabVIEW software and a custom-built auto tester apparatus. Each wafer, consisting of 20 TFTs, was stored in a nitrogen glovebox (O_2 < 1 ppm) and tested immediately upon exposure to air. Electrical characterization of all 20 TFTs took ~ 30 min, with no significant variation in performance observed between the first and last transistors tested. Each unique transistor was tested four times, with all transfer curves collected in the linear regime. The following equation was used to model the linear regime source-drain current with the gate-source voltage:

$$I_{SD} = \frac{W\mu C_i}{L}\left((V_{GS} - V_T)V_{SD} - \frac{V_{SD}^2}{2}\right) \quad (1)$$

I_{SD} is the source-drain current, W is the channel width, L is the channel length, μ is the field-effect mobility, C_i is the dielectric capacitance density, V_T is the measured threshold voltage, V_{SD} is the source-drain voltage, and V_{GS} is the gate-source voltage. Field-effect mobility was calculated using the following equation:

$$\mu = \frac{L}{WC_iV_{SD}}\frac{dI_{SD}}{dV_{GS}} \quad (2)$$

The threshold voltage was measured from the x-intercept of the transfer curve using the following equation:

$$V_T = V_{GS}(\textit{x-intercept}) - \frac{V_{SD}}{2} \quad (3)$$

The hysteresis was calculated as the absolute difference between the forward and reverse sweep threshold voltages.

Each device was tested four times. Mobility and threshold voltage values reported in **Figure 3.4** and **Figure 3.16** are an average of the forward and reverse sweeps for each individual transistor. I_{ON} was the current at the maximum voltage (V_{GS} = -30 V), while I_{OFF} was the minimum current recorded.

For vacuum testing experiments, devices were transported under vacuum ($P < 0.1$ Pa) and tested using a custom electrical four-point probe station with an environmental chamber to control the atmosphere. Devices were characterized using identical parameters and equations outlined above. Immediately after testing in vacuum, the chips were exposed to air and characterized using the auto tester apparatus outlined above.

3.6 Acknowledgements

The authors would like to thank Dr. Kelly Akers of ProSpect Scientific and Dr. Richard Bormett of Renishaw Inc. for providing access to the Renishaw inVia Qontor spectrometer. The authors also thank NanoIntegris Technologies/Raymor Industries for providing the G/D ratio for the semi-purified plasma SWNTs used in this study. This work was supported by the NSERC Green Electronics Network (GreEN) (grant number: NETGP 508526-17), NSERC Discovery Grant RGPIN 2015-03987 (B.H.L), the Canada Research Chairs Program 950-230724 (B.H.L). We are also thankful for the following fellowships: NSERC CGS-D for B. M. and W. J. B., NSERC PGS-D to N.T.B. and D.F., and NSERC PDF for N. A. R. Infrastructure used to complete this work was acquired using CFI-JELF #30488 (B.H.L) and NSERC RTI 472921-2015 (B.H.L).

3.7 Supporting Information

3.7.1 Absorption Peak Ratio

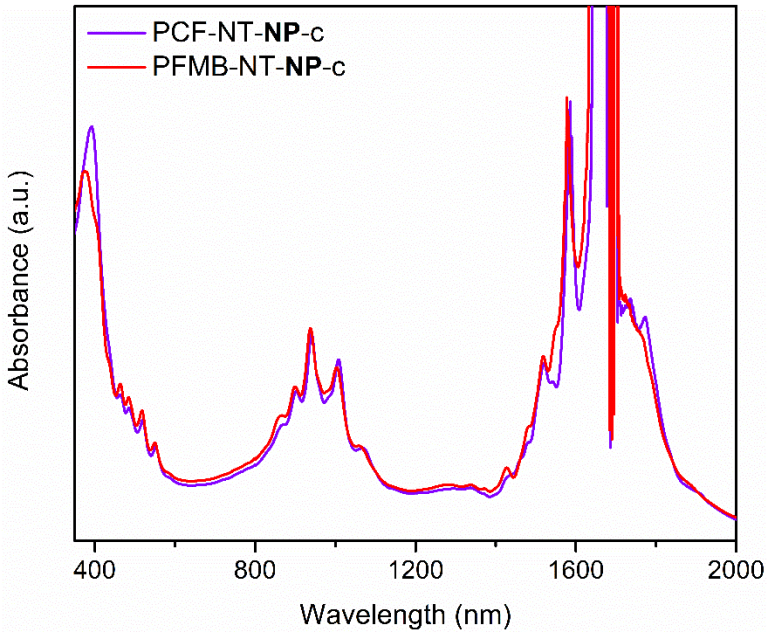

Figure 3.8: UV-Vis-NIR absorbance spectra of PFMB-NT-**NP**-c and PCF-NT-**NP**-c.

The absorption peak ratio (ϕ_i) was used to evaluate sc-SWNT purity in both polymer-SWNT dispersions following the procedure published by Malenfant *et al.*,[9] where $\phi_i > 0.40$ indicates a sc-SWNT purity of > 99 %. For PCF-NT-**NP**-c $\phi_i = 0.41$, while for PFMB-NT-**NP**-c $\phi_i = 0.43$, indicating a high degree of sc-SWNT purity for both dispersions. These values are valid for the **EP** and all polymer-added dispersions since the **NP** dispersion was filtered directly from **EP**, and used to prepare all polymer-added dispersions. The **EP** dispersions were not used for ϕ_i calculations to avoid challenges associated with subtracting the background absorbance tail from excess polymer in the M_{11} region.

3.7.2 Additional Raman Spectra

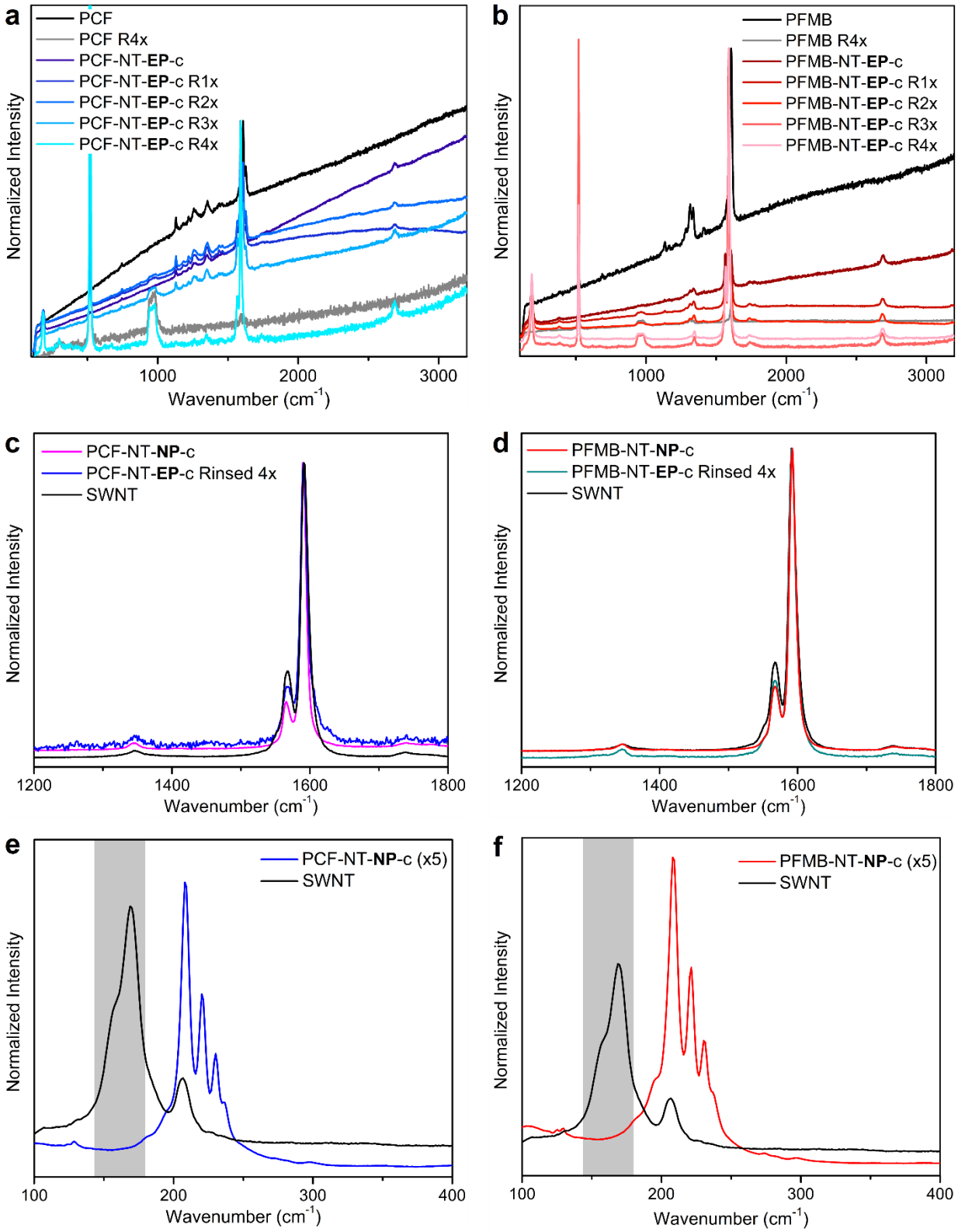

Figure 3.9: Full Raman (excitation wavelength of 514 nm) spectra depicting removal of excess polymer through loss of background fluorescence for (a) PCF and PCF-NT-**EP**-c and (b) PFMB and PFMB-NT-**EP**-c (R = Rinsed). Confirmation that the *G*-band region for **EP**-c (Rinsed 4x) at 514 nm is analogous to both **NP**-c and raw SWNTs (before polymer addition) for both (c) PCF-NT-**EP**-c and (d) PFMB-NT-**EP**-c. RBM scans (excitation wavelength = 785 nm) for (e) PCF-NT-**NP**-c and (f) PFMB-NT-**NP**-c, confirming the removal of metallic SWNT species (grey box); polymer-SWNT spectra have been multiplied by a factor of 5.

3.7.3 XPS Data

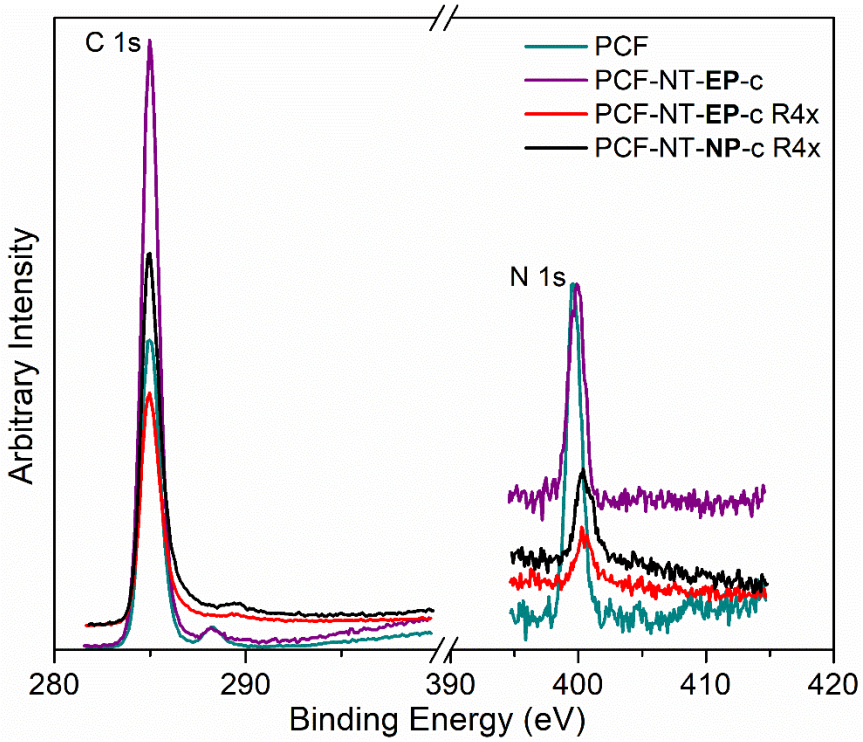

Figure 3.10: XPS of thin-films of PCF, PCF-NT-**EP**-c (R = Rinsed), and PCF-NT-**NP**-c showing C 1s and N 1s peaks.

The N 1s peak in XPS can be used as a chemical handle to evaluate the effectiveness of the rinsing step. Thin-films of PCF, PCF-NT-**EP**-c and PCF-NT-**NP**-c were drop-cast onto OTS-treated SiO_2. Two films for PCF-NT-**EP**-c were investigated, one rinsed (R4x) and the other unrinsed, while the neat polymer films were not rinsed with toluene.

Analysis of the peak intensities for PCF shows close to the expected ratio of nitrogen to carbon for the conjugated polymer backbone (calculated 3.8 %, found 4.6 %). Although similar analysis has been used previously to determine the amount of polymer present on the SWNTs,[16]

these experiments were performed on dense mats of SWNTs, affording higher signal intensity. While we were able to observe the N 1s peaks in polymer-sorted SWNT films, the thin nature of the monolayer films precluded calculation of the amount of nitrogen present.

A shift in the N 1s spectra position was observed for all samples containing SWNTs. Peak shapes and location were identical for PCF-NT-**EP**-c R4x and PCF-NT-**NP**-c R4x (both at 400.5 eV), suggesting the nitrogen atoms are in the same environments in both films. The increase in binding energy compared to PCF (399.7 eV) could be attributed to withdrawal of valence electron charge from the nitrogen atoms in the polymer backbone through π-π interactions with the SWNTs, suggesting that all polymer chains are in contact with nanotubes. The shift in peak maximum for PCF-NT-**EP**-c (no-rinse, 399.9 eV) is within instrumental error (± 0.2 eV) compared to PCF, however the broadening of the peak shape towards higher binding energy suggests that two environments are occurring in this thin-film: free unbound polymer (which is dominant) and polymer bound to the surface of SWNT. These results corroborate Raman experiments, confirming that our rinsing protocol is sufficient to remove all excess unbound polymer from the SWNT **EP** thin-films.

3.7.4 How Much Unbound Excess Polymer is Ideal?

The similar or superior performance of **EP** TFTs relative to **NP** TFTs at the same SWNT concentrations for the two different polymer-sorted SWNT systems suggests that this phenomenon is not limited to a single polymer system. However, the polymer-addition experiments indicate that there are limitations on how much excess polymer can be present before TFT performance is negatively affected, and this limit is polymer-dependent. In this report, we found the PCF-NT system more forgiving, with 4 × 1 mL rinses sufficient to rinse off all unbound polymer at all SWNT concentrations and polymer additions (excepting PCF-NT-**A4**-c and d1). The addition of up to 3 mg/mL of excess unbound polymer resulted in only a minor depression in μ_h for devices prepared from c and d1 dispersions. For PFMB-NT samples, μ_h declined rapidly upon polymer addition, with the combination of Raman rinsing studies and analysis of AFM height profiles demonstrating that 4 × 1 mL rinses were not sufficient above 2 mg/mL polymer addition for most SWNT concentrations. Optimization of the rinsing step is facile and can be translated to any conjugated polymer-SWNT supramolecular system with substrates of various sizes. Determination

of the number (and volume) of the rinses will depend on the polymer structure and substrate area, with simple Raman and AFM analysis used to confirm removal.

Quantifying the exact amount of excess polymer present in the **EP** dispersions is challenging, with the presence of both bound and unbound polymer, possible dynamic binding/unbinding of polymer chains from the SWNTs, and the potential for multiple chains aggregating onto a single SWNT, all contributing to polymer absorption signals in UV-Vis-NIR spectra. Furthermore, the polymer absorption peaks overlap with the S_{33} absorption range for SWNTs, complicating attempts to calculate the excess polymer concentration in the **EP** dispersion through UV-Vis-NIR absorption spectroscopy. Quantification through XPS analysis was also not possible as the drop-cast films were too thin.

Based on the combined results from Raman rinsing studies, TFT performance, and AFM analysis, we estimate that the concentration of unbound excess polymer is around or below 2 mg/mL for both PCF-NT-**EP**-c and PFMB-NT-**EP**-c. While these dispersions resulted in preeminent device performance in this report and are also the fastest and most economical to produce, it is possible they may not be indicative of the "optimal" concentration. Ultimately, determination of the precise ratio of unbound polymer to polymer-SWNT for a given polymer system will be a combination of several factors: polymer structure, solvent, solubility (of both the polymer and supramolecular composites), desired TFT device performance, and shelf life and stability of the ink.

3.7.5 A Comparison of PCF and PFMB

Both conjugated polymers PCF and PFMB have been demonstrated to be effective at sorting and dispersing large diameter sc-SWNTs.[36,37] Both polymer backbones consist of a fluorene moiety: PCF consists of a fluorene copolymerized with a carbazole, and PFMB consists of fluorene copolymerized with a dimethoxybenzene. The alkyl side chain of PFMB is longer with 16 carbons, compared to 12 and 14 carbons for the fluorene and carbazole moieties on PCF, respectively. The longer alkyl side chain length suggests that PFMB may be more effective at selectively sorting larger diameter sc-SWNTs. In this study, the dispersion prepared using PFMB had an absorption peak ratio of ϕ_i = 0.43, while the dispersion prepared using PCF had an absorption peak ratio of ϕ_i = 0.40. To the extent that it could be measured spectroscopically, the PFMB-SWNT dispersion seems to be slightly purer than the PCF-SWNT dispersion. Though, it is

difficult to say to what extent the difference in ϕ_i was due to sc-SWNT purity as opposed to error in the UV-vis-NIR measurement and ϕ_i calculation. When incorporated into TFTs, both dispersions could produce TFTs with high $I_{ON/OFF}$, so any differences in sc-SWNT purity were not manifested in TFT performance. With respect to the molecular weight, PFMB and PCF had a number-average molecular weight of 75.8 kDa ($Đ$ = 1.99) and 46.3 kDa ($Đ$ = 3.15), respectively. Thus, PFMB and PCF have a number-average degree of polymerization of 101 and 46 repeat units, respectively.

When incorporated into TFTs, it was observed that PFMB-SWNT dispersions exhibited more hysteresis compared to PCF-SWNT dispersions. This could be due to the polymer backbone of PFMB, which contains a highly electron-withdrawing dimethoxybenzene group. The dimethoxybenzene group could be responsible for an increase in charge trapping, which would manifest has current hysteresis in the transfer curves.

3.7.6 Number of TFTs Characterized

Table 3.3: Number of TFT devices tested and averaged for each condition, where SWNT concentration is denoted by: c (concentrated, 2.7 a.u. at ~937 nm), d1 (dilution 1, 1.7 a.u.) and d2 (dilution 2, 1.2 a.u.).

	PCF-NT			PFMB-NT		
	c	**d1**	**d2**	**c**	**d1**	**d2**
NP	40	30	46	62	71	64
A2	27	49	27	42	43	66
A3	55	42	27	29	52	52
A4	26	35	26	28	28	26
EP	30	31	26	25	29	68

At least two chips (with 20 individual TFTs per substrate) were prepared for each polymer-sorted SWNT condition. Data from non-ideal devices were not included in averages, including devices with shorted electrodes. An adhesion layer was not incorporated on account of the incompatible work function overlap between chromium and our polymer-sorted SWNT dispersions. Due to the weak adhesion of gold to the SiO_2 surface, some electrode pads were damaged when the chips were placed in the auto tester. The resulting devices were excluded due to non-ideal behaviour, such as behaving more like open circuits. Additional wafers were fabricated in situations where 25 working devices were not obtained from the first two wafers.

3.7.7 Additional TFT Data

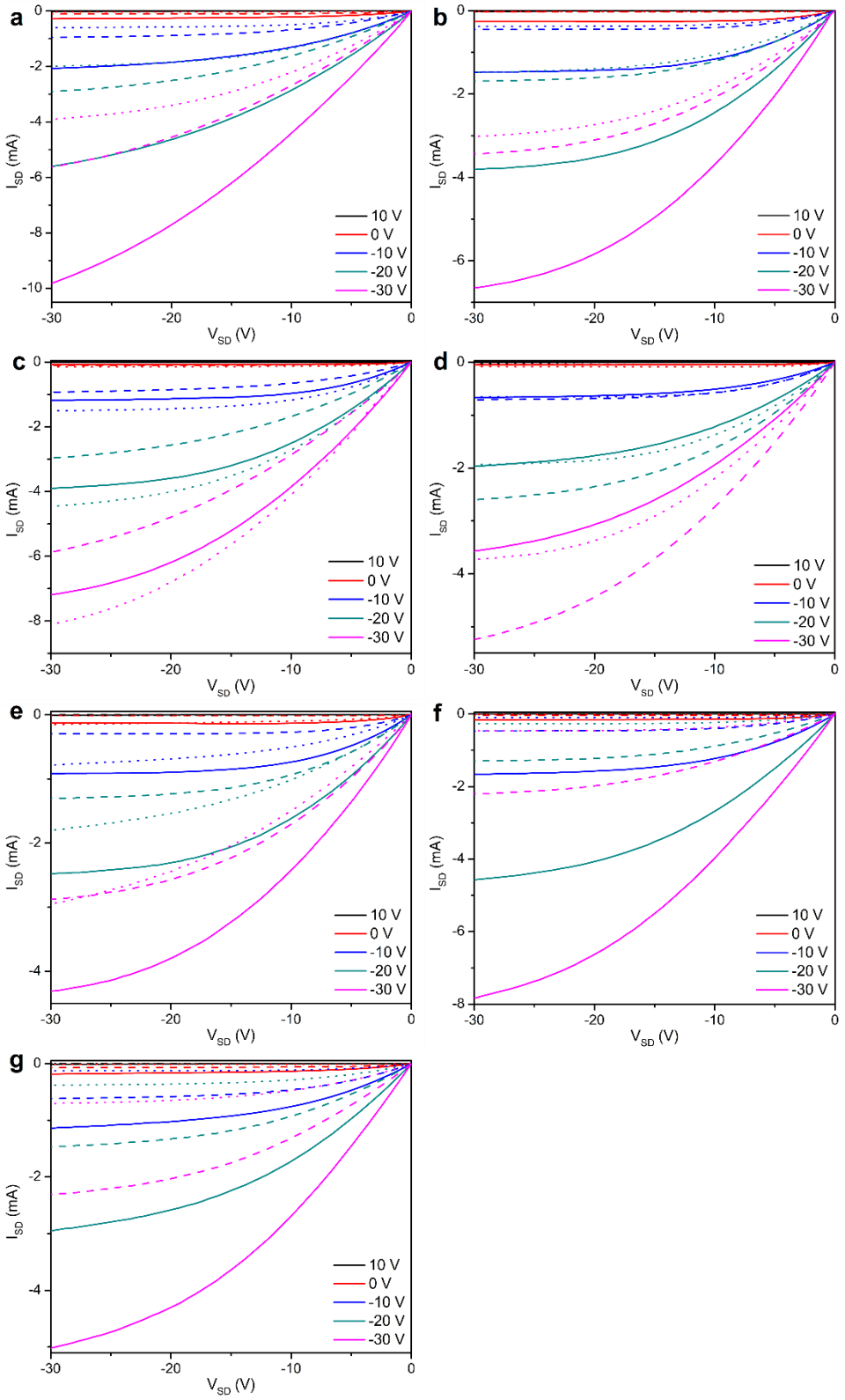

Figure 3.11: Representative output curves for all PCF-NT dispersions, at all SWNT concentrations, for (a) **NP**, (b) **EP**, (c) **A0.4**, (d) **A0.8**, (e) **A2**, (f) **A3** and (g) **A4**. Solid lines represent c samples, dashed lines d1 samples, and dotted lines d2 samples.

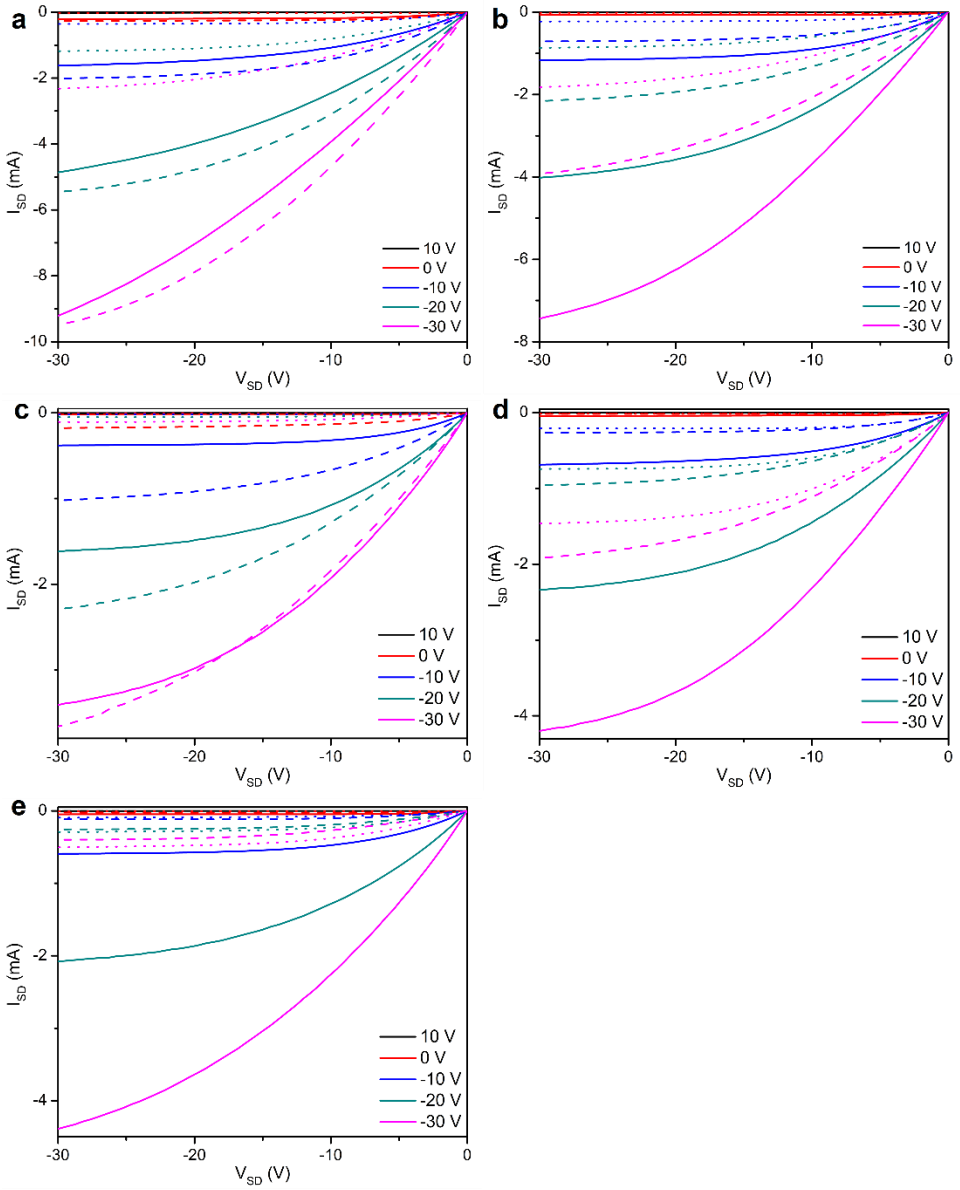

Figure 3.12: Representative output curves for all PFMB-NT dispersions, at all SWNT concentrations, for (a) **NP**, (b) **EP**, (c) **A2**, (d) **A3**, and (e) **A4**. Solid lines represent c samples, dashed lines d1, and dotted lines d2.

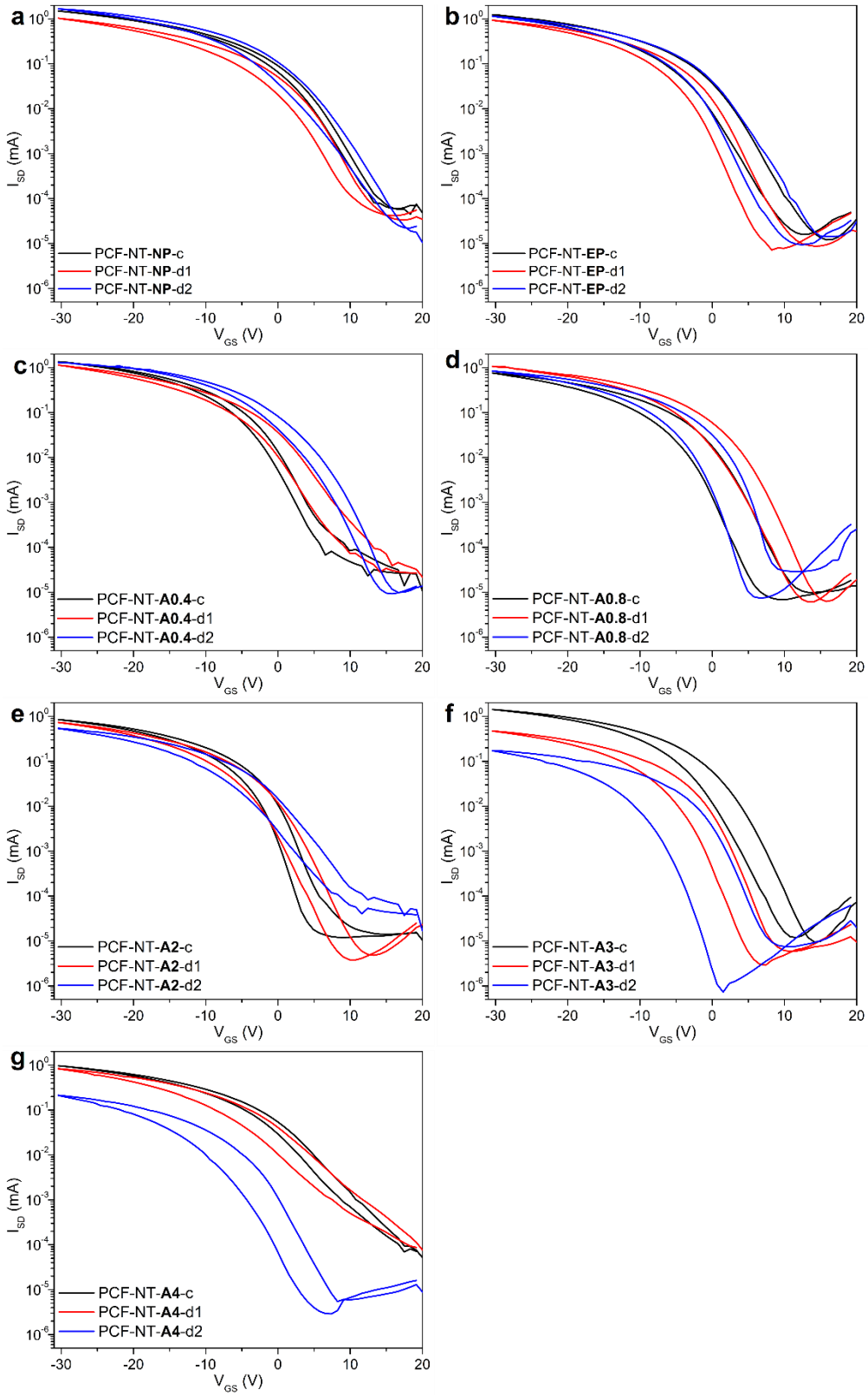

Figure 3.13: Representative transfer curves for PCF-NT dispersions at all SWNT concentrations (a) **NP**, (b) **EP**, (c) **A0.4**, (d) **A0.8**, (e) **A2**, (f) **A3**, and (g) **A4**.

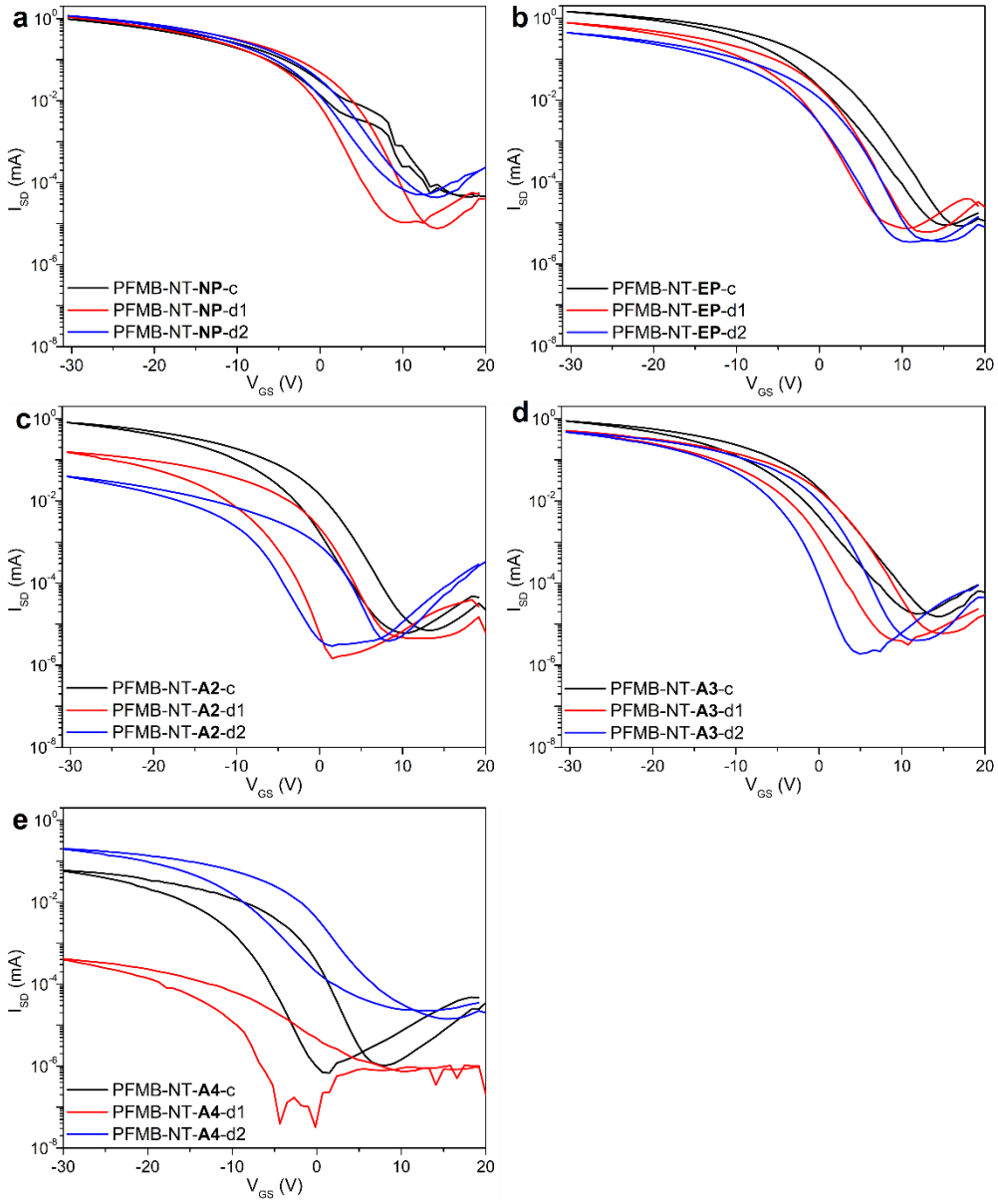

Figure 3.14: Representative transfer curves for all SWNT concentrations for PFMB-NT samples (a) **NP**, (b) **EP**, (c) **A2**, (d) **A3**, and (e) **A4**.

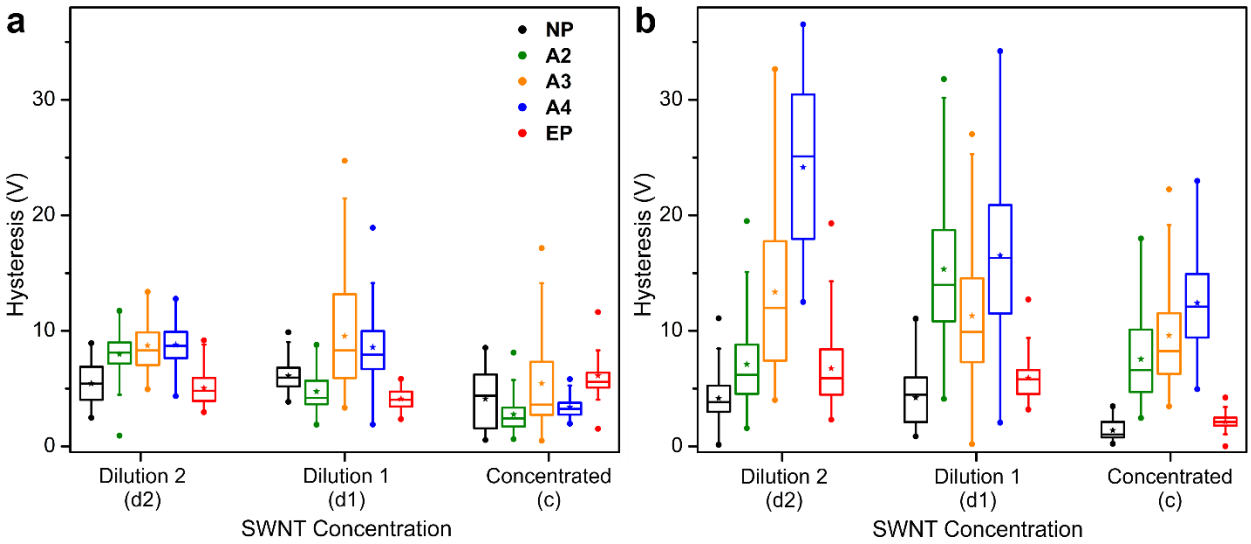

Figure 3.15: Box plots of hysteresis (*H*) values for (a) PCF-NT and (b) PFMB-NT. The box indicates the interquartile range, the horizontal line (within the box) is the median, and the star is the mean. Vertical lines indicate the difference between the 5th and 95th percentile, with the maximum and minimum values denoted by circles.

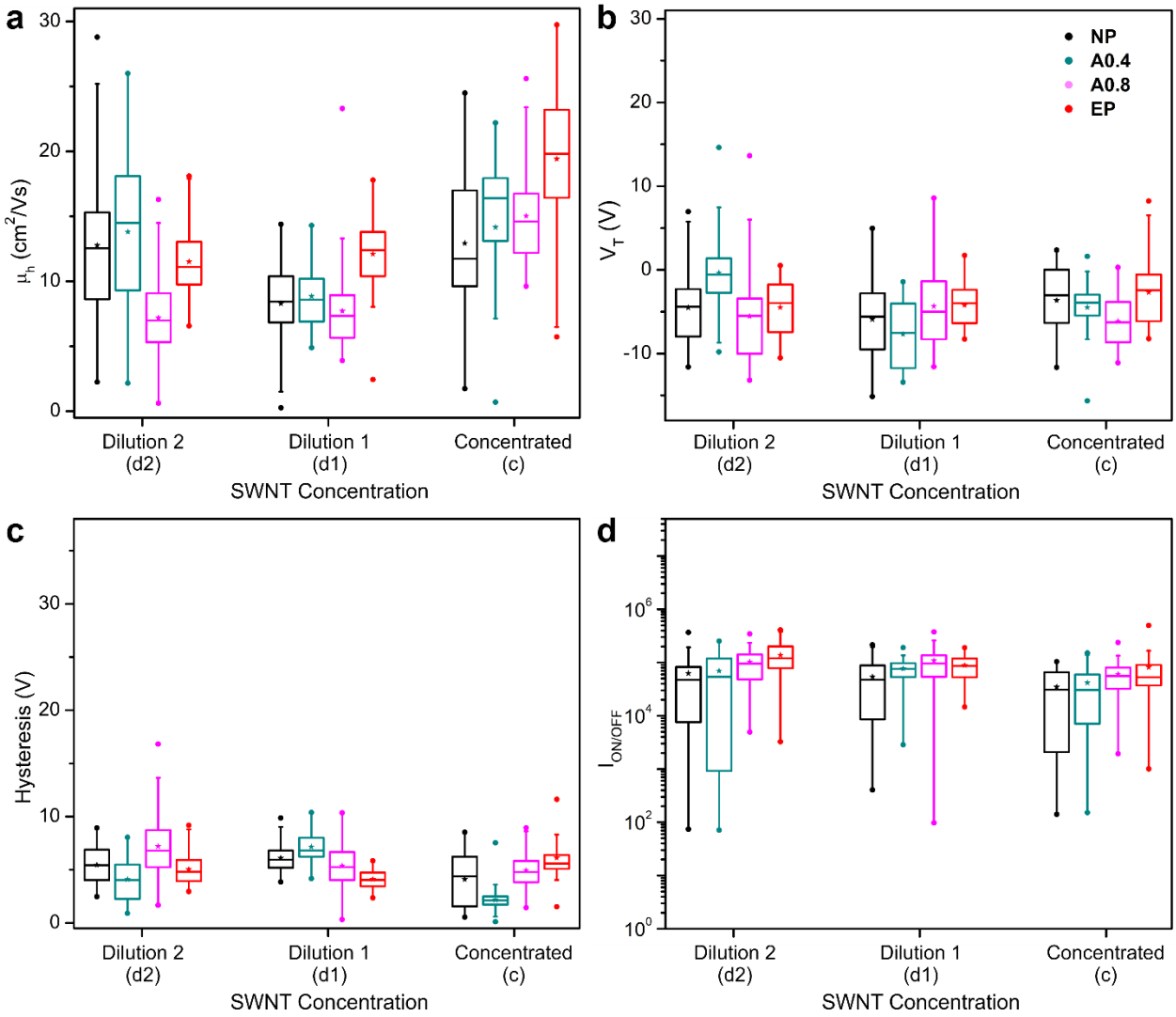

Figure 3.16: Box plots of (a) average hole mobility (μ_h), (b) threshold voltage (V_T), (c) hysteresis (H) and (d) on/off ratio ($I_{ON/OFF}$) for TFTs fabricated from PCF-NT samples with 0.4 mg/mL (**A0.4**) or 0.8 mg/mL (**A0.8**) of excess polymer added. Data for PCF-NT-**NP** and PCF-NT-**EP** are also shown for comparison. The box indicates the interquartile range, with the horizontal line and star within the box denoting the median and mean, respectively; the vertical lines show the difference between the 5th and 95th percentile, and the dots represent the maximum and minimum values.

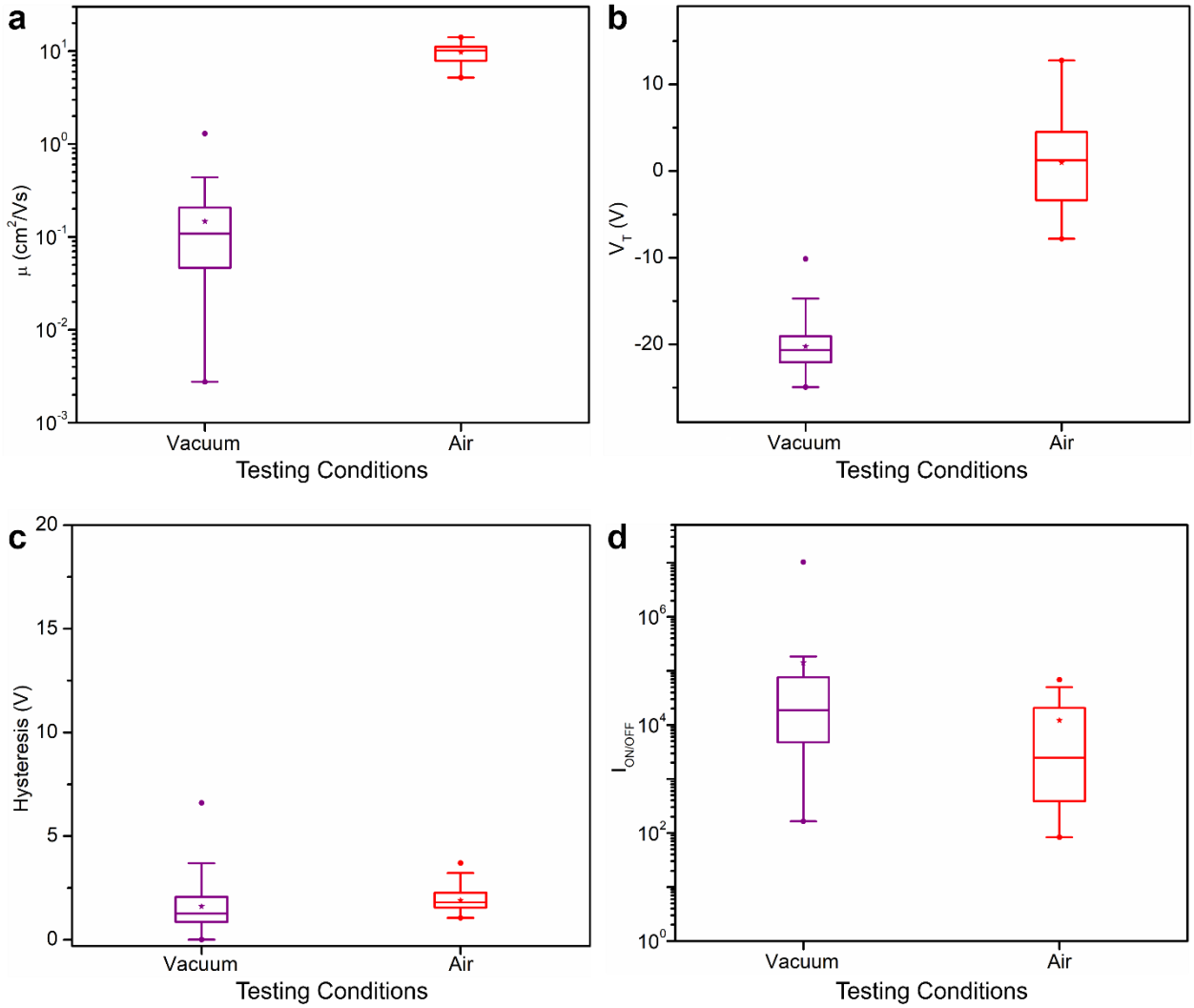

Figure 3.17: Box plots of (a) average mobility (μ_h), (b) threshold voltage (V_T), (c) hysteresis (H) and (d) on/off ratio ($I_{ON/OFF}$) for TFTs prepared from PCF-NT-**EP**-d1 tested in various environments. Devices (n = 32) were first characterized in vacuum (P < 0.1 Pa) using a probe station, then exposed to air and tested using auto tester apparatus. The same testing ranges and parameters were used for both experiments. Mobility is plotted on a log scale due to a large difference in values.

3.7.8 Additional Raman Maps

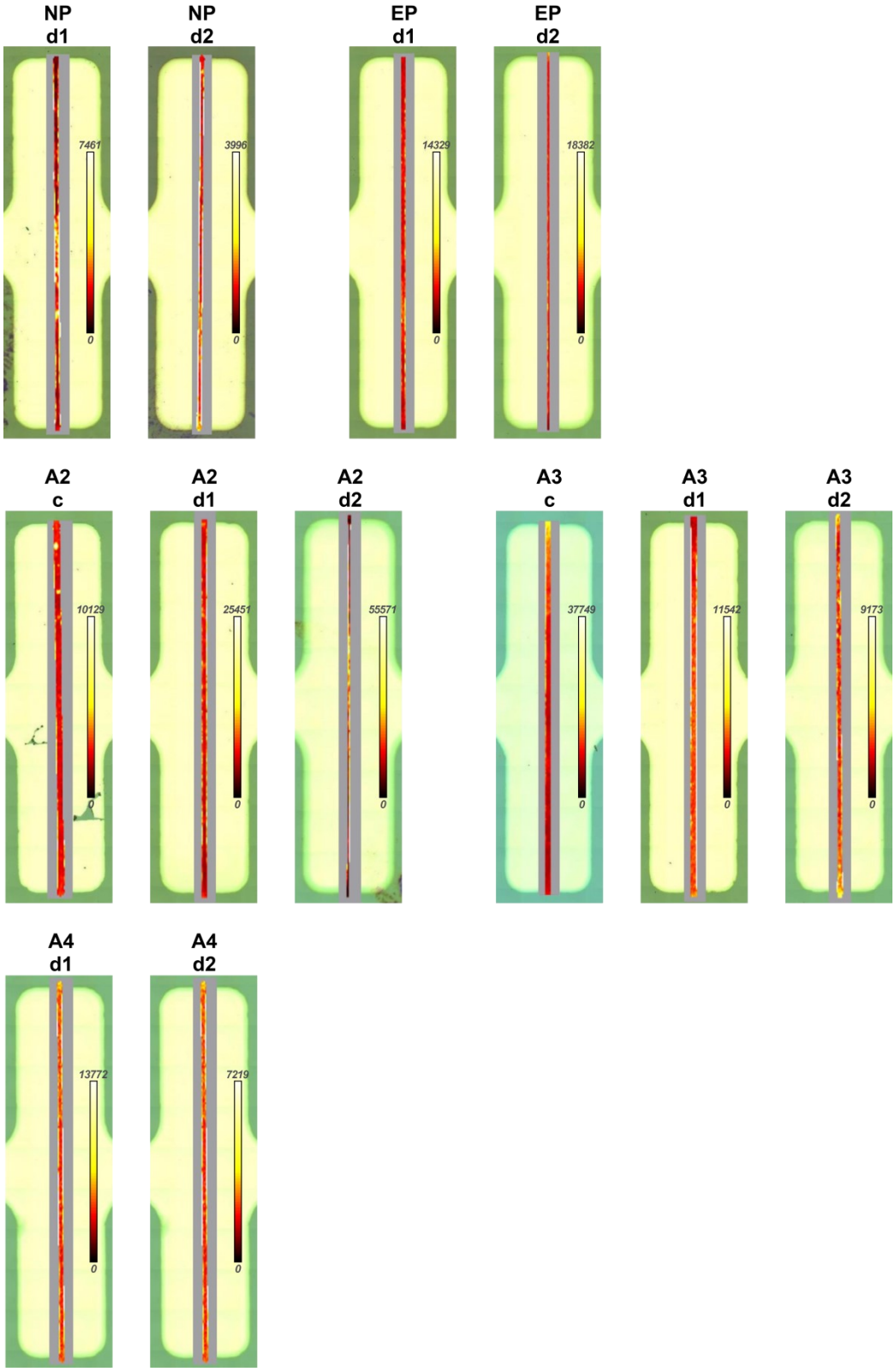

Figure 3.18: Representative Raman maps for all other PCF-NT dispersions at the various SWNT concentrations and excess polymer additions. Data points that overlapped with the gold electrodes (grey boxes) were not included in the intensity measurements shown in **Figure 3.5**d. Note: c = concentrated, d1 = dilution 1 and d2 = dilution 2, in reference to SWNT concentration.

3.7.9 Additional AFM Images and Analysis

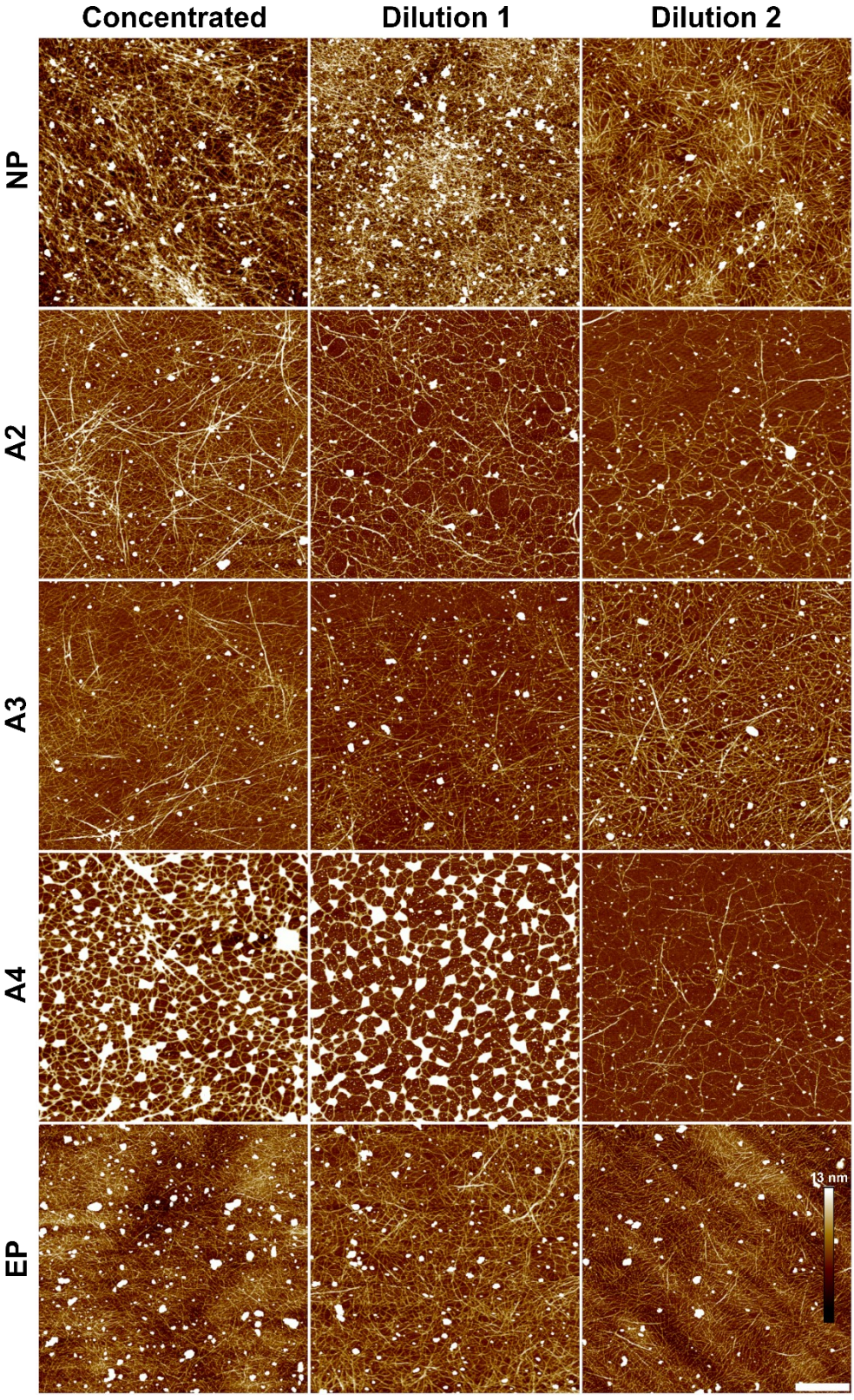

Figure 3.19: Representative AFM images for all PFMB-NT TFTs at all SWNT concentrations and polymer additions. Images have been plotted on a height scale of 13 nm, with the white scale bar representing 1 μm.

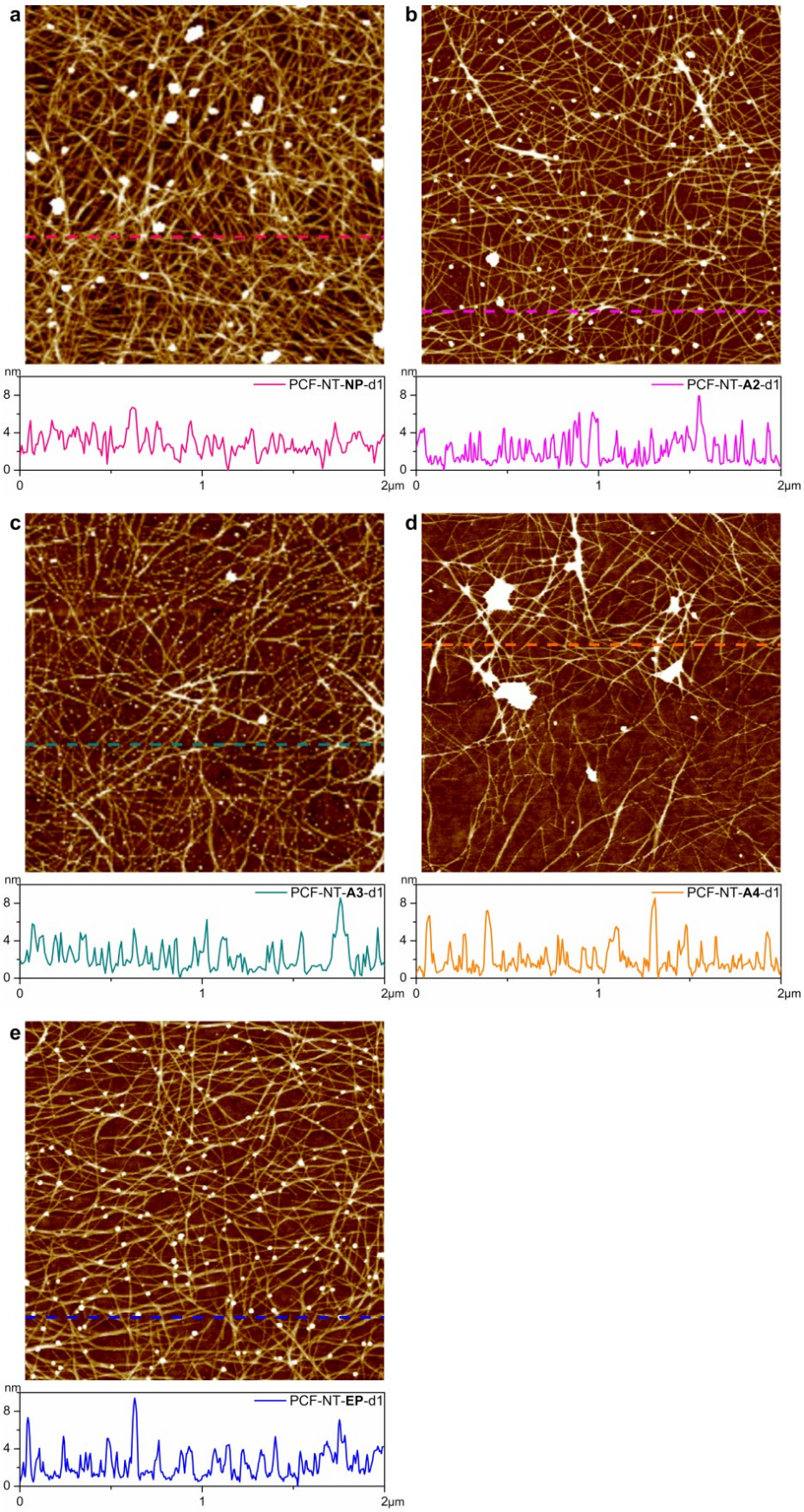
a
b
c
d
e
nm
8
4
0
0
1
2μm
PCF-NT-NP-d1
PCF-NT-A2-d1
PCF-NT-A3-d1
PCF-NT-A4-d1
PCF-NT-EP-d1

Figure 3.20: Representative AFM images with line-height profiles for PCF-NT (a) **NP**-d1, (b) **A2**-d1, (c) **A3**-d1, (d) **A4**-d1 and (e) **EP**-d1. The coloured dashed lines represent the location of the height profile located below each AFM image. All images have been cropped to 2 μm for clarity, and are plotted with a height scale of 10 nm.

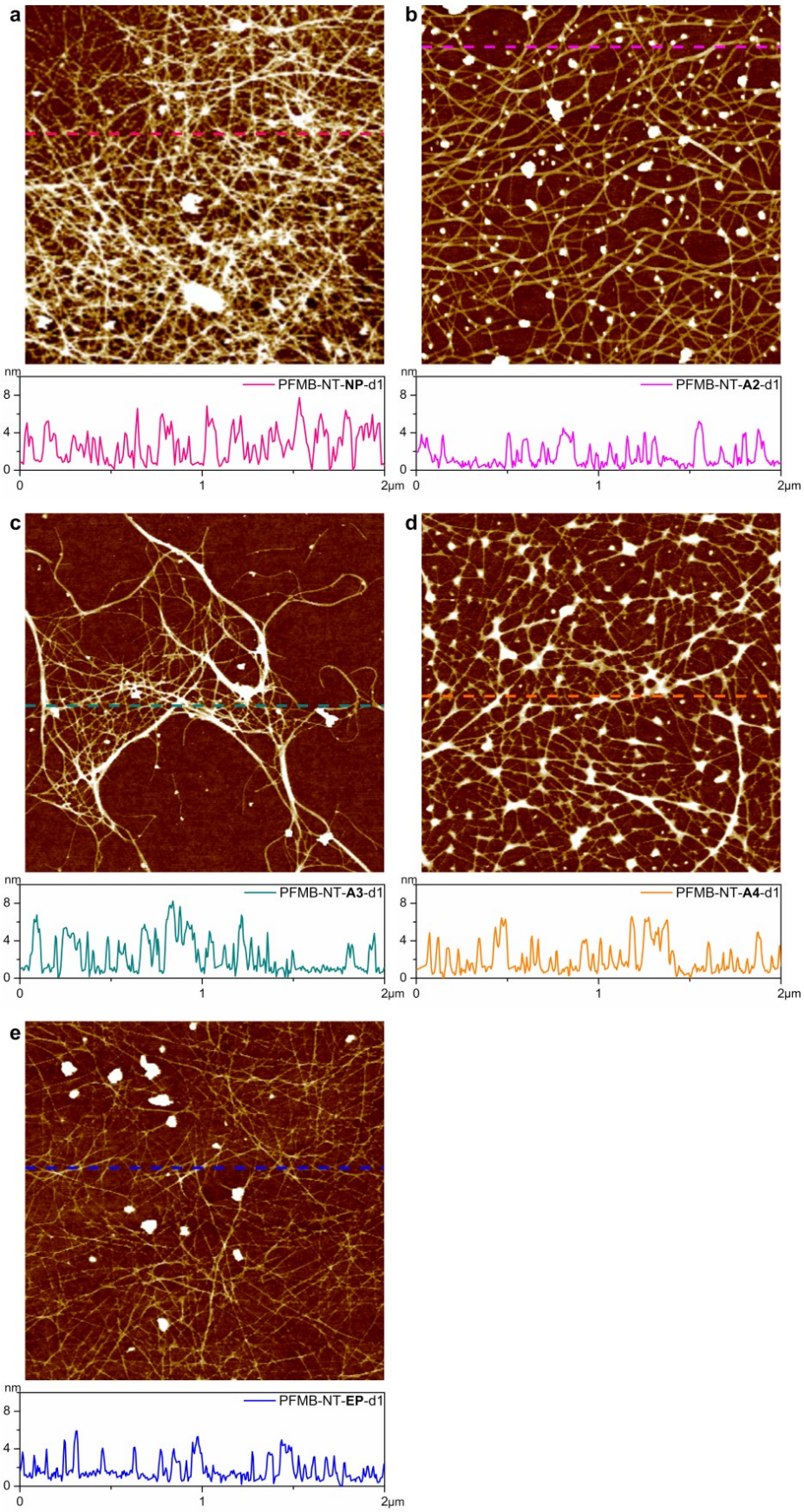
a
b
c
d
e
nm
8
4
0
0
1
2μm
PFMB-NT-NP-d1
PFMB-NT-A2-d1
PFMB-NT-A3-d1
PFMB-NT-A4-d1
PFMB-NT-EP-d1

Figure 3.21: Representative AFM images with line-height profiles for PFMB-NT (a) **NP**-d1, (b) **A2**-d1, (c) **A3**-d1, (d) **A4**-d1 and (e) **EP**-d1. The coloured dashed lines represent the location of the height profile located below each AFM image. All images have been cropped to 2 μm for clarity, and are plotted with a height scale of 10 nm.

Table 3.4: Summary of surface coverage for PFMB-NT TFTs, determined from analysing AFM images using our novel algorithm. Excess polymer residue made the determination of surface coverage in **A3** and **A4** samples challenging.

	Surface Coverage (%)		
Sample	**c**	**d1**	**d2**
PFMB-NT-NP	$36^{*} \pm 10$	$28^{*} \pm 20$	$34^{*} \pm 2$
PFMB -NT-A2	32 ± 4	22 ± 7	19 ± 10
PFMB -NT-A3	$28^{\dagger} \pm 4$	$24^{\dagger} \pm 10$	$25^{\dagger} \pm 6$
PFMB -NT-A4	$28^{\dagger} \pm 3$	$23^{\dagger} \pm 4$	$13^{\dagger} \pm 4$
PFMB -NT-EP	32 ± 5	23 ± 9	31 ± 6

**Significant bundling in films.*
†*Value overestimated due to presence of excess polymer.*

Surface coverage in AFM images was calculated after using the thresholding algorithms to segment the images into binary white (SWNT) and black (non-SWNT) pixels. It was defined as the number of white pixels in the final image.

Our novel algorithm can generate a significant amount of information about the SWNTs, including length, orientation, and location (in x-y coordinates). These aspects are not discussed in the manuscript. The dense and random nature of our thin-films makes several of these parameters, particularly orientation, irrelevant and beyond the scope of this study. These aspects of the algorithm will be investigated in future studies.

3.7.10 Algorithm for Analysis of AFM Images

The algorithm process for the analysis of AFM images is summarized below, with detailed descriptions on the following pages:

1. Convert the AFM image from colour to greyscale using the OpenCV COLOR_BGR2GRAY conversion.[59]
2. (Optional) Crop the image to 512 × 512-pixels, centred in the middle of the original data. This significantly reduces the computational time for the genetic algorithm (Step 7).
3. Preprocessing step to remove visual artefacts (background substrate, clumps of excess polymer, dust particulate) by removing all pixels above or below fixed thresholds of brightness:
    a. Pixels with a brightness of less than 16 out of 255 were removed.
    b. Pixels with a brightness of more than 248 out of 255 were removed.
4. Convert the greyscale image to a black and white image, where black represents non-nanotube space and white represents SWNTs:
    a. Several variations of thresholding algorithms were evaluated, with Otsu's method and Yen thresholding found to work the best for our images. Refinement of the choice of algorithm was made on the thickness of the SWNT films.[57,58,61]
        i. Both two and three class variations of the Otsu algorithm were explored. The number of classes is a parameter of Otsu's method that can be tuned to optimize detection quality, allowing the sensitivity of the algorithm to be chosen depending on the film morphology.
    b. The thresholding algorithms were used as follows for image segmentation:
        i. A sliding window is passed over the image, and the pixel in the centre is compared to the threshold produced for the window. If the pixel is brighter than the output of the thresholding algorithm, it is set to white; otherwise, it is set to black.
        ii. Additionally, a variation was explored where the pixels in the centre of the sliding window were compared to both the threshold of the window itself and the threshold of the entire image. This variation seemed to perform better for sparse films of SWNTs.

iii. Finally, various window sizes were explored, such as 20 × 20 pixels, 30 × 30 and 50 × 50 pixels.

c. (Optional) Small visual artefacts can be removed by applying a median blur with a radius of 7 pixels after the segmentation.[59]

5. Define a fitness function for the solver. In our case, the quality of the solution is the number of pixels matching between the original image and the candidate solution.
6. Define parameters for which we iteratively solve: angles, widths, lengths and positions of many rectangles (each rectangle corresponding to a nanotube).
7. Use a genetic algorithm to iteratively solve for the set of nanotubes found within the image.[62]
8. Export the set of nanotubes detected in the image for further processing.
9. (Optional) Use a post-processing step to reconcile overlapping nanotubes, as well as colinear segments into the correct nanotubes.

3.7.10.1 Colour to Grey Conversion

To properly analyze the images, we converted the AFM images from colour to greyscale to permit the establishment of a relationship between the pixel brightness (from black (0) to white (255)) and the height of the film. This conversion is accomplished using the COLOR_BGR2GRAY method in Python from the open-source OpenCV library.[59] This facilitates analysis of AFM images from any image format or colour scale, making our algorithm translatable to images obtained from a variety of microscopes.

3.7.10.2 Image Cropping

Images with more pixels require significantly greater computing time. To offset this, we investigated the validity of analyzing a cropped 512 × 512 px image (corresponding to 1.25 × 1.25 μm^2) instead of the full 5 × 5 μm^2 image. For this study, cropped images were always confined to the image's centre. However, it is facile to shift this to another area of the image if desired. A comparison of the average surface area coverage of the images before (**Table 3.2**) and after (**Table 3.5**) cropping showed the same trends in surface coverage values, and all values matched within experimental error. A slight increase in standard deviation was noted for many of the cropped images. This was attributed to the presence of larger features (such as dust particles and/or excess polymer) having a greater impact on the calculation for a smaller surface area.

Table 3.5: Summary of surface coverage and number of SWNTs in AFM images of PCF-NT TFTs. Values were calculated from cropped (1.25 × 1.25 μm^2) images to reduce analysis time.

	Surface Coverage (%)			Number of SWNTs (in 1.25 × 1.25 μm^2)		
Sample	**c**	**d1**	**d2**	**c**	**d1**	**d2**
PCF-NT-NP	47* ± 20	50* ± 10	40* ± 20	400 ± 80	390 ± 60	330 ± 100
PCF-NT-A0.4	65 ± 5	43 ± 10	55 ± 20	460 ± 30	400 ± 80	420 ± 90
PCF-NT-A0.8	64 ± 3	62 ± 10	66 ± 3	450 ± 20	460 ± 60	450 ± 30
PCF-NT-A2	53 ± 20	55 ± 20	10 ± 3	400 ± 100	400 ± 80	80 ± 30
PCF-NT-A3	63 ± 6	24 ± 3	14 ± 3	440 ± 40	240 ± 30	140 ± 40
PCF-NT-A4	51† ± 20	16 ± 5	16 ± 5	390 ± 90	140 ± 70	160 ± 60
PCF-NT-EP	54 ± 10	54 ± 20	58 ± 10	400 ± 40	400 ± 80	430 ± 21

**Significant bundling in films.*
†Value overestimated due to presence of excess polymer.

3.7.10.3 Preprocessing

Once the height-to-brightness scale is established, artefacts such as excess polymer, dust or glitches (caused by the probe tip skipping) can be automatically removed by removing all exceptionally bright pixels. As most of these artefacts are typically much taller than the polymer-coated SWNTs, the algorithm removes all pixels above a certain brightness threshold, which translates to removing entities that were measured to be above a certain height in the film. Additionally, pixels below a specified brightness can be removed as well, leading to better detection of low-density regions of the SWNT films and preventing artefacts in the background wafer from being included in the analysis.

3.7.10.4 Image Segmentation

The contour detection stage is one of the two essential operations in the algorithm, with the objective of converting the image from height map data to a binary contour, allowing us to process the SWNT contours directly. The main advantage of this process is that the analysis only depends on the presence or absence of a nanotube in each pixel rather than analyzing height data (which is a continuous value). The technique used to detect contours from the original height data is a modified approach using Otsu and Yen thresholding.[57,58,61]

A naïve approach to detecting contours would be to take every pixel above a certain height and classify it as a nanotube. This approach is deficient in that a fixed threshold probably would not work equally well across all input images. Additionally, polymer-coated SWNTs may not all appear to be the same height, and dense mats of tubes will have drastically different height features, with certain SWNTs very prominent in the foreground and others barely distinguishable from the background. The solution is to use dynamic or adaptive thresholding. Otsu and Yen thresholding are techniques that analyze the pixels in an image and determine a threshold that separates the image pixels into two distributions based on brightness: the foreground and the background.[57,58,61]

As shown in **Figure 3.21**, Otsu thresholding is reasonably effective at detecting SWNTs but fails in regions with faint (thinner) SWNTs, as well as in high-density regions where the background might appear brighter than some of the fainter nanotubes. This problem can be resolved using local thresholding. In a typical (or global) threshold, a single separation threshold between the foreground and background is computed for the entire image. However, it is essential to note that in random SWNT films, different regions of the film might have differing foreground and background brightness. A threshold for each small region within the image should be computed such that the separation between the film's foreground and background depends only on a small local region, as opposed to the overall profile of the film (**Figure 3.22**).

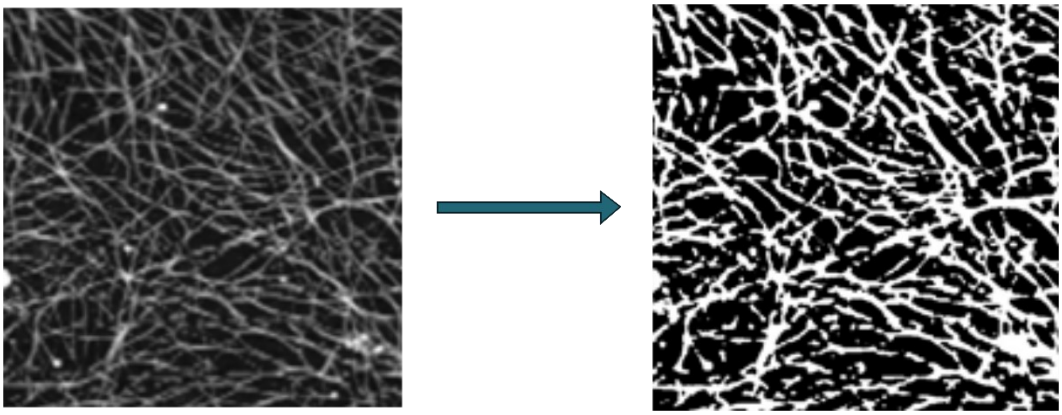

Figure 3.22: Example of global Otsu thresholding of a greyscale AFM image. Note the gaps in the SWNTs that are close in colour to the background, as well as the filled gaps between tubes in regions of high nanotube density.

Comparison of **Figure 3.21** and **Figure 3.22** clearly shows that local Otsu thresholding provides much better contour detection of individual SWNTs, in both low profile and high-density regions. Following the local Otsu thresholding, the final component in the contour detection step is to apply a median blur to remove any sharp edges or small protrusions (detected as a contour by the local Otsu thresholding) that should not be counted as a nanotube.

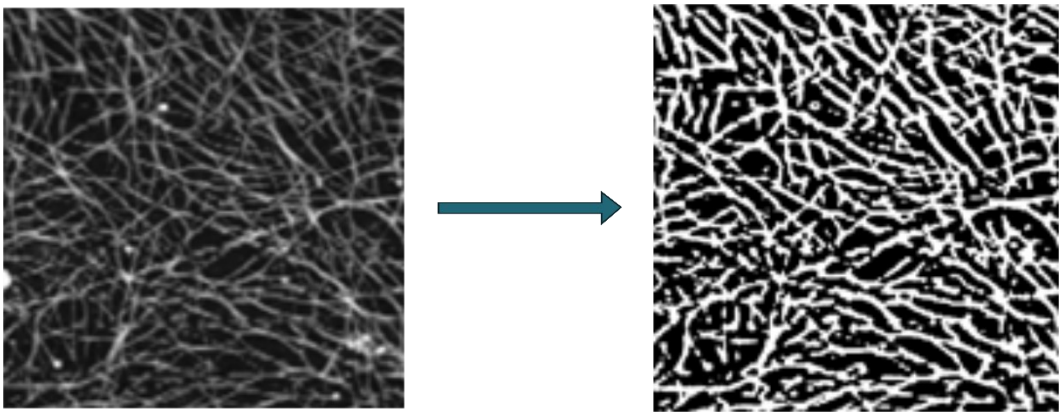

Figure 3.23: Example of local Otsu thresholding of a greyscale image. Gaps observed in fainter (thinner) SWNTs have been dramatically reduced, with greater distinction of SWNTs in high-density regions.

A vital benefit of this approach is that local thresholding and segmentation can be applied to numerous thresholding algorithms with many parameters that can be tuned. This allows for facile selection of the proper thresholding algorithm for optimal performance across a wide range of film morphologies. Parameters such as the window sizes or, in the case of Otsu's method, the number of classes, affected the quality of the segmentation significantly, allowing the algorithms to be easily tuned for optimum nanotube detection. We found that Otsu and Yen thresholding worked best for SWNT films, with a local and global 3-class Otsu method and a 50 × 50 pixel window for dense films (**Figure 3.23**), while a local and global 2-class Otsu method with a 50 × 50 pixel window was better suited for removal of background features in sparse networks (**Figure 3.24**).[58]

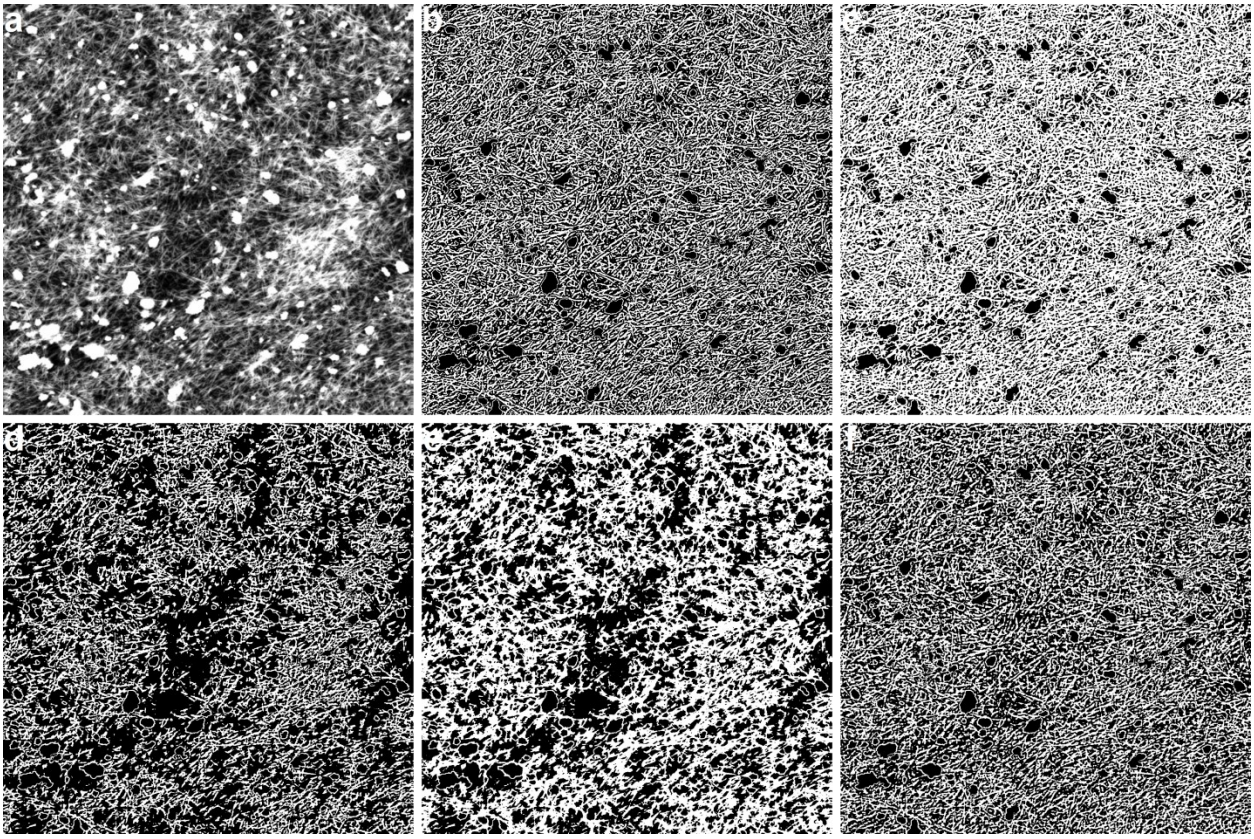

Figure 3.24: Demonstration of variations in sensitivity and detection quality for a dense SWNT film. (a) Original greyscale image of PCF-NT-**NP**-c with the same image analyzed using various detection algorithms: (b) 2 class local Otsu, (c) 3 class local Otsu, (d) local Yen compared to global Yen, (e) 3 class local Otsu compared and 2 class global Otsu and (f) local Yen. All images are 5×5 μm^2.

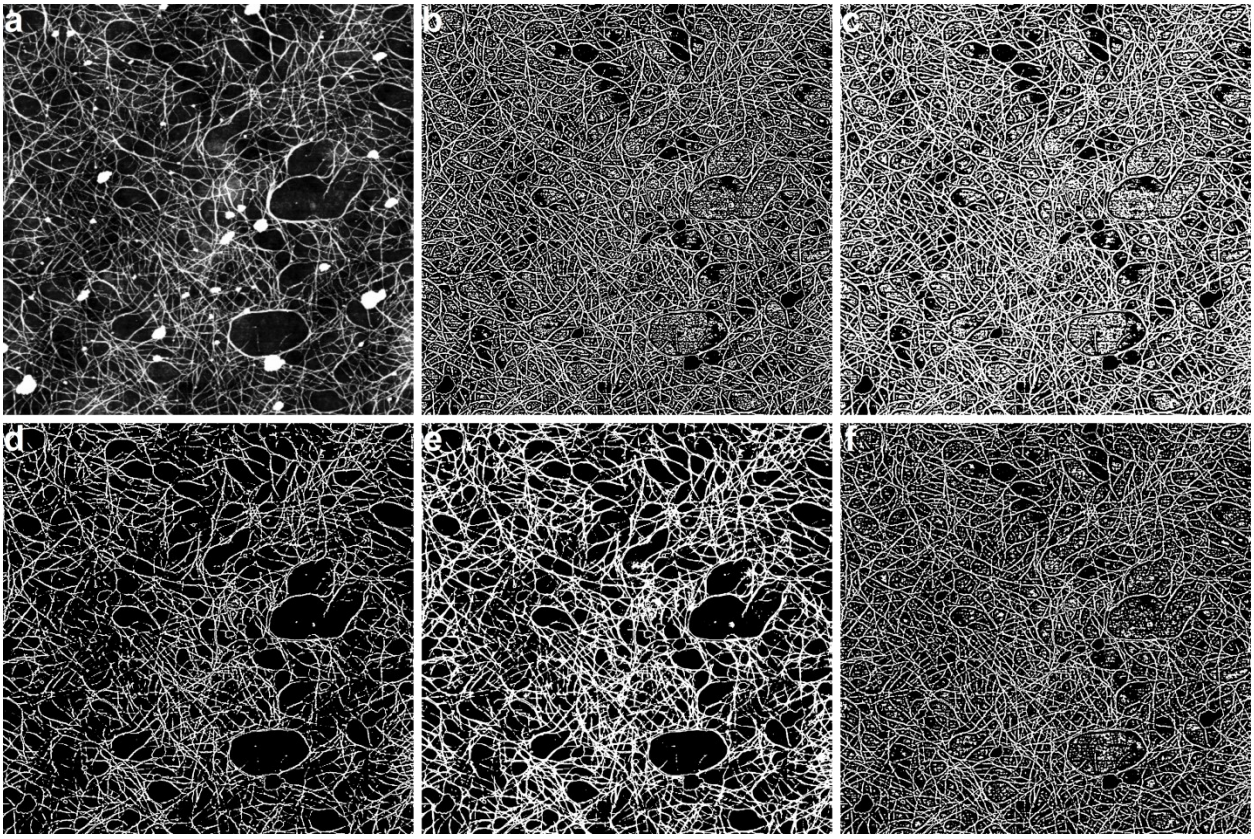

Figure 3.25: Demonstration of variations in sensitivity and detection quality for a sparse SWNT film. (a) Original greyscale image of PCF-NT-**NP**-d2 with the same image analyzed using various detection algorithms: (b) 2 class local Otsu, (c) 3 class local Otsu, (d) local Yen compared to global Yen, (e) 3 class local Otsu compared and 2 class global Otsu and (f) local Yen. All images are 5×5 μm^2.

3.7.10.5 Genetic Algorithm

A simple genetic algorithm was used, implemented by the PyEasyGa module in Python.[62] When using a genetic algorithm, three things must be defined: the parameters being optimized, the update operations that are allowed when iterating the solution, and a "fitness function" which describes numerically how acceptable a given solution is. In a genetic algorithm, an "individual" is a set of specific parameter values applicable to the problem being solved. The set of all individuals being considered is called the "population." The genetic algorithm iteratively updates and combines individuals through operations inspired by biology while selecting those with the best fitness from the population to iteratively converge to a final set of parameters, emulating evolution in nature, hence the name "genetic algorithm."

In the case of SWNT films, an individual is a collection of nanotubes replicating the given AFM data. Analogously, in nature, an organism's genome is comprised of a set of genes. In this approach, individuals are comprised of sets of genes, where each gene represents an individual nanotube in the film. In practice, the genes of the individual consist of the parameters for the nanotubes (length, width, orientation, position). When iterating the solutions, each individual is subject to random changes to various parameters called "mutations." Additionally, two individuals can be combined to form a new individual in a process called "crossover."

The allowed mutations are random modification of position, length or orientation of a current gene, the addition of a new random gene, or the deletion of a current gene. This permits genetic algorithms to iteratively solve for the number of SWNTs in the image and their size, position, and orientation. Finally, the best individual (or solution) was chosen based on how many pixels matched between the segmented AFM data and the proposed set of nanotubes, such that the solution is as close to the AFM data as possible. The objective function used was a simple sum of different pixels in the source images and the solution. More advanced schemes could be used, such as prioritizing true recall or precision, but were not explored in this paper.

3.7.10.6 Post-Processing Step

The final step of the algorithm is to combine duplicate nanotubes into a single entity. For example, if the solution detects a single nanotube as two smaller nanotubes that are aligned end-to-end, there should be a consolidation stage to bring the two segments of the nanotube into a single entity. The algorithm for this step is as follows:

1. For all pairs of nanotubes detected *a*, *b*
    a. Calculate the distance between the center of *a* and *b* projected along the length axis and the width axis of *a*, called *dist_length*, *dist_width*
    b. If following conditions are met, nanotubes are segments of the same tube
        i. abs(*a.angle* – *b.angle*) <= tolerance
        ii. *dist_length* <= (*a.length* + *b.width*) / 2
        iii. *dist_width* <= (*a.width* + *b.width*) / 2
    c. else
        i. calculate intersection of *a* and *b* along the length axis, called point *c*

ii. calculate projected distance along the length axis of *a* to *c* and *b* to *c*, called *dist_ac* and *dist_bc*

iii. if following conditions are met, nanotubes are segments of the same tube

    1. abs(*a.angle* – *b.angle*) <= tolerance
    2. *dist_ac* <= (*a.length* + *a.width*) / 2
    3. *dist_bc* <= (*b.length* + *b.width*) / 2

iv. otherwise nanotubes are separate

3.8 References

(1) Nish, A.; Hwang, J.-Y.; Doig, J.; Nicholas, R. J. Highly Selective Dispersion of Single-Walled Carbon Nanotubes Using Aromatic Polymers. *Nat. Nanotechnol.* **2007**, *2*, 640–646.

(2) Jakubka, F.; Schießl, S. P.; Martin, S.; Englert, J. M.; Hauke, F.; Hirsch, A.; Zaumseil, J. Effect of Polymer Molecular Weight and Solution Parameters on Selective Dispersion of Single-Walled Carbon Nanotubes. *ACS Macro Lett.* **2012**, *1*, 815–819.

(3) Fong, D.; Adronov, A. Recent Developments in the Selective Dispersion of Single-Walled Carbon Nanotubes Using Conjugated Polymers. *Chem. Sci.* **2017**, *8*, 7292–7305.

(4) Mistry, K. S.; Larsen, B. A.; Blackburn, J. L. High-Yield Dispersions of Large-Diameter Semiconducting Single-Walled Carbon Nanotubes with Tunable Narrow Chirality Distributions. *ACS Nano* **2013**, *7*, 2231–2239.

(5) Wang, K.; Dong, H.; Zhou, D.; Ito, Y.; Hu, L.; Zhang, Z.; Zhu, X. Facile Fabrication of Semiconducting Single-Walled Carbon Nanotubes Patterns on Flexible Substrate Based on a Photoimmobilization Technique. *ACS Appl. Mater. Interfaces* **2020**, *12*, 8722–8729.

(6) Lei, T.; Shao, L. L.; Zheng, Y. Q.; Pitner, G.; Fang, G.; Zhu, C.; Li, S.; Beausoleil, R.; Wong, H. S. P.; Huang, T. C.; Cheng, K. -T.; Bao, Z. Low-Voltage High-Performance Flexible Digital and Analog Circuits Based on Ultrahigh-Purity Semiconducting Carbon Nanotubes. *Nat. Commun.* **2019**, *10*, 2161.

(7) Gomulya, W.; Costanzo, G. D.; de Carvalho, E. J. F.; Bisri, S. Z.; Derenskyi, V.; Fritsch, M.; Fröhlich, N.; Allard, S.; Gordiichuk, P.; Herrmann, A.; Marrink, S. J.; dos Santos, M. C.; Scherf, U.; Loi, M. A. Semiconducting Single-Walled Carbon Nanotubes on Demand by Polymer Wrapping. *Adv. Mater.* **2013**, *25*, 2948–2956.

(8) Wang, H.; Mei, J.; Liu, P.; Schmidt, K.; Jiménez-Osés, G.; Osuna, S.; Fang, L.; Tassone, C. J.; Zoombelt, A. P.; Sokolov, A. N.; Houk, K. N.; Toney, M. F.; Bao, Z. Scalable and Selective Dispersion of Semiconducting Arc-Discharged Carbon Nanotubes by Dithiafulvalene/Thiophene Copolymers for Thin Film Transistors. *ACS Nano* **2013**, *7*, 2659–2668.

(9) Ding, J.; Li, Z.; Lefebvre, J.; Cheng, F.; Dubey, G.; Zou, S.; Finnie, P.; Hrdina, A.; Scoles, L.; Lopinski, G. P.; Kingston, C. T.; Simard, B.; Malenfant, P. R. L. Enrichment of Large-Diameter Semiconducting SWCNTs by Polyfluorene Extraction for High Network Density Thin Film Transistors. *Nanoscale* **2014**, *6*, 2328–2339.

(10) Wang, H.; Koleilat, G. I.; Liu, P.; Jiménez-Osés, G.; Lai, Y.-C.; Vosgueritchian, M.; Fang, Y.; Park, S.; Houk, K. N.; Bao, Z. High-Yield Sorting of Small-Diameter Carbon Nanotubes for Solar Cells and Transistors. *ACS Nano* **2014**, *8*, 2609–2617.

(11) Dowgiallo, A. M.; Mistry, K. S.; Johnson, J. C.; Reid, O. G.; Blackburn, J. L. Probing Exciton Diffusion and Dissociation in Single-Walled Carbon Nanotube-C_{60} Heterojunctions. *J. Phys. Chem. Lett.* **2016**, *7*, 1794–1799.

(12) Han, S. J.; Tang, J.; Kumar, B.; Falk, A.; Farmer, D.; Tulevski, G.; Jenkins, K.; Afzali, A.; Oida, S.; Ott, J.; Hannon, J.; Haensch, W. High-Speed Logic Integrated Circuits with Solution-Processed Self-Assembled Carbon Nanotubes. *Nat. Nanotechnol.* **2017**, *12*, 861–865.

(13) Zhu, C.; Chortos, A.; Wang, Y.; Pfattner, R.; Lei, T.; Hinckley, A. C.; Pochorovski, I.; Yan, X.; To, J. W.; Oh, J. Y.; Tok, J. B.-H.; Bao, Z.; Murmann, B. Stretchable Temperature-Sensing Circuits with Strain Suppression Based on Carbon Nanotube Transistors. *Nat. Electron.* **2018**, *1*, 183–190.

(14) Lee, D.; Yoon, J.; Lee, J.; Lee, B.-H.; Seol, M.-L.; Bae, H.; Jeon, S.-B.; Seong, H.; Im, S. G.; Choi, S.-J.; Choi, Y.-K. Logic Circuits Composed of Flexible Carbon Nanotube Thin-Film Transistor and Ultra-Thin Polymer Gate Dielectric. *Sci. Rep.* **2016**, *6*, 26121.

(15) Tang, J.; Cao, Q.; Tulevski, G.; Jenkins, K. A.; Nela, L.; Farmer, D. B.; Han, S.-J. Flexible CMOS Integrated Circuits Based on Carbon Nanotubes with Sub-10 ns Stage Delays. *Nat. Electron.* **2018**, *1*, 191–196.

(16) Brady, G. J.; Way, A. J.; Safron, N. S.; Evensen, H. T.; Gopalan, P.; Arnold, M. S. Quasi-Ballistic Carbon Nanotube Array Transistors with Current Density Exceeding Si and GaAs. *Sci. Adv.* **2016**, *2*, e1601240.

(17) Schießl, S. P.; Fröhlich, N.; Held, M.; Gannott, F.; Schweiger, M.; Forster, M.; Scherf, U.; Zaumseil, J. Polymer-Sorted Semiconducting Carbon Nanotube Networks for High-Performance Ambipolar Field-Effect Transistors. *ACS Appl. Mater. Interfaces* **2015**, *7*, 682–689.

(18) Joo, Y.; Brady, G. J.; Arnold, M. S.; Gopalan, P. Dose-Controlled, Floating Evaporative Self-Assembly and Alignment of Semiconducting Carbon Nanotubes from Organic Solvents. *Langmuir* **2014**, *30*, 3460–3466.

(19) Brady, G. J.; Joo, Y.; Wu, M.-Y.; Shea, M. J.; Gopalan, P.; Arnold, M. S. Polyfluorene-Sorted, Carbon Nanotube Array Field-Effect Transistors with Increased Current Density and High On/Off Ratio. *ACS Nano* **2014**, *8*, 11614–11621.

(20) Park, S.; Pitner, G.; Giri, G.; Koo, J. H.; Park, J.; Kim, K.; Wang, H.; Sinclair, R.; Wong, H. S. P.; Bao, Z. Large-Area Assembly of Densely Aligned Single-Walled Carbon Nanotubes Using Solution Shearing and Their Application to Field-Effect Transistors. *Adv. Mater.* **2015**, *27*, 2656–2662.

(21) Rother, M.; Brohmann, M.; Yang, S.; Grimm, S. B.; Schießl, S. P.; Graf, A.; Zaumseil, J. Aerosol-Jet Printing of Polymer-Sorted (6,5) Carbon Nanotubes for Field-Effect Transistors with High Reproducibility. *Adv. Electron. Mater.* **2017**, *3*, 1700080.

(22) Cao, C.; Andrews, J. B.; Franklin, A. D. Completely Printed, Flexible, Stable, and Hysteresis-Free Carbon Nanotube Thin-Film Transistors via Aerosol Jet Printing. *Adv. Electron. Mater.* **2017**, *3*, 1700057.

(23) Wang, H.; Cobb, B.; van Breemen, A.; Gelinck, G.; Bao, Z. Highly Stable Carbon Nanotube Top-Gate Transistors with Tunable Threshold Voltage. *Adv. Mater.* **2014**, *26*, 4588–4593.

(24) Liu, Z.; Zhao, J.; Xu, W.; Qian, L.; Nie, S.; Cui, Z. Effect of Surface Wettability Properties on the Electrical Properties of Printed Carbon Nanotube Thin-Film Transistors on SiO_2/Si Substrates. *ACS Appl. Mater. Interfaces* **2014**, *6*, 9997–10004.

(25) Xu, W.; Zhao, J.; Qian, L.; Han, X.; Wu, L.; Wu, W.; Song, M.; Zhou, L.; Su, W.; Wang, C.; Nie, S.; Cui, Z. Sorting of Large-Diameter Semiconducting Carbon Nanotube and Printed Flexible Driving Circuit for Organic Light Emitting Diode (OLED). *Nanoscale* **2014**, *6*, 1589–1595.

(26) Homenick, C. M.; James, R.; Lopinski, G. P.; Dunford, J.; Sun, J.; Park, H.; Jung, Y.; Cho, G.; Malenfant, P. R. L. Fully Printed and Encapsulated SWCNT-Based Thin Film Transistors via a Combination of R2R Gravure and Inkjet Printing. *ACS Appl. Mater. Interfaces* **2016**, *8*, 27900–27910.

(27) Bucella, S. G.; Salazar-Rios, J. M.; Derenskyi, V.; Fritsch, M.; Scherf, U.; Loi, M. A.; Caironi, M. Inkjet Printed Single-Walled Carbon Nanotube Based Ambipolar and Unipolar Transistors for High-Performance Complementary Logic Circuits. *Adv. Electron. Mater.* **2016**, *2*, 1600094.

(28) Norton-Baker, B.; Ihly, R.; Gould, I. E.; Avery, A. D.; Owczarczyk, Z. R.; Ferguson, A. J.; Blackburn, J. L. Polymer-Free Carbon Nanotube Thermoelectrics with Improved Charge Carrier Transport and Power Factor. *ACS Energy Lett.* **2016**, *1*, 1212–1220.

(29) Joo, Y.; Brady, G. J.; Kanimozhi, C.; Ko, J.; Shea, M. J.; Strand, M. T.; Arnold, M. S.; Gopalan, P. Polymer-Free Electronic-Grade Aligned Semiconducting Carbon Nanotube Array. *ACS Appl. Mater. Interfaces* **2017**, *9*, 28859–28867.

(30) Chortos, A.; Pochorovski, I.; Lin, P.; Pitner, G.; Yan, X.; Gao, T. Z.; To, J. W. F.; Lei, T.; Will, J. W.; Wong, H. S. P.; Bao, Z. Universal Selective Dispersion of Semiconducting Carbon Nanotubes from Commercial Sources Using a Supramolecular Polymer. *ACS Nano* **2017**, *11*, 5660–5669.

(31) Arias, D. H.; Sulas-Kern, D. B.; Hart, S. M.; Kang, H. S.; Hao, J.; Ihly, R.; Johnson, J. C.; Blackburn, J. L.; Ferguson, A. J. Effect of Nanotube Coupling on Exciton Transport in Polymer-Free Monochiral Semiconducting Carbon Nanotube Networks. *Nanoscale* **2019**, *11*, 21196–21206.

(32) Smith, J.; Hamilton, R.; McCulloch, I.; Stingelin-Stutzmann, N.; Heeney, M.; Bradley, D. D. C.; Anthopoulos, T. D. Solution-Processed Organic Transistors Based on Semiconducting Blends. *J. Mater. Chem.* **2010**, *20*, 2562–2574.

(33) Niazi, M. R.; Li, R.; Qiang Li, E.; Kirmani, A. R.; Abdelsamie, M.; Wang, Q.; Pan, W.; Payne, M. M.; Anthony, J. E.; Smilgies, D. M.; Thoroddsen, S. T.; Giannelis, E. P.; Amassian, A. Solution-Printed Organic Semiconductor Blends Exhibiting Transport Properties on Par with Single Crystals. *Nat. Commun.* **2015**, *6*, 8598.

(34) Rice, N. A.; Magnan, F.; Melville, O. A.; Brusso, J. L.; Lessard, B. H. Organic Thin Film Transistors Incorporating Solution Processable Thieno[3,2-b]Thiophene Thienoacenes. *Materials* **2018**, *11*, 8.

(35) Kang, J.; Shin, N.; Do, Y. J.; Prabhu, V. M.; Yoon, D. Y. Structure and Properties of Small Molecule-Polymer Blend Semiconductors for Organic Thin Film Transistors. *J. Am. Chem. Soc.* **2008**, *130*, 12273–12275.

(36) Mirka, B.; Fong, D.; Rice, N. A.; Melville, O. A.; Adronov, A.; Lessard, B. H. Polyfluorene-Sorted Semiconducting Single-Walled Carbon Nanotubes for Applications in Thin Film Transistors. *Chem. Mater.* **2019**, *31*, 2863–2872.

(37) Rice, N. A.; Bodnaryk, W. J.; Mirka, B.; Melville, O. A.; Adronov, A.; Lessard, B. H. Polycarbazole-Sorted Semiconducting Single-Walled Carbon Nanotubes for Incorporation into Organic Thin Film Transistors. *Adv. Electron. Mater.* **2019**, *5*, 1800539.

(38) Sarker, B. K.; Shekhar, S.; Khondaker, S. I. Semiconducting Enriched Carbon Nanotube Aligned Arrays of Tunable Density and Their Electrical Transport Properties. *ACS Nano* **2011**, *5*, 6297–6305.

(39) Brady, G. J.; Joo, Y.; Roy, S. S.; Gopalan, P.; Arnold, M. S. High Performance Transistors via Aligned Polyfluorene-Sorted Carbon Nanotubes. *Appl. Phys. Lett.* **2014**, *104*, 083107.

(40) Redecker, M.; Bradley, D. D. C.; Inbasekaran, M.; Woo, E. P. Nondispersive Hole Transport in an Electroluminescent Polyfluorene. *Appl. Phys. Lett.* **1998**, *73*, 1565–1567.

(41) Bird, M. J.; Reid, O. G.; Cook, A. R.; Asaoka, S.; Shibano, Y.; Imahori, H.; Rumbles, G.; Miller, J. R. Mobility of Holes in Oligo- and Polyfluorenes of Defined Lengths. *J. Phys. Chem. C* **2014**, *118*, 6100–6109.

(42) Nicolai, H. T.; Wetzelaer, G. A. H.; Kuik, M.; Kronemeijer, A. J.; De Boer, B.; Blom, P. W. M. Space-Charge-Limited Hole Current in Poly(9,9-Dioctylfluorene) Diodes. *Appl. Phys. Lett.* **2010**, *96*, 172107.

(43) Kreouzis, T.; Poplavskyy, D.; Tuladhar, S. M.; Campoy-Quiles, M.; Nelson, J.; Campbell, A. J.; Bradley, D. D. C. Temperature and Field Dependence of Hole Mobility in Poly(9,9-Dioctylfluorene). *Phys. Rev. B* **2006**, *73*, 235201.

(44) Melville, O. A.; Rice, N. A.; Therrien, I.; Lessard, B. H. Organic Thin-Film Transistors Incorporating a Commercial Pigment (Hostasol Red GG) as a Low-Cost Semiconductor. *Dye. Pigment.* **2018**, *149*, 449–455.

(45) Cao, Q.; Han, S. J.; Tulevski, G. S.; Franklin, A. D.; Haensch, W. Evaluation of Field-Effect Mobility and Contact Resistance of Transistors That Use Solution-Processed Single-Walled Carbon Nanotubes. *ACS Nano* **2012**, *6*, 6471–6477.

(46) Li, Z.; Ding, J.; Guo, C.; Lefebvre, J.; Malenfant, P. R. L. Decomposable s-Tetrazine Copolymer Enables Single-Walled Carbon Nanotube Thin Film Transistors and Sensors with Improved Sensitivity. *Adv. Funct. Mater.* **2018**, *28*, 1705568.

(47) Brohmann, M.; Berger, F. J.; Matthiesen, M.; Schießl, S. P.; Schneider, S.; Zaumseil, J. Charge Transport in Mixed Semiconducting Carbon Nanotube Networks with Tailored Mixing Ratios. *ACS Nano* **2019**, *13*, 7323–7332.

(48) Bishop, M. D.; Hills, G.; Srimani, T.; Lau, C.; Murphy, D.; Fuller, S.; Humes, J.; Ratkovich, A.; Nelson, M.; Shulaker, M. M. Fabrication of Carbon Nanotube Field-Effect Transistors in Commercial Silicon Manufacturing Facilities. *Nat. Electron.* **2020**, *3*, 492–501.

(49) Cao, X.; Wu, F.; Lau, C.; Liu, Y.; Liu, Q.; Zhou, C. Top-Contact Self-Aligned Printing for High-Performance Carbon Nanotube Thin-Film Transistors with Sub-Micron Channel Length. *ACS Nano* **2017**, *11*, 2008–2014.

(50) Schießl, S. P.; Gannott, F.; Etschel, S. H.; Schweiger, M.; Grünler, S.; Halik, M.; Zaumseil, J. Self-Assembled Monolayer Dielectrics for Low-Voltage Carbon Nanotube Transistors with Controlled Network Density. *Adv. Mater. Interfaces* **2016**, *3*, 1600215.

(51) Jin, S. H.; Islam, A. E.; Kim, T.-I.; Kim, J.; Alam, M. A.; Rogers, J. A. Sources of Hysteresis in Carbon Nanotube Field-Effect Transistors and Their Elimination Via Methylsiloxane Encapsulants and Optimized Growth Procedures. *Adv. Funct. Mater.* **2012**, *22*, 2276–2284.

(52) Li, Z.; Ding, J.; Finnie, P.; Lefebvre, J.; Cheng, F.; Kingston, C. T.; Malenfant, P. R. L. Raman Microscopy Mapping for the Purity Assessment of Chirality Enriched Carbon Nanotube Networks in Thin-Film Transistors. *Nano Res.* **2015**, *8*, 2179–2187.

(53) Vobornik, D.; Zou, S.; Lopinski, G. P. Analysis Method for Quantifying the Morphology of Nanotube Networks. *Langmuir* **2016**, *32*, 8735–8742.

(54) Selmani, S.; Hawes, G. F.; Schipper, D. J. Liquid-Crystal Phase Optimization Using the Alignment Relay Technique for the Deposition of Single-Walled Carbon Nanotubes. *ACS Appl. Nano Mater.* **2020**, *3*, 2118–2122.

(55) Selmani, S.; Schipper, D. J. π-Concave Hosts for Curved Carbon Nanomaterials. *Chem. Eur. J.* **2019**, *25*, 6673–6692.

(56) Bradski, G.; Kaehler, A. *Learning OpenCV: Computer Vision in C++ with the OpenCV Library*, 2nd ed.; O'Reilly Media, Inc., Newton, MA, 2013.

(57) Van der Walt, S.; Schönberger, J. L.; Nunez-Iglesias, J.; Boulogne, F.; Warner, J. D.; Yager, N.; Gouillart, E.; Yu, T. Scikit-Image: Image Processing in Python. *PeerJ* **2014**, *2*, e453.

(58) Otsu, N. A Threshold Selection Method from Gray-Level Histograms. *IEEE Trans. Syst. Man. Cybern.* **1979**, *9*, 62–66.

(59) Bradski, G. The OpenCV Library. *Dr. Dobb's J. Softw. Tools* **2000**, *25*, 120–125.

(60) Ding, J.; Li, Z.; Lefebvre, J.; Cheng, F.; Dunford, J. L.; Malenfant, P. R. L.; Humes, J.; Kroeger, J. A Hybrid Enrichment Process Combining Conjugated Polymer Extraction and Silica Gel Adsorption for High Purity Semiconducting Single-Walled Carbon Nanotubes (SWCNT). *Nanoscale* **2015**, *7*, 15741–15747.

(61) Yen, J.-C.; Chang, F.-J.; Chang, S. A New Criterion for Automatic Multilevel Thresholding. *IEEE Trans. Image Process.* **1995**, *4*, 370–378.

(62) Remi-Omosowon, A. pyeasyga 0.3.1 https://pypi.org/project/pyeasyga/.

Chapter 4: Contact Engineering in Single-Walled Carbon Nanotube Thin-Film Transistors: Implications for Silane-Treated SiO_2 Substrates

This chapter was published in the journal "ACS Applied Nano Materials": Mirka, B.; Rice, N. A.; Richard, C. M.; Lefebvre, D.; Bodnaryk, W. J.; Fong, D.; Adronov, A.; Lessard, B. H. Contact Engineering in Single-Walled Carbon Nanotube Thin-Film Transistors: Implications for Silane-Treated SiO_2 Substrates. ACS Appl. Nano. Mater. 2022, Manuscript ID an-2022-02052f.

Context

In our work in **Chapter 3,** we experienced issues with gold source-drain contact adhesion to SiO_2 substrates. Damaged contacts are common in single-walled carbon nanotube transistors when gold electrodes are used without a contact interlayer. We wanted to explore different contact interlayers to improve electrode adhesion and their effect on single-walled carbon nanotube device performance. Though Cr is a common interlayer, we also wanted to explore Mn and MoO_3, which are used less commonly. Mn and MoO_3 can be deposited using physical vapour deposition and can therefore be incorporated into laboratory-scale thin-film transistors.

Contributions

Dr. Rice and I contributed equally to this chapter. Dr. Rice, Prof. Lessard, and I planned the required research. The copolymers PCF and PFMB were synthesized by Dr. Bodnaryk and Dr. Fong, respectively. Dr. Rice and I prepared the polymer-SWNT dispersions. Dr. Rice, Ms. Richard, Ms. Lefebvre, and I contributed to device fabrication, characterization, and data analysis. I prepared the manuscript with input from Dr. Rice, Prof. Lessard, and Prof. Adronov.

4.1 Abstract

Semiconducting single-walled carbon nanotubes (sc-SWNTs) are promising candidates for thin-film transistors (TFTs). The interface between this semiconducting material and the metal electrodes is critical for both device performance and mechanical robustness, such as adhesion. Sc-SWNTs were incorporated into top-contact TFTs with different source-drain contact interlayers as a means of improving gold adhesion to silane-treated SiO_2 substrates, and to study the effect of the contact interlayers on TFT performance. Molybdenum trioxide (MoO_3), manganese (Mn), chromium (Cr), and 2,9-dimethyl-4,7-diphenyl-1,10-phenanthroline (BCP) were all investigated as potential contact interlayers. The incorporation of contact interlayers significantly improved TFT device yield; additionally, the presence of a MoO_3 or Mn interlayer resulted in much higher yield of working TFTs compared to devices made using bare Au. Sc-SWNT TFTs characterized in air showed a smaller dependence on the contact interlayer compared to TFTs characterized in nitrogen, despite differences in the work function of the contact electrodes. In air, there was little to no difference in contact resistance and other metrics when comparing MoO_3-Au and Au contacts, while a drop in performance was observed for Mn-Au, Cr-Au, and BCP-Au based devices. When testing in nitrogen, Mn-Au was comparable to Au and MoO_3-Au contacts. These differences suggest oxygen adsorption at the contact surface and the contact interface is contributing to changes in electrical performance depending on the choice of contact material.

4.2 Introduction

Significant research and market interest has been devoted to flexible and inexpensive electronics due to their extensive range of applications.[1,2] Single-walled carbon nanotubes (SWNTs) are ideal materials for such applications due to their high electrical conductivity, chemical stability, and flexibility.[3-5] Developments in the sorting and dispersion of semiconducting single-walled carbon nanotubes (sc-SWNTs) have facilitated their incorporation into electronic devices using economical, and potentially scalable, solution processing techniques.[6] These advancements in refinement and purity have resulted in numerous reports of networks of sc-SWNTs utilized as the semiconducting layer in thin-film transistors (TFTs). Despite this, the performance of sc-SWNT TFTs have failed to achieve theoretical performances, with many devices also too fragile for many applications.

Contact engineering aims to improve charge injection through optimization of the TFT source-drain contacts. This can involve exploration of different electrode architectures based on the semiconducting material, including top-contact, bottom-contact, and double-contact architectures,[7,8] with top-contact architectures often preferred due to superior contact between the metal and sc-SWNT network.[9-11] Ideally, the source-drain contacts should provide minimal contact resistance between the electrode and the nanotube network. Contact resistance emerges from the applied potential required to inject charges from the contacts into the semiconducting layer.[12] Presently, typical SWNT TFTs are based on Si/SiO_2 substrates, using high work function (WF) metals as the source-drain contacts, such as Pt or Au.[13] Au contacts facilitate hole injection into the sc-SWNT network due to a small energy barrier between the Au WF and the frontier sc-SWNT valence band. However, a common problem encountered with Au contacts is poor adhesion to the SiO_2 substrate.[14,15] There may be a trade-off between the reduced contact resistance offered by Au contacts and device stability due to poor Au adhesion. Adhesion of Au to SiO_2 can be improved using electrode interlayers, such as metallic interlayers like Mn, Cr, or Ti,[15-18] metal oxides including MoO_3, WO_3, and V_2O_5,[19] and polymer or small molecule interlayers.[20,21] The inclusion of interlayers is also a common strategy to reduce contact resistance in organic thin-film transistors (OTFTs).[17,22] In top-contact architectures, the interlayer is deposited on the SWNT network, followed by the bulk electrode, resulting in the interlayer making direct contact with the SWNT network. Therefore, energetic mismatch between the interfacial layer's WF and the sc-SWNT

valence band, and the presence of interfacial dipoles, could negatively affect charge injection into the SWNT network.

Metal oxides are often used to tune the WF of the electrodes *via* effects at the surface, such as adsorption or charge transfer.[23] In particular, MoO_x and MoO_3 have been studied as hole injection layers in organic light emitting diodes (OLEDs), organic photovoltaics (OPVs), and OTFTs due to their deep HOMO level.[19,24-26] Yi and coworkers found that MoO_3 interlayers with Au electrodes or Al electrodes induce large interfacial dipoles, which can significantly lower the electrode's WF relative to the vacuum level, thereby improving hole injection.[25] Kano and coworkers reported reduced contact resistance when using thermally evaporated MoO_x as an interlayer with Au electrodes for the organic semiconductor 2,7-dioctyl[1]benzothieno[3,2-b][1]benzothiophene (C8-BTBT).[27] Furthermore, MoO_3 can be deposited in the nanoparticle state using solution processing techniques, making it compatible with fully solution-processed TFTs.[23,28] Layers of MoO_x have been used to induce hole doping in SWNT networks and increase the SWNT conductivity.[29,30] Bathocuproine (BCP), a conjugated organic molecule, can also be used to facilitate electron injection due to favourable energetics between its the LUMO level and the organic semiconductor in OTFTs or OLEDs.[17,31]

It is common to use Cr as a contact interlayer to promote Au adhesion when fabricating SWNT TFTs.[32-34] Thin layers of Cr (~2 to 5 nm) are deposited onto a glass or Si/SiO_2 substrate, followed by deposition of Au source-drain contacts. However, use of Mn as a contact interlayer is uncommon, likely due to its low conductivity and lower WF compared to Au. Mn has been used as a contact interlayer for n-type organic semiconductors.[17,35] However, to the best of our knowledge, Mn has not been used as a contact interlayer in SWNT TFTs. Mn interlayers provide good Au adhesion and are simple to fabricate using physical vapour deposition, thereby warranting its investigation as a contact interlayer for SWNT TFTs.

This study compares the use of several interlayers with Au source-drain contacts in sc-SWNT TFTs, including Cr-Au, Mn-Au, MoO_3-Au, and BCP-Au. The semiconducting layer in the TFTs was produced from solution-deposited networks of polymer-wrapped sc-SWNTs, prepared using one of two conjugated copolymers: poly(carbazole-*co*-fluorene) (PCF) or poly(fluorene-*co*-dimethoxybenzene) (PFMB). We found that the use of interlayers improved the number of functioning devices by reducing electrode mechanical failure, thus improving TFT device yield.

SWNT TFTs were fabricated and electrically characterized under p-type conditions in air and nitrogen for each interlayer condition. Hole mobility, threshold voltage, hysteresis, current on/off ratio, off current, and contact resistance were used to characterize each TFT. The adhesion strength of each contact interface was measured on octyltrichlorosilane-treated SiO_2 substrates. Due to the energetics of BCP, it was hypothesized that incorporation of a BCP-Au contact would facilitate n-type behaviour in SWNT TFTs. However, when testing under n-type conditions in nitrogen, no field-effect was observed in the output curves. Since there was no evidence of n-type operation in the output curves, the n-type data has not been included.

4.3 Results and Discussion

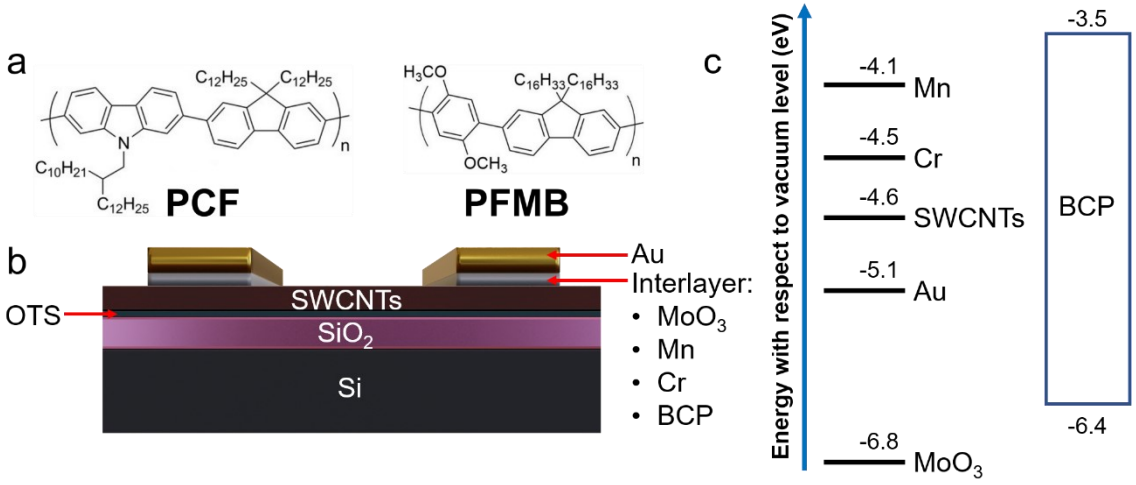

Figure 4.1: a) polymer structures of PCF and PFMB, b) top-contact device architecture with different contact interlayers, and c) energy-level diagram of each interlayer, Au contacts, and SWNTs. Work function (WF) values for Au, Mn, and Cr were obtained from ref. 17, WF for MoO_3-Au was obtained from ref. 25, and HOMO/LUMO levels for BCP were obtained from ref. 31. WF values are reported for bulk Mn and bulk Cr. WF value is reported for the MoO_3 (10 nm) – Au (50 nm) hybrid.

Dispersions of sc-SWNTs were prepared in toluene using either the PCF or PFMB copolymers and incorporated as the semiconducting layer in bottom-gate top-contact (BGTC) TFTs on Si/SiO_2 wafers. The linear density of the SWNT films was estimated using AFM to be ~12 μm^{-1}. Different contact interlayers were first deposited onto the sc-SWNT network, followed immediately by 50 nm of Au to complete the source-drain contacts. A schematic of the SWNT

TFT architecture is shown in **Figure 4.1**. The following interlayers were incorporated into BGTC TFTs: Mn (10 nm), MoO_3 (10 nm), Cr (2 nm), and BCP (10 nm).

Figure 4.2 depicts characteristic output curve origins for **PCF-SWNT** TFTs for each contact interface. Each output curve shows the data for Au contacts (solid lines) and the Au-interfacial layer (dashed lines). **Figure 4.2a-d** represent the output curves measured in air and **Figure 4.2e-h** represent the output curves measured in nitrogen. As expected, devices prepared using Au contacts resulted in output curves with linear origins, indicating more ohmic contacts.[41,42] Devices fabricated with Mn-Au and MoO_3-Au contacts also exhibit linear origins in both air and nitrogen, indicating more ohmic contacts. Devices fabricated using Cr-Au and BCP-Au contacts show a change in concavity at the origin, with a more pronounced effect in nitrogen, suggesting increased contact resistance. **Figure 4.7** in the ESI depicts output curve origins for **PFMB-SWNT** TFTs in air and nitrogen. **PFMB-SWNT** TFTs exhibited the same pattern with respect to the origins.

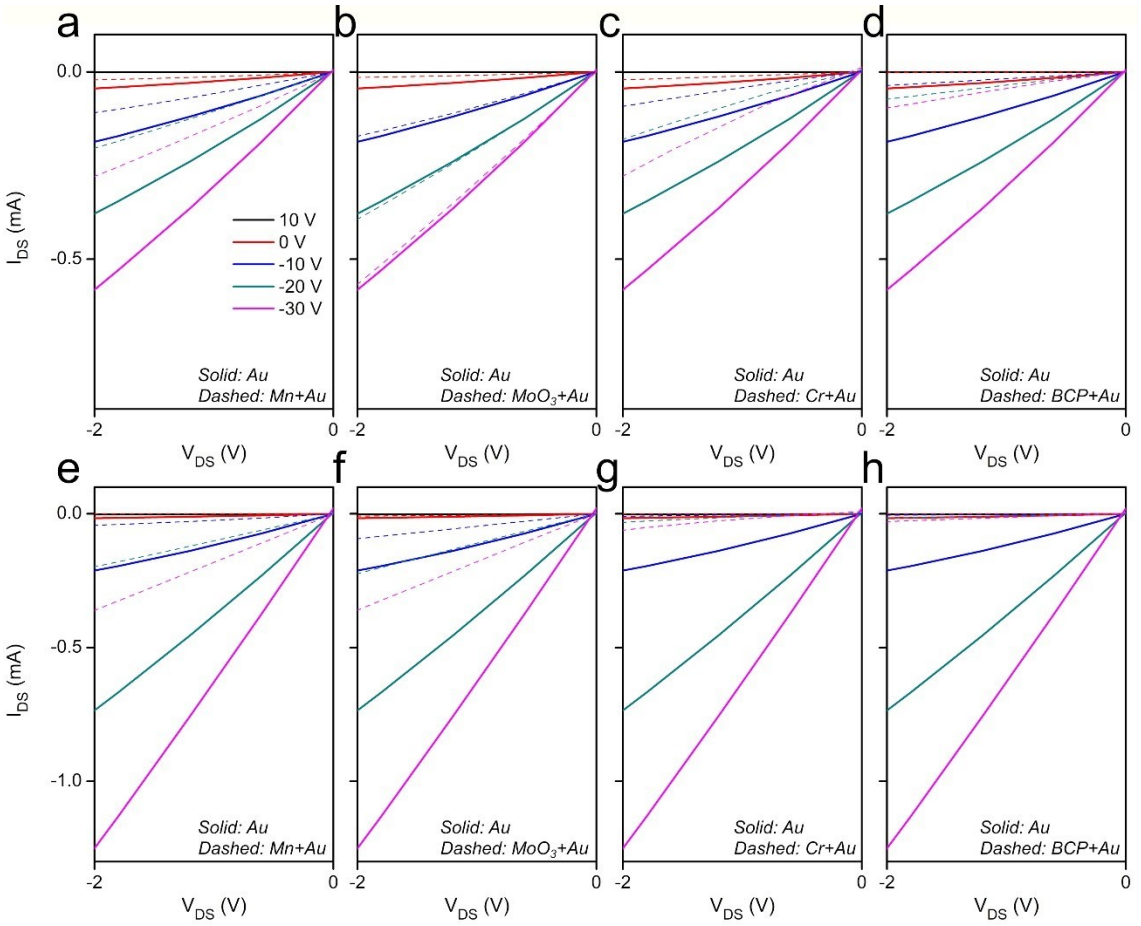

Figure 4.2: Characteristic output curve origins for **PCF-SWNT** TFTs with different contact interfaces measured under p-type conditions in (a-d) air and (e-h) nitrogen. Solid lines represent data for Au contacts, and dashed lines represent data for interface-Au contacts.

Figure 4.3 displays the effect of contact interface on the device transfer characteristics. The characteristic transfer curves suggest that the I_{SD}-V_{GS} characteristics are more consistent in air compared to nitrogen when comparing different contact interfaces. The transfer characteristics in nitrogen for Mn-Au, Cr-Au, and BCP-Au show more ambipolar behaviour, consistent with their low WF values, which are presented in **Figure 4.1**. The discrepancy in transfer characteristics suggests both a strong influence of oxygen and ambient moisture, as well as choice of interlayer on device performance. While interlayer composition has little effect on TFT performance when characterized in air, TFTs characterized in nitrogen show a stronger dependence on interlayer composition, which suggests that effects of oxygen and moisture are dominant over effects of interlayer composition. These finding are consistent with reports showing that the effect of

oxidation at the contact/semiconductor interface is strong enough such that differences in the contact's WF do not manifest.[22] Furthermore, this observation is similar to the findings of Martel et al., who report conversion of unipolar p-type SWNT-TFTs to ambipolar TFTs after altering the chemical nature of the substrate to remove the influence of adsorbed moisture.[43] These results further suggest that the substrate has a significant effect on n-/p-type behaviour to the extent that differences due to contact Schottky barriers are less significant.[43] Similar results were observed for **PFMB-SWNT** TFTs (**Figure 4.8**), suggesting that the phenomenon is unrelated to the wrapping polymer.

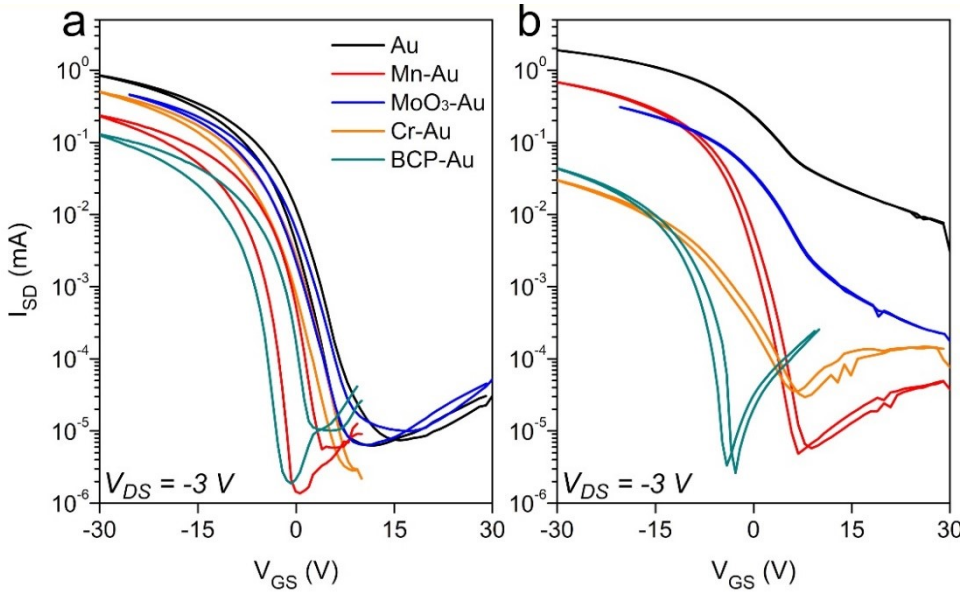

Figure 4.3: Characteristic transfer curves for PCF-SWCNT TFTs measured under p-type conditions in a) air and b) nitrogen.

Table 4.1: Width-normalized contact resistances (R_CW), effective hole mobility (μ_{eff}), and R_CW-corrected hole mobility (μ_0) for **PCF-SWNT** TFTs measured under p-type conditions in air and nitrogen.

Contact Interface	*P-type in Air*			*P-type in N_2*		
	R_CW (Ω cm) [a)]	μ_{eff} ($cm^2V^{-1}s^{-1}$)	μ_0 ($cm^2V^{-1}s^{-1}$)	R_CW (Ω cm) [a]	μ_{eff} ($cm^2V^{-1}s^{-1}$)	μ_0 ($cm^2V^{-1}s^{-1}$)
Au	7.7 (± 11) × 10^2	9.8 ± 5.3	11 ± 4.8	1.8 (± 3.5) × 10^3	9.5 ± 7.6	9.9 ± 6.8
Mn-Au	1.7 (± 0.99) × 10^3	4.0 ± 1.2	6.4 ± 2.0	9.9 (± 14) × 10^2	6.0 ± 4.0	7.9 ± 5.0
MoO_3-Au	4.0 (± 4.2) × 10^2	6.1 ± 2.2	9.9 ± 4.0	1.2 (± 0.80) × 10^3	2.6 ± 1.6	5.1 ± 3.4
Cr-Au	1.8 (± 1.8) × 10^3	3.8 ± 2.5	6.3 ± 4.0	1.3 (± 2.4) × 10^4	0.41 ± 0.31	0.60 ± 0.54
BCP-Au	3.4 (± 1.4) × 10^3	1.7 ± 0.6	2.2 ± 0.66	1.8 (± 1.4) × 10^4	0.31 ± 0.30	0.31 ± 0.30

a) R_CW values were estimated using the Y-function method.

Width-normalized contact resistance (R_CW) values are reported in **Table 4.1** for each contact interface, alongside the effective mobility (μ_{eff}) and the contact resistance-corrected mobility (μ_0). Data for R_CW were measured under p-type conditions in both air and nitrogen atmospheres and estimated using the Y-function method.[23] Values of R_CW for Au electrodes are in the range of $10^2 – 10^3$ Ω cm, which is comparable to other reports for which Au contacted the SWNT layer.[39,44] Compared to air, values of R_CW increase by an order of magnitude for TFTs tested in nitrogen with MoO_3-Au, Cr-Au, and BCP-Au contacts. R_CW values did not change for Au and Mn-Au contacts when switching from an air to a nitrogen atmosphere. The discrepancy could be attributed to the presence of oxygen, which is known to affect sc-SWNT TFT p-type behaviour. In an ambient atmosphere, oxygen can adsorb onto the sc-SWNT layer and at the contact interface; adsorption of oxygen at the sc-SWNT surface can increase the hole density in the sc-SWNT layer. Adsorbed oxygen causes pinning of the Fermi level close to the valence band maximum at the metal-SWNT interface, facilitating hole injection.[13,45] Additionally, oxygen can adsorb onto the contact surface, or diffuse through the contact to the interface, which can alter the Au WF.[22,46-49] R_CW, μ_{eff}, and μ_0 for **PFMB-SWNT** TFTs are displayed in **Table 4** in the ESI.

Figure 4.4a-b depicts R_CW in box-plot format for **PCF-SWNT** TFTs measured in air and nitrogen, respectively. **PCF-SWNT** TFTs characterized in air display minor differences in R_CW for different contact interfaces compared to TFTs characterized in nitrogen. The use of Au and MoO_3-Au contacts exhibit the smallest R_CW in air in the range of $10^2 – 10^3$ Ω cm, while the use of Mn-Au, Cr-Au, and BCP-Au contacts leads to devices that exhibit a larger R_CW in the range of $10^3 – 10^4$ Ω cm. The equivalent R_CW measured for devices with Au and MoO_3-Au contacts shows that the MoO_3 layer does not further hinder hole injection. This is consistent with the findings of Yi et al., who report large interfacial dipoles when studying MoO_3 interlayers with Au contacts.[25] The reason that devices with MoO_3-Au contacts do not exhibit reduced R_CW compared to those with Au contacts could be due to the lower conductivity of MoO_3 compared to Au.[24] TFTs characterized in nitrogen exhibit a larger R_CW for Cr-Au and BCP-Au contact interfaces. Similar to the transfer characteristics, differences in R_CW between contact interfaces manifest in a nitrogen atmosphere and are less apparent in air. Discrepancies in R_CW between air and nitrogen atmospheres suggest that differences in the contact interface do not have a substantial effect in air but manifest in nitrogen. This is consistent with work showing that the contact WF is not the best predictor of R_CW in ambient atmospheres due to the effect of oxygen.[22] Kumatani et al. suggest

that in ambient environments, the formation of an oxide layer at the contact/semiconductor interface can improve hole injection.[22] Thus, for practical ambient environments, the effect of the contact's standard electrode potential may serve as a better predictor of R_CW than the contact's WF.[22] The standard electrode potential, which is analogous to WF, represents the potential required for a metal to gain or lose electrons via reduction-oxidation.[22] **Figure 4.9a-b** displays the R_CW values for **PFMB-SWNT** TFTs characterized in air and nitrogen atmospheres, respectively. **PFMB-SWNT** TFTs exhibit similar R_CW patterns in air and nitrogen atmospheres.

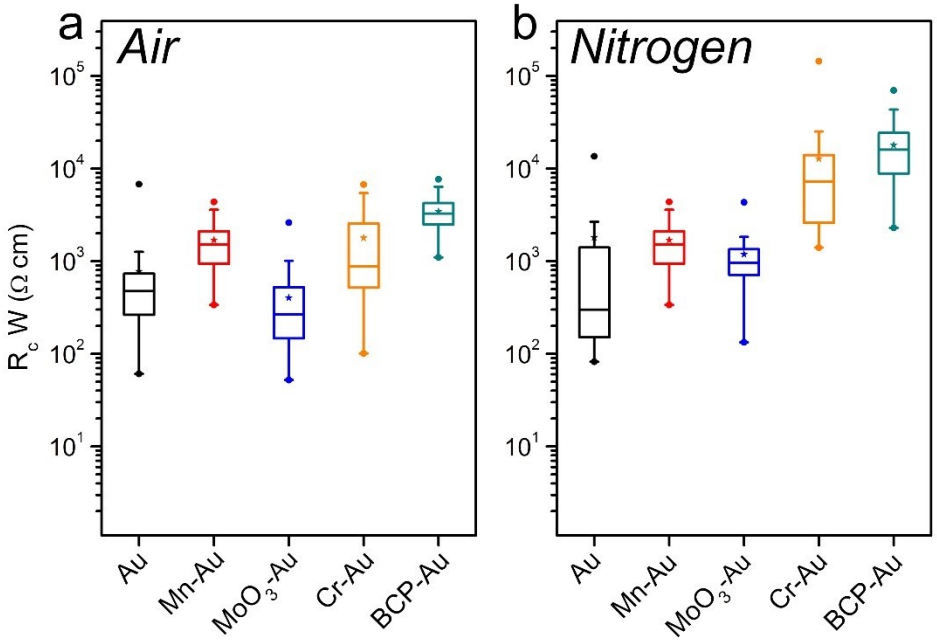

Figure 4.4: Width-normalized contact resistance (R_CW) for PCF-SWCNT TFTs measured under p-type conditions in a) air and b) nitrogen. R_CW values were estimated using the Y-function method. The data are represented using box plots, where the box indicates the interquartile range, the horizontal line within the box indicates the median, the star indicates the mean, the dots indicate the minimum and maximum, and the horizontal lines indicate the 5th and 95th percentile.

Figure 4.5 and **Figure 4.6** display the metrics for **PCF-SWNT** TFTs tested under p-type conditions in air and nitrogen, respectively. The metrics include the contact resistance-corrected hole mobility (μ_0), hole threshold voltage ($V_{T,h}$), hysteresis (H), current on/off ratio ($I_{on/off}$), off-current (I_{off}), and the device yield as a percentage. As shown in **Figure 4.5**, TFT metrics measured in air do not show a strong relationship with the contact interlayer. Au and MoO_3-Au contacts

exhibit the highest μ_0, Cr-Au and Mn-Au exhibit a slightly smaller μ_0 and BCP-Au exhibits the smallest μ_0, which was expected given that BCP is usually used to facilitate electron transfer. Devices with Au contacts had the smallest $V_{T,h}$, but also had the largest distribution/variability. Devices with MoO_3-Au interlayers displayed the same average $V_{T,h}$ but a smaller distribution/variability, while $V_{T,h}$ for devices fabricated with Mn-Au, Cr-Au, and BCP-Au electrodes were similar and did not show statistically significant differences. All contact interlayers had a similar H average and distribution, except for BCP-Au, which had a higher average and distribution of H. Statistically significant differences are not observed in $I_{on/off}$ ratios and are not strong in I_{off}.

Most significantly, the device yield was improved drastically when using Mn-Au or MoO_3-Au contact interlayers compared to Au contacts, with > 90 % device yield compared to 70 %. Even the use of Cr-Au and BCP-Au contact interlayers showed slight improvements in TFT device yield compared to Au. While the use of Mn-Au resulted in a slight decline in μ_0 and a slight increase in $V_{T,h}$, and the incorporation of MoO_3 had little effect on these device characteristics, both interlayers also improved TFT device yield. TFT device yield improved from 70 % with Au contacts to 93 % and 96 % for Mn-Au and MoO_3-Au contacts, respectively, which is a critical factor in the development of large-scale commercially-viable TFTs. Our results show that incorporation of simple interlayer materials facilitates improvements in TFT device yield, without significant sacrifices in device metrics. When measured in air, TFT metrics do not show a strong dependence on the contact interlayer, similar to the R_CW data and the transfer characteristics. **Figure 4.10** shows the metrics for **PFMB-SWNT** TFTs tested under p-type conditions in air.

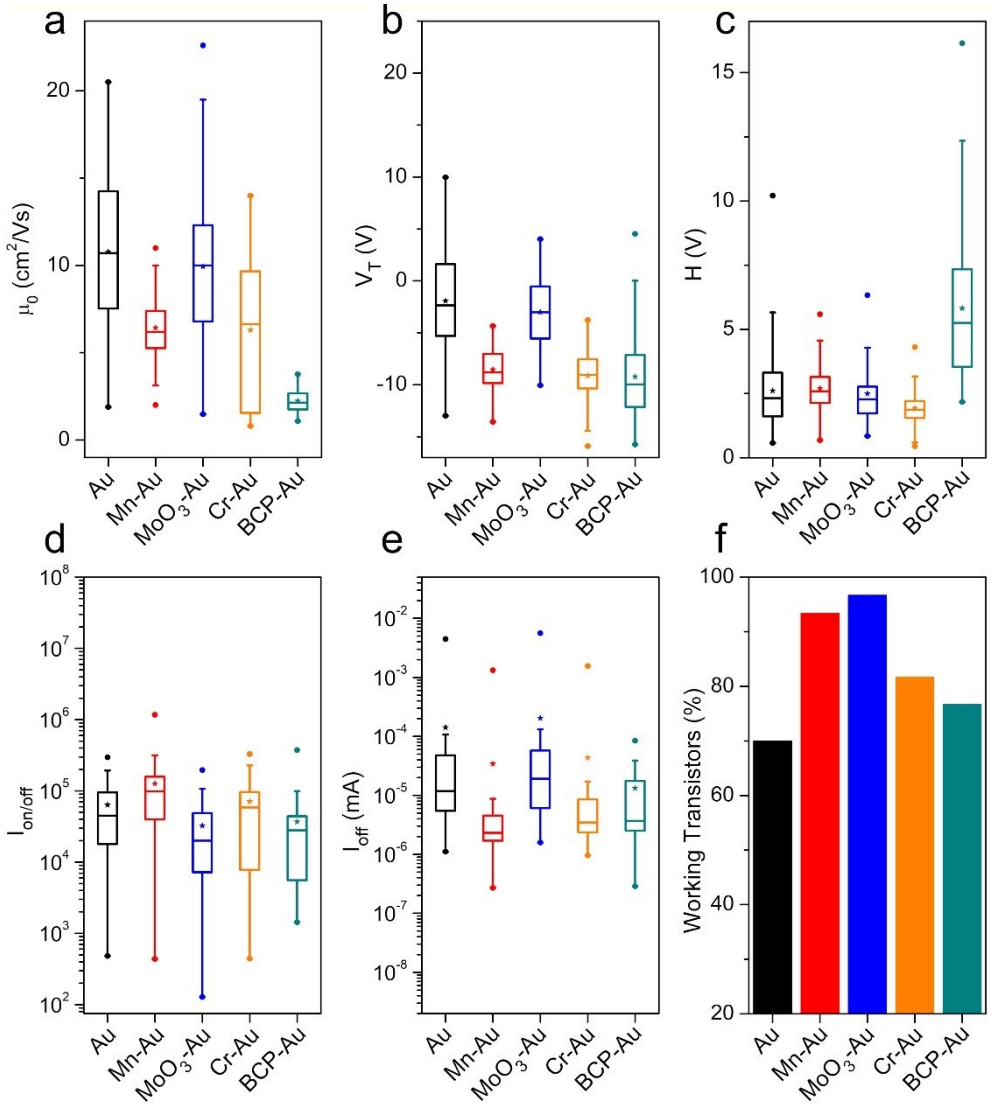

Figure 4.5: Data for **PCF-SWNT** TFTs tested in p-type conditions in air, which include a) contact resistance-corrected hole mobility (μ_0), b) hole threshold voltage ($V_{T,h}$), c) hysteresis (H), d) current on-off ratio ($I_{on/off}$), e) off-current (I_{off}), and f) the device yield. The data are represented using box plots, where the box indicates the interquartile range, the horizontal line within the box indicates the median, the star indicates the mean, the dots indicate the minimum and maximum, and the horizontal lines indicate the 5th and 95th percentile.

SWNT TFTs were prepared and characterized in an ambient environment in order to be more representative of commercially-viable applications that will also be prepared and operated in an ambient environment. However, to gain insight into the fundamentals of contact interfaces, SWNT TFTs were also characterized in a nitrogen environment. **Figure 4.6** displays p-type TFT metrics measured in nitrogen, which have statistically significant differences in TFT metrics

compared to testing in an ambient atmosphere, suggesting that the contact interface does have an important impact on device performance in an inert environment. The performance discrepancy between air and nitrogen atmospheres is consistent with other reports, which have demonstrated an influence of adsorbed oxygen on the contact's WF.[49] The μ_0 for devices fabricated with Au and Mn-Au electrodes is approximately the same, and is slightly lower for devices fabricated using a MoO_3-Au contact interface. Cr-Au and BCP-Au contacts display a significantly smaller μ_0. Both the average and distribution of $V_{T,h}$ for devices fabricated with Cr-Au and BCP-Au electrodes are also greater compared to devices fabricated with Au. This trend in mobility is consistent with the trend that was observed for R_CW in nitrogen, shown in **Figure 4.4b**, where R_CW for Au and Mn-Au contacts was similar, slightly larger for MoO_3-Au, and larger for Cr-Au and BCP-Au. However, when testing in nitrogen μ_0 for Mn-Au contacts was larger than μ for Cr-Au contacts, despite a larger WF for Cr compared to Mn and oxygen and moisture are removed when testing in nitrogen. Similarly, Mn-Au had a lower R_CW than Cr-Au in nitrogen. This is inconsistent with our observations. While H for devices with Au, Mn-Au, and MoO_3-Au contact interfaces are similar, H for devices with Cr-Au are slightly larger, and H for devices with BCP-Au electrodes are significantly larger in average and distribution. The $I_{on/off}$ ratios for devices with Au, Mn-Au, and MoO_3-Au contact interfaces are similar, averaging around 10^3. The use of BCP-Au has a higher $I_{on/off}$ ratio due to a smaller I_{off}.

Similar to the data measured in air, Mn-Au and MoO_3-Au contact interfaces improve the TFT device yield. The device yield was ca. 85 % and 95 % for devices with Mn-Au and MoO_3-Au electrodes, respectively, compared to ca. 55 % for devices with Au electrodes. Like the data measured in air, the use of Mn-Au and MoO_3-Au interlayers improved the TFT device yield without significantly affecting other TFT metrics. The use of Cr-Au and BCP-Au exhibited ca. 70 % and 65 % working TFTs, respectively. However, the use of Cr-Au and BCP-Au contact interfaces showed a drop in TFT performance, similar to the trend in contact resistance in nitrogen. The TFT performance discrepancies in nitrogen suggest that the interfaces significantly affect TFT performance in the absence of oxygen and moisture. **Figure 4.11** shows the metrics for **PFMB-SWNT** TFTs tested under p-type conditions in nitrogen.

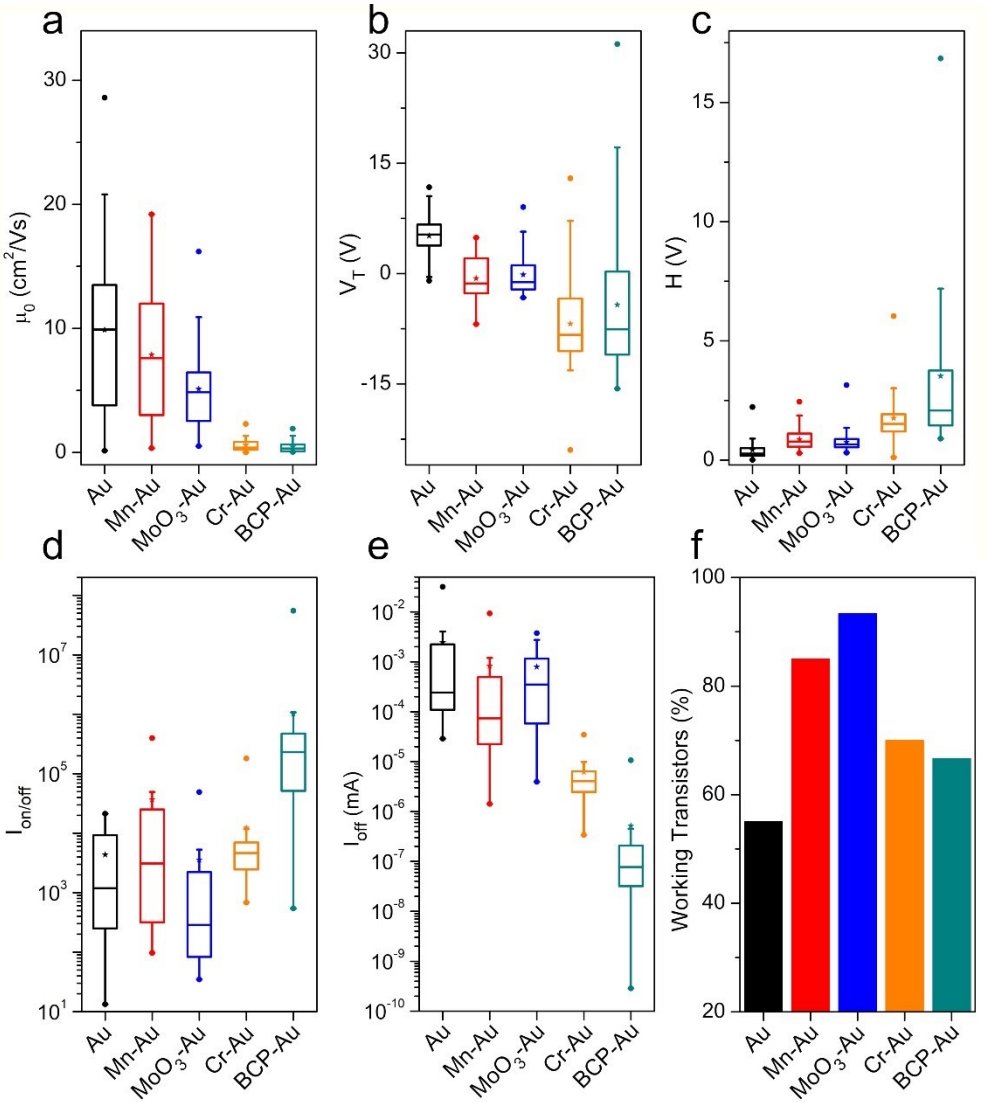

Figure 4.6: Data for **PCF-SWNT** TFTs tested in p-type conditions in nitrogen, which include a) contact resistance-corrected mobility (μ_0), b) hole threshold voltage (V_T), c) hysteresis (H), d) current on-off ratio ($I_{on/off}$), e) off-current (I_{off}), and f) the device yield. The data are represented using box plots, where the box indicates the interquartile range, the horizontal line within the box indicates the median, the star indicates the mean, the dots indicate the minimum and maximum, and the horizontal lines indicate the 5th and 95th percentile.

Each contact interface was subjected to a cross-hatch adhesion test (ASTM F1842-09).[50,51] The results from the adhesion test are depicted in **Figure 4.12** in the ESI. Briefly, in order of worst to best, the quality of adhesion was Au, BCP-Au, Mn-Au, MoO_3-Au and Cr-Au (BCP-Au and Mn-Au were equally poor in adhesion). Details of the test can be found in the ESI. A representative image of a damaged Au contact is shown in **Figure 4.13**. The adhesion test results provide further

insight into the device yield, since non-functional devices can result from damaged contacts (short circuits, bad contact with the probes, or possible penetration of the oxide with the contact). Since Au electrodes had the poorest adhesion to OTS-treated SiO_2, it's not surprising that Au devices also had the lowest device yield. However, Cr-Au had a moderate device yield compared to Mn-Au and MoO_3-Au, despite having the strongest adhesion to OTS-treated SiO_2. Since Cr-Au had the strongest adhesion, it's unlikely that the moderate device yield is due to electrode damage, but rather a result of defects in the SiO_2 causing gate leakage.

4.4 Conclusion

In conclusion, **PCF-SWNT** and **PFMB-SWNT** TFTs were fabricated using different top-contact interlayers, including Mn-Au, MoO_3-Au, Cr-Au, and BCP-Au. TFTs were characterized under p-type conditions in both air and nitrogen atmospheres. Using a contact interlayer significantly improved the device yield by providing more robust electrodes that are more resistant to wear and tear. However, different contact interlayers affected TFT performance, particularly in a nitrogen atmosphere. In air, TFTs with Au and MoO_3-Au contacts had the smallest R_CW, while TFTs with Mn-Au, Cr-Au, and BCP-Au had greater R_CW. In nitrogen, R_CW for TFTs with Au and Mn-Au were similar, while R_CW for TFTs with Au-MoO3, Au-Cr, and Au-BCP became larger. The effect of different contact interlayers on TFT metrics for devices characterized in air was less pronounced than in nitrogen. In air, Au and MoO_3-Au contacts had similar μ_h, $V_{T,h}$, H, and $I_{on/off}$, while Mn-Au, Cr-Au, and BCP-Au showed slight drops in μ_h. However, in nitrogen, reduction in μ_h was significant for devices using Cr-Au and BCP-Au, and moderate for devices fabricated with MoO_3-Au; there was no change for devices using Mn-Au. The use of Mn-Au and MoO_3-Au contacts still showed improved TFT device yield. The discrepancy in performance between air and nitrogen atmospheres could be due to the presence of oxygen or moisture. In the presence of a nitrogen atmosphere, the effect of the interlayer manifests itself in the contact resistance. Overall, the use of Mn and MoO_3 contact interlayers improves device yield providing a route to more robust TFT-based applications.

4.5 Experimental

4.5.1 Substrate cleaning and surface treatment

Si/SiO_2 wafers with an oxide thickness of 250 nm were cleaned by sonicating for 5 minutes sequentially in soapy water, distilled water, acetone, and methanol. The substrates were dried using a steady stream of nitrogen, and then treated in oxygen plasma for 15 minutes. Following plasma treatment, substrates were rinsed with distilled water and isopropanol, dried with nitrogen, and immersed in a 1 % (v/v) solution of octyltrichlorosilane (OTS) in toluene. Treatment with OTS forms a self-assembled monolayer on the SiO_2 surface.[36,37] The immersed wafers were left on a hotplate at 70 °C for ca. 24 hours. The substrates were then rinsed with toluene, blown dry with nitrogen, and dried in an oven at 70 °C under vacuum for one hour.

4.5.2 Device Fabrication

Plasma torch CNTs were purchased from Raymor NanoIntegris (Batch: RNB738-120, diameter: 0.9 – 1.5 nm, length: 0.3 – 4 μm). Semiconducting SWNTs were sorted using copolymers of either carbazole-*co*-fluorene (PCF) or fluorene-*co*-dimethoxybenzene (PFMB) (structures can be found in Supporting Information) and dispersed in toluene using previously reported procedures.[38] Previous publications provide details on the synthesis of these polymers.[39,40] UV-vis-NIR spectroscopy was used to adjust the concentration of sc-SWNTs in the dispersion by adding toluene to the dispersion until the S_{22} peak absorbance was 2.0 (1.0 cm cuvette). The sc-SWNT dispersions were sonicated for 10 minutes prior to drop-casting 0.5 μL drops onto the OTS-treated SiO_2 wafers, in the regions where the top-contact electrodes would be deposited. Once the toluene evaporated, each substrate was rinsed with toluene four times in 1 mL increments at a 45° angle, drying with nitrogen between each rinse. Next, the substrates were annealed at 200 °C in air for one hour. Gold electrodes (99.99 %, purchased from Angstrom Engineering Inc.) and interlayers were deposited using physical vapour deposition (Angstrom Engineering EvoVac thermal evaporator) and shadow masks (purchased from Ossila). Each TFT channel was 30 μm long and 1000 μm wide, with a total of 20 devices per SiO_2 wafer. Mn, Cr, MoO_3, and BCP interlayers were deposited with thicknesses of 10 nm (0.5 Å/s), 2 nm (0.5 Å/s), 10 nm (0.3 Å/s), and 10 nm (0.5 Å/s), respectively. Each wafer contained 20 individual TFTs. 50 nm of gold was then immediately deposited on top of the interlayer at a rate of 1 Å/s, without breaking vacuum.

4.5.3 Electrical Characterization

TFTs were characterized using a custom-built auto-tester and a Keithley 2614B SourceMeter. TFTs were first characterized in nitrogen inside a glovebox (O_2 < 1 ppm), followed by characterization in air, with each TFT tested four times in both environments in the linear regime using a source-drain voltage of -3 V. The electrical data was extracted using the linear regime source-drain current model, and the mobility was extracted from the transconductance.

$$I_{SD} = \frac{W\mu C_i}{L}\left((V_{GS} - V_T)V_{SD} - \frac{V_{SD}^2}{2}\right) \quad (1)$$

$$\mu = \frac{L}{WC_iV_{SD}}\frac{dI_{SD}}{dV_{GS}} \quad (2)$$

$$V_T = V_{GS}(x - intercept) - \frac{V_{SD}}{2} \quad (3)$$

The above equations were used to model and estimate TFT metrics; I_{SD} is the source-drain current, W is the channel width, μ is the mobility, C_i is the gate capacitance density (estimated using the parallel plate model), L is the channel length, V_{GS} is the gate-source voltage, V_T is the threshold voltage, and V_{SD} is the source-drain voltage. Equations (1) and (2) assume that the mobility is constant. However, the mobility does depend on V_{GS}. Mobility was extracted in the V_{GS} range of -25 to -30 V. Channel lengths were measured using an optical microscope and the mobility values were corrected for channel length variations. The hysteresis was calculated as the absolute difference between the threshold voltages of the forward and reverse scans. Contact resistance was estimated using the Y-function method; g_m is the transconductance and R_C is the contact resistance. Contact resistance values were normalized to the electrode width (R_CW, W = 1000 μm). Contact resistance-corrected mobility was calculated using Equation 9.

$$g_m = \frac{\partial I_{SD}}{\partial V_{GS}} \quad (4)$$

$$Y = \frac{I_{SD}}{\sqrt{g_m}} \quad (5)$$

$$S_1 = \frac{\partial Y}{\partial V_{GS}} \quad (6)$$

$$S_2 = \frac{\partial\left(1/\sqrt{g_m}\right)}{\partial V_{GS}} \tag{7}$$

$$R_C = \frac{S_2}{S_1} V_{SD} \tag{8}$$

$$\mu = \frac{L}{W C_i V_{SD}} S_1^2 \tag{9}$$

4.6 Supporting Information

4.6.1 Polymer Molecular Weight

The polymers, poly[9,9'-didodecylfluorene-*co*-N-(2'-decyltetradecane)-carbazole] (PCF) and poly[(2,7-(9,9-dihexade-cylfluorene)-*alt*-2,5-dimethoxybenzene)] (PFMB) were synthesized using procedures reported previous publications.[39,40] The number-average molecular weight (M_n) and the polydispersity (*PD*) for each polymer are reported in **Table 4.2** below.

Table 4.2: Number-average molecular weight (M_n) and polydispersity (*PD*) of PCF and PFMB.

Polymer	***M_n***	***PD***
PCF	65	2.7
PFMB	89	1.9

Table 3: Number of TFTs characterized.

PCF-SWNT	**P-Type in Air**	**P-Type in Nitrogen**
Au	56	33
Mn-Au	56	51
MoO_3-Au	58	56
Cr-Au	49	42
BCP-Au	46	40
PFMB-SWNT	**P-Type in Air**	**P-Type in Nitrogen**
Au	46	20
Mn-Au	47	47
MoO_3-Au	50	47
Cr-Au	56	40
BCP-Au	30	29

4.6.2 PFMB-SWCNT TFT Data

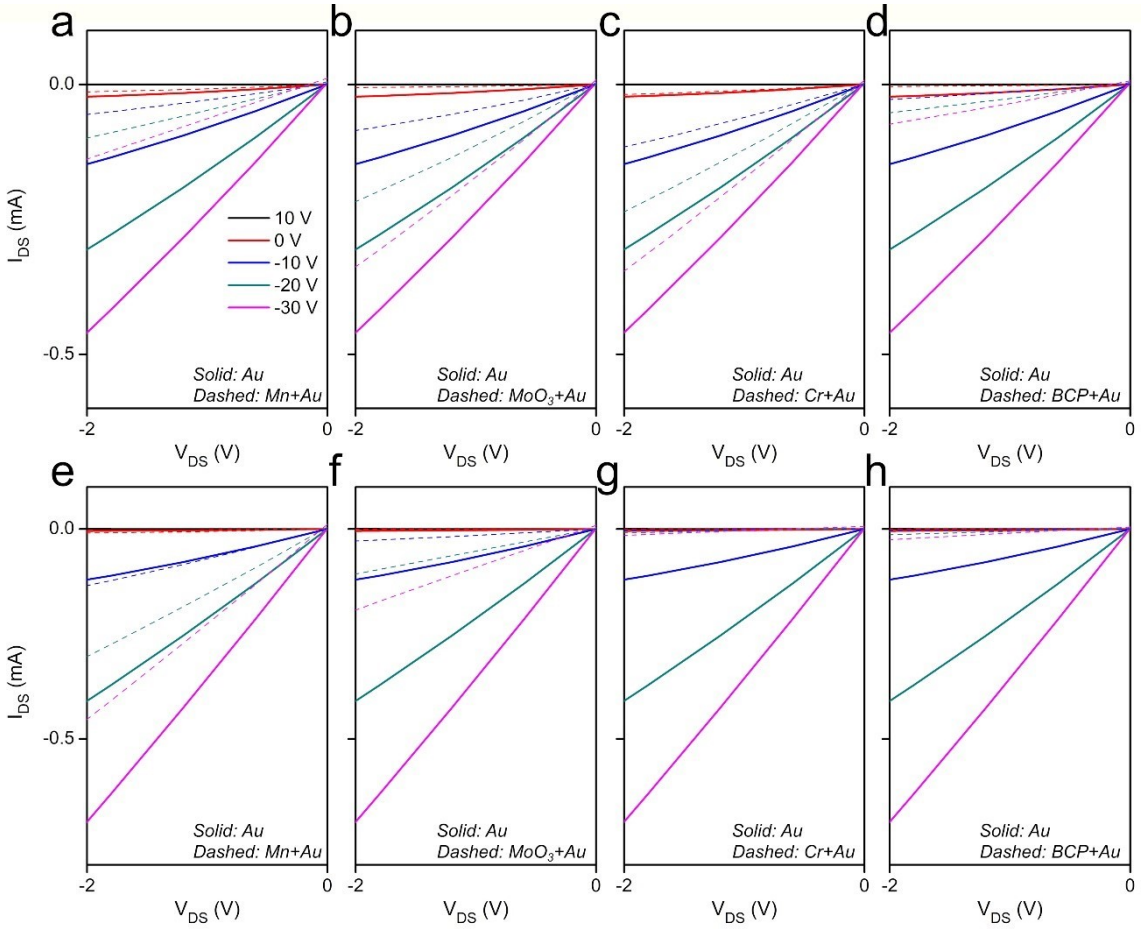

Figure 4.7: Characteristic output curve origins for **PFMB-SWNT** TFTs with different electrode interfaces measured under p-type conditions in (a-d) air and (e-h) nitrogen. Data for Au electrodes are shown using solids lines, and the data for Interface-Au electrodes are shown using dashed lines.

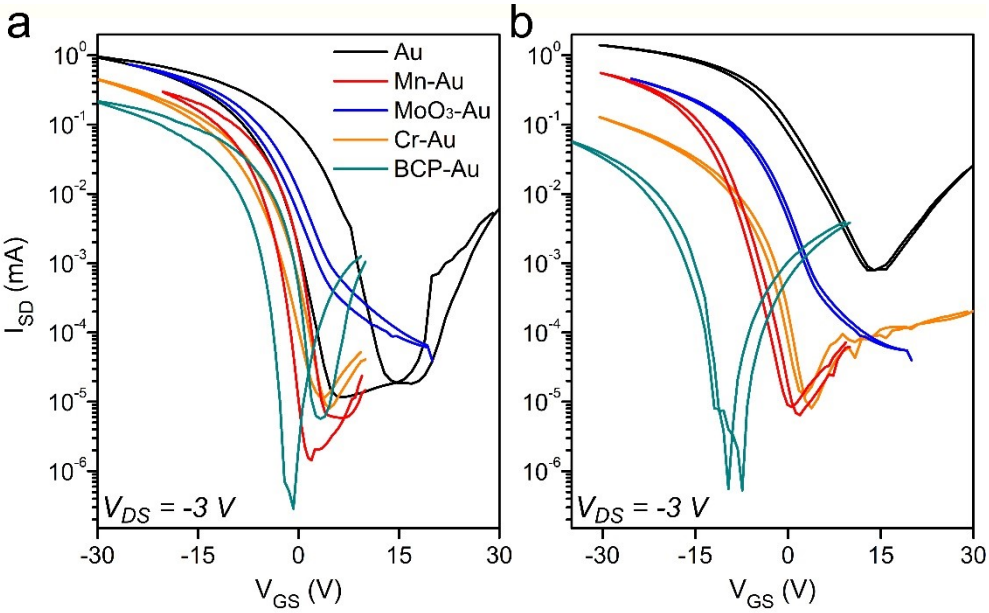

Figure 4.8: Characteristic transfer curves for **PFMB-SWNT** TFTs measured under p-type conditions in a) air and b) nitrogen.

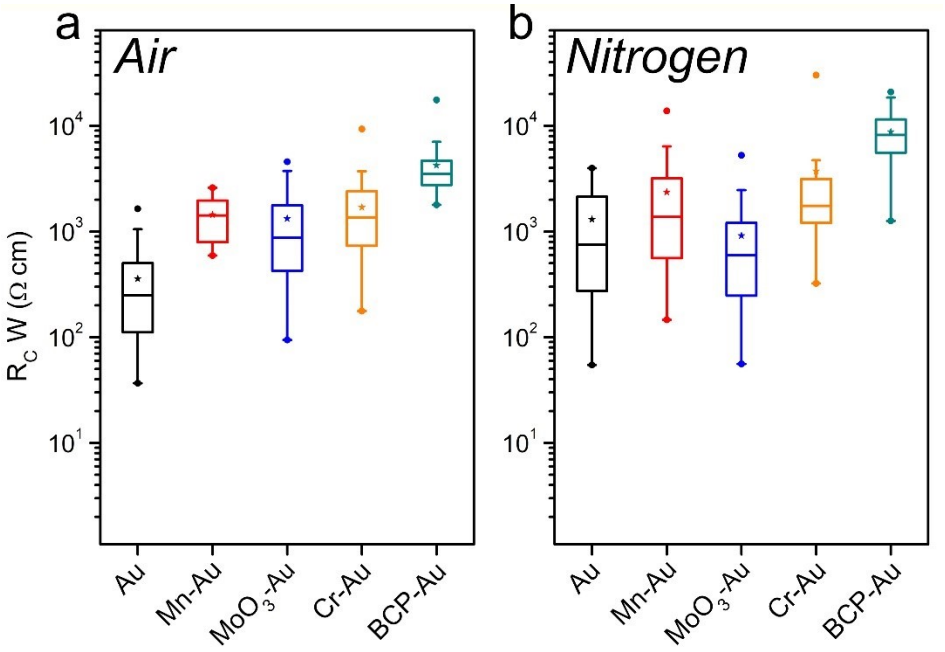

Figure 4.9: Width-normalized contact resistance (R_CW) for **PFMB-SWNT** TFTs measured under p-type conditions in a) air and b) nitrogen. R_CW values were calculated using the Y-function method. The data are represented using box plots, where the box indicates the interquartile range, the horizontal line within the box indicates the median, the star indicates the mean, the dots indicate the minimum and maximum, and the horizontal lines indicate the 5th and 95th percentile.

Table 4: Width-normalized contact resistances ($R_C W$), effective hole mobility (μ_{eff}), and contact resistance-corrected hole mobility (μ_0) for **PFMB-SWNT** TFTs measured under p-type conditions in air and nitrogen.

Contact Interface	*P-type in Air*			*P-type in N_2*		
	$R_C W$ (Ω cm)	μ_{eff} ($cm^2V^{-1}s^{-1}$)	μ_0 ($cm^2V^{-1}s^{-1}$)	$R_C W$ (Ω cm)	μ_{eff} ($cm^2V^{-1}s^{-1}$)	μ_0 ($cm^2V^{-1}s^{-1}$)
Au	$3.6 (\pm 3.7) \times 10^2$	13 ± 5.3	10 ± 5.4	$1.3 (\pm 1.3) \times 10^3$	9.8 ± 9.2	6.0 ± 5.3
Mn-Au	$1.4 (\pm 0.62) \times 10^3$	3.7 ± 1.5	11 ± 2.8	$2.4 (\pm 2.6) \times 10^3$	4.3 ± 3.1	5.5 ± 4.5
MoO_3-Au	$1.3 (\pm 1.3) \times 10^3$	6.8 ± 3.3	8.8 ± 4.5	$9.1 (\pm 10) \times 10^2$	5.7 ± 3.5	7.1 ± 5.9
Cr-Au	$1.7 (\pm 1.4) \times 10^3$	3.7 ± 2.3	7.2 ± 3.4	$3.7 (\pm 5.8) \times 10^3$	1.2 ± 1.0	2.3 ± 2.5
BCP-Au	$4.2 (\pm 2.9) \times 10^3$	2.0 ± 1.0	3.0 ± 1.3	$8.8 (\pm 4.9) \times 10^3$	0.56 ± 0.35	0.82 ± 0.50

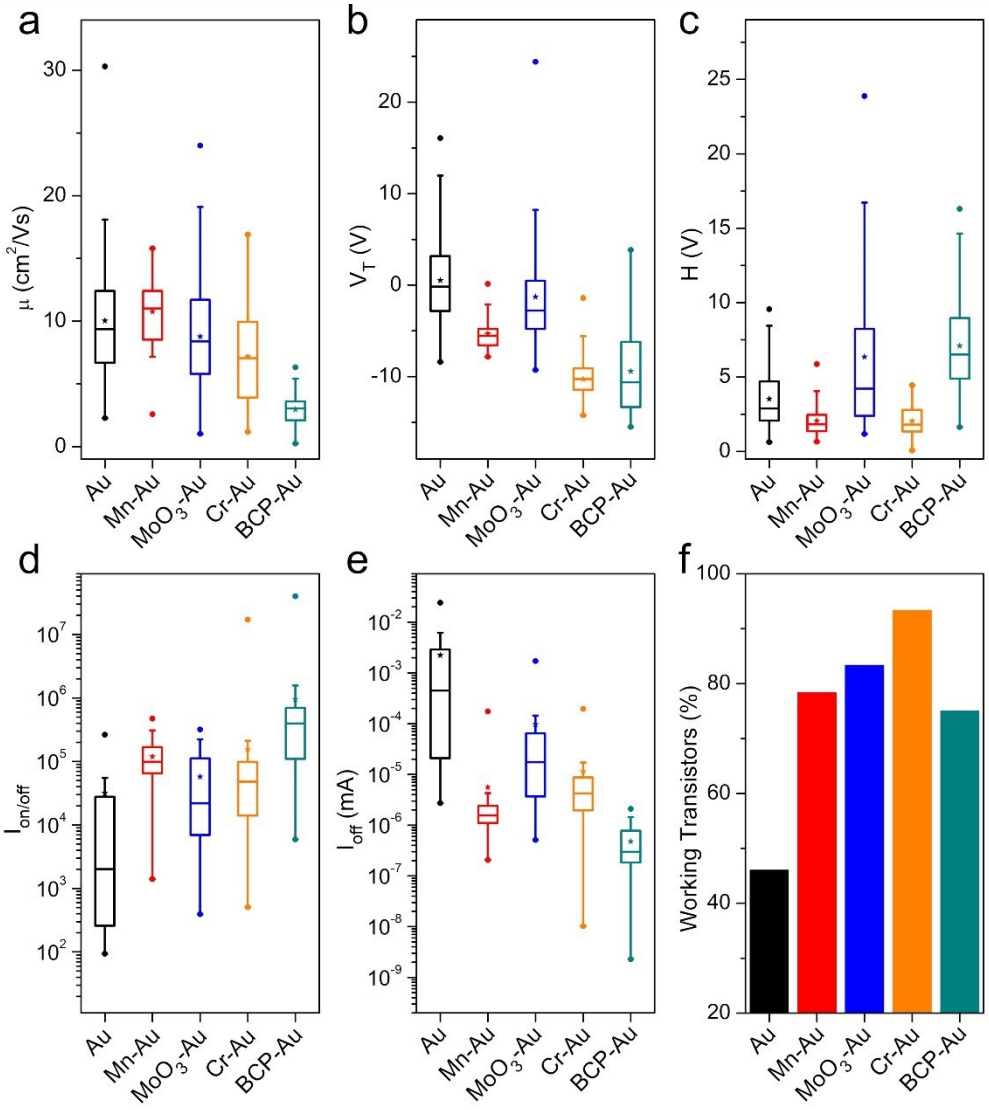

Figure 4.10: Data for **PFMB-SWNT** TFTs tested in p-type conditions in air, which include a) contact resistance-corrected mobility (μ_0), b) hole threshold voltage (V_T), c) hysteresis (H), d) current on-off ratio ($I_{on/off}$), e) off-current (I_{off}), and f) the device yield. The data are represented using box plots, where the box indicates the interquartile range, the horizontal line within the box indicates the median, the star indicates the mean, the dots indicate the minimum and maximum, and the horizontal lines indicate the 5th and 95th percentile.

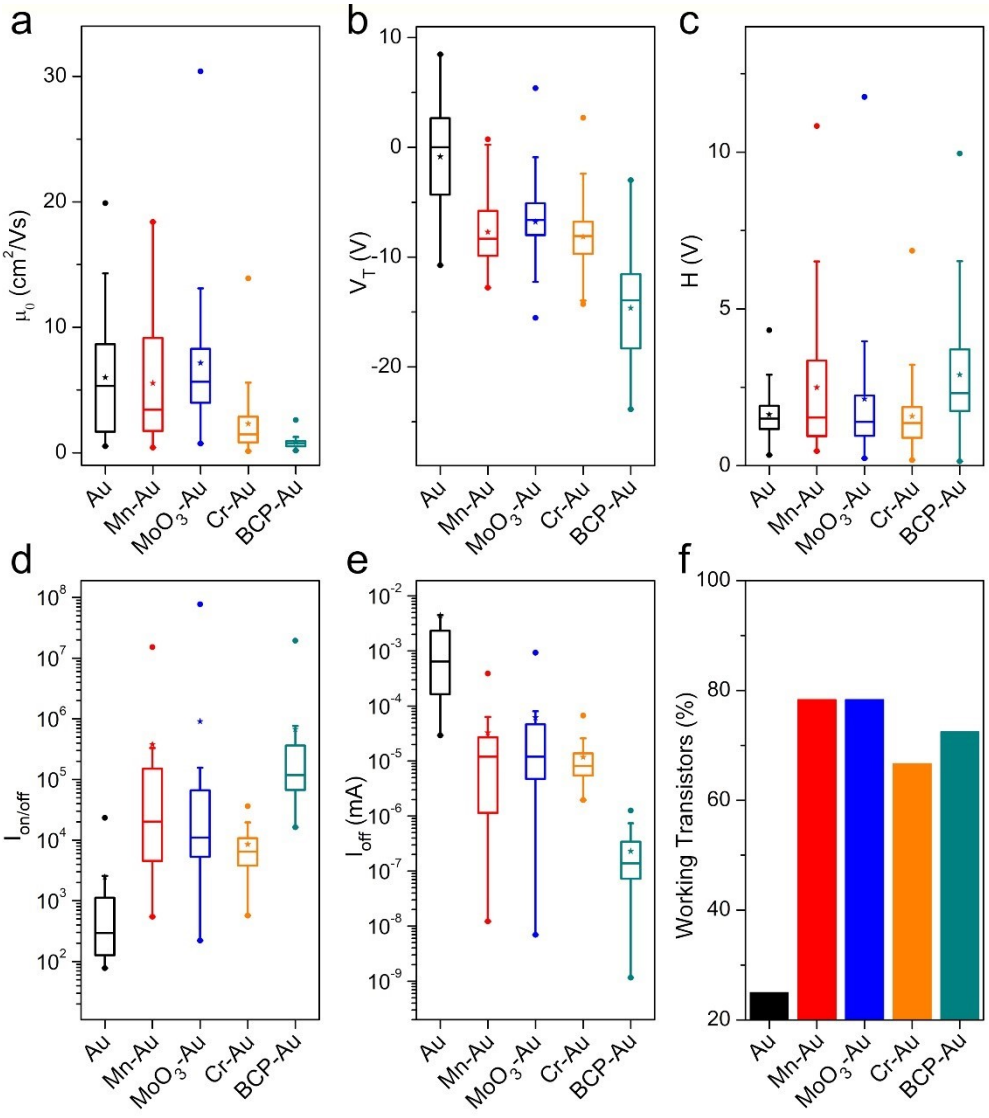

Figure 4.11: Data for **PFMB-SWNT** TFTs tested in p-type conditions in nitrogen, which include a) contact resistance-corrected mobility (μ_0), b) hole threshold voltage (V_T), c) hysteresis (H), d) current on-off ratio ($I_{on/off}$), e) off-current (I_{off}), and f) the device yield. The data are represented using box plots, where the box indicates the interquartile range, the horizontal line within the box indicates the median, the star indicates the mean, the dots indicate the minimum and maximum, and the horizontal lines indicate the 5th and 95th percentile.

4.6.3 Calculation of Minimum Channel Length

The minimum channel length, at which the contact resistance is equal to the channel resistance, was calculated as described in Ref. 52. In Equation 1 below, the channel resistance was set to equal the contact resistance, the L was calculated as L_{Min}. **Table 5** and **Table 6** display the estimated L_{Min} for **PCF-SWNT** and **PFMB-SWNT** TFTs, respectively.

$$\frac{R_{Tot}W}{L} = \frac{1}{\mu C_i(V_{GS}-V_T)} + \frac{R_C W}{L} \quad (10)$$

Table 5: Minimum channel length (L_{Min}) at which the contact resistance is equal to the channel resistance for **PCF-SWNT** TFTs measured under p-type conditions in air and nitrogen.

Contact Interface	***P-type in Air***	***P-type in N_2***
	L_{Min} (µm) ***$R_C = R_{Ch}$***	***L_{Min} (µm)*** ***$R_C = R_{Ch}$***
Au	16 ± 9.9	9.3 ± 8.7
Mn-Au	20 ± 11	6.8 ± 4.5
MoO_3-Au	10 ± 11	16 ± 9.6
Cr-Au	14 ± 9.7	11 ± 5.9
BCP-Au	23 ± 11	15 ± 6.1

Table 6: Minimum channel length (L_{Min}) at which the contact resistance is equal to the channel resistance for **PFMB-SWNT** TFTs measured under p-type conditions in air and nitrogen.

Contact Interface	***P-type in Air***	***P-type in N_2***
	L_{Min} (µm) ***$R_C = R_{Ch}$***	***L_{Min} (µm)*** ***$R_C = R_{Ch}$***
Au	10 ± 8.5	10 ± 5.5
Mn-Au	18 ± 6.8	11 ± 6.5
MoO_3-Au	25 ± 26	9.8 ± 8.1
Cr-Au	18 ± 11	7.8 ± 4.1
BCP-Au	31 ± 14	13 ± 4.3

4.6.4 Adhesion Test

The adhesion to SiO_2 for each electrode interface was measured using the cross-hatch adhesion test (ASTM F1842-09).[50,51] Contact interlayers were deposited on OTS-treated SiO_2 substrates using physical vapour deposition with the following thicknesses: Mn (10 nm), MoO_3 (10 nm), Cr (2 nm), and BCP (10 nm). 50 nm of Au was deposited on top of each interlayer. A multi-tooth cutter blade was lightly dragged across the electrode surface in a cross-hatch pattern. An abrasive brush was pressed against the surface and swept three times. Next, adhesive tape was pressed against the electrode surface and peeled off.

Images of each electrode surface are displayed in **Figure 4.12**. For each electrode surface, the procedure is depicted from left to right in the following order: neat electrode surface, application of a cross-hatch pattern, application of the abrasive brush, and the peel test using scotch tape. The Au surface was removed entirely after the brush step. The BCP-Au and Mn-Au surfaces were largely removed after the brush step, and were entirely removed after the peel step. The MoO_3-Au surface was largely intact after the brush step, but was largely removed after the peel step. The Cr-Au surface remained intact after the brush and peel steps. The adhesion classification for the Au, BCP-Au, Mn-Au, and MoO_3-Au electrode surfaces was 0B, and the Cr-Au electrode surface was 5B.

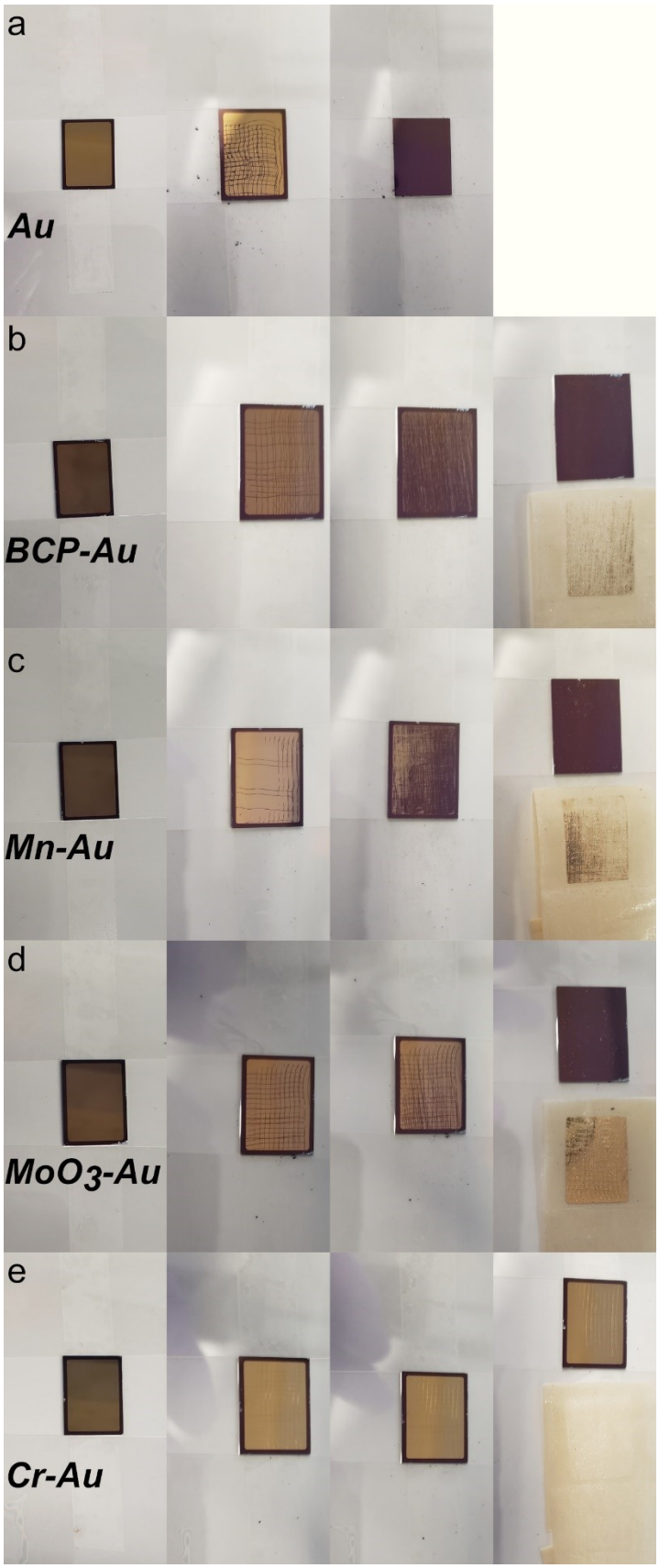
a
Au
b
BCP-Au
c
Mn-Au
d
MoO3-Au
e
Cr-Au

Figure 4.12: Cross-hatch adhesion test for a) Au, b) BCP-Au, c) Mn-Au, d) MoO_3-Au, and e) Cr-Au contacts on OTS-treated Si/SiO_2 substrates. The images are in the following order for each contact from left to right: neat surface, cross-hatch pattern from the multi-tooth blade, brushed with an abrasive brush, and peeled scotch tape.

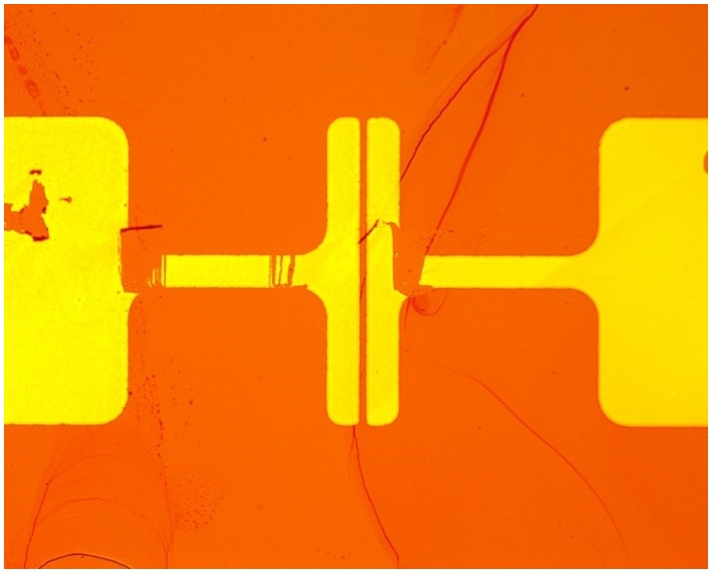

Figure 4.13: Representative image of a damaged Au contact.

4.6.5 Atomic Force Microscopy

AFM images were collected using a Bruker Dimension Icon AFM in tapping mode using Scan Asyst-Air tips. Each image was measured at a scanning rate of 1 Hz and, an image size of 5 μm × 5 μm, and a resolution of 512 lines. AFM images of **PCF-SWNT** and **PFMB-SWNT** films within the TFT channel are shown in **Figure 4.14**.

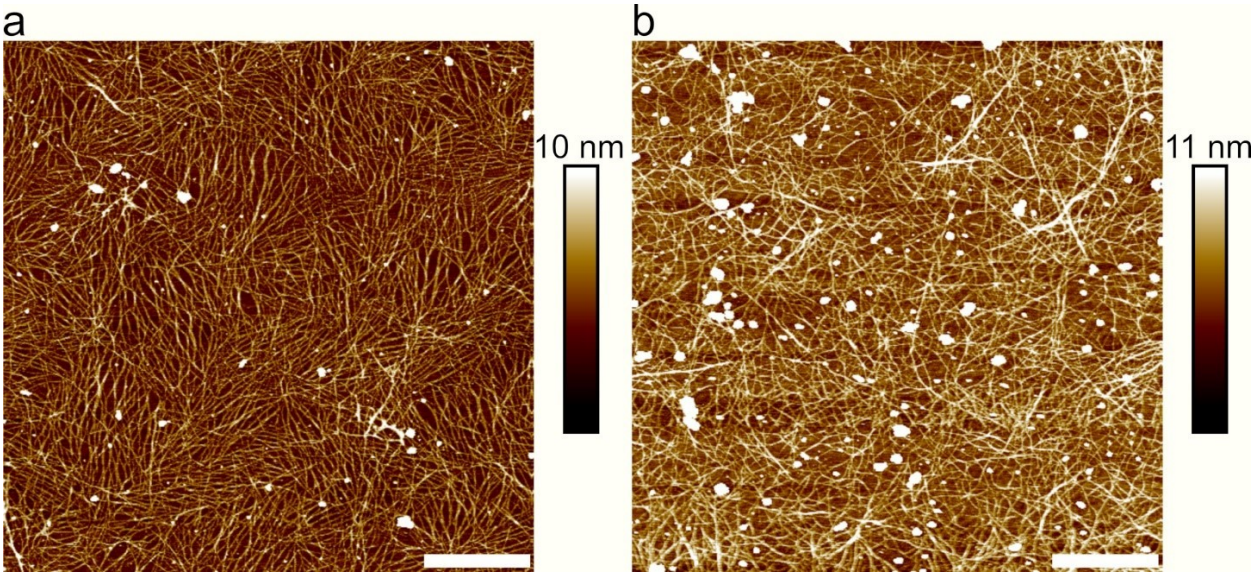

Figure 4.14: AFM images of a) PCF-SWNT and b) PFMB-SWNT films within the TFT channel. Each image is 5 µm × 5 µm and the scale bar in the bottom corner represents 1 µm.

4.6.6 UV-vis-NIR Spectroscopy

Absorption spectra were measured using a Cary 5000 Spectrometer in dual beam mode with a 1.0 cm cuvette. **Figure 4.*15*** shows the absorption spectrum of PCF-SWNT. The S_{22} peak height (~930 nm) was used as a concentration marker and was set to 2.0 prior to fabricating devices.

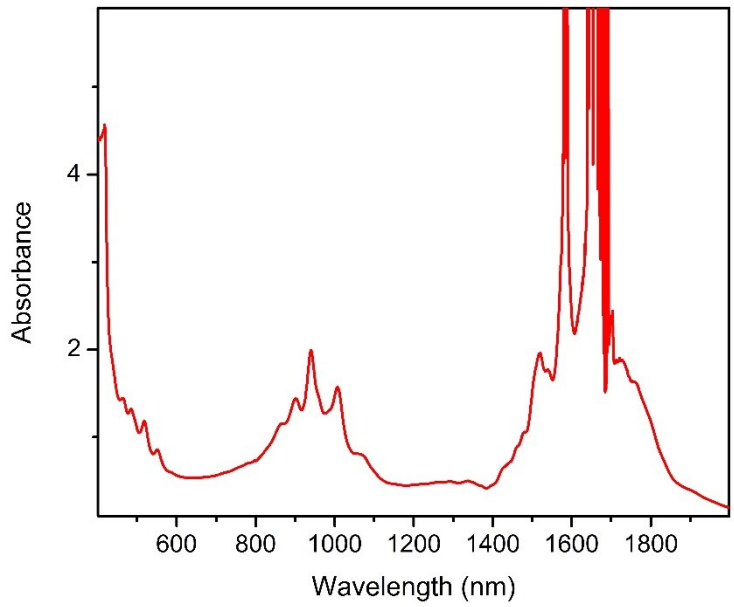

Figure 4.15: Absorption spectrum of PCF-SWNT.

4.7 References

(1) Lu, S.; Franklin, A. D. Printed Carbon Nanotube Thin-Film Transistors: Progress on Printable Materials and the Path to Applications. *Nanoscale* **2020**, *12*, 23371–23390.

(2) Kang, B.; Lee, W. H.; Cho, K. Recent Advances in Organic Transistor Printing Processes. *ACS Appl. Mater. Interfaces* **2013**, *5*, 2302–2315.

(3) Zorn, N. F.; Zaumseil, J. Charge Transport in Semiconducting Carbon Nanotube Networks. *Appl. Phys. Rev.* **2021**, *8*, 041318.

(4) Lei, T.; Shao, L. L.; Zheng, Y. Q.; Pitner, G.; Fang, G.; Zhu, C.; Li, S.; Beausoleil, R.; Wong, H. S. P.; Huang, T. C.; Cheng, K.-T.; Bao, Z. Low-Voltage High-Performance Flexible Digital and Analog Circuits Based on Ultrahigh-Purity Semiconducting Carbon Nanotubes. *Nat. Commun.* **2019**, *10*, 2161.

(5) Schnorr, J. M.; Swager, T. M. Emerging Applications of Carbon Nanotubes. *Chem. Mater.* **2011**, *23*, 646–657.

(6) Wang, H.; Mei, J.; Liu, P.; Schmidt, K.; Jiménez-Osés, G.; Osuna, S.; Fang, L.; Tassone, C. J.; Zoombelt, A. P.; Sokolov, A. N.; Houk, K. N.; Toney, M. F.; Bao, Z. Scalable and Selective Dispersion of Semiconducting Arc-Discharged Carbon Nanotubes by Dithiafulvalene/Thiophene Copolymers for Thin Film Transistors. *ACS Nano* **2013**, *7*, 2659–2668.

(7) Cao, C.; Andrews, J. B.; Kumar, A.; Franklin, A. D. Improving Contact Interfaces in Fully Printed Carbon Nanotube Thin-Film Transistors. *ACS Nano* **2016**, *10*, 5221–5229.

(8) Cao, C.; Andrews, J. B.; Kumar, A.; Franklin, A. D. Correction to: Improving Contact Interfaces in Fully Printed Carbon Nanotube Thin-Film Transistors (ACS Nano (2016) 10:5 (5221-5229) DOI: 10.1021/Acsnano.6b00877). *ACS Nano* **2017**, *11*, 4374.

(9) Aikawa, S.; Einarsson, E.; Thurakitseree, T.; Chiashi, S.; Nishikawa, E.; Maruyama, S. Deformable Transparent All-Carbon-Nanotube Transistors. *Appl. Phys. Lett.* **2012**, *100*, 063502.

(10) Wang, C.; Takei, K.; Javey, A. Carbon Nanotube Electronics - Moving Forward. *Chem. Soc. Rev.* **2013**, *42*, 2592–2609.

(11) Zhao, J.; Gao, Y.; Gu, W.; Wang, C.; Lin, J.; Chen, Z.; Cui, Z. Fabrication and Electrical Properties of All-Printed Carbon Nanotube Thin Film Transistors on Flexible Substrates. *J. Mater. Chem.* **2012**, *22*, 20747–20753.

(12) Lamport, Z. A.; Barth, K. J.; Lee, H.; Gann, E.; Engmann, S.; Chen, H.; Guthold, M.; McCulloch, I.; Anthony, J. E.; Richter, L. J.; DeLongchamp, D. M.; Jurchescu O. D. A Simple and Robust Approach to Reducing Contact Resistance in Organic Transistors. *Nat. Commun.* **2018**, *9*, 5130.

(13) Martel, R.; Derycke, V.; Lavoie, C.; Appenzeller, J.; Chan, K. K.; Tersoff, J.; Avouris, P. Ambipolar Electrical Transport in Semiconducting Single-Wall Carbon Nanotubes. *Phys. Rev. Lett.* **2001**, *87*, 256805.

(14) Benjamin, P.; Weaver, C. Adhesion of Metal Films to Glass. *Proc. R. Soc. Lond. A. Math. Phys. Sci.* **1960**, *254*, 177−183.

(15) Le-The, H.; Tiggelaar, R. M.; Berenschot, E.; van den Berg, A.; Tas, N.; Eijkel, J. C. T. Postdeposition UV-Ozone Treatment: An Enabling Technique to Enhance the Direct Adhesion of Gold Thin Films to Oxidized Silicon. *ACS Nano* **2019**, *13*, 6782–6789.

(16) Ding, J.; Li, Z.; Lefebvre, J.; Cheng, F.; Dubey, G.; Zou, S.; Finnie, P.; Hrdina, A.; Scoles, L.; Lopinski, G. P.; Kingston, C. T.; Simard, B.; Malenfant, P. R. L. Enrichment of Large-Diameter Semiconducting SWCNTs by Polyfluorene Extraction for High Network Density Thin Film Transistors. *Nanoscale* **2014**, *6*, 2328–2339.

(17) Melville, O. A.; Grant, T. M.; Lochhead, K.; King, B.; Ambrose, R.; Rice, N. A.; Boileau, N. T.; Peltekoff, A. J.; Tousignant, M.; Hill, I. G.; Lessard, B. H. Contact Engineering Using Manganese, Chromium, and Bathocuproine in Group 14 Phthalocyanine Organic Thin-Film Transistors. *ACS Appl. Electron. Mater.* **2020**, *2*, 1313–1322.

(18) Wang, H.; Cobb, B.; van Breemen, A.; Gelinck, G.; Bao, Z. Highly Stable Carbon Nanotube Top-Gate Transistors with Tunable Threshold Voltage. *Adv. Mater.* **2014**, *26*, 4588–4593.

(19) Chu, C.-W.; Li, S.-H.; Chen, C.-W.; Shrotriya, V.; Yang, Y. High-Performance Organic Thin-Film Transistors with Metal Oxide/Metal Bilayer Electrode. *Appl. Phys. Lett.* **2005**, *87*, 193508.

(20) Leandro, L.; Malureanu, R.; Rozlosnik, N.; Lavrinenko, A. Ultrathin, Ultrasmooth Gold Layer on Dielectrics without the Use of Additional Metallic Adhesion Layers. *ACS Appl. Mater. Interfaces* **2015**, *7*, 5797–5802.

(21) Min, K.; Umar, M.; Ryu, S.; Lee, S.; Kim, S. Silk Protein as a New Optically Transparent Adhesion Layer for an Ultra-Smooth Sub-10nm Gold Layer. *Nanotechnology* **2017**, *28*, 115201.

(22) Kumatani, A.; Li, Y.; Darmawan, P.; Minari, T.; Tsukagoshi, K. On Practical Charge Injection at the Metal/Organic Semiconductor Interface. *Sci. Rep.* **2013**, *3*, 1026.

(23) Liu, C.; Xu, Y.; Noh, Y.-Y. Contact Engineering in Organic Field-Effect Transistors. *Mater. Today* **2015**, *18*, 79–96.

(24) Kumaki, D.; Umeda, T.; Tokito, S. Reducing the Contact Resistance of Bottom-Contact Pentacene Thin-Film Transistors by Employing a MoO_x Carrier Injection Layer. *Appl. Phys. Lett.* **2008**, *92*, 013301.

(25) Yi, Y.; Jeon, P. E.; Lee, H.; Han, K.; Kim, H. S.; Jeong, K.; Wan Cho, S. The Interface State Assisted Charge Transport at the MoO_3/Metal Interface. *J. Chem. Phys.* **2009**, *130*, 094704.

(26) Gwinner, M. C.; Pietro, R. Di; Vaynzof, Y.; Greenberg, K. J.; Ho, P. K. H.; Friend, R. H.; Sirringhaus, H. Doping of Organic Semiconductors Using Molybdenum Trioxide: A Quantitative Time-Dependent Electrical and Spectroscopic Study. *Adv. Funct. Mater.* **2011**, *21*, 1432–1441.

(27) Kano, M.; Minari, T.; Tsukagoshi, K. Improvement of Subthreshold Current Transport by Contact Interface Modification in P-Type Organic Field-Effect Transistors. *Appl. Phys. Lett.* **2009**, *94*, 143304.

(28) Meyer, J.; Khalandovsky, R.; Görrn, P.; Kahn, A. MoO_3 Films Spin-Coated from a Nanoparticle Suspension for Efficient Hole-Injection in Organic Electronics. *Adv. Mater.* **2011**, *23*, 70–73.

(29) Esconjauregui, S.; D'Arsie, L.; Guo, Y.; Yang, J.; Sugime, H.; Caneva, S.; Cepek, C.; Robertson, J. Efficient Transfer Doping of Carbon Nanotube Forests by MoO_3. *ACS Nano* **2015**, *9*, 10422–10430.

(30) Park, R. S.; Kim, H. J. K.; Pitner, G.; Neumann, C.; Mitra, S.; Wong, H.-S. P. Molybdenum Oxide on Carbon Nanotube: Doping Stability and Correlation with Work Function. *J. Appl. Phys.* **2020**, *128*, 045111.

(31) Hill, I. G.; Kahn, A. Organic Semiconductor Heterointerfaces Containing Bathocuproine. *J. Appl. Phys.* **1999**, *86*, 4515–4519.

(32) Wang, H.; Koleilat, G. I.; Liu, P.; Jiménez-Osés, G.; Lai, Y.-C.; Vosgueritchian, M.; Fang, Y.; Park, S.; Houk, K. N.; Bao, Z. High-Yield Sorting of Small-Diameter Carbon Nanotubes for Solar Cells and Transistors. *ACS Nano* **2014**, *8*, 2609–2617.

(33) Rother, M.; Schießl, S. P.; Zakharko, Y.; Gannott, F.; Zaumseil, J. Understanding Charge Transport in Mixed Networks of Semiconducting Carbon Nanotubes. *ACS Appl. Mater. Interfaces* **2016**, *8*, 5571–5579.

(34) Bucella, S. G.; Salazar-Rios, J. M.; Derenskyi, V.; Fritsch, M.; Scherf, U.; Loi, M. A.; Caironi, M. Inkjet Printed Single-Walled Carbon Nanotube Based Ambipolar and Unipolar Transistors for High-Performance Complementary Logic Circuits. *Adv. Electron. Mater.* **2016**, *2*, 1600094.

(35) Dallaire, N. J.; Brixi, S.; Claus, M.; Blawid, S.; Lessard, B. H. Benchmarking Contact Quality in N-Type Organic Thin Film Transistors through an Improved Virtual-Source Emission-Diffusion Model. *Appl. Phys. Rev.* **2022**, *9*, 011418.

(36) Melville, O. A.; Rice, N. A.; Therrien, I.; Lessard, B. H. Organic Thin-Film Transistors Incorporating a Commercial Pigment (Hostasol Red GG) as a Low-Cost Semiconductor. *Dye. Pigment.* **2018**, *149*, 449–455.

(37) Ito, Y.; Virkar, A. A.; Mannsfeld, S.; Oh, J. H.; Toney, M.; Locklin, J.; Bao, Z. Crystalline Ultrasmooth Self-Assembled Monolayers of Alkylsilanes for Organic Field-Effect Transistors. *J. Am. Chem. Soc.* **2009**, *131*, 9396–9404.

(38) Mirka, B.; Rice, N. A.; Williams, P.; Tousignant, M. N.; Boileau, N. T.; Bodnaryk, W. J.; Fong, D.; Adronov, A.; Lessard, B. H. Excess Polymer in Single-Walled Carbon Nanotube Thin-Film Transistors: Its Removal Prior to Fabrication Is Unnecessary. *ACS Nano* **2021**, *15*, 8252–8266.

(39) Mirka, B.; Fong, D.; Rice, N. A.; Melville, O. A.; Adronov, A.; Lessard, B. H. Polyfluorene-Sorted Semiconducting Single-Walled Carbon Nanotubes for Applications in Thin-Film Transistors. *Chem. Mater.* **2019**, *31*, 2863–2872.

(40) Rice, N. A.; Bodnaryk, W. J.; Mirka, B.; Melville, O. A.; Adronov, A.; Lessard, B. H. Polycarbazole-Sorted Semiconducting Single-Walled Carbon Nanotubes for Incorporation into Organic Thin Film Transistors. *Adv. Electron. Mater.* **2019**, *5*, 1800539.

(41) Klauk, H. *Organic Electronics: Materials, Manufacturing, and Applications*; Wiley-VCH: Weinheim, Germany, 2006.

(42) Bao, Z.; Locklin, J. *Organic Field-Effect Transistors*; CRC Press: Boca Raton, FL, USA, 2007.

(43) Aguirre, C. M.; Levesque, P. L.; Paillet, M.; Lapointe, F.; St-Antoine, B. C.; Desjardins, P.; Martel, R. The Role of the Oxygen/Water Redox Couple in Suppressing Electron Conduction in Field-Effect Transistors. *Adv. Mater.* **2009**, *21*, 3087–3091.

(44) Schießl, S. P.; Fröhlich, N.; Held, M.; Gannott, F.; Schweiger, M.; Forster, M.; Scherf, U.; Zaumseil, J. Polymer-Sorted Semiconducting Carbon Nanotube Networks for High-Performance Ambipolar Field-Effect Transistors. *ACS Appl. Mater. Interfaces* **2015**, *7*, 682–689.

(45) Derycke, V.; Martel, R.; Appenzeller, J.; Avouris, P. Controlling Doping and Carrier Injection in Carbon Nanotube Transistors. *Appl. Phys. Lett.* **2002**, *80*, 2773–2775.

(46) Wan, A.; Hwang, J.; Amy, F.; Kahn, A. Impact of Electrode Contamination on the A-NPD/Au Hole Injection Barrier. *Org. Electron.* **2005**, *6*, 47–54.

(47) Rentenberger, S.; Vollmer, A.; Zojer, E.; Schennach, R.; Koch, N. UV/ozone Treated Au for Air-Stable, Low Hole Injection Barrier Electrodes in Organic Electronics. *J. Appl. Phys.* **2006**, *100*, 053701.

(48) Zangwill, A. *Physics at Surfaces*; Cambridge University Press: Cambridge, United Kingdom, 1988.

(49) Heinze, S.; Tersoff, J.; Martel, R.; Derycke, V.; Appenzeller, J.; Avouris, P. Carbon Nanotubes as Schottky Barrier Transistors. *Phys. Rev. Lett.* **2002**, *89*, 106801.

(50) ASTM F1842-09: Standard Test Method for Determining Ink or Coating Adhesion on Plastic Substrates for Membrane Switch Applications.

(51) Kell, A. J.; Paquet, C.; Mozenson, O.; Djavani-Tabrizi, I.; Deore, B.; Liu, X.; Lopinski, G. P.; James, R.; Hettak, K.; Shaker, J.; Momciu, A.; Ferrigno, J.; Ferrand, O.; Hu, J. X.; Lafrenière, S.; Malenfant, P. R. L. Versatile Molecular Silver Ink Platform for Printed Flexible Electronics. *ACS Appl. Mater. Interfaces* **2017**, *9*, 17226–17237.

Chapter 5: Concluding Remarks and Recommendations for Future Work

5.1 Concluding Remarks

Single-walled carbon nanotubes are exceptional candidates for flexible, next-generation electronic devices. Though they are synthesized as a mixture of semiconducting and metallic species, conjugated polymers can selectively sort semiconducting single-walled carbon nanotubes into ultra-pure dispersions. In addition, sorting and dispersing using conjugated polymers facilitates solution processing of SWNTs. Dispersions of semiconducting SWNTs can be incorporated into electronic devices using solution processing techniques, thereby reducing manufacturing barriers. Flexible, conformable, and inexpensive thin-film transistors are of particular interest for sensing applications, wearable electronic devices, and active-matrix backplanes. Polymer-sorted sc-SWNTs are ideal materials for such applications.

In **Chapter 2**, a novel copolymer poly(fluorene-*co*-dimethoxybenzene) (PFMB) was used to sort and disperse large-diameter sc-SWNTs for integration into TFTs. The polymer was designed to sort large-diameter SWNTs. The increased length of the alkyl chain and the polymer backbone's rigidity contributed to the selection of larger diameter SWNTs. Additionally, an electron-rich dimethoxybenzene group was incorporated into the polymer backbone to adjust the electronic nature to better select for electron-poor sc-SWNTs. The absorption peak ratio analysis using UV-vis-NIR spectroscopy and the radial breathing mode and *G*-band modes using Raman spectroscopy showed that the polymer could sort sc-SWNTs into ultra-pure dispersions. PFMB-SWNT dispersions were incorporated into TFTs using a solution-based drop-casting technique. TFTs were fabricated using PFMB-SWNT dispersions that had been filtered (to remove the excess, unbound polymer) and dispersions that had not been filtered (with the excess polymer remaining in the dispersion). The rationale for comparing these two dispersion conditions was to determine whether or not a filtration step would be necessary. If filtration were unnecessary, its elimination would improve the scalability of conjugated polymer extraction. Interestingly, TFTs fabricated using excess polymer dispersions performed no worse than TFTs fabricated using filtered dispersions. However, the data did not support any firm conclusions, and more work was necessary.

The work done in **Chapter 3** focused on a more comprehensive investigation of the question that was asked in **Chapter 2**: is it necessary to remove the excess polymer before TFT fabrication? Two different SWNT dispersions were prepared using two copolymers: a poly(fluorene-*co*-carbazole) (PCF) and a poly(fluorene-*co*-dimethoxybenzene) (PFMB). Both polymer-SWNT dispersions were divided into different polymer conditions: no excess polymer (dispersions that were filtered), excess polymer (dispersions that were not filtered), and polymer added (dispersions that were filtered and then had controlled amounts of polymer added). Raman spectroscopy showed that a solvent rinse step could effectively remove the excess polymer from the film after SWNT deposition. Thus, it was concluded that filtration was unnecessary prior to SWNT TFT fabrication. Each polymer-SWNT dispersion, including each polymer condition, was incorporated into SWNT TFTs. Electrical characterization showed that TFTs fabricated with excess polymer dispersions performed no worse than those with excess polymer removed. Thus, the TFT data did not justify excess polymer removal. Investigation of the thin-film morphology provided further insight into the role of excess polymer in SWNT film formation. Raman mapping of the TFT channels showed that the SWNT film was more homogenous for dispersions with excess polymer than films formed from dispersions without excess polymer. Atomic force microscopy also confirmed this finding. For the conjugated polymers used in this work, PCF and PFMB, it was demonstrated that dispersion filtration is unnecessary, thus making dispersion preparation more amenable to a large-scale operation.

The work done in **Chapter 4** focused on contact engineering techniques to improve the reproducibility of SWNT TFTs fabricated in a laboratory. Laboratory-scale SWNT TFTs with gold source-drain contacts deposited using physical vapour deposition suffer from poor gold adhesion to the substrate. Poor adhesion results in damaged contacts and non-functional TFTs. It is common to deposit a thin contact interlayer to facilitate gold adhesion and make the contacts mechanically robust. In this study, different contact interlayers in top-contact SWNT TFTs were investigated to improve TFT reproducibility and study the effect on device performance. The contact interlayers investigated included molybdenum trioxide (MoO_3), manganese (Mn), chromium (Cr), and 2,9-dimethyl-4,7-diphenyl-1,10-phenanthroline (BCP). SWNT TFTs were electrically characterized in air and nitrogen atmospheres. The incorporation of a contact interlayer improved electrode adhesion significantly. The use of contact interlayers increased the number of functioning TFTs due to fewer damaged contacts, primarily the use of MoO_3-Au and Mn-Au contacts. TFTs with

MoO_3-Au contacts yielded far fewer non-functioning TFTs from contact damage. Furthermore, despite the differences in work function (WF), SWNT TFTs characterized in air did not strongly depend on the contact interlayer, whereas TFTs characterized in nitrogen showed a stronger dependence on the contact interlayer. This finding suggests that the effects of oxygen adsorption at the contact-SWNT interface affect device performance more than differences in WF. TFTs characterized in air with MoO_3-Au and Au contacts exhibited a similar mobility and contact resistance, with the added benefit of improved reproducibility using MoO_3-Au contacts. For TFTs characterized in nitrogen, Mn-Au contacts provided the best results in terms of TFT reproducibility, and mobility and contact resistance similar to Au contacts, despite the difference in WF between Mn and Au.

5.2 Recommendations for Future Work

There is great promise for polymer-sorted semiconducting single-walled carbon nanotubes. Certain conjugated polymers have been demonstrated to selectively sort sc-SWNTs in ultra-pure dispersions, facilitating their incorporation into electronic devices. Adronov and coworkers demonstrated that the electronic nature of the conjugated polymer backbone affects selectivity towards sc-SWNTs.[1,2] The conjugated polymer backbone can be tuned so that it is either more electron-donating or more electron-withdrawing. When controlling for other factors, conjugated polymers that are more electron-donating show selectivity towards electron-poor sc-SWNTs, and polymers that are more electron-withdrawing will bias towards dispersing electron-rich m-SWNTs. Rice *et al*. synthesized two structurally similar poly(fluorene-*co*-phenylene) copolymers; one copolymer included an electron-donating methoxy functionality, and the other copolymer included an electron-withdrawing nitro functionality.[2] The copolymer with the electron-donating methoxy functionality preferentially dispersed sc-SWNTs, and the copolymer with an electron-withdrawing nitro functionality biased selectivity towards dispersion of metallic SWNTs.[2] Bodnaryk, Fong, and Adronov used the same rationale to prepare enriched dispersions of metallic SWNTs using an electron-withdrawing copolymer, poly(fluorene-*co*-pyridine).[3] Therefore, sc-SWNTs sorted using an electron-donating polymer might have a larger electron density.

In SWNTs, changes in charge density caused by an external electric field can shift the frequency of the *G*-band phonon mode.[4] In sc-SWNTs, application of a gate voltage (V_g) causes

an increase (decrease) in the G^+-band frequency for hole (electron) doping,[5] though this phenomenon may differ small diameter sc-SWNTs due to curvature effects.[6] For m-SWNTs, an applied V_g causes the frequency of the G^--band to increase for electron and hole doping due to the Kohn anomaly.[5,7] Thus, in-situ Raman spectroscopy can measure the level of doping in semiconducting and metallic SWNTs. Conjugated polymers with different degrees of electron-donating or electron-withdrawing character may show V_g dependent shifts in the *G*-band frequency. Raman spectra for different polymer-SWNT complexes can be measured in-situ while applying a V_g. An investigation could begin by preparing different films of sc-SWNTs sorted using conjugated polymers with different degrees of electron-donating/-withdrawing character. External electronic interactions should be controlled for, such as charge doping from adsorbed molecules or electric fields created by trapped chargers at the substrate. To control for these environmental interactions, SWNT films can be prepared in a nitrogen atmosphere, and a self-assembled monolayer can be deposited onto the substrate. Additionally, an encapsulating layer can be used, and the films can be characterized in a nitrogen atmosphere. A V_g can be applied across the polymer-SWNT film, and the *G*-band spectra can be measured while the film is under bias. Changes in the location of the *G*-band will provide insight into the degree of electron or hole doping from the conjugated polymer to the sc-SWNT. Furthermore, the degree of doping from the polymer will provide additional insight into charge transfer throughout the polymer-SWNT network. It should be noted, however, that the doping-induced shift of the G^--band for sc-SWNTs is small, and that doping effects may not be observable.

The influence of the polymer backbone on charge transfer in SWNT films is not well understood. It is often assumed that the effect on charge transfer is insignificant due to the non-covalent interaction between the polymer and the sc-SWNT. However, it is not entirely clear to what extent the polymer is involved in charge transport within the SWNT network. Other researchers have demonstrated energy transfer between the conjugated polymer and sc-SWNTs.[8] Furthermore, the electronic nature of the polymer backbone may influence the hysteresis effect in SWNT TFTs by introducing charge traps. Certain polymer-SWNT complexes may behave as unipolar p-type in air, while others may be closer to ambipolar. In-situ Raman spectroscopy on SWNTs may provide insight into different conjugated polymers' electronic effects. The electronic nature of the polymer backbone can be used to tune the selectivity toward sc-SWNTs. Additionally, the change in *G*-band frequency for different polymer-SWNT complexes would

provide insight into charge transport within the polymer-SWNT network. Insight into the degree of electron or hole doping from the conjugated polymer to the sc-SWNT would provide further insight into polymer design for SWNT electronic applications.

5.3 References

(1) Fong, D.; Bodnaryk, W. J.; Rice, N. A.; Saem, S.; Moran-Mirabal, J. M.; Adronov, A. Influence of Polymer Electronics on Selective Dispersion of Single-Walled Carbon Nanotubes. *Chem. - A Eur. J.* **2016**, *22*, 14560–14566.

(2) Rice, N. A.; Subrahmanyam, A. V.; Coleman, B. R.; Adronov, A. Effect of Induction on the Dispersion of Semiconducting and Metallic Single-Walled Carbon Nanotubes Using Conjugated Polymers. *Macromolecules* **2015**, *48*, 5155–5161.

(3) Bodnaryk, W. J.; Fong, D.; Adronov, A. Enrichment of Metallic Carbon Nanotubes Using a Two-Polymer Extraction Method. *ACS Omega* **2018**, *3*, 16238–16245.

(4) Tsang, J. C.; Freitag, M.; Perebeinos, V.; Liu, J.; Avouris, P. H. Doping and Phonon Renormalization in Carbon Nanotubes. *Nat. Nanotechnol.* **2007**, *2*, 725–730.

(5) Das, A.; Sood, A. K.; Govindaraj, A.; Saitta, A. M.; Lazzeri, M.; Mauri, F.; Rao, C. N. R. Doping in Carbon Nanotubes Probed by Raman and Transport Measurements. *Phys. Rev. Lett.* **2007**, *99*, 136803.

(6) Grimm, S.; Schießl, S. P.; Zakharko, Y.; Rother, M.; Brohmann, M.; Zaumseil, J. Doping-Dependent G-Mode Shifts of Small Diameter Semiconducting Single-Walled Carbon Nanotubes. *Carbon* **2017**, *118*, 261–267.

(7) Piscanec, S.; Lazzeri, M.; Robertson, J.; Ferrari, A. C.; Mauri, F. Optical Phonons in Carbon Nanotubes: Kohn Anomalies, Peierls Distortions, and Dynamic Effects. *Phys. Rev. B* **2007**, *75*, 035427.

(8) Kuang, Z.; Berger, F. J.; Luis Pérez Lustres, J.; Wollscheid, N.; Li, H.; Lüttgens, J.; Balci Leinen, M.; Flavel, B. S.; Zaumseil, J.; Buckup, T. Charge Transfer from Photoexcited Semiconducting Single-Walled Carbon Nanotubes to Wide-Bandgap Wrapping Polymer. *J. Phys. Chem. B* **2021**, *125*, 8125–8136.

Chapter 6: Additional Literature Contributions

6.1 Air and Temperature Sensitivity of n-type Polymer Materials to Meet and Exceed the Standard of N2200

Samantha Brixi, Owen A. Melville, Brendan Mirka, Yinghui He, Arthur D. Hendsbee, Han Meng, Yuning Li, and Benoît H. Lessard

Publication Date: 04 March 2020

Citation: *Scientific Reports* **2020**, *10*, 4014.

DOI: 10.1038/s41598-020-60812-x

Abstract

N-type organic semiconductors are notoriously unstable in air, requiring the design of new materials that focus on lowering their LUMO energy levels and enhancing their air stability in organic electronic devices such as organic thin-film transistors (OTFTs). Since the discovery of the notably air-stable and high electron mobility polymer poly{[n,n′-bis (2-octyldodecyl)-naphthalene-1,4,5,8- bis(dicarboximide)-2,6-diyl]-alt-5,5′-(2,29-bisthiophene)} (N2200), it has become a popular n-type semiconductor, with numerous materials being designed to mimic its structure. Although N2200 itself is well-studied, many of these comparable materials have not been sufficiently characterized to compare their air stability to N2200. To further the development of air-stable and high mobility n-type organic semiconductors, N2200 was studied in organic thin-film transistors alongside three N2200-based analogues as well as a recently developed polymer based on a (3E,7E)-3,7-bis(2-oxoindolin-3- ylidene)benzo[1,2-b:4,5-b′]difuran-2,6(3 H,7 H)-dione (IBDF) core. This IBDF polymer has demonstrated promising field-effect mobility and air stability in drop-cast OTFTs. While N2200 outperformed its analogues, the IBDF-based polymer displayed superior air and temperature stability compared to N2200. Overall, polymers with more heteroatoms displayed greater air stability. These findings will support the development of new air-stable materials, and further demonstrate the persistent need to develop novel n-type semiconductors.

Contribution

I performed the atomic force microscopy (AFM) experiments and edited the AFM images for this study. I also reviewed the prepared manuscript.

6.2 Metal Phthalocyanine Organic Thin-Film Transistors: Changes in Electrical Performance and Stability in Response to Temperature and Environment

Nicholas T. Boileau, Rosemary Cranston, Brendan Mirka, Owen A. Melville and Benoît H. Lessard

Publication Date: 10 July 2019

Citation: *RSC Adv*. **2019**, *9*, 21478–21485.

DOI: 10.1039/c9ra03648b

Abstract

Metal phthalocyanines (MPcs) are a widely studied class of materials that are used frequently in organic thin-film transistors (OTFTs), organic photovoltaics (OPVs) and organic light-emitting diodes (OLEDs). The stability of these devices and the materials used in their fabrication is important to realize their widespread adoption. Seven P-type MPcs: zinc (ZnPc), magnesium (MgPc), aluminum (AlClPc), iron (FePc), cobalt (CoPc), and titanium (TiOPc) were investigated as semiconductors in OTFTs under varying temperatures (25 °C to 150 °C) and environmental conditions (air and vacuum, $P < 0.1$ Pa). Devices using the divalent MPcs (except MgPc) showed significant shifts in threshold voltage and field-effect mobility with rising temperature in both air and vacuum. AlClPc and TiOPc, on the other hand, had more stable electrical properties, making them useful for applications requiring consistent performance. Distinct variations in film morphology as determined by atomic force microscopy may explain the different thermal responses between the two groups of MPcs, while thermal gravimetric analysis in air and nitrogen provides additional insight into their susceptibility to oxidation at elevated temperatures. To demonstrate proof-of-concept thermal sensing under realistic operating conditions, current changes were monitored in response to temperature stimuli using two more sensitive divalent MPcs. In this comparative study of the effect of central atom inclusion in MPcs, the resulting material stability and thin-film characteristics will facilitate the design of future sensors and other OTFT applications.

Contribution

I performed the AFM experiments and AFM image processing and analysis for this study. I also reviewed the prepared manuscript.

6.3 Ambipolarity and Air Stability of Silicon Phthalocyanine Organic Thin-Film Transistors

Owen A. Melville, Trevor M. Grant, Brendan Mirka, Nicholas T. Boileau, Jeongwon Park, and Benoît H. Lessard

Publication Date: 06 May 2019

Citation: *Adv. Electron. Mater.* **2019**, *5*, 1900087.

DOI: 10.1002/aelm.201900087

Abstract

Silicon phthalocyanines (SiPcs) are a class of conjugated, planar molecules that have recently been investigated for use in organic photovoltaics (OPVs), organic light-emitting diodes (OLEDs), and organic thin-film transistors (OTFTs) due to their variable structure and ease of synthesis. Bottom-gate, bottom-contact OTFTs with four SiPc derivatives used as the semiconducting layers are prepared using physical vapour deposition. Devices using bis(pentafluorophenoxy) silicon phthalocyanine (F10-SiPc) deposited on 140 °C substrates demonstrate electron field-effect mobilities (μ) of up to 0.54 $cm^2V^{-1}s^{-1}$, among the best currently reported for n-type phthalocyanine-based transistors. All materials show dramatic changes in charge transport when characterized under vacuum ($P < 0.1$ Pa) compared to in air at atmospheric pressure, typically switching from electron majority charge carriers to holes, with the change dependent on material structure and energetics. F10-SiPc is close to balanced ambipolar in air, with μ around 5×10^{-3} $cm^2V^{-1}s^{-1}$ for both holes and electrons. These results demonstrate SiPcs' potential as n-type semiconductors in OTFTs as well as their adjustable charge transport as affected by the operating environment.

Contribution

For this study, I performed some the device characterization experiments. I also performed the AFM experiments and processed the AFM images. I reviewed the prepared manuscript.

6.4 P- and n-Type Copper Phthalocyanines as Effective Semiconductors in Organic Thin-Film Transistor Based DNA Biosensors at Elevated Temperatures

Nicholas T. Boileau, Owen A. Melville, Brendan Mirka, Rosemary Cranston and Benoît H. Lessard

Publication Date: 15 January 2019

Citation: *RSC Adv*. **2019**, *9*, 2133–2142.

DOI: 10.1039/c8ra08829b

Abstract

Many health-related diagnostics are expensive, time-consuming and invasive. Organic thin-film transistor (OTFT) based devices show promise to enable rapid, low-cost diagnostics that are an important aspect of enabling increased access and availability to healthcare. Here, we describe OTFTs based upon two structurally similar p- (copper phthalocyanine – CuPc) and n-type (hexdecafluoro copper phthalocyanine – F_{16}-CuPc) semiconductor materials and demonstrate their potential for use as both temperature and DNA sensors. Bottom-gate, bottom-contact (BGBC) OTFTs with either CuPc or F_{16}-CuPc semiconducting layers were characterized within a temperature range of 25 °C to 90 °C in both air and under vacuum. CuPc devices showed small positive shifts in threshold voltage (V_T) in air and significant linear increases in mobility with increasing temperature. F_{16}-CuPc devices showed large negative shifts in V_T in air and linear increases in mobility under the same conditions. Similar OTFTs were exposed to DNA in different hybridization states, and both series of devices showed positive V_T increases upon DNA exposure, with a larger response to single-stranded DNA. The n-type F_{16}-CuPc devices showed a much greater sensing response than the p-type CuPc. These findings illustrate the use of these materials, especially the n-type semiconductor, as both temperature and DNA sensors and further elucidate the mechanism of DNA sensing in OTFTs.

Contributions

I performed the AFM experiments and AFM image processing and analysis for this study. I also reviewed the prepared manuscript.

6.5 Polycarbazole-Sorted Semiconducting Single-Walled Carbon Nanotubes for Incorporation into Organic Thin-Film Transistors

Nicole A. Rice, William J. Bodnaryk, Brendan Mirka, Owen A. Melville, Alex Adronov, and Benoît H. Lessard

Publication Date: 12 November 2018

Citation: *Adv. Electron. Mater.* **2019**, *5*, 1800539.

DOI: 10.1002/aelm.201800539

Abstract

The realization of organic thin-film transistors (OTFTs) with performances that support low-cost and large-area fabrication remains an important and challenging topic of investigation. The unique electrical properties of single-walled carbon nanotubes (SWNTs) make them promising building blocks for next-generation electronic devices. Significant advances in the enrichment of semiconducting SWNTs, particularly *via* π-conjugated polymers for purification and dispersal, have allowed the preparation of high-performance OTFTs on a small scale. The intimate interaction of the conjugated polymer with both SWNTs and the dielectric necessitates the investigation of a variety of conjugated polymer derivatives for device optimization. Here, the preparation of polymer–SWNT composites containing carbazole moieties, a monomer unit that has remained relatively overlooked for the dispersal of large-diameter semiconducting SWNTs, is reported. This polymer selectively discriminates semiconducting SWNTs using a facile procedure. OTFTs prepared from these supramolecular complexes are ambipolar and possess superior mobilities and on/off ratios compared to homo poly(fluorene) dispersions, with hole mobilities from random-network devices reaching 21 $cm^2V^{-1}s^{-1}$. Atomic force microscopy measurements suggest the poly(carbazole)–SWNT composites form more uniform thin-films compared to the poly(fluorene) dispersion. Additionally, treating the silicon dioxide dielectric with octyltrichlorosilane is a simple and effective way to reduce operational hysteresis in SWNT OTFTs.

Contribution

For this study, I assisted in preparing polymer-sorted single-walled carbon nanotube dispersions. In addition, I assisted with UV-vis-NIR and Raman spectroscopy experiments. I contributed to device characterization, including transmission-line contact resistance measurements. Finally, I reviewed the prepared manuscript.

6.6 Poly(ionic liquid) Dielectric for High Performing P- and N-type Single Walled Carbon Nanotube Transistors

Mathieu N. Tousignant, May Ourabi, Jukka Niskanen, Brendan Mirka, William J. Bodnaryk, Alex Adronov, and Benoît H. Lessard

Submission Date: 19 April 2022

Journal: Flexible and Printed Electronics

Manuscript ID: FPE-100695.R1

Abstract

There is an increasing demand for low-cost and high-performance electronics, which has stimulated a need for new high-performance gating materials. We have developed a facile synthesis of poly(2-(methacryloyloxy)ethyl trimethylammonium bis(trifluoromethylsulfonyl)azanide-*ran*-methyl methacrylate) (P(METATFSI-MMA)), a polymeric ionic liquid that can be used as a high-performance gating material for semiconducting single-walled carbon nanotube (sc-SWNT) thin-film transistors (TFTs). The P(METATFSI-MMA) polymer was synthesized at both 35 and 62 mol% of 2-(methacryloyloxy)ethyl trimethylammonium bis(trifluoromethylsulfonyl)azanide and produced p- and n-type devices that functioned under ambient conditions. These TFTs were then used to study the impact of electrochemical doping on the performance of sc-SWNT TFTs when switching from n-type, where an electrical double layer is formed, to p-type, where the TFSI anions are free to interact with the sc-SWNTs. The TFTs operating in p-type had higher current on/off ratios and a larger transconductance, which is characteristic of electrochemically doped transistors compared to the n-type devices. Furthermore, we tested the impact of operating frequency on device performance and discovered that decreasing the operating frequency of the TFTs resulted in a decreased hysteresis. The decrease in hysteresis was also more significant for the 35 mol% polymer.

Contribution

For this study, I prepared the polymer-sorted single-walled carbon nanotube dispersions. I reviewed the prepared manuscript.

6.7 Furan Functionalized Naphthalenediimide Semiconductors with Different N-alkyl Chains for n-type Organic Thin-Film Transistor Applications

Shailesh S. Birajdar, Brendan Mirka, Vilas K. Gawade, Avinash L. Puyad, Benoît H. Lessard, Sidhanath V. Bhosale, Sheshanath V. Bhosalec.

Submission Date: 16 March 2022

Journal: Dyes and Pigments

Citation: *Dyes and Pigments*, **2022**, *206*, 110603

Abstract

The development of n-type organic semiconductors (OSCs) is necessary in order to develop complementary electronics based on organic thin-film transistors (OTFTs). In this investigation, we designed and synthesized a series of four novel imide- and core-substituted naphthalene diimide (NDI) molecules. The molecular architecture was altered *via* the introduction of different alkyl side chains (octyl and 2-ethylhexyl) to the imide-N positions, and 2-dicyanomethylene-3-cyano-4,5,5-trimethyl-2,5-dihydrofuran (TCF) to the NDI core. The NDI-TCF derivatives are abbreviated as NDI-TCF1A, NDI-TCF1B, NDI-TCF2A, and NDI-TCF2B, using a "1" or "2" to indicate the number of TCF subunits at the NDI core, and an "A" or a "B" to indicate an octyl or a 2-ethylhexyl alkyl chain at the imide-N position, respectively. All four compounds displayed similar photophysical properties but exhibited different electrochemical properties with lower LUMO levels of -4.25 eV, -4.33 eV, -4.27 eV and -4.35 eV for NDI-TCF1A, NDI-TCF1B, NDI-TCF2A, and NDI-TCF2B, respectively. These LUMO levels suggest a capacity for electron transport. Furthermore, the NDI-TCF chromophores were incorporated into OTFTs and systematically studied the relationship between the NDI-TCF molecular architecture and electron transport properties. NDI-TCF1A and NDI-TCF1B displayed more consistent OTFT performance than NDI-TCF2A and NDI-TCF2B. NDI-TCF1A and NDI-TCF1B exhibited low threshold voltages (V_T) of -0.43 V ± 4.78 V and 6.12 V ± 6.63 V, respectively, and electron mobilities (μ_e) of ca. 3×10^{-5} $cm^2V^{-1}s^{-1}$, and on/off ($I_{ON/OFF}$) ratios of ca. 10^3. Insofar that TCF facilitates electron transport, the OTFT data suggest that the number of TCF subunits affects OTFT performance *via* thin-film morphology.

Contribution

For this study, I prepared and characterized all of the organic thin-film transistor devices, and processed and analyzed all of the transistor data. I also performed the AFM experiments and

processed and analyzed the AFM images. I prepared samples for mass spectroscopy and x-ray diffraction experiments. Finally, I wrote the thin-film transistor section of the manuscript and assisted in preparing and revising other sections of the manuscript.